Identification and Mitigation of T&D Operational Security Vulnerabilities in Inverter Dominated Power Systems

Final Project Report

T-65

Power Systems Engineering Research Center
Empowering Minds to Engineer
the Future Electric Energy System

Identification and Mitigation of T&D Operational Security Vulnerabilities in Inverter Dominated Power Systems

Final Project Report

Project Team
Saeed Lotfifard, Project Leader
Washington State University

Sakis A. P. Meliopoulos
George J. Cokkinides
Georgia Institute of Technology

Venktataramana Ajjarapu
Iowa State University

Graduate Students
Hassan Yazdani
Washington State University

Syed Sohail Feroz Syed Afroz
Georgia Institute of Technology

Aditya Shankar Kar
Iowa State University

PSERC Publication 23-06

November 2023

For information about this project, contact:

Saeed Lotfifard
Washington State University
School of Electrical Engineering and Computer Science
Pullman, Washington 99164-2752
Phone: 509-335-0903
Email: s.lotfifard@wsu.edu

Power Systems Engineering Research Center

The Power Systems Engineering Research Center (PSERC) is a multi-university Center conducting research on challenges facing the electric power industry and educating the next generation of power engineers. More information about PSERC can be found at the Center's website: http://www.pserc.wisc.edu.

For additional information, contact:

Power Systems Engineering Research Center
Arizona State University
527 Engineering Research Center
Tempe, Arizona 85287-5706
Phone: 480-965-1643
Fax: 480-727-2052

Notice Concerning Copyright Material

PSERC members are given permission to copy without fee all or part of this publication for internal use if appropriate attribution is given to this document as the source material. This report is available for downloading from the PSERC website.

© 2023 Washington State University. All rights reserved.

Acknowledgments

This is the final report for the Power Systems Engineering Research Center (PSERC) research project T-65 titled "Identification and Mitigation of T&D operational security vulnerabilities in inverter-dominated power systems". We also express our appreciation for the support provided by PSERC's industrial members and the National Science Foundation's Industry / University Cooperative Research Center program. We would like to recognize the following project advisors for their support and contributions to the project.

Aftab Alam (CAISO)
Alan Engelmann(ComEd)
Evangelos Farantatos (EPRI)
Aboutaleb Haddadi (EPRI)
Deepak Ramasubramanian (EPRI)
Parag Mitra (EPRI)
Masoud Abbaszadeh, (GE Research)
Kwok Cheung (GE Renewable Energy)
Deepak Konka, (GE Renewable Energy)
Miaolei Shao, (GE Research)
Bishnu Sapkota, (GE)
Mehmet Cintuglu (Hitachi)
Bo Yang (Hitachi)
Panitarn (Joseph) Chongfuangprinya (Hitachi)
Mingguo Hong (ISO-NE)
Yonghong Chen (MISO)
Felicia Ruiz (MISO)
Adarsh Nagarajan (NREL)
Venkat Krishnan (NREL)
Murali Baggu (NREL)
Ben Kroposki (NREL)
Yingchen Zhang (NREL)
Atena Darvishi (NYPA)
Jianzhong Tong (PJM)
Yohan Sutjandra (The Energy Authority)
Doug Bowman (SPP)
Harvey Scribner (SPP)
Mostafa Sedighizadeh (SPP)
Wisam Alsudani (WAPA)

Executive Summary

This project focused on identifying operational security vulnerabilities in T&D assets that grid integration of massive amounts of inverter-based resources creates. The project focused on the following three main factors (1) Grid Synchronization Instability of Inverter Based Resources, (2) Protection Systems Response, (3) Load and Inverter Based Resources Dynamic Response Analysis which are explained as follows:

Part 1: Grid Synchronization Instability of Inverter Based Resources

Part I of this report was focused on the factors affecting grid synchronization stability of inverter base resources (IBRs). Impacts of different parameters of controllers on the grid synchronization stability were studied. Moreover, the impacts of the grid strength were studies and scenarios were created to show how the outages of lines may cause IBRs to lose grid synchronization stability. Accordingly, mitigative strategies were proposed. The main results of the projects are as follows:

- Different factors on the grid synchronization stability of IBRs were studied using Bode plots, Generalized Nyquist Criterion and time domain simulations.
- MIMO (multiple input, multiple output) transfer function of inverters was derived and using Bolde plots the impacts of PLLs parameters on the grid synchronization stability were studied.
- The Generalized Nyquist Criterion was applied to the MIMO transfer function of inverters, and it was shown as the strength of the host power grid at the point of common coupling (PCC) reduces the inverter may face grid synchronization instability.
- Time domain simulations were performed, and it was also shown the decrease in the grid strength after outages of lines may lead to instability of inverters.
- It was shown reducing the bandwidth of PLLs may improve the grid synchronization stability of inverters. However, it may reduce the ability of PLLs to track fast changes in the system.
- To enhance the grid synchronization stability of inverters a supplementary controller structure was implemented that enhances the grid synchronization stability of inverters by adding supplementary signals to the main controllers of inverters to damp out power oscillations.

Part 2: Protection System Response

The increasing deployment of inverter interfaced resources in the modern power system changes the characteristics of the power grid. The new characteristics affect the performance of practically all subsystems of the power system. This project and in particular thrust 2 of the project focuses on the effects of inverters to the protection and control system. During faults, inverters may follow different control strategies such as suppression of fault current levels, suppression of negative and zero sequence current, suppression of active power fluctuations, or suppression of reactive power fluctuations. Certain protective relays depend on the presence of negative and zero sequence fault currents to determine fault direction as well as they depend on the level of fault current to determine the onset of faults. As a result, relays may mis-operate depending on the inverter control strategies.

This part of the report is focused on item 2. Based on the identified vulnerabilities, we propose mitigation strategies. Specifically, we propose new protection schemes that are immune to the characteristic of inverter dominated power systems.

Recent events of power system disturbances have identified the cause of these disturbances being the interactions of relays with inverters and in particular, inverter controls. These events have been reported by NERC and it appears that their frequency has increased. As the level of inverter penetration in power systems increases, these events will occur more often. We reviewed a number of events that resulted in major disturbances and blackouts due to the interaction of inverter based resources and the protection and control systems. In addition, we reviewed the literature and the research activities for the purpose of understanding and mitigating these complex interactions.

Early in the research it was recognized that the accuracy and fidelity of simulation models to reproduce the actual performance of the system is very important in assessing the new challenges and problems posed by the proliferation of inverters in the power system. Section 3 of the report describes the problem and provides an example to illustrate the issues.

The impact of inverters on the performance of the protection and control system depends on the specific protection function employed by it. This means the impact of inverters on the performance of protection and control systems must be assess for each individual protection function. In order to provide the background, section 4 introduces the major protection functions that are of interest in this problem. Then, in section 5, the assessment of the effects of inverters on the protection system is performed by simulations of appropriate example test systems. Specifically, an example test system has been developed that consists of sections that are dominated by synchronous machines and sections that are dominated by inverters. Several contingencies have been utilized which represent systems that are well interconnected between synchronous machine dominated sections and inverter dominated sections or very loosely interconnected. The results indicate that the performance of the protection and control system deteriorates as the various parts of the system are loosely interconnected. Similarly, the level of inverters affects the performance of protection and control. This means as the systems move toward 100% inverter based systems, major deterioration of protection performance should be expected. These results make it clear that new approaches for protection and control are needed.

Section 7 presents new technology that provides reliable protection, immune to the new characteristics generated by inverters. The new technology is protection algorithms that are based on dynamic state estimation. The new protection function directly determines any abnormality in a protection zone, independently of fault current levels, components of fault currents, transients, harmonic content and other usual transients during faults. This technology provides a reliable answer to the challenges created by inverters.

For completeness, the report provides an approach for testing protection function in the laboratory with hardware in the loop. These methods have been implemented at the Georgia Tech laboratory. The methods support testing with hardware in the loop of legacy protective relays as well as newer technology of merging units and IEC 61850 approaches.

Finally, it is important to note that the subject of this project is very complex and the present report does not address all the issues. Research should continue to provide more understanding of the problems and issues as well as to improve new technologies.

Part III: Load and Inverter Based Resources Dynamic Response Analysis

Part III of this report focuses on the dynamic response analysis of load and inverter-based resources in distribution system. In particular, we develop a simplified model of the overall distribution system that captures the key responses of the distribution system to faults in the transmission system and identify the critical settings of inverter-based resources (IBRs) in distribution system for dynamic support.

Main results of this report include the following:

- We show that the aggregation of entire distribution system into a single composite load model (CLM) cannot accurately capture the dynamics of full distribution system. Especially when the significant fraction of single-phase induction motors is present in the distribution system with stalling behavior.
- We propose the reduced order distribution system models (RDSM) composed of sub-models that are analogous to the WECC CLM and aggregates the distribution system into load areas while ensuring the overall dynamics are retained. Full distribution system simulation data is employed to estimate the parameters of RDSM by matching the dynamics of the full DS model though the parameter optimization.
- Proposed RDSM models will facilitates the faster simulation of distribution system models integrated to transmission system for dynamic studies. Single phase models of RDSM can be easily integrated into any transmission system phasor simulation software such as PSS$^{@}$E to further accelerate the co-simulation by eliminating the data exchange delays between the transmission and distribution system simulators.
- Critical parameters of the IBRs are identified though the global sensitivity analysis of grid forming invert based solar photovoltaic (PV) generation. Real and reactive power control loop parameters of GFM inverter along with the maximum current rating are ranked according to their sensitivity on real and reactive power outputs of IBRs during the voltage disturbances.

Project Publications:

[1] Hassan Yazdani, Saeed Lotfifard, "Parametric Study of Grid Synchronism Stability of Inverter Based Resources" to be submitted IEEE PES General Meeting, 2024.

[2] *Aditya Shankar Kar*, *Venkataramana Ajjarapu*, "Robust Aggregated VAR Capability Curve of DER with Uncertain Renewable Generation" *to be submitted* IEEE PES General Meeting, 2024.

[3] Amarsagar Reddy Ramapuram Matavalam, R. Venkatraman and V. Ajjarapu, "Accurate Representation of Distribution System Dynamics in Bulk System Studies by Clusters of Composite Load Models", *accepted at* IEEE Industry Applications Society Annual Meeting (IAS), 2023.

Student Theses:

[1] Hassan Yazdani, Expected Ph.D thesis title "Grid Synchronization Stability Enhancement of Inverter Based Resources", Washington State University.

[2] *Aditya Shankar Kar*, "Quantification and Impact of Uncertainty for Voltage Stability Studies in Power System with High Penetration of Distributed Energy Resources" *Expected thesis.*

Part I

Grid Synchronization Instability of Inverter Based Resources

Saeed Lotfifard
Hassan Yazdani, Graduate Student

Washington State University

For information about this project, contact

Saeed Lotfifard
Washington State University
School of Electrical Engineering and Computer Science
Pullman, Washington 99164-2752
Phone: 509-335-0903
Email: s.lotfifard@wsu.edu

Power Systems Engineering Research Center

The Power Systems Engineering Research Center (PSERC) is a multi-university Center conducting research on challenges facing the electric power industry and educating the next generation of power engineers. More information about PSERC can be found at the Center's website: http://www.pserc.wisc.edu.

For additional information, contact:

Power Systems Engineering Research Center
Arizona State University
527 Engineering Research Center
Tempe, Arizona 85287-5706
Phone: 480-965-1643
Fax: 480-727-2052

Notice Concerning Copyright Material

PSERC members are given permission to copy without fee all or part of this publication for internal use if appropriate attribution is given to this document as the source material. This report is available for downloading from the PSERC website.

© 2023 Washington State University. All rights reserved

Table of Contents

List of Figures

List of Tables

NOMENCLATURE

Acronym

CPA	Cauchy's principle of argument
GNC	Generalized Nyquist criterion
IBR	Inverter-based resource
MIMO	Multi-input multi-output
PI	Proportional integral
PLL	Phase-locked loop
POI	Point of injection
PWM	Pulse width modulation
SCR	Short circuit ratio
SG	Synchronous generator
SISO	Single-input single-output
SRF	Synchronous reference frame
SS	Small signal
VSC	Voltage source converter

Parameters

v_{dc}	DC-side voltage of the VSC
R_f	Resistance of the VSC filter
L_f	Inductance of the VSC filter
Z_f	Matrix representation of the VSC filter
R_g	Resistance of the grid
L_g	Inductance of the grid
Z_g	Matrix representation of the grid impedance
ω_0	Synchronous speed
k_p, k_i	Current controller PI coefficients
k_p^{PLL}, k_i^{PLL}	PLL PI coefficients

i_{dq}^{ref}	Current references in the dq frame
Z_{vsc}	Output impedance of the VSC
Y_{vsc}	Output admittance of the VSC
$V_{i,dq}^{c}, V_{i,dq}^{s}$	Steady state input voltage of the VSC in the controller and system dq frames, respectively
$V_{o,dq}^{c}, V_{o,dq}^{s}$	Steady state output voltage of the VSC in the controller and system dq frames, respectively
I_{dq}^{c}, I_{dq}^{s}	Steady state output current of the VSC in the controller and system dq frames, respectively
V_{vsc}, I_{vsc}	Thevenin and Norton source equivalents of the VSC, respectively
Z_{line}	Impedance of the transmission line
Y_{load}	Admittance of the load
Z_{SG}	Impedance of the synchronous generator

Operators

$\mathbf{G}_{ci}$	Matrix representation of the PI controller
$\mathbf{G}_{dei}$	Decoupling matrix
$\mathbf{T}_{dq}$	dq frame transformation matrix
$\mathbf{T}_{\Delta\theta}$	System to controller dq transformation matrix
$\mathbf{T}_{PLL}$	Transfer function of the PLL
$\mathbf{T}_{vi}$	Voltage to current transformation of PLL dynamics
$\mathbf{T}_{vv}$	Voltage to voltage transformation of PLL dynamics
$\overline{\boldsymbol{\sigma}}(.), \underline{\boldsymbol{\sigma}}(.)$	Maximum and minimum singular values, respectively
$d(s)$	Characteristic function of the generic control system
$m(s)$	Transfer function of the generic control system
$g(s), h(s)$	Gain and feedback of the SISO generic control system
$\mathbf{G}(s), \mathbf{H}(s)$	Gain and feedback of the MIMO generic control system

Variables

$v_{i,abc}^{s}$	Input voltage of the VSC in the abc frame
$v_{o,abc}^{s}$	Output voltage of the VSC in the abc frame
i_{abc}	Output current of the VSC in the abc frame

v_g	Thevenin equivalent of the grid's voltage
x_{abc}	Sample signal in the abc frame
θ	Angle in the dq frame
i_{dq0}	Output current of the VSC in the abc frame
$v_{o,dq0}$	Output voltage of the VSC in the abc frame
$v_{i,dq0}$	Input voltage of the VSC in the abc frame
$\Delta\theta$	Angle difference between the controller and the grid dq frames
$\Delta v_{i,dq}^c, \Delta v_{i,dq}^s$	Small signal perturbation of input voltage of the VSC in the controller and system dq frames, respectively
$\Delta v_{o,dq}^c, \Delta v_{o,dq}^s$	Small signal perturbation of output voltage of the VSC in the controller and system dq frames, respectively
$\Delta I_{dq}^c, \Delta I_{dq}^s$	Small signal perturbation of output current of the VSC in the controller and system dq frames, respectively
u, y	Input and output of the generic control system
λ_1, λ_2	Eigenvalues of the MIMO characteristic loop gain

1. Grid synchronization instability of inverter based resources

1.1 Background

With the proliferation of renewable resources, the number of grid integrated inverter-based resources increases. Studying the grid synchronization stability of IBRs is critical. In this project impacts of different parameters such as PLL bandwidth and strength of the system are studies. Especially, IBRs dominated power grids may face significant reduction in the grid strength. Some situations that may lead to weak power grids at IBRs sites are as follows[1]:

- Installation of IBRs at remote wind/solar rich areas far from generation/load centers which are connected to the rest of the power grid through long distance lines. Examples of such sites are west Texas area wind farms [2] and several Australian power plants such as Musselroe and Silverton wind power plants [3] and Kennedy energy-park [4]. For instance, in the case of Kennedy energy-park in Australia in normal condition SCR is about 1.5 and during N-1 contingency SCR is about 0.7.
- Installation of IBRs at sites that despite being located at the vicinity of the generation/load center areas, they are not well integrated into the main power grid. For instance, Tehachapi wind site in California is located near the load center but connected to the main grid by a weak 66 kV system [5].
- Sudden reduction of the power system strength subsequent to outages of lines as the result of a fault occurrence in the power grid. For instance, First Solar PV power plant in Arizona experienced a significant reduction in the system strength due to line outages [6]. According to the report case study results, at SCR of 4 the damping was insufficient and the PV power plant was tripped.
- Installation of IBRs at islanded power system such as a Mediterranean island that is studies in [7]. Also, system splits that may occur due to cascading outages or controlled islanding could lead to islands with reduced system strength at IBRs sites [8].

In this project to systematically show the impacts of different parameters on grid synchronization stability of IBRs, bode plots and Generalized Nyquist Criterion (GNC) based on impedance-based stability analysis are utilized. To this end, the transfer functions of grid connected inverter is derived. The model includes the dynamic response of PLL which will be used by GNC and bode plots to show the impacts of different parameters on the grid synchronization stability of inverters. Then, to enhance the grid synchronization stability of inverter, a supplementary controller is implemented that adds damping to the main controllers of IBRs to damp out the oscillations on the output powers of IBRs subsequent to the occurrences of outages in the power system.

1.2 Modeling of transfer function of inverters controllers

In this section first a brief review of the structure of inverters controllers is presented. Then the procedure for deriving transfer functions of inverters is explained. The derived transfer functions will be used to study the impacts of different factors on the synchronization stability of inverters such as the parameters of synchronization mechanism of inverters and strength of the host power grid.

1.2.1 Brief review of the structure of controllers

In this section the structure of controllers of inverters is briefly explained which will be used in later sections for study the response of inverters to the disturbances. More detailed explanations of the inverter controllers can be found in [9]. Figure 1.1 shows a typical grid connected three-phase inverter. Based on its control logic, a IBRs can be operated either as a grid following source using a PLL, or as a grid forming source that mimics the behavior of legacy synchronous generators. In this report we consider the former. As depicted in Figure 1.1, the grid model is represented as Thevenin equivalent, which is a three-phase source, series with a resistor and an inductor.

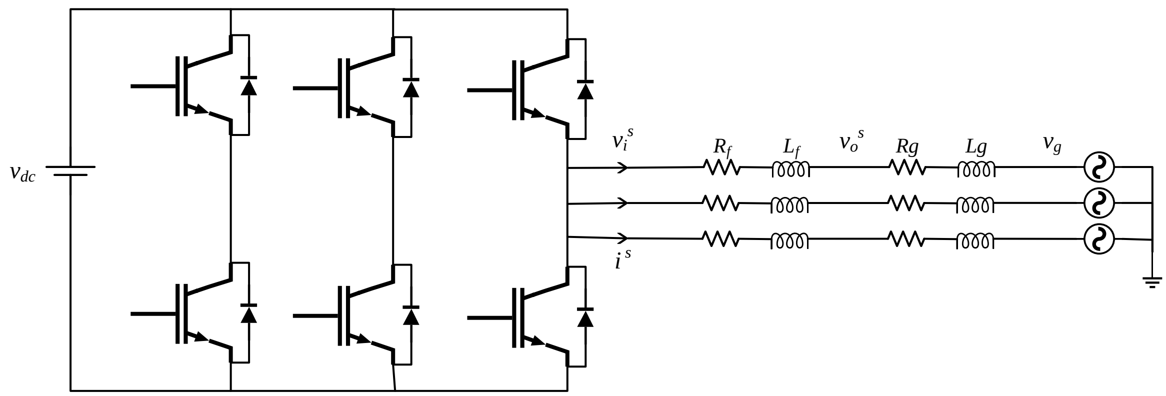

Figure 1.1 Schematic of a generic grid connected inverter

To begin with, the equations in the abc frame, between the input voltage and the output voltage of the inverter is written as (1.1) where v_{ia}, v_{ib}, and v_{ic} denote the input voltage of the inverter on each phase and similarly, v_{oa}, v_{ob}, and v_{oc} are the output voltages, and i_a, i_b, and i_c are the output currents. Also, R_f and L_f are the resistance and the inductance of the series filter. For simplicity, since the signals are all in the same reference frame, superscript s is not shown in the following equations.:

$$\begin{bmatrix} v_{ia} \\ v_{ib} \\ v_{ic} \end{bmatrix} - \begin{bmatrix} v_{oa} \\ v_{ob} \\ v_{oc} \end{bmatrix} = R_f \begin{bmatrix} i_a \\ i_b \\ i_c \end{bmatrix} + L_f \frac{d}{dt} \begin{bmatrix} i_a \\ i_b \\ i_c \end{bmatrix} \tag{1.1}$$

To simplify the analysis of the equations in (1.1), the park transformation (also known as dq transformation) is used. This transformation was first introduced in the early 1920s as a mathematical tool to facilitate the analysis of rotating electrical machines, in particular, the SGs, and offers numerous advantages. For instance, in the abc frame, the relationship between the phases is trigonometric, whereas in the dq frame there are two axes related in a linear fashion. Moreover, by using the dq frame, the control frame is aligned with the rotor frame with the synchronous frequency, allowing the utilization of synchronous reference frame control which is much more intuitive. In addition, in the dq frame control of the inverter, the design allows the independent control of active power and reactive power, which is extremely beneficial in managing the output of the inverter, facilitating its voltage and frequency alignment with the grid's reference frame. Using the Park transformation matrix, any three-phase signal x in the abc frame can be transformed to the $dq0$ frame, as depicted in (1.2):

$$\begin{bmatrix} x_d \\ x_q \\ x_0 \end{bmatrix} = \underbrace{\frac{2}{3}\begin{bmatrix} \cos(\theta) & \cos(\theta - \frac{2\pi}{3}) & \cos(\theta + \frac{2\pi}{3}) \\ -\sin(\theta) & -\sin(\theta - \frac{2\pi}{3}) & -\sin(\theta + \frac{2\pi}{3}) \\ \frac{1}{\sqrt{2}} & \frac{1}{\sqrt{2}} & \frac{1}{\sqrt{2}} \end{bmatrix}}_{\mathbf{T}_{dq}} \begin{bmatrix} x_a \\ x_b \\ x_c \end{bmatrix} \tag{1.2}$$

The inverse of $\mathbf{T}_{dq}$ is represented in (1.3) and by definition, $\mathbf{T}_{dq} \times \mathbf{T}_{dq}^{-1} = I_{3\times3}$.

1

$$\mathbf{T}_{dq}^{-1} = \begin{bmatrix} \cos(\theta) & -\sin(\theta) & 1 \\ \cos\left(\theta - \frac{2\pi}{3}\right) & \sin\left(\theta - \frac{2\pi}{3}\right) & 1 \\ \cos\left(\theta + \frac{2\pi}{3}\right) & \sin\left(\theta + \frac{2\pi}{3}\right) & 1 \end{bmatrix} \tag{1.3}$$

By applying this transformation to (1.1), (1.4) is derived as follows:

$$\mathbf{T}_{dq}^{-1} \times \left(\begin{bmatrix} v_{ia} \\ v_{ib} \\ v_{ic} \end{bmatrix} - \begin{bmatrix} v_{oa} \\ v_{ob} \\ v_{oc} \end{bmatrix}\right) = R_f \mathbf{T}_{dq}^{-1} \times \begin{bmatrix} i_a \\ i_b \\ i_c \end{bmatrix} + L_f \frac{d}{dt}\left(\mathbf{T}_{dq}^{-1} \times \begin{bmatrix} i_a \\ i_b \\ i_c \end{bmatrix}\right) \tag{1.4}$$

The derivative of the second term on the right-hand side of (1.4) can be further simplified using the chain rule, as stated in (1.5):

$$L_f \frac{d}{dt}\left(\mathbf{T}_{dq}^{-1} \times \begin{bmatrix} i_a \\ i_b \\ i_c \end{bmatrix}\right) = L_f \left(\frac{d}{dt}\mathbf{T}_{dq}^{-1}\right)\begin{bmatrix} i_a \\ i_b \\ i_c \end{bmatrix} + L_f \mathbf{T}_{dq}^{-1} \times \frac{d}{dt}\left(\begin{bmatrix} i_a \\ i_b \\ i_c \end{bmatrix}\right) \tag{1.5}$$

To further simplify (1.5), first the derivative of the Park transformation is calculated as shown in (1.6)

1

$$\frac{d}{dt}\mathbf{T}_{dq}^{-1} = \begin{bmatrix} 0 & \frac{d}{dt}\theta & 0 \\ -\frac{d}{dt}\theta & 0 & 0 \\ 0 & 0 & 0 \end{bmatrix} \mathbf{T}_{dq}^{-1} \tag{1.6}$$

Then, by assuming the dq frame rotates with the synchronous speed, it results $\theta = \omega_s t$. By multiply $\mathbf{T}_{dq}$ to equation (1.4), (1.7) is derived. In (1.7), v_{id}, v_{iq}, and v_{i0} are the $dq0$ axes signals of the input voltage and similarly, v_{od}, v_{oq}, and v_{o0} are the output voltages in the $dq0$ frame. Also, i_d, i_q, and i_0 are the output currents in the $dq0$ frame.

$$\begin{bmatrix} v_{id} \\ v_{iq} \\ v_{i0} \end{bmatrix} - \begin{bmatrix} v_{od} \\ v_{oq} \\ v_{o0} \end{bmatrix} = R_f \begin{bmatrix} i_d \\ i_q \\ i_0 \end{bmatrix} + L_f \frac{d}{dt} \begin{bmatrix} i_d \\ i_q \\ i_0 \end{bmatrix} + L_f \frac{d}{dt} \begin{bmatrix} \omega_s i_q \\ -\omega_s i_d \\ 0 \end{bmatrix} \tag{1.7}$$

By rearranging the right-hand side, and since the 0 axis is equal to zero, (1.8) is derived in which s is the Laplace operator.

$$\begin{bmatrix} v_{id} \\ v_{iq} \end{bmatrix} - \begin{bmatrix} v_{od} \\ v_{oq} \end{bmatrix} = \begin{bmatrix} sL_f + R_f & -\omega_0 L_f \\ \omega_0 L_f & sL_f + R_f \end{bmatrix} \begin{bmatrix} i_d \\ i_q \end{bmatrix} \tag{1.8}$$

This can also be written as the two axis current equations, as written in (1.9) and (1.10). The d-axis current in (1.10) represents a signal that is in-phase with the inverter's output voltage, through which the active power output of the inverter can be controlled. On the other hand, the q-axis current is 90 degrees out of phase with the inverter's output voltage, through which the reactive power output of the inverter is controlled.

$$\frac{di_d}{dt} = \frac{1}{L_f}(v_{id} - R_f i_d + \omega_0 L_f i_q - V_{od}) \tag{1.9}$$

$$\frac{di_q}{dt} = \frac{1}{L_f}(v_{iq} - R_f i_d - \omega_0 L_f i_d - V_{oq}) \tag{1.10}$$

The inverter is equipped with a current controller, also known as the inner loop controller, as depicted in Figure 1.2. The objective of this controller is to set the inverter to output a specified amount of current, i_d^{ref} and i_q^{ref}, which can be achieved by manipulating the output voltage of the inverter through an PWM switching scheme. For simplicity, the PWM switching delays are considered negligible (fast) enough to be ignored.

This current controller is implemented according to the following stages. First, the reference values for the controller to track are generated. In most practical cases, an outer loop is also implemented, and the current reference values are generated through that higher level controller. Otherwise, these references should be calculated separately for the inverter to meet a specific criterion. Next, output current of the inverter is measured to generate the error value. Once these errors are generated, using a PI controller, a control action and an integral action accompanied by the coupling terms generate input voltage values for the VSC, such that the desired reference tracking of the dq frame current is achieved. Finally, in a closed loop fashion, these voltage values are utilized to adjust the switching patterns of the inverter, such that the control objective is satisfied dynamically.

Based on Figure 1.2, the equations for the inverter's voltage on each axis is written as (1.11) and (1.12), respectively. These voltage equations are the fundamental characteristic of the inverter and could be utilized to tune the current controller bandwidth through manipulating the PI controller coefficients.

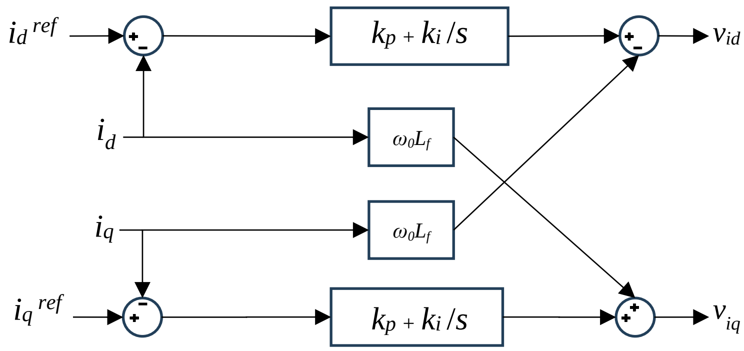

Figure 1.2 Current (inner) controller of the inverter

$$v_{id} = -\omega_0 L_f i_q + k_p\left(i_d^{ref} - i_d\right) + k_i \int (i_d^{ref} - i_d)dt \tag{1.11}$$

$$v_{iq} = \omega_0 L_f i_d + k_p\left(i_q^{ref} - i_q\right) + k_i \int (i_q^{ref} - i_q)dt \tag{1.12}$$

1.2.2 Transfer function without the PLL

In this section and next section, the transfer functions of inverters are derived. In deriving the transfer function procedures presented in [10-11] will be followed. However, compared to them the transfer functions derived in this project are more suitable for grid integration studies as transfer functions are derived such that they do not become too complex by ignoring fast dynamic components such as PWM and measurement filters. Equations (1.11) and (1.12) are rewritten as (1.13) where $\mathbf{G}_{ci}$ and $\mathbf{G}_{dei}$ are the current controller and decoupling matrices, respectively.

$$\begin{aligned} \begin{bmatrix} v_{id} \\ v_{iq} \end{bmatrix} = & \underbrace{\begin{bmatrix} k_p + \frac{k_i}{s} & 0 \\ 0 & k_p + \frac{k_i}{s} \end{bmatrix}}_{\mathbf{G}_{ci}} \begin{bmatrix} i_d^{ref} \\ i_q^{ref} \end{bmatrix} \\ & - \left(\begin{bmatrix} k_p + \frac{k_i}{s} & 0 \\ 0 & k_p + \frac{k_i}{s} \end{bmatrix} + \underbrace{\begin{bmatrix} 0 & \omega_0 L_f \\ -\omega_0 L_f & 0 \end{bmatrix}}_{\mathbf{G}_{dei}} \right) \begin{bmatrix} i_d \\ i_q \end{bmatrix} \end{aligned} \tag{1.13}$$

Using this representation, the block diagram of the system is formed, as shown in Figure 1.3 where Z_f is the matrix representation of the VSC filter.

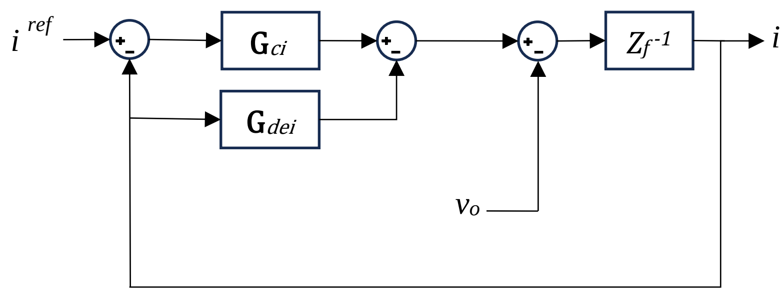

Figure 1.3 Block diagram of the transfer function of the system without considering PLL

Looking at this block diagram, it is evident that the output current is calculated with a combination of the output voltage and the reference value of the current. The goal is to calculate the output impedance of the VSC. Given the linearity of the system, the superposition rule can be applied. By assuming $i^{ref} = \begin{bmatrix} i_d^{ref} \\ i_q^{ref} \end{bmatrix} = 0$, the impedance of the VSC is calculated as in (1.14).

$$i = -Z_f^{-1} v_o + Z_f^{-1}(\mathbf{G}_{ci}(i^{ref} - i) - \mathbf{G}_{dei} i) \tag{1.14}$$

$$Z_{vsc} = \frac{v_o}{i} = -\left(Z_f + \mathbf{G}_{ci} + \mathbf{G}_{dei}\right) = -\begin{bmatrix} sL_f + R_f + k_p + \frac{k_i}{s} & 0 \\ 0 & sL_f + R_f + k_p + \frac{k_i}{s} \end{bmatrix}$$
$$= \frac{1}{Y_{vsc}}$$

Note that since this model is linear, the resulting impedance is valid for a wide range of frequencies. In practice, the PWM switching frequencies should be considered and the impedance values are valid up to half the switching frequencies.

1.2.3 Effects of the PLL dynamics

In the grid following architecture, the inverter is set to follow the grid's angle and frequency. This is achieved by utilizing a synchronous reference frame PLL. In power systems, PLL is a control mechanism that helps in synchronizing a local signal, typically a voltage of frequency, with a reference value that is often obtained from the grid. The control block diagram of a PLL is depicted in Figure 1.4. where k_p^{PLL} and k_i^{PLL} denote the PLL controller coefficients. In an inverter, the voltage is in the abc frame. First, this signal needs to be transformed to either the $\alpha\beta$ frame using Clark's transformation or the synchronous reference frame using the dq (Park's) transformation.
The PLL ensures the proper operation of the inverter by ensuring that the two reference frames, the grid, and the control, are perfectly aligned.

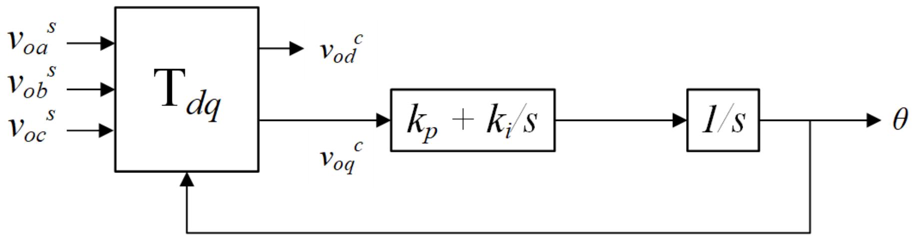

Figure 1.4 Schematic of synchronous reference frame PLL

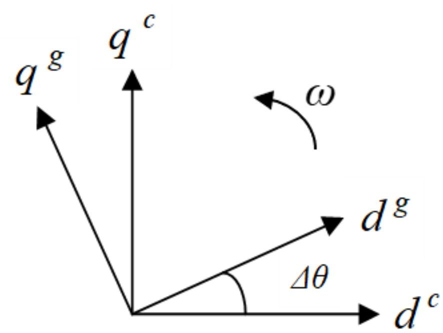

Figure 1.5 *dq* synchronous reference frames of the system and the controller

Once a small disturbance in the grid's voltage occurs, this perturbation is transferred to the inverter through the dynamics of the PLL. This results in two different dq axes: the grid and the PLL. The grid's frame is called "system", and denote it with the superscript s, and the PLL frame is called the controller frame, denoted by the superscript c. The phase difference between the two frames is depicted in Figure 1.5. In steady state, the two frames are aligned and there is no angle difference between them ($\Delta\theta = 0$). The steady-state values in the controller frame and the system frame for the input voltage of the inverter, its output voltage, and its current are depicted with capital letters in (1.15). where V_{id}^{c}, V_{iq}^{c}, V_{id}^{s}, and V_{iq}^{s} are the input voltage steady-state values for the controller dq frame and the system dq frame, and similarly, V_{od}^{c}, V_{oq}^{c}, V_{od}^{s}, and V_{oq}^{s} the steady-state output voltage values. Also, I_{d}^{c}, I_{q}^{c}, I_{d}^{s}, and I_{q}^{s} are the steady-state currents in the controller dq frame and the system dq frame, respectively.

$$\begin{bmatrix} V_{id}^{c} \\ V_{iq}^{c} \end{bmatrix} = \begin{bmatrix} V_{id}^{s} \\ V_{iq}^{s} \end{bmatrix}; \begin{bmatrix} V_{od}^{c} \\ V_{oq}^{s} \end{bmatrix} = \begin{bmatrix} V_{od}^{s} \\ V_{oq}^{s} \end{bmatrix}; \begin{bmatrix} I_{d}^{c} \\ I_{q}^{c} \end{bmatrix} = \begin{bmatrix} I_{d}^{s} \\ I_{q}^{s} \end{bmatrix} \tag{1.15}$$

Once a disturbance occurs, the difference between the two signals in the system frame and the controller frame is modelled using a transformation matrix $T_{\Delta\theta}$, as shown in (1.16). In the inverter control, this transformation is utilized to convert the grid's signal to a frame that is aligned with the inverter's controller frame.

$$T_{\Delta\theta} = \begin{bmatrix} cos(\Delta\theta) & sin(\Delta\theta) \\ -sin(\Delta\theta) & cos(\Delta\theta) \end{bmatrix} \tag{1.16}$$

As is evident, this transformation is highly nonlinear and is suitable for large signal analysis. To conduct a small-signal analysis, first we calculate the nominal operating points that were discussed in (1.15). Then, assuming the angle perturbation $\Delta\theta$ is small, the relationship between the controller and system frame signals can be linearized in the presence of small perturbations, as shown in (1.17), (1.18), and (1.19) where Δ denotes the small-signal perturbations.:

$$\begin{bmatrix} V_{id}^{c} + \Delta v_{id}^{c} \\ V_{iq}^{c} + \Delta v_{iq}^{c} \end{bmatrix} = \underbrace{\begin{bmatrix} 1 & \Delta\theta \\ -\Delta\theta & 1 \end{bmatrix}}_{T_{\Delta\theta}} \begin{bmatrix} V_{id}^{s} + \Delta v_{id}^{s} \\ V_{iq}^{s} + \Delta v_{iq}^{s} \end{bmatrix} \tag{1.17}$$

$$\begin{bmatrix} V_{od}^{c} + \Delta v_{od}^{c} \\ V_{oq}^{c} + \Delta v_{oq}^{c} \end{bmatrix} = \begin{bmatrix} 1 & \Delta\theta \\ -\Delta\theta & 1 \end{bmatrix} \begin{bmatrix} V_{od}^{s} + \Delta v_{od}^{s} \\ V_{oq}^{s} + \Delta v_{oq}^{s} \end{bmatrix} \tag{1.18}$$

$$\begin{bmatrix} I_{d}^{c} + \Delta i_{d}^{c} \\ I_{q}^{c} + \Delta i_{q}^{c} \end{bmatrix} = \begin{bmatrix} 1 & \Delta\theta \\ -\Delta\theta & 1 \end{bmatrix} \begin{bmatrix} I_{d}^{s} + \Delta i_{d}^{s} \\ I_{q}^{s} + \Delta i_{q}^{s} \end{bmatrix} \tag{1.19}$$

Since the steady state values of the system and controller are equal, these relations can be further simplified. Equation (1.20) shows an example of this simplification:

$$\begin{bmatrix} \Delta v_{id}^{c} \\ \Delta v_{iq}^{c} \end{bmatrix} \approx \begin{bmatrix} \Delta v_{id}^{s} + \Delta\theta V_{iq}^{s} \\ \Delta v_{iq}^{s} - \Delta\theta V_{id}^{s} \end{bmatrix} \tag{1.20}$$

Next, PLL dynamics are added separately. The block diagram representation of the PLL is depicted in 1.4. Based on this diagram, grid voltage in the abc frame is first transferred to the dq frame and using a PI controller, the angle difference is estimated.
Based on this representation, the output angle of the PLL is written as in (1.21).

$$\Delta\theta = (k_p^{PLL}\Delta v_{oq}^{c} + k_i^{PLL}\int \Delta v_{oq}^{c} dt)\frac{1}{s} \tag{1.21}$$

To write this system in the state space form, an auxiliary variable $\Delta\psi$ is defined, and the resulting state space is written in (1.22)

$$\Delta\psi = \int \Delta v_{oq}^{c} dt \tag{1.22}$$

$$\frac{d}{dt}\begin{bmatrix} \Delta\theta \\ \Delta\psi \end{bmatrix} = \begin{bmatrix} 0 & k_i^{PLL} \\ 0 & 0 \end{bmatrix} \begin{bmatrix} \Delta\theta \\ \Delta\psi \end{bmatrix} - \begin{bmatrix} 0 & k_p^{PLL} \\ 0 & 1 \end{bmatrix} \begin{bmatrix} \Delta v_{od}^{c} \\ \Delta v_{oq}^{c} \end{bmatrix} \tag{1.23}$$

Again, to get a uniform state space, the control frame signals are moved to the system frame as discussed before, with the transformation in (1.24).

$$\begin{bmatrix} \Delta v_{od}^{c} \\ \Delta v_{oq}^{c} \end{bmatrix} \approx \begin{bmatrix} \Delta v_{od}^{s} + \Delta\theta V_{oq}^{s} \\ \Delta v_{oq}^{s} - \Delta\theta V_{od}^{s} \end{bmatrix} \tag{1.24}$$

The resulting state space of the PLL in the controller frame is stated in (1.25).

$$\underbrace{\frac{d}{dt}\begin{bmatrix}\Delta\theta\\ \Delta\psi\end{bmatrix}}_{\dot{X}} = \underbrace{\begin{bmatrix}-k_p^{PLL}V_{od}^s & k_i^{PLL}\\ -V_{od}^s & 0\end{bmatrix}}_{A}\underbrace{\begin{bmatrix}\Delta\theta\\ \Delta\psi\end{bmatrix}}_{X} + \underbrace{\begin{bmatrix}0 & k_p^{PLL}\\ 0 & 1\end{bmatrix}}_{B}\underbrace{\begin{bmatrix}\Delta v_{od}^c\\ \Delta v_{oq}^c\end{bmatrix}}_{u} \tag{1.25}$$

1.2.4 The transfer function model with PLL dynamics

In this section the small signal representation of the system is derived in the block diagram form. This is buildup on the block diagram that was derived in section 1.2.21.2.2, where the PLL dynamics are added according to the derivation of section 1.2.3. To do so, the system frame signals, including the voltage and the current are transformed to the control stage. Finally, the input voltage of the controller which is in the control frame is transformed to the system frame.

The relationship between the output level voltage of the system is transformed to the system level, as stated in (1.26) and (1.27).

$$\begin{bmatrix}V_{od}^c + \Delta v_{od}^c\\ V_{oq}^c + \Delta v_{oq}^c\end{bmatrix} = \begin{bmatrix}1 & \Delta\theta\\ -\Delta\theta & 1\end{bmatrix}\begin{bmatrix}V_{od}^s + \Delta v_{od}^s\\ V_{oq}^s + \Delta v_{oq}^s\end{bmatrix} \tag{1.26}$$

$$\begin{bmatrix}\Delta v_{od}^c\\ \Delta v_{oq}^c\end{bmatrix} \approx \begin{bmatrix}\Delta v_{od}^s + V_{oq}^s\Delta\theta\\ \Delta v_{oq}^s - V_{od}^s\Delta\theta\end{bmatrix} \tag{1.27}$$

Next, based on the block diagram of the PLL, the relationship between the voltage and the angle is written as in (1.28), in which an auxiliary variable $\mathbf{T}_{PLL}$ is introduced to simplify the relations.

$$\Delta\theta = \Delta v_{oq}^c.\underbrace{(k_p^{PLL} + \frac{k_i^{PLL}}{s}).\frac{1}{s}}_{\mathbf{T}_{PLL}} = \Delta v_{oq}^c.\mathbf{T}_{PLL} \tag{1.28}$$

$$\Delta v_{od}^c = \Delta v_{od}^s + V_{oq}^s.\Delta v_{oq}^c.\mathbf{T}_{PLL} \tag{1.29}$$

$$\Delta v_{oq}^c = \Delta v_{oq}^s - V_{od}^s.\Delta v_{oq}^c.\mathbf{T}_{PLL} \tag{1.30}$$

By further simplifying (1.30), (1.31) is derived.

$$(1 + V_{od}^s\mathbf{T}_{PLL})\Delta v_{oq}^c = \Delta v_{oq}^s \tag{1.31}$$

Inserting (1.31) into (1.29), (1.32) is derived.

$$\Delta v_{od}^c = \Delta v_{od}^s + V_{oq}^s\left(\frac{1}{1 + V_{od}^s\mathbf{T}_{PLL}}\right)\Delta v_{oq}^s \tag{1.32}$$

These relations are summarized in the transformation matrix form, depicted in (1.33)

$$\begin{bmatrix}\Delta v_{od}^{c}\\ \Delta v_{oq}^{c}\end{bmatrix}=\begin{bmatrix}1 & \dfrac{V_{oq}^{s}\mathbf{T}_{PLL}}{1+V_{od}^{s}\mathbf{T}_{PLL}}\\ 0 & \dfrac{1}{1+V_{od}^{s}\mathbf{T}_{PLL}}\end{bmatrix}\begin{bmatrix}\Delta v_{od}^{s}\\ \Delta v_{oq}^{s}\end{bmatrix} \tag{1.33}$$

The same procedure is repeated for the output current, and the relationship is written in (1.36), in which the controller frame current perturbations are written as a function of grid frame voltages, because of PLL dynamics. The transfer function $\mathbf{T}_{vi}$ transforms the grid's voltage signals to the current signals.

$$\begin{bmatrix}I_{d}^{c}+\Delta i_{d}^{c}\\ I_{q}^{c}+\Delta i_{q}^{c}\end{bmatrix}=\begin{bmatrix}1 & \Delta\theta\\ -\Delta\theta & 1\end{bmatrix}\begin{bmatrix}I_{d}^{s}+\Delta i_{d}^{s}\\ I_{q}^{s}+\Delta i_{q}^{s}\end{bmatrix} \tag{1.34}$$

$$\begin{bmatrix}\Delta i_{d}^{c}\\ \Delta i_{q}^{c}\end{bmatrix}\approx\begin{bmatrix}\Delta i_{d}^{s}+I_{q}^{s}\Delta\theta\\ \Delta i_{q}^{s}-I_{d}^{s}\Delta\theta\end{bmatrix} \tag{1.35}$$

$$\begin{bmatrix}\Delta i_{d}^{c}\\ \Delta i_{q}^{c}\end{bmatrix}=\begin{bmatrix}\Delta i_{d}^{s}\\ \Delta i_{q}^{s}\end{bmatrix}+\underbrace{\begin{bmatrix}0 & \dfrac{I_{q}^{s}\mathbf{T}_{PLL}}{1+V_{od}^{s}\mathbf{T}_{PLL}}\\ 0 & -\dfrac{I_{d}^{s}\mathbf{T}_{PLL}}{1+V_{od}^{s}\mathbf{T}_{PLL}}\end{bmatrix}}_{\mathbf{T}_{vi}}\begin{bmatrix}\Delta v_{od}^{s}\\ \Delta v_{oq}^{s}\end{bmatrix} \tag{1.36}$$

Repeating a similar procedure, the input voltage of the inverter is transformed from the control frame to the system frame, as stated in (1.39). Similarly, the transfer function T_{vv} transforms the grid's output voltage signals to the input voltages in system frame.

$$\begin{bmatrix}V_{id}^{c}+\Delta v_{id}^{c}\\ V_{iq}^{c}+\Delta v_{iq}^{c}\end{bmatrix}=\begin{bmatrix}1 & \Delta\theta\\ -\Delta\theta & 1\end{bmatrix}\begin{bmatrix}V_{id}^{s}+\Delta v_{id}^{s}\\ V_{iq}^{s}+\Delta v_{iq}^{s}\end{bmatrix} \tag{1.37}$$

$$\begin{bmatrix}\Delta v_{id}^{c}\\ \Delta v_{iq}^{c}\end{bmatrix}\approx\begin{bmatrix}\Delta v_{id}^{s}+V_{iq}^{s}\Delta\theta\\ \Delta v_{iq}^{s}-V_{id}^{s}\Delta\theta\end{bmatrix} \tag{1.38}$$

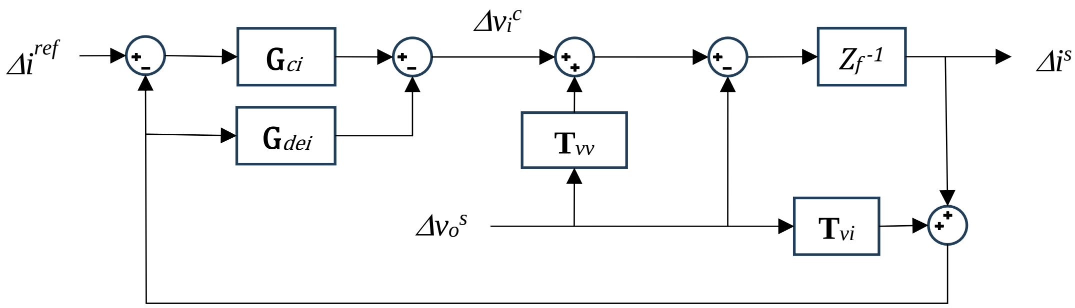

Figure 1.6 Block diagram of the transfer function of system with PLL dynamics

$$\begin{bmatrix}\Delta v_{id}^{s}\\ \Delta v_{iq}^{s}\end{bmatrix} \approx \begin{bmatrix}\Delta v_{id}^{c}\\ \Delta v_{iq}^{c}\end{bmatrix} + \underbrace{\begin{bmatrix}0 & -\dfrac{V_{iq}^{s}\mathbf{T}_{PLL}}{1+V_{od}^{s}\mathbf{T}_{PLL}}\\ 0 & \dfrac{V_{id}^{s}\mathbf{T}_{PLL}}{1+V_{od}^{s}\mathbf{T}_{PLL}}\end{bmatrix}}_{T_{vv}} \begin{bmatrix}\Delta v_{od}^{s}\\ \Delta v_{oq}^{s}\end{bmatrix} \tag{1.39}$$

Now that the relationships between the controller frame and the grid frame is derived, these transformations are put together to form the block diagram of the system, as depicted in Figure 1.6.

This is a MIMO system with inputs $[\Delta i_d^{ref}, \Delta i_q^{ref}, \Delta v_d^s, \Delta v_q^s]$ and the output $[\Delta i_d^s, \Delta i_q^s]$. Based on this block diagram and using the superposition rule, the output admittance of the system is calculated as presented in (1.41), where the components of this admittance are stated in (1.42), (1.43), (1.44), and (1.45).

$$\frac{\Delta i^s}{\Delta v_o^s} = \frac{-\mathbf{I} - (\mathbf{G}_{ci} + \mathbf{G}_{dei})\mathbf{T}_{vi} + \mathbf{T}_{vv}^{PLL}}{Z_f + \mathbf{G}_{ci} + \mathbf{G}_{dei}} \tag{1.40}$$

$$Y_{vsc} = \begin{bmatrix} -\dfrac{s}{\sigma_2} & -\dfrac{\sigma_3}{\sigma_1}\\ 0 & \dfrac{\sigma_4}{\sigma_1}\end{bmatrix} \tag{1.41}$$

$$\sigma_1 = \left(s^2 + V_{od}^s k_p^{PLL} s + V_{od}^s k_i^{PLL}\right)\sigma_2 \tag{1.42}$$

$$\sigma_2 = k_i + (R_f + k_p)s + L_f s^2 \tag{1.43}$$

$$\sigma_3 = I_q^s k_i k_i^{PLL} + (V_{iq}^s k_i^{PLL} + I_q^s k_i k_p^{PLL} + I_q^s k_p k_i^{PLL} - I_d^s L_f k_i^{PLL} \omega)s + (V_{iq}^s k_p^{PLL} + I_q^s k_p k_p^{PLL} - I_d^s L_f k_p^{PLL} \omega)s^2 \quad (1.44)$$

$$\sigma_4 = I_d^s k_i k_i^{PLL} + (V_{id}^s k_i^{PLL} - V_{od}^s k_i^{PLL} + I_d^s k_i k_i^{PLL} + I_d^s k_p k_i^{PLL} + I_q^s L_f k_i^{PLL} \omega)s^2 - s^3 \quad (1.45)$$

1.3 Impedance-based stability analysis

Once the impedance of the inverter is derived, this can be used to study the impacts of different parameters on the grid synchronization stability of the inverters. That is because the behavior of the inverter in a spectrum of frequencies can accurately be captured by its impedance. To this end, the impedance-based stability analysis is used. The main idea of this method is to divide a system into two subsystems, one being the element under study and two the rest of the power grid, as shown in Figure 1.7, provided that each of them is independently stable. This stability analysis is also known as the impedance ratio analysis. The grid and the inverter impedances are represented in the format of Figure 1.8, and denoted by Z_g for the grid and Z_{vsc} for the converter. Assuming that the system is a SISO, using the function $1 + \frac{Z_g}{Z_{vsc}}$ it is possible to assess the stability. This criterion states that if this transfer function has no zeros in the closed right half plane, then the system is stable. This is based on the Nyquist theorem (which will be elaborated on in the following section), where the number of closed right half plane zeros is equal to the number of encirclements of the function $\frac{Z_g}{Z_{vsc}}$ around the point $(-1, j0)$. This condition is satisfied if for all frequencies, the magnitude of the grid's impedance is smaller than the magnitude of the inverter's impedance, as stated in (1.46), implying that the grid must be strong.

$$\|Z_g(j\omega)\| < \|Z_{vsc}(j\omega)\| \quad (1.46)$$

Consider an inverter that is simplified as a current source I_{vsc} parallel with an impedance Z_{vsc}, connected to a grid that is modelled by a voltage source V_g series with an impedance Z_g. The goal is to assess whether the flow of current I between the two systems remains stable or not.
Writing a KCL to find the current gives the equation) 1.48).

$$I(s) = \frac{I_{vsc} Z_{vsc}}{Z_{vsc} + Z_g} - \frac{V_g}{Z_{vsc} + Z_g} \quad (1.48)$$

Simplifying this results in (1.49).

$$I(s) = [I_{vsc} - \frac{V_g}{Z_{vsc}}] \times \frac{1}{1 + \frac{Z_g}{Z_{vsc}}} \quad (1.49)$$

The first term of the equation can be assumed to be stable. Now, for the interconnected system to be stable, the stability of the second term must be investigated.

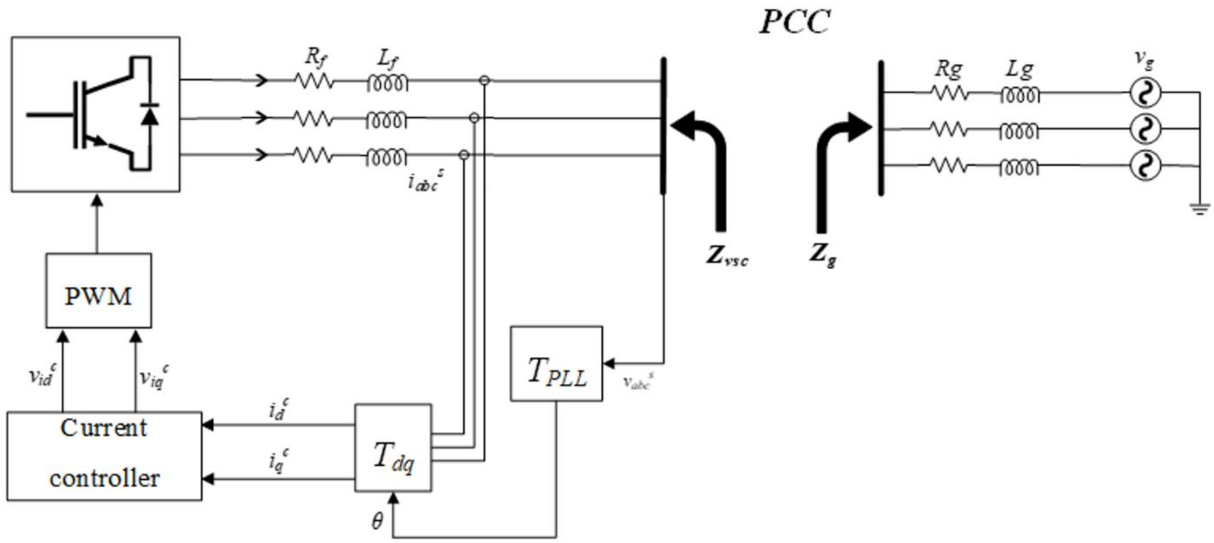

Figure 1.7 Schematic of the impedance based modeling of the grid connected VSC

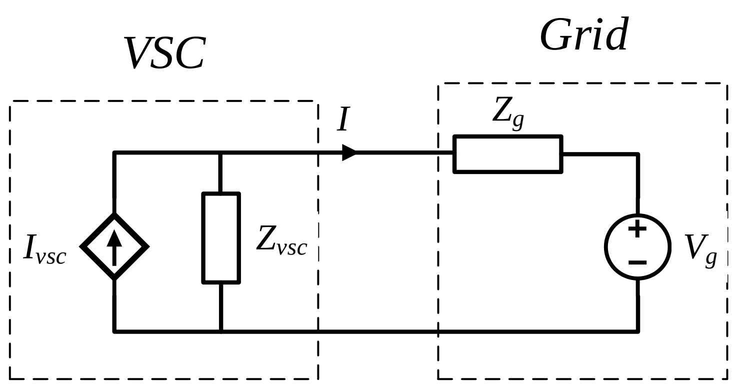

Figure 1.8 Schematic of the interconnection of the grid and VSC equivalents

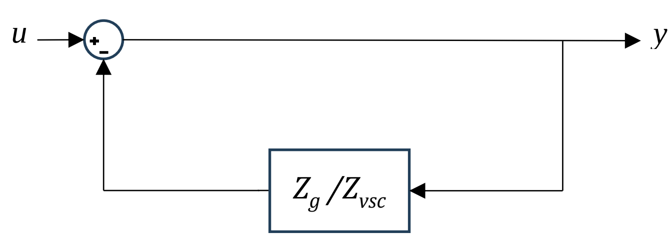

Figure 1.9 Representation of impedance stability analysis as a closed loop system

This term perfectly fits the application of the classic Nyquist stability criterion because the impedance ratio represents the open-loop gain, with the controller block diagram depicted in Figure 1.9. With this structure, classical control methods, like the Nyquist and bode plots could be applied to comment on the stability. But, since the impedance ratio is a matrix, which is due to the

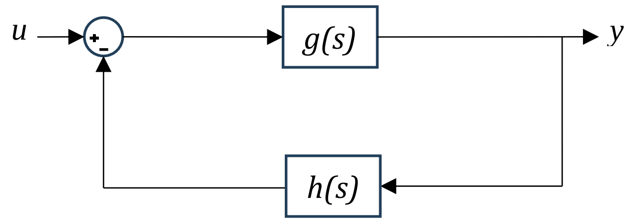

Figure 1.10 Generic model of SISO feedback system

MIMO structure of the system, the generalized version of the Nyquist criterion must be used. Next, we briefly discuss the principles of the Nyquist criterion in SISO systems and how it is extended to MIMO systems, which is the case of inverter stability analysis.

1.4 The Nyquist criterion: SISO to MIMO

In this section, we discuss the principles of using the Nyquist criterion on stability analysis of SISO linear time invariant systems. This criterion applies the *Cauchy's principle of argument* on the *open loop* transfer function of a system and from there, we can comment on the *closed loop* stability. Consider the closed loop transfer function of the feedback system in Figure 1.10, as stated in (1.50).

$$m(s) = \frac{g(s)}{1 + g(s)h(s)} \tag{1.50}$$

The closed loop poles of the system are achieved by finding the zeros of (1.51), which is called the system characteristic equation.

$$d(s) = 1 + g(s)h(s) \tag{1.51}$$

Now, to derive the Nyquist plot, one can create the closed region in the s-plane as shown in Figure 1.11, and find the mapping of the function $d(s) = 1 + g(s)h(s)$ whose zeros are the closed-loop poles of the transfer function.
The number of unstable closed-loop poles is equal to the number of unstable open-loop poles, plus the number of encirclements of the origin of the Nyquist plot of the complex function $d(s)$.

$$N = Z - P \tag{1.52}$$

where Z and P stand for the number of zeros and poles of the function $d(s)$ inside the contour. The above criterion can be slightly modified if instead of plotting the function $d(s) = 1 + g(s)h(s)$ and counting the clockwise encirclement of the origin, we consider the function $g(s)h(s)$, and count the encirclements around the point $(-1, j0)$.

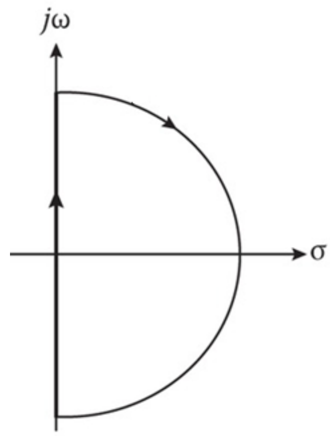

Figure 1.11 s-plane contour of the right half plane

To extend this concept to MIMO systems, first consider the generic 2×2 system as depicted in Figure 1.12, where $G = \begin{bmatrix} G_{11} & G_{12} \\ G_{21} & G_{22} \end{bmatrix}$ and $H = \begin{bmatrix} H_{11} & 0 \\ 0 & H_{22} \end{bmatrix}$. If there is no coupling between the channels ($G_{12} = G_{21} = 0$), the system turns into two independent SISO systems. To apply the Nyquist criterion to this MIMO system, we need to know the definition of poles and zeros in a MIMO system, which is acquired with the Smith-McMillan form of a transfer function matrix [12]. Once the number of poles and zeros are obtained, the collective encirclements of the loop gain eigenvalues are utilized to check for the Nyquist stability criterion.

The power system equivalent of this system is a 2×2 MIMO system, in which the loop gain has two eigenvalues λ_1 and λ_2. One important thing to consider is that the return ratio of the loop gain must be a rational function, meaning that the order of the numerator is less than the order of the denominator. If the two subsystems are modelled as Thevenin/Norton equivalents which leads to a $Z + Y$ connection, the resulting return ratio will always be rational. For models which result in a $Z + Z$ or $Y + Y$ representations, as depicted in Figure 1.13 for various combinations, alternative methods should be applied to assess the stability [13] One thing to note is that the representations in Figure 1.13 are equivalent, if $Y_{vsc} = Z_{vsc}^{-1}$ and $Y_g = Z_g^{-1}$.

1.5 Analysis of impacts of different parameters on the stability of the inverters

In this section, the impacts of different parameters such as the grid strength and parameters of the synchronization mechanism (i.e. PLL) on the stability of inverter is studies. First, bode plots for each element of the admittance and the impedance matrices are plotted. After that, the GNC plots for various grid strengths has been plotted to demonstrate how a weak grid results in an unstable interconnection. The parameters for this study have been summarized in the Table 1.

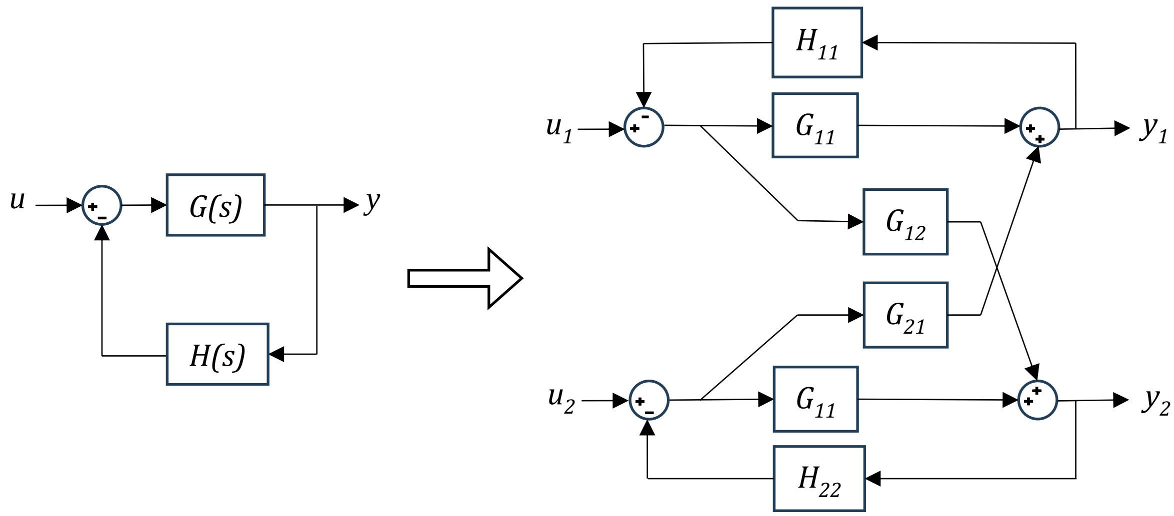

Figure 1.12 Schematic of a 2 × 2 MIMO system

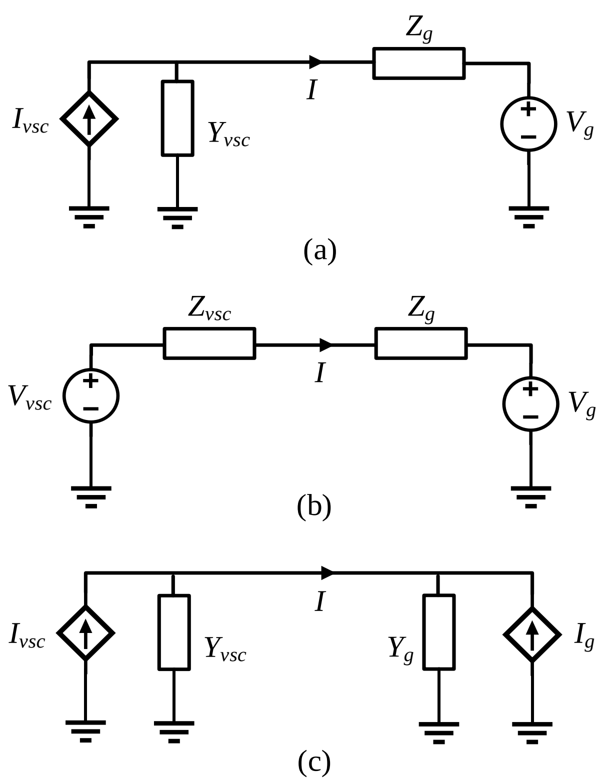

Figure 1.13 Different combinations of VSC and grid equivalent models

Table 1 Parameters of the VSC [10]

Parameter	Value
$\boldsymbol{k_p}$	0.023
$\boldsymbol{k_i}$	25.59
$\boldsymbol{k_p^{PLL}}$	4.46, 8.92, 17.84
$\boldsymbol{k_i^{PLL}}$	991, 3964, 15860
$\boldsymbol{\omega}$	$2\pi \times 60\ rad/s$
$\boldsymbol{R_f}$	120 $m\Omega$
$\boldsymbol{L_f}$	970 μH
$\boldsymbol{I_d^s}$	-11 Amp
$\boldsymbol{I_q^s}$	0 Amp
$\boldsymbol{v_{id}^s}$	100 v
$\boldsymbol{v_{iq}^s}$	0 v
$\boldsymbol{v_{od}^s}$	99.9 v
$\boldsymbol{v_{oq}^s}$	0 v

1.5.1 Results without considering the PLL dynamics

In this scenario, the impedance (admittance) matrix is purely diagonal, and the values are identical on each axis ($Z_{dd} = Z_{qq}$ and $Y_{dd} = Y_{qq}$). Consequently, only the output impedance and admittance of the VSC on one axis is plotted in Figure 1.14 and Figure 1.15, respectively.

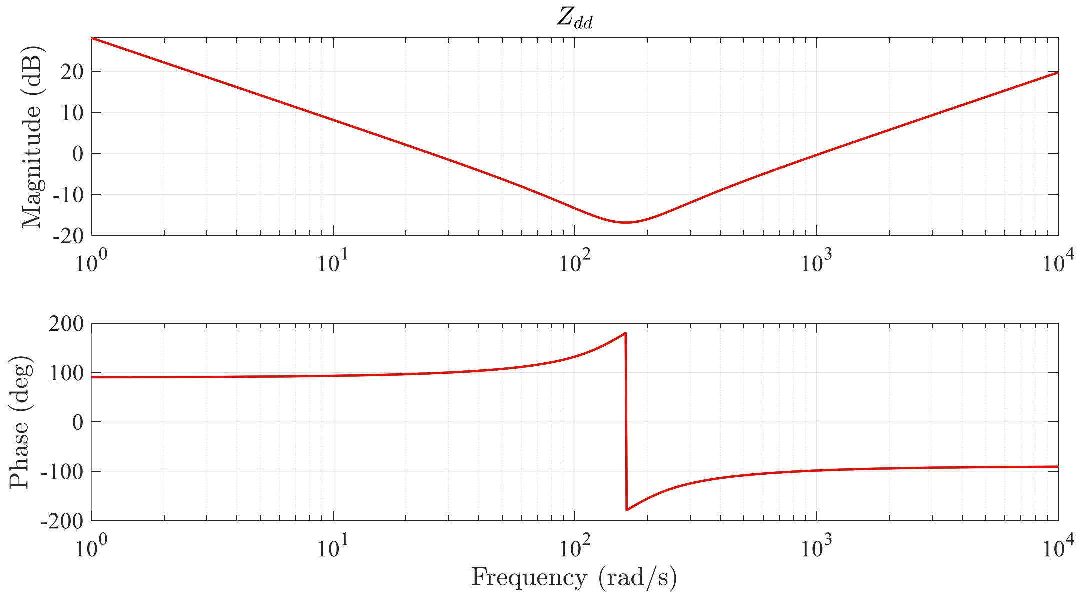

Figure 1.14 Z_{dd} impedance of the VSC in the absence of PLL dynamics

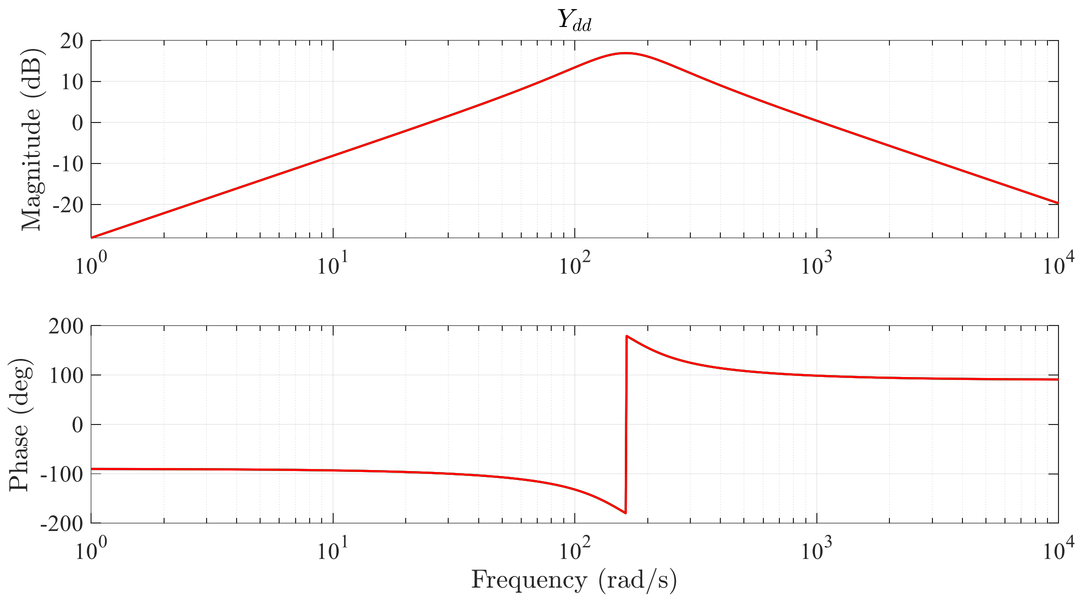

Figure 1.15 Y_{dd} admittance of the VSC in the absence of PLL dynamics

1.5.2 Impedance/admittance with the PLL dynamics

Once the PLL is added, the impedance matrix is no longer diagonal. Z_{dd} and Z_{qd} will be identical to the no PLL case, but Z_{dq} will no longer be zero. To further probe the effects of PLL, three different PLL coefficients are considered. The impedances and admittances of the VSC are depicted in Figure 1.16 to Figure 1.19. As depicted in Figure 1.16 the dq channel gain is relatively small. Figure 1.18 shows that while synchronizing a VSC with the grid, the qq channel behaves as a negative incremental resistance. This behavior is a result of including PLL dynamics, where the PLL bandwidth determines the frequency range at which the impedance is negative. For instance, $k_p^{PLL} = 4.46$ & $k_i^{PLL} = 991$, the negative impedance starts to damp out around 50 Hz with a relatively steep rate, but for $k_p^{PLL} = 17.84$ & $k_i^{PLL} = 15860$ this decrease happens with a lower slope and in higher frequencies.

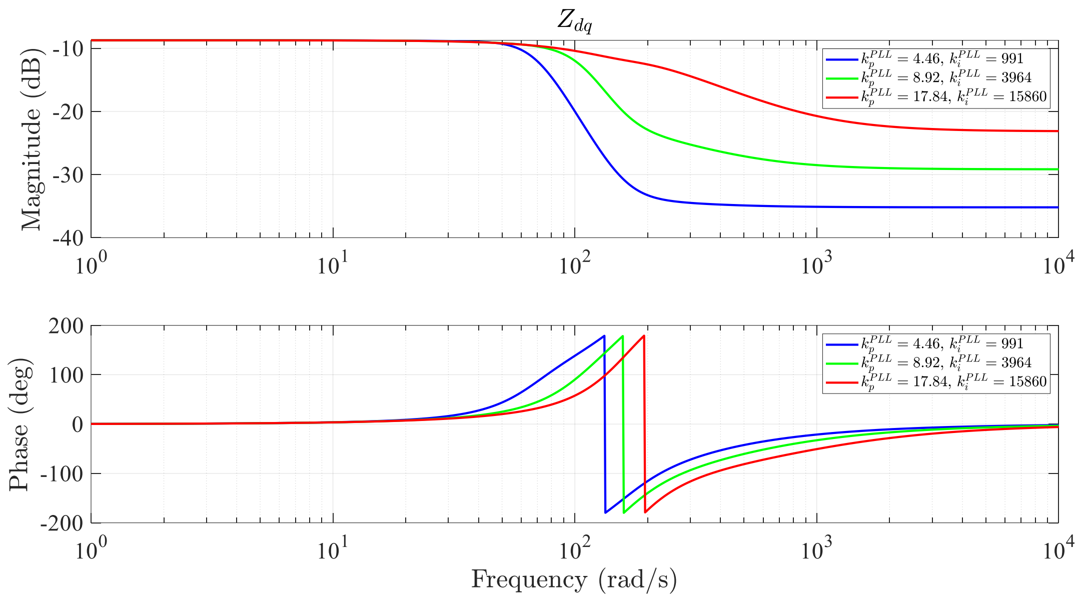

Figure 1.16 dq channel impedance of the VSC

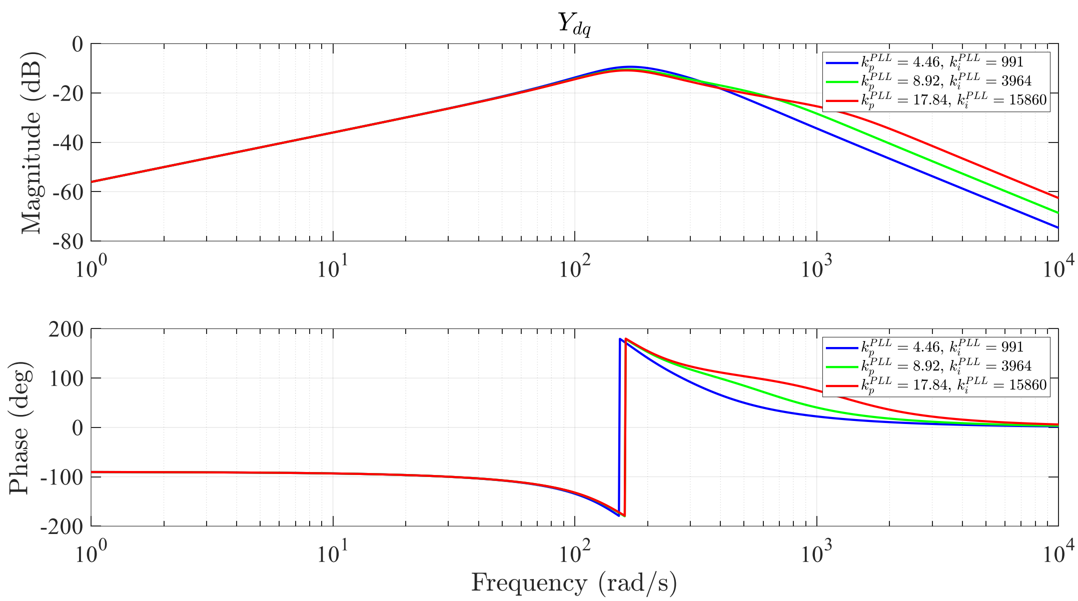

Figure 1.17 dq channel admittance of the VSC

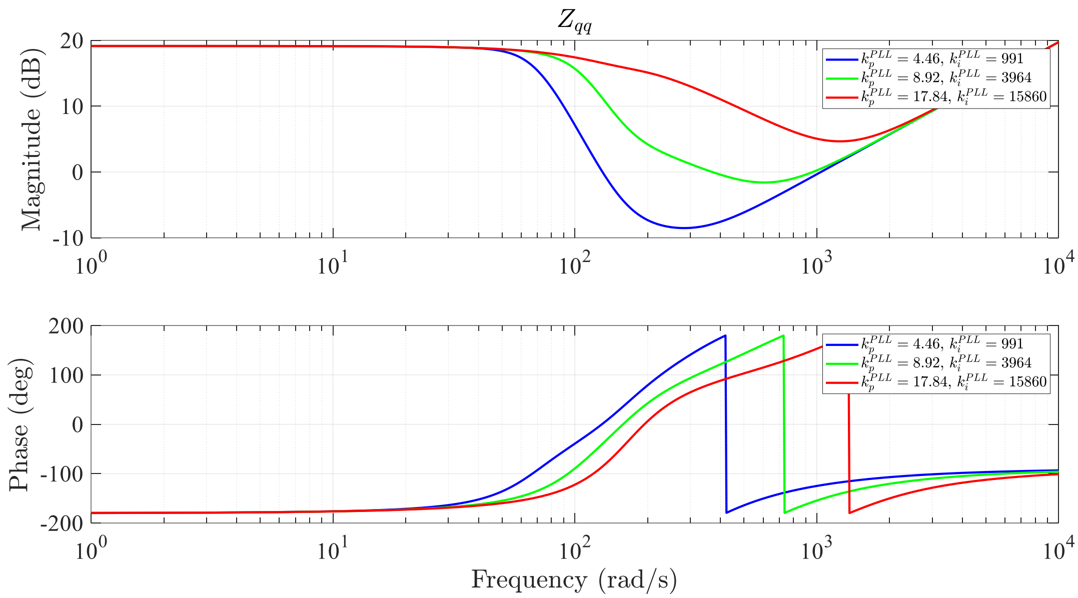

Figure 1.18 qq channel impedance of the VSC

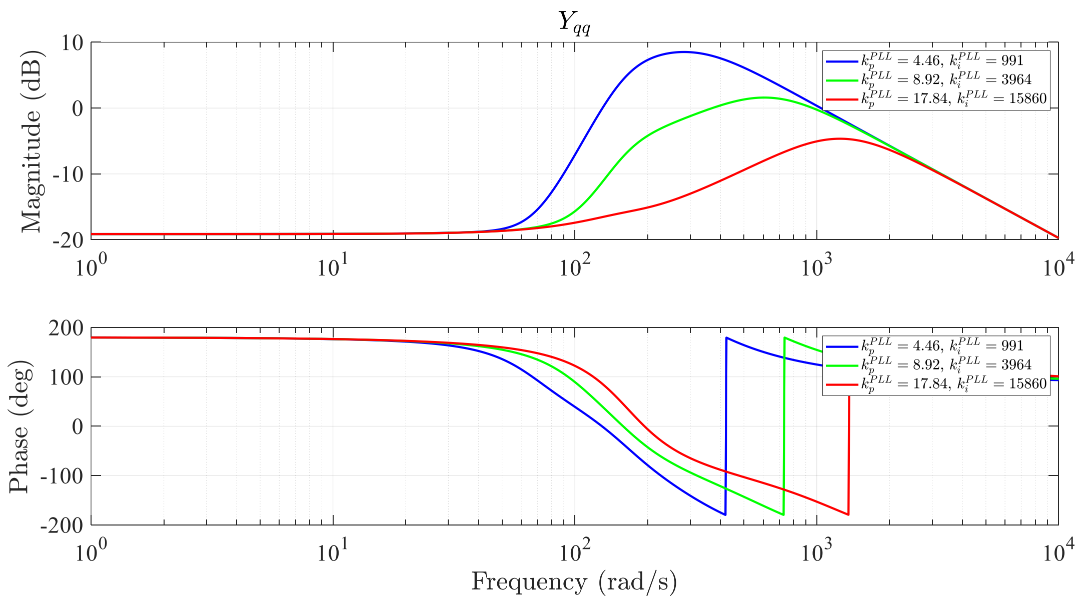

Figure 1.19 qq channel admittance of the VSC

1.5.3 Stability analysis using the GNC plots.

Generally, a power system's strength is related to the amount of available short circuit current in a certain part of the system, which affects its ability to recover from disturbances. The most common method to define the strength of the system at the point of injection (POI) of the inverter at is the short circuit ratio (SCR), which is the ratio of short circuit in a given location, to the rating of the source connected to that location. Accordingly, SCR is represented as follows:

$$SCR_{POI} = \frac{\mathrm{SC}\ MVA_{POI}}{MW_{POI}} \tag{1.53}$$

Consequently, a strong grid has a high SCR and can maintain its voltage during disturbances. To demonstrate the impact of the grid strength on inverter stability the GNC plots are used. First, the inverter is connected to a power grid with $R_g = 0.08\ \Omega$ and $L_g = 8 \times 10^{-4}$ H. The GNC plot for this case is plotted in Figure 1.20. As depicted, none of the eigen loci graphs encircle the critical point $(-1{,}0j)$, which indicates that the system is stable. Then, as the strength of the grid is reduced by increasing its impedance as shown in Figure 1.21 and Figure 1.22, respectively, the loci graphs move towards the critical point and both encircle it, indicating the instability of the system in a weak grid connection.

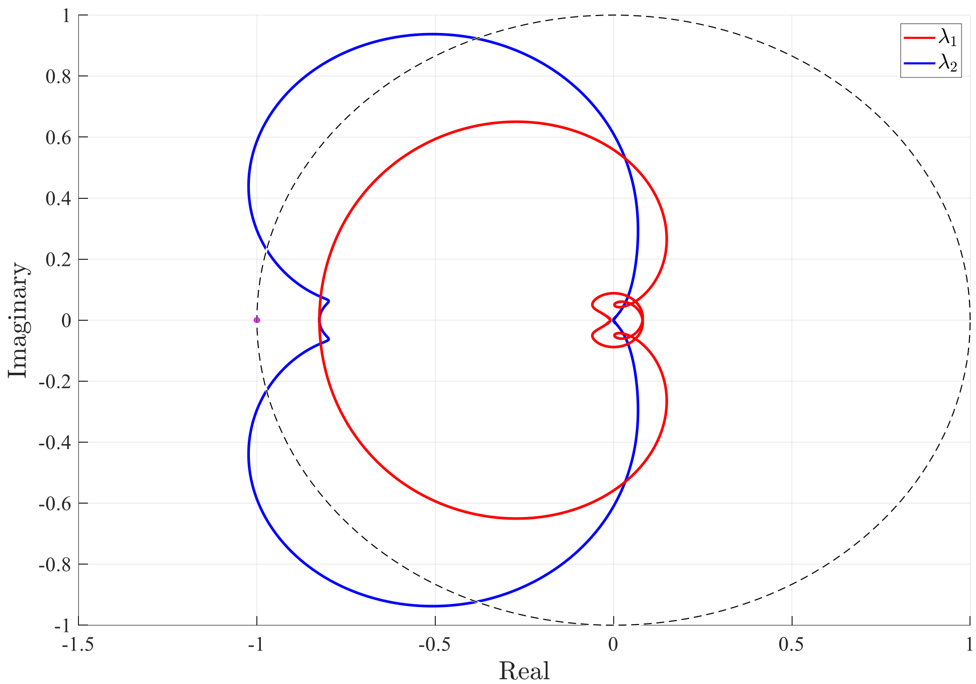

Figure 1.20 GNC plots for $R_g = 0.08\ \Omega$ and $L_g = 8 \times 10^{-4}$ H

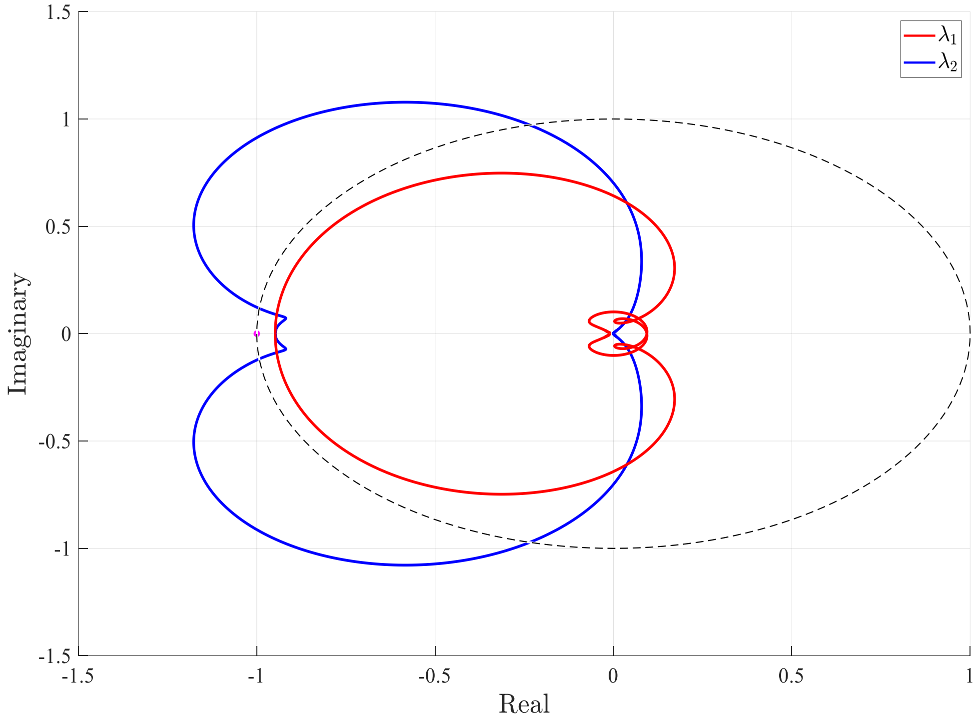

Figure 1.21 GNC plots for $R_g = 0.09\ \Omega$ and $L_g = 9 \times 10^{-4}$ H

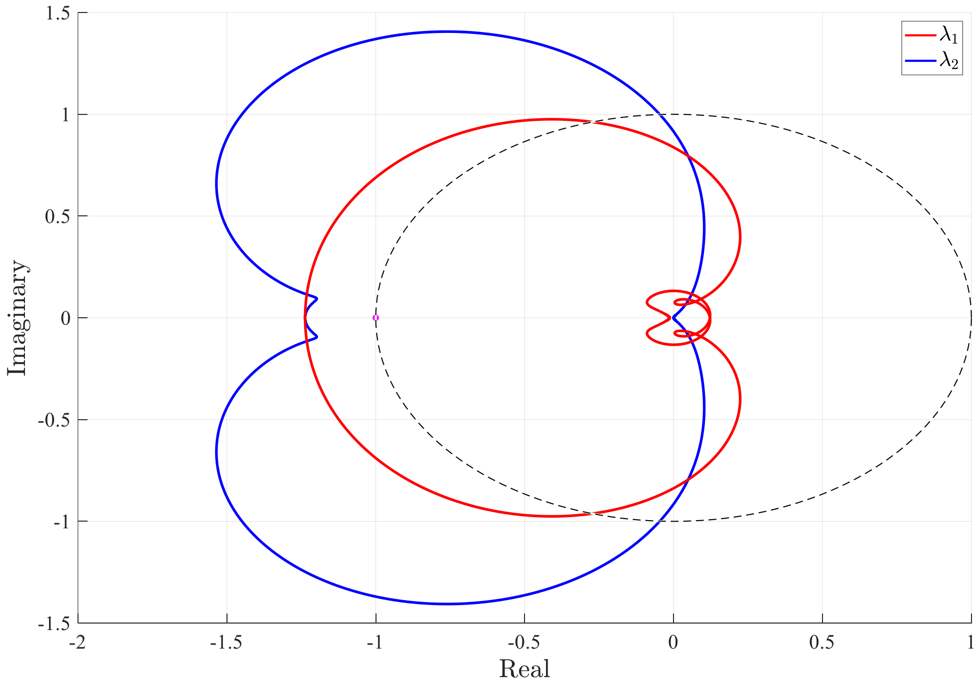

Figure 1.22 GNC plots for $R_g = 0.12\ \Omega$ and $L_g = 1.2 \times 10^{-3}$ H.

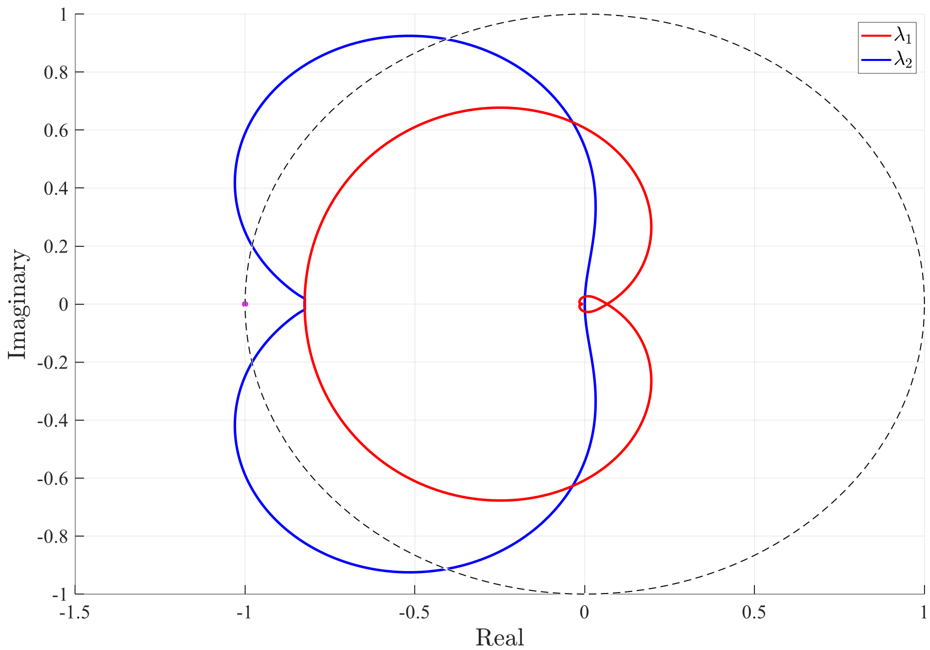

Figure 1.23 GNC plots ignoring the off-diagonals for $R_g = 0.08\ \Omega$ and $L_g = 8 \times 10^{-4}$ H.

In some studies, the off-diagonal elements of the 2×2 MIMO are ignored. Therefore, the stability analysis is simplified as the MIMO system becomes two independent SISO systems. For strong power grid this simplification is acceptable, but as it is shown later this simplification fails in a weak grid condition. First, consider the strong grid for which the GNC was depicted in Figure 1.20. Now, if the model is simplified by ignoring the off-diagonal elements, still the stability is reported correctly as shown in Figure 1.23.

Now consider a different case with $R_g = 0.092\ \Omega$ and $L_g = 9.2 \times 10^{-4}$ H and $k_p^{PLL} = 4.46$ and $k_i^{PLL} = 991$. The GNC plot of this case is depicted in Figure 1.24, and its simplified counterpart is depicted in Figure 1.25. The complete setup with a full matrix indicates the instability of the system, but the simplified setup wrongly reports that as stable.

Similarly, if from the start the PLL dynamics is not considered, a diagonal impedance as discussed in the modelling section is derived. It was already observed that $R_g = 0.092\ \Omega$ and $L_g = 9.2 \times 10^{-4}$ H represent a weak grid and the VSC interconnection with PLL dynamics is unstable. Figure 1.26 shows the result of applying the Nyquist criterion to the impedance model without the PLL dynamics, where the algorithm incorrectly indicates the stability.

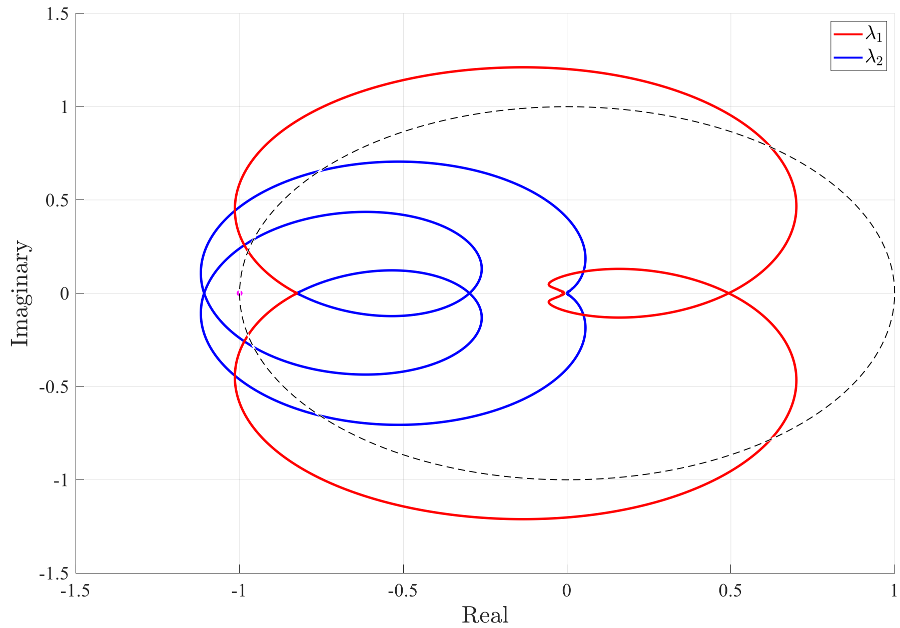

Figure 1.24 Complete and unstable case with $R_g = 0.092\ \Omega$ and $L_g = 9.2 \times 10^{-4}$ H and $k_p^{PLL} = 4.46$ and $k_i^{PLL} = 991$.

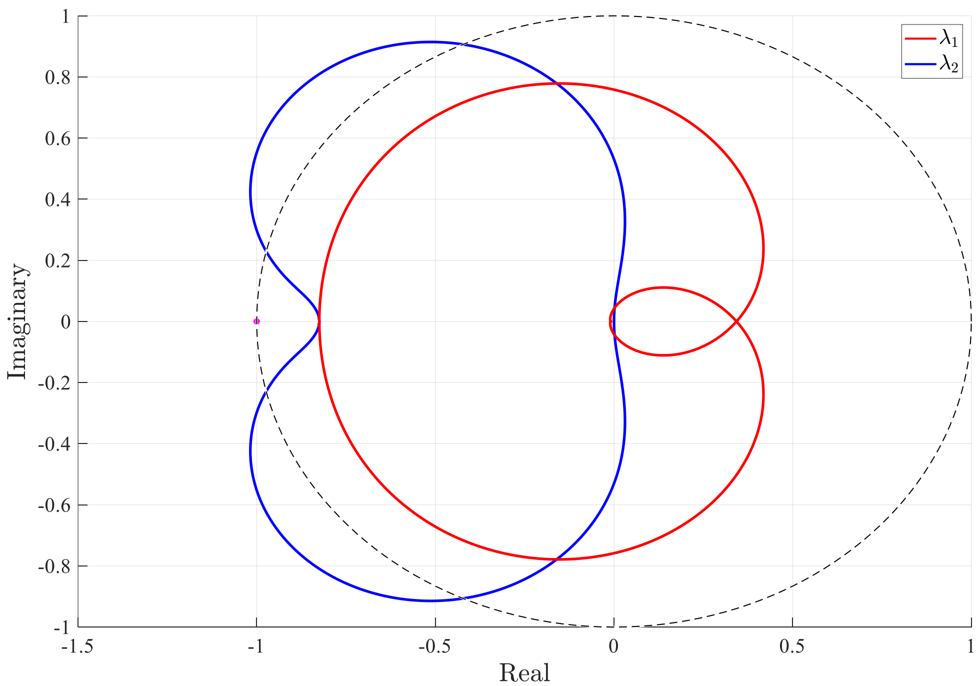

Figure 1.25 Simplified cased with $R_g = 0.092\ \Omega$ and $L_g = 9.2 \times 10^{-4}$ H and $k_p^{PLL} = 4.46$ and $k_i^{PLL} = 991$, wrongly reported as stable.

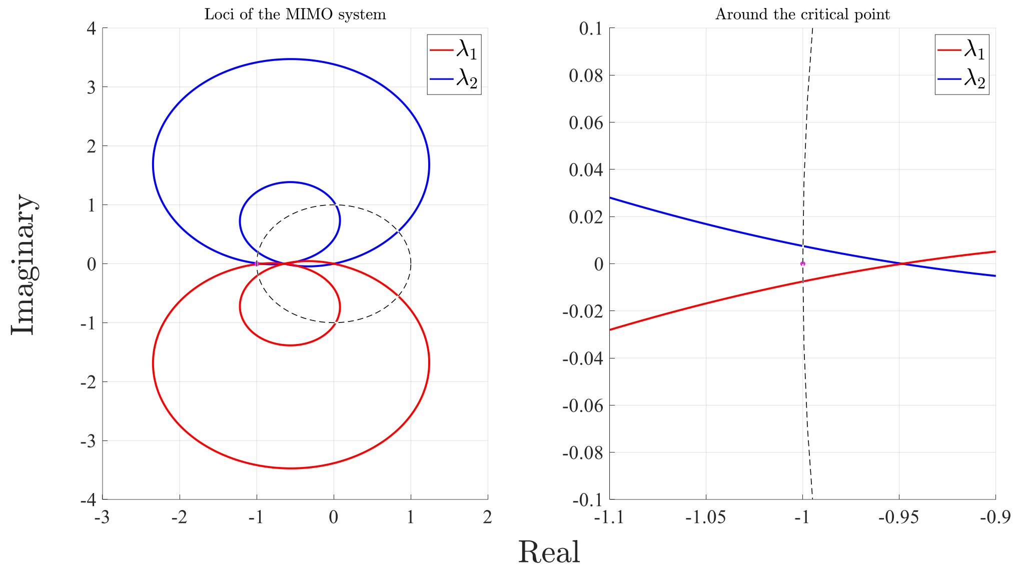

Figure 1.26 GNC for a weak grid while ignoring the PLL dynamics

1.6 Case study of impacts of line outages on grid synchronization stability of inverters

Once faults occur in power grids, due to the subsequent line outages and/or possible power system splitting, the strength of the system may reduce. The sudden reduction in the strength of the system may cause loss of grid synchronism of inverters. A real-world example of such a scenario occurred in 2017 in First Solar 550 MW utility-scale PV plant. Figure 1.27 shows an inverter connected to the power grid simulated in Matlab/Simulink. At t=0.3, the system becomes weaker by taken the parallel line out of service leading to SCR$\approx$ 1. As shown in Figures 1.28 inverter lose its synchronization stability. As shown in Figures 1.29 by increasing the time response of PLL, grid synchronism stability of the IBR can be increased in facing sudden change in the strength of the system. However, slow PLL does not provide desirable response in tracking the fast change in the system quantities such as frequency of the grid during large disturbances. Therefore, alternative solutions should be proposed. Specifically, in the next section a supplementary controller is implemented to increasing the damping of the controllers so that output oscillations are damped out effectively which leads to increased grid synchronization of IBRs.

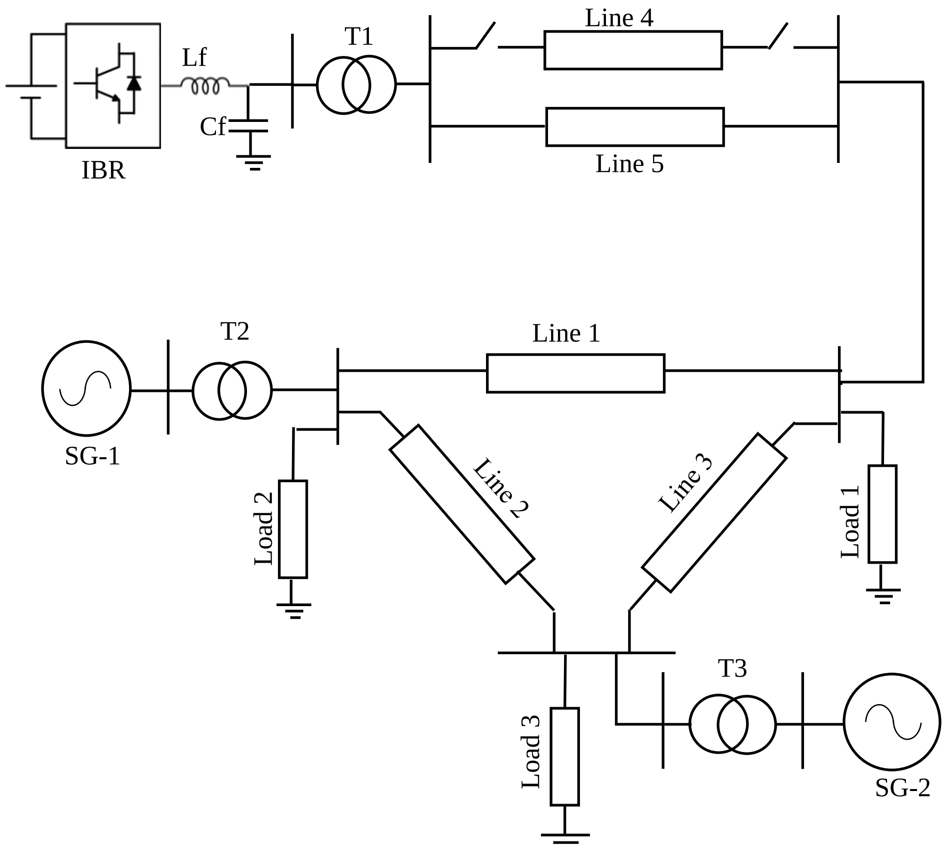

Figure 1.27 Schematic of the simulated multi-machine power system including an IBR

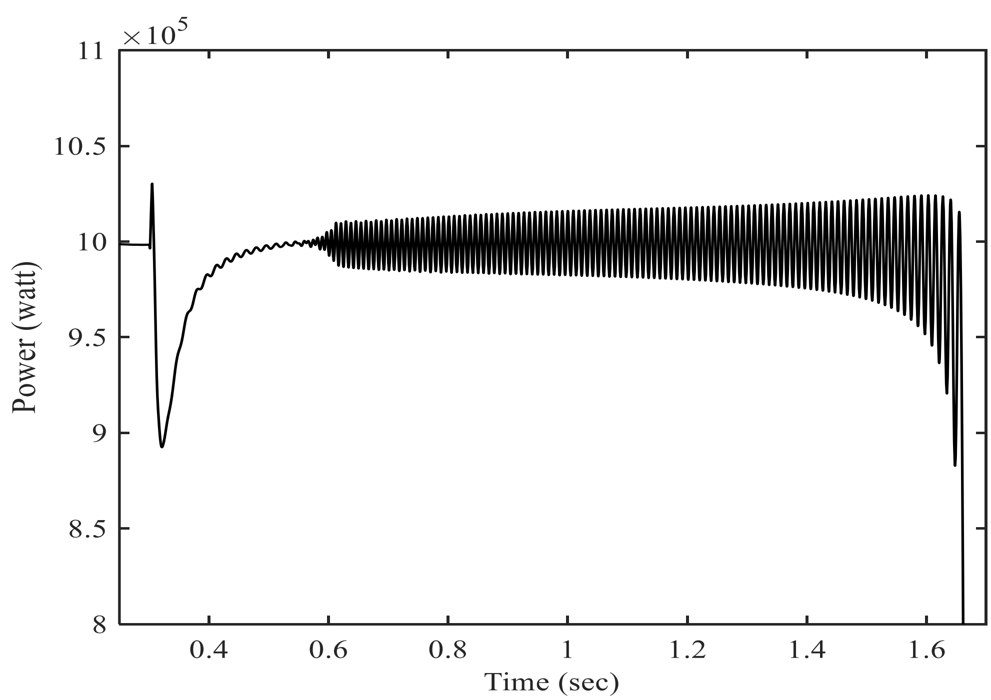

Figure 1.28 Output power of IBR, showing loss of grid synchronization

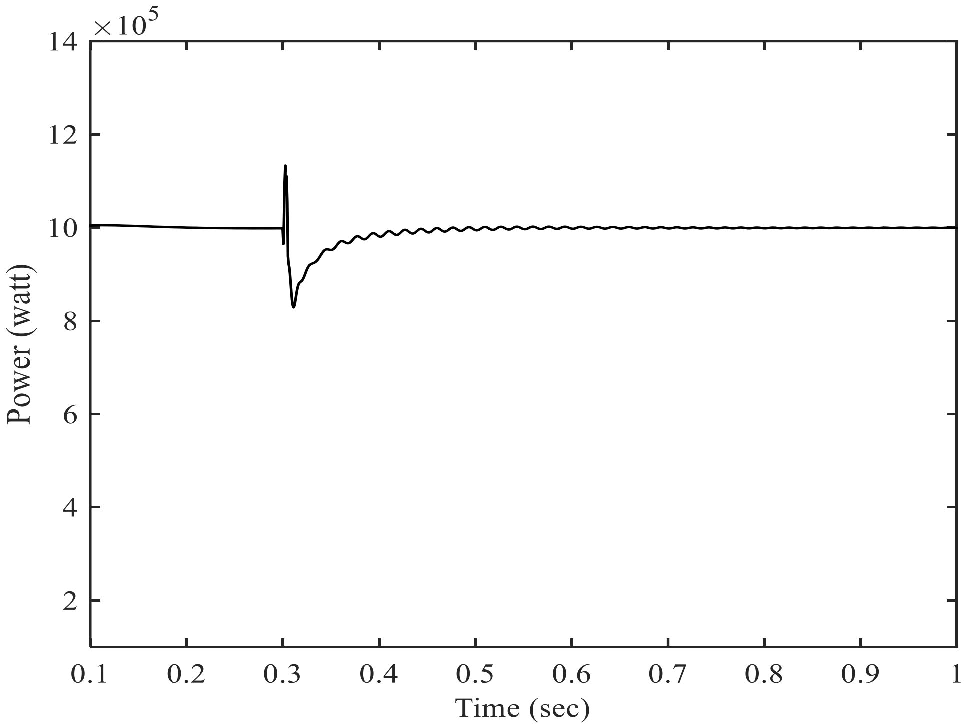

Figure 1.29 Output power of IBR, showing IBR retain its synchronization with the grid by slowing the PLL dynamic response.

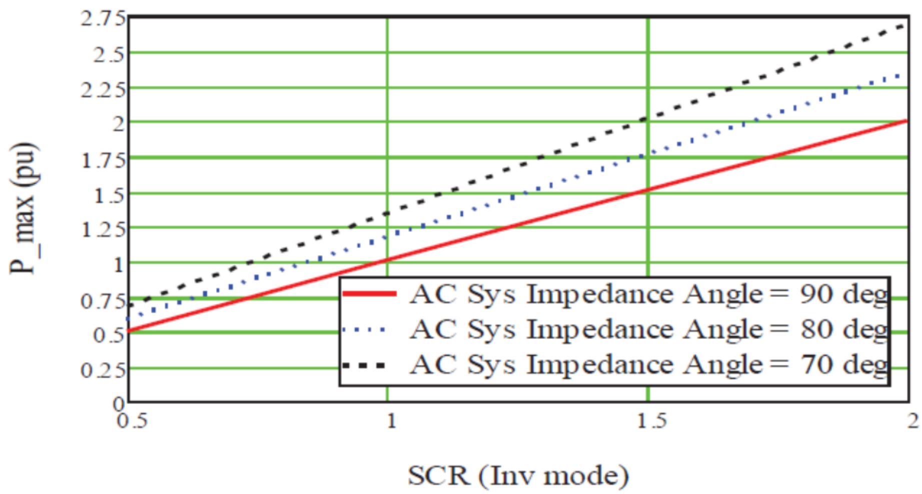

Figure 1.30 Inverter P_max vs SCR for different impedance angles [14]

1.7 Supplementary controller for enhancing inverters grid synchronization stability

According to Cigré Working Group B4.62 a connection is considered to be very weak if SCR at the Point of Interconnection (POI) is less than 3 in which SCR is defined as follows:

$$SCR = \frac{S_{SC}}{S_{Inverter}} = \frac{V_t^2}{|Z_s| S_{Inverter}} \tag{1.54}$$

Figure 1.30 [14] show the static transfer capacity limit as a function of SCR in which

$$P_{max}(P.U.) \approx SCR \cdot (1 + \frac{R_s}{|Z_s|}) \tag{1.55}$$

If dynamic stability limit is considered the situation is even worsened. It has been reported in [15] in some very weak systems SCR=1, only 40% of the maximum capacity of VSC can be used, even by turning the controllers parameters this limit can only reach to 60%. Therefore, proposing methods to enhance the grid synchronization stability of inverters is of special interest. Specifically, as discussed in the previous section, subsequent to the occurrence of events in power grids, depending on the post-event conditions of the system voltage, power and frequency oscillations may be experienced at the terminal of IBRs. If the strength of the system reduces, such oscillations are even further amplified and in extreme cases may lead to the disconnection of IBRs. While the existing controllers of IBRs have desirable tracking performances, their dynamic responses should be enhanced to overcome the above explained challenges in facing large disturbances in the power grid.

A supplementary controller is developed to overcome the above-mentioned shortcomings of existing controllers without replacing them. Figure 1.31, and 1.32 show the structure of the supplementary controller. The controller is designed based on the perturbed model of the control system. Washout filters are used to extract the perturbed components of the signals. In this way, it is possible to focus on high frequency components of the signals to damp out the high frequency

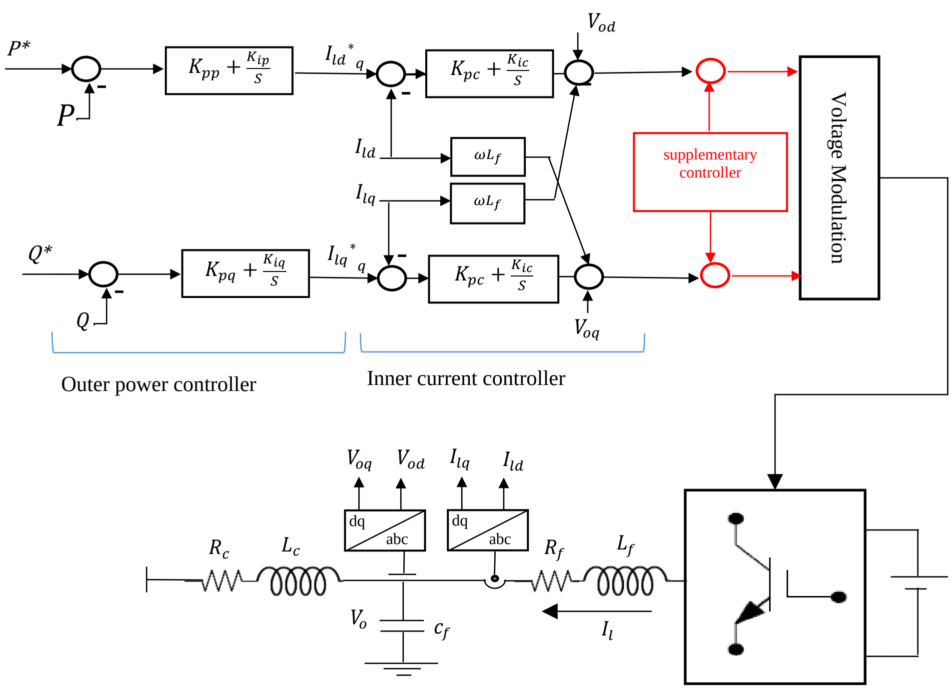

Figure 1.31 Schematic of the supplementary controller

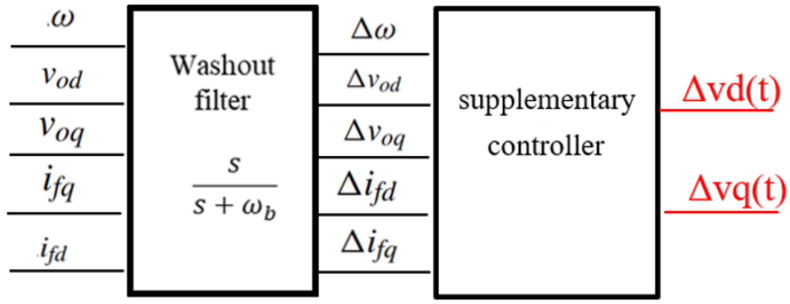

Figure 1.32 Schematic of the supplementary controller input and output signals

components. The advantage of the supplementary controller is it does not affect the tracking response of the main controller while it improves the transient response of the main controller. The perturbed model of IBRs in synchronous reference frame (SRF) should be derive as follow:

According to Figure 1.31, the state space model of synchronous reference frame (SRF) PLL is as follows:

$$\dot{\omega} = k_{P-PLL}(-\omega v_{od} + \frac{i_{fq}}{C_f} - \frac{i_{oq}}{C_f}) + k_{i-PLL}v_{oq}. \tag{1.56}$$

And also the dynamic of the output filter of the inverter is as follows:

$$C_f\dot{v}_{od} = C_f\omega v_{oq} + i_{fd} - i_{od} \tag{1.57}$$

$$C_f\dot{v}_{oq} = -C_f\omega v_{od} + i_{fq} - i_{oq} \tag{1.58}$$

$$L_f\dot{i}_{fd} = L_f\omega i_{fq} - v_{od} + v_{id} \tag{1.59}$$

$$L_f\dot{i}_{fq} = -L_f\omega i_{fd} - v_{oq} + v_{iq} \tag{1.60}$$

The state values are decomposed into the low frequency component and the high frequency component. Therefore, it is assumed $\omega = \omega_0 + \Delta\omega, v_{od} = V_{od} + \Delta v_{od}$, $v_{oq} = V_{oq} + \Delta v_{oq}$, $i_{oq} = I_{oq} + \Delta i_{oq}$ and $i_{fq} = I_{fq} + \Delta i_{fq}$ where ω_0 is the low frequency component of the angular frequency and $\Delta\omega$ is the high frequency component of the angular frequency. Replacing the above values in (1.56)-(1.60), the dynamic of perturbed model becomes as follows

$$\Delta\dot{\omega} = -k'_{P-PLL}C_fV_{od}\Delta\omega + k'_{P-PLL}\Delta i_{fq} + \Delta d_1. \tag{1.61}$$

Where

$$\Delta d_1 = k'_{P-PLL}\left[-C_f\Delta\omega\Delta v_{od} - C_f\omega_0\Delta v_{0d} - C_f\omega_0 V_{od} + I_{fd} - \left(I_{oq} + \Delta i_{oq}\right)\right] + k_{i-PLL}(V_{oq} + \Delta v_{oq}) - \dot{\omega}_0 \quad (1.62)$$

Similarly

$$C_f\Delta\dot{v}_{od} = C_f\Delta\omega\Delta v_{oq} + \Delta i_{fd} + \Delta d_2 \quad (1.63)$$

$$C_f\Delta\dot{v}_{oq} = -C_f\Delta\omega\Delta v_{od} + \Delta i_{fq} + \Delta d_3 \quad (1.64)$$

where $\Delta d_2, \Delta d_3$ are known inputs associated with the voltage dynamics and are derived as follows:

$$\Delta d_2 = C_f V_{oq}\Delta\omega + C_f\omega_0\Delta v_{0q} + C_f\omega_0 V_{oq} - (I_{od} + \Delta i_{od}) + I_{fd} - C_f\dot{V}_{od} \quad (1.65)$$

$$\Delta d_3 = -C_f V_{od}\Delta\omega - C_f\omega_0\Delta v_{0d} - C_f\omega_0 V_{od} - (\Delta i_{oq} + I_{oq}) + I_{fq} - C_f\dot{V}_{oq} \quad (1.66)$$

Similarly

$$L_f\Delta\dot{i}_{fd} = L_f\Delta\omega\Delta i_{fq} - \Delta v_{od} + \Delta v_{id} + \Delta d_4 \quad (1.67)$$

$$L_f\Delta\dot{i}_{fq} = -L_f\Delta\omega\Delta i_{fd} - \Delta v_{oq} + \Delta v_{iq} + \Delta d_5 \quad (1.68)$$

Where Δd_4 and Δd_5 are expressed as follows:

$$\Delta d_4 = L_f\Delta\omega I_{fq} + L_f\omega_0\Delta i_{fq} + L_f\omega_0 I_{fq} - V_{od} + v_{id}^{ref} - L_f\dot{I}_{fd} \quad (1.69)$$

$$\Delta d_5 = -L_f\Delta\omega I_{fd} - L_f\omega_0\Delta i_{fd} - L_f\omega_0 I_{fd} - V_{oq} + v_{iq}^{ref} - L_f\dot{I}_{fq} \quad (1.70)$$

Where L_f and C_f are inductance and capacitance of output filter, Δi_{od}, Δi_{oq} are direct/quadratic perturbed components of output current, I_{fd},I_{fq},I_{od},I_{oq} are DC components of direct/quadratic currents, Δi_{fd}, Δi_{fq} direct/quadratic perturbed components of current at the output filter of the inverter, V_{od}, V_{oq} are DC components of direct/quadratic voltages, Δv_{od}, Δv_{oq} direct/quadratic perturbed components of voltage at output capacitor, K_{P-PLL}, k_{i-PLL} proportional and integral gains for PLL, ω, ω_C, ω_n, ω_0, $\Delta\omega$, Angular frequency, DC components of angular frequency, angular frequency perturbation, the cut-off frequency of the filter and nominal angular frequency

Equations (1.61), (1.63), (1.64), (1.67) and (1.68) constitute the perturbed state space model of the IBR. To derive the perturbed term, a set of wash-out filters are used. According to the perturbed model of IBR, we are developing controllers to attenuate the disturbances (i.e. perturbed terms), which is the ongoing task.

Once the state space model of the perturbed system is developed, a variety of controllers can be designed. Specifically, in [1] we developed a supplementary controller based on the interconnection damping assignment passivity based (IDA-PB) control strategy. The controller is applied to the IBR in Figure 1.27. At t=5 the strength of the system is reduced by taking the line out. Figure 1.33-(a) shows output of the inverter. As Figure 1.33-(b) shows the supplementary controller successfully damped out the oscillations and prevented instability.

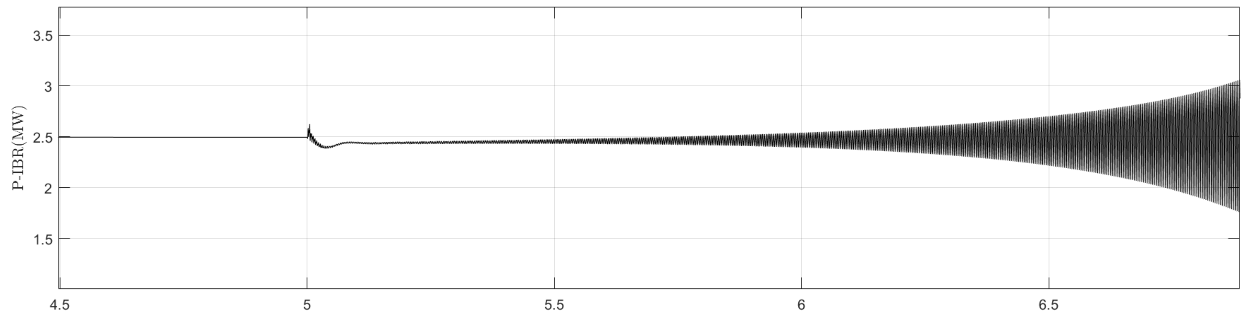

(a)

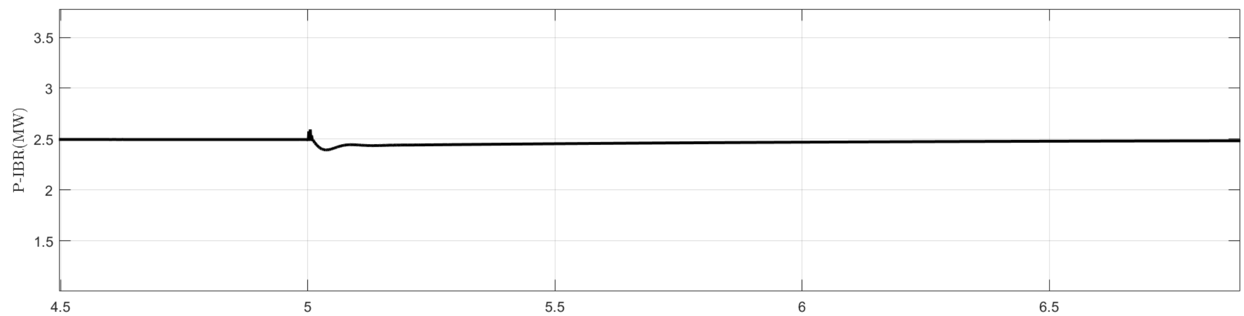

(b)

Figure 1.33 Output power of inverter (a) without the supplementary controller (b) with the supplementary controller

1.8 Conclusions

In this project the grid synchronization stability of inverter-based resources was studied. Using Bode plots and Generalized Nyquist Criterions (GNC) the impacts of different parameters such as the synchronization mechanism via PLL and grid strength were studied. The case studies results showed in weak power grids the bandwidth of PLL is influential on the grid synchronization stability. To accurately study the impact of grid strength GNC was utilized, and off-diagonal elements were not ignored. This is crucial for correct assessment of the grid synchronization stability. The simulation results demonstrated by making the PLL slower the grid synchronization stability can be improved but a slow PLL can not track fast changing of the system. To address this problem a supplementary controller was implemented based on perturbed model of the system. It adds damping to the system to damp out the output power oscillations leading to enhanced synchronization stability. It does not change the main controllers of the inverters and only adds supplementary signals to the controller which becomes zero at the steady state condition. Therefore, the supplementary controller improves the transient response of the controller which does not affect its proper tracking characteristics.

References

[1] M. Azimi, S. Lotfifard, ”Supplementary Controller for Inverter-based Resources in Weak Power Grids” IEEE Transactions on Smart Grid, vol.13, no.4, pp. 2886-2896, 2022.

[2] J. Schmall, S. Huang, Y. Li, J. Billo, J. Conto, Y. Zhang, “Voltage Stability of Large-Scale Wind Plants Integrated in Weak Networks: An ERCOT Case Study” IEEE PES General Meeting, pp.1-5, 2015.

[3] P.C. Kjaer, M. Gupta, A. Martinez, S. Saylors, “Experiences with Wind Power Plants with Low SCR” IEEE PES General Meeting, 2015.

[4] L. Petersen, B. Hesselbæk, A. Martinez, R. M. Borsotti-Andruszkiewicz, G. C. Tarnowski, N. Steggel, D. Osmond, “Vestas Power Plant Solutions Integrating Wind, Solar PV and Energy Storage”. 3rd International Hybrid Power Systems Workshop, 2018.

[5] T. Ackermann “Wind Power in Power Systems” Wiley, 2005.

[6] M. Morjaria “Deploying Utility-Scale PV Power Plants in Weak Grids” PES general meeting, 2017.

[7] R. Musca, G. Zizzo, M. Bongiorno “Grid-Forming Converters in Weak Grids – The Case of a Mediterranean Island” 18th International Workshop on Large-Scale Integration of Wind Power into Power Systems as well as on Transmission Networks for Offshore Wind Power Plants, pp. 1-6, 2019.

[8] S. Liemann, T. Hennig, L. Robitzky, C. Rehtanz, and M. Finkelmann,“Analysis of the stability and dynamic responses of converter-based gener-ation in case of system splits,”IET Gener., Transmiss. Distribution, vol. 13,no. 16, pp. 3696–3703, 20 8 2019.

[9] A. Yazdani, R. Iravani,”Voltage-Sourced Converters in Power Systems: Modeling, Control, and Applications” Wiley-IEEE Press, 2010.

[10] B. wen, D. Boroyevich, R. Burgos, P. Mattavelli and Z. Shen, "Analysis of DQ small-signal impedance of grid-tied inverters," IEEE Transactions on Power Electronics, vol. 31, no. 1, pp. 675-687, 2015.

[11] J. Yu, X. Lin, D. Song, R. Yu, Y. Li, and M. Su “Harmonic Instability and Amplification for Grid-Connected Inverter With Voltage Harmonics Compensation Considering Phase-Locked Loop” IEEE Journal of Emerging and Selected Topics in Power Electronics, vol. 8, no 4, 2020.

[12] C. Desoer and Y. T. Wang, "On the generalized Nyquist stability criterion," IEEE Transactions on Automatic Control, vol. 25, no. 2, pp. 187-196, 1980.

[13] M. Cheah-Mane, A. Egea-Alvarez, E. Prieto-Araujo, H. Mehrjerdi, O. Gomis-Bellmunt, L. Xu, “Modeling and analysis approaches for small-signal stability assessment of power-electronic-dominated systems” Wiley Interdisciplinary Reviews: Energy and Environment, pp. 1-22, 2023.

[14] J. Z. Zhou, and A. M. Gole VSC “Transmission limitations imposed by AC system strength and AC impedance characteristics” 10th IET International Conference on AC and DC Power Transmission, 2012.

[15] M. Ashabani and Y. Abdel-Rady I. Mohamed, “Integrating VSCs to Weak Grids by Nonlinear Power Damping Controller With Self-Synchronization Capability” IEEE Transactions on Power Systems, vol. 29, no. 2, 805-814, 2014.

Part II

Protection System Response

Sakis A. P. Meliopoulos, Thrust Leader
George J. Cokkinides
Syed Sohail Feroz Syed Afroz, Graduate Student

Georgia Institute of Technology

For information about this project, contact:

Sakis A.P. Meliopoulos
Georgia Power Distinguished Professor
Georgia Institute of Technology
School of Electrical and Computer Engineering
Atlanta, Georgia 30332-0250
Phone: 404-894-2926
E-mail: sakis.m@gatech.edu

Power Systems Engineering Research Center

The Power Systems Engineering Research Center (PSERC) is a multi-university Center conducting research on challenges facing the electric power industry and educating the next generation of power engineers. More information about PSERC can be found at the Center's website: http://www.pserc.wisc.edu.

For additional information, contact:

Power Systems Engineering Research Center
Arizona State University
527 Engineering Research Center
Tempe, Arizona 85287-5706
Phone: 480-965-1643
Fax: 480-965-0745

Notice Concerning Copyright Material

PSERC members are given permission to copy without fee all or part of this publication for internal use if appropriate attribution is given to this document as the source material. This report is available for downloading from the PSERC website.

© 2023 Georgia Institute of Technology. All rights reserved.

Table of Contents

List of Figures

1. Protection Systems Performance in Inverter Dominated Power Systems

1.1 Introduction

Low inertia inverter-dominated power systems affect the trajectory of the apparent impedance and measurements which have direct impacts on the operation of certain protective algorithms. In low inertia power systems, the scheme may mis-operate as fast power swings may be interpreted as genuine fault inducing instability. Due to low inertia, the frequency drop may become so fast that the post disturbance under frequency load shedding may not be effective due to delays associated with the implemented algorithms in the relay and operation time of switches (this case happened in 2016 Southern Australia blackout). This risk to the operation of protective devices is especially of concern when the system faces low levels of strength that may be experienced due to system splitting. As the strength of the network reduces voltage deviations due to disturbances generated by load shedding increases which may lead to operation of over-voltage protection of PV or Wind farms. A new method for determining the settings of UFLS and the amount of load shedding at each step should be proposed for low inertia and weak systems to consider the increased coupling and interactions between different protective functions.

A systematic investigation of what protection functions are vulnerable to the effects of IBRs, and which are immune will be undertaken. This investigation will also address the issue at what penetration level of IBRs these effects are manifested. The results of this investigation are crucial for proper representation of protection systems in dynamic and cascading failure analyses of power systems. A comprehensive investigation of mitigation methods will be conducted. Mitigation methods include requirements to impose inverter control changes to make inverter fault current contribution to include negative/zero sequence components so that they “look” similar to synchronous generator-based systems, estimation-based protection and other protection approaches that immunize against the new characteristics of inverter-based resources. The capabilities and limitations of each one of the approaches will be studied and documented. An important question that will be addressed is at what penetration level of IBRs the legacy protection and control system is seriously compromised.

During faults, inverters may follow different control strategies such as suppression of negative sequence current, suppression of active power fluctuations, or suppression of reactive power fluctuations. Certain protective relays may mis-operate depending on the inverter control strategies. For instance, if inverters operate based on suppression of negative sequence current, negative sequence polarized directional relays may mis-operate. Prior work has identified some of the causes of relaying mis-operations due to the presence of substantial penetration of IBRs, for example inverter controls result in new fault current characteristics (suppression of negative) which affect the capability of relays to determine fault direction and subsequently mis-operate.

1.2 Objectives

The objectives of this project were to investigate the interactions of protection and control systems with the new characteristics of power systems created by the proliferation on inverter interfaced resources. Specifically:

- To study the different methods of protection of the transmission and distribution network and to analyze the effect of the inverter-based resources on the protection of the network.
- To simulate and recreate the fault characteristics of the inverter-based resources on the transmission and distribution systems and to improve the network by addressing the drawbacks of the inverter-based resources on legacy protection systems.

2. Background Investigation

The inverter protection interactions have been researched and there are many reported problems in the literature. It is important to recognize protection and control systems are the leading contributor to system disturbances. While it is expected that protection and control systems should clear fault and other anomalies in a very short time with minimal impact on the system, sometimes there are mis-operations or subsequent events that lead to major disturbances. We provide a short review of the 2003 blackout that identified the role of protection and control systems in contributing to blackouts. At the time, the issue of protection and inverter interactions were not of concern. Recently, major disturbances occurred because of the interaction between protection and inverters. A provide examples of events where the interaction caused major disturbance. Finally, a critical review of the existing literature is provided in this section. We present several papers that report on these interactions and provide a critical review of the reported research.

2.1 Impact of Relays on Blackouts – The 2003 Blackout

The event that caused researchers to investigate the role of numerical relays to system performance was the north-east blackout of 2003. It was a massive power outage that occurred on August 14,2003, and affected parts of North-Eastern and Mid-Western United States and parts of Canada. It was caused by a combination of equipment failures, human errors, and communication problems. The 2003 investigation did not uncover any issues with inverter-based generation, since the level of inverter based resources was not very high at the time of the event.

The event began at 4:10 pm EDT when a power line in Ohio sagged into a tree and triggered an alarm. However, the alarm was not properly communicated to the system operators, who did not take action to prevent the cascade of power failures that followed.

Over the next several hours, a series of failures occurred in the power grid that resulted in shutdown of more than 100 power plants and leaving an estimated 55 million people without electricity. The blackout affected cities such as New York, Detroit, Cleveland, and Toronto, causing chaos and confusion as transportation systems stopped and people were left without air conditioning or other essential services.

The blackout lasted for several days in some areas and had a significant economic impact with estimated losses being about 4 billion to 10 billion dollars. This event exposed serious weaknesses in the power grid and led to improvements in the system.

Some of the issues identified was (a) the failure of some protective relays to detect and isolate fault conditions in the power grid and (b) the tripping of circuits by third zone distance relays because of their settings. This highlighted the need for more advanced and reliable protective relays, which has led to the research and development of better methods for setting and coordinating relays. In addition, at Georgia Tech, the research led to the development of setting-less relays to improve the safety and reliability of the protection and control systems.

2.2 Inverters – Protection Interactions Leading to Major Disturbances

In recent years, a number of events that lead to major disturbances have been reported. The investigation indicated that the major disturbances were caused by the interaction of protection and control systems with inverter interfaced generation. While there are a lot of these events recently, we describe only samples of these events.

Event of August 16, 2016, California, USA: On August 16, 2016, a fault induced a total of 1,178 MW of PV solar interruption. The faults were caused by a fire that started at the Cajon Pass in California, USA and moved towards a major transmission corridor with three 500 kV lines and two 287 kV lines. There were multiple faults over a period of time, thirteen on the 500 kV system and two on the 287 kV system. The fault that induced the loss of 1.178 MW occurred at 11:45 am PST and successfully cleared in less than three cycles. The mode of interruption was that the inverters of the solar PV plants ceased output as a result to the fault in the system. Specifically: (a) the majority of inverters trip instantaneously based on frequency measurements; it was determined that these inverters are susceptible to erroneous tripping due to frequency changes; this response accounted for 700 MW of the lost generation; and (b) a number of inverters that tripped were configured to cease current injection if the voltage goes above 1.1 pu or below 0.9 pu; the inverters were returned to pre-disturbance level at a slow ramp rate; this response accounted for about 450 MW of lost generation. Approximately 66% of lost generation was restored within five minutes.
The frequency during the above described event is shown in Fig. 2.1 and the waveform distortion is shown in Fig. 2.2. These figures provide evidence of the response of the inverters. The phase shift observed in the waveforms generates a large instantaneous frequency change in most frequency tracking algorithms and in this case triggered the inverter response. Note that the frequency of the system in Fig. 2.1 does not show the spikes as it was obtained with PMUs that show average frequency over longer windows. Note also that the voltage during the fault dropped below 60% triggering the ride-through function which in this case did not return to the pre-disturbance values fast enough.

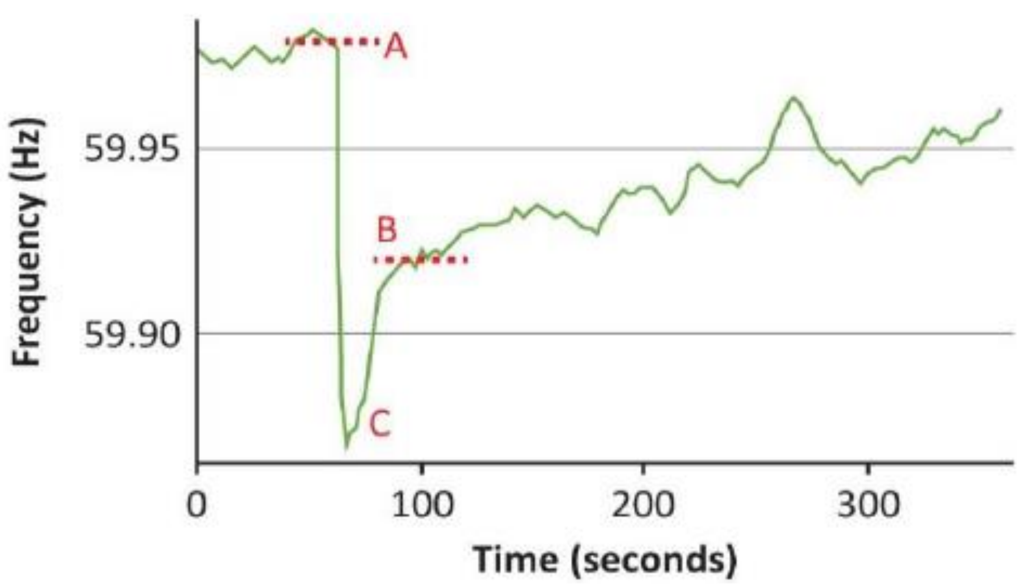

Figure 2.1 Western Interconnection Frequency During the 11:45am PST Fault [33].

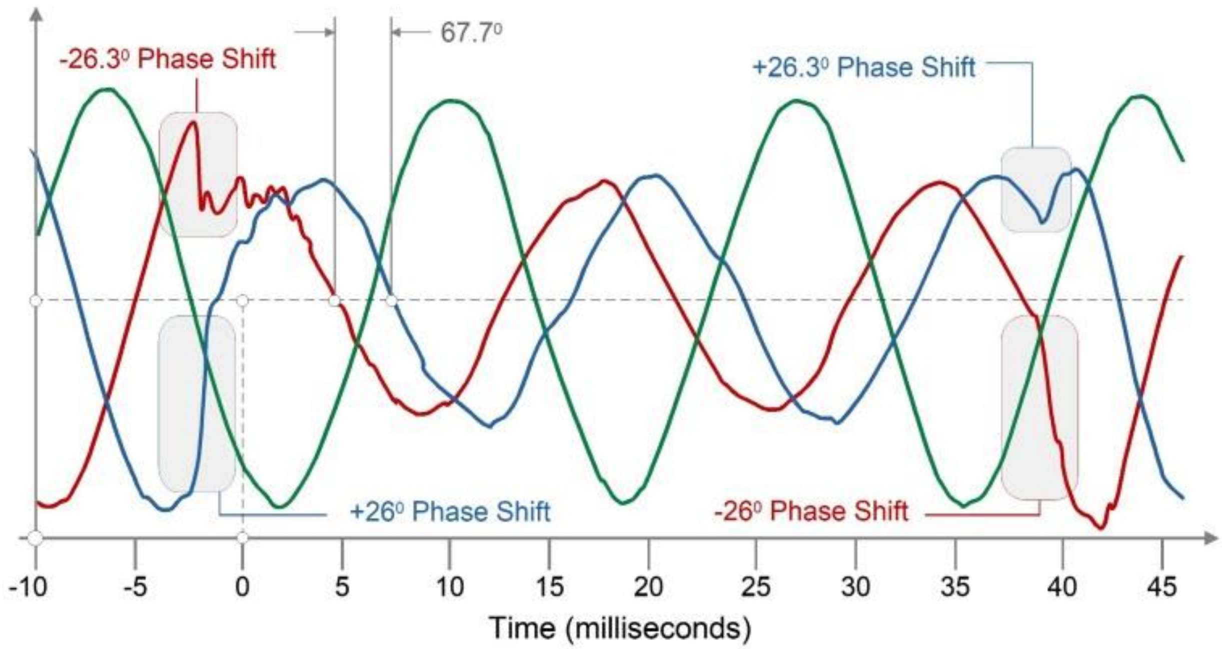

Figure 2.2 Distortion of Sine Waves During the 11:45am PST Fault [33].

Event of October 9, 2017, California, USA: On October 9, 2017, a fire in California (Canyon 2 fire) caused two transmission line faults 2 minutes and 14 seconds apart on a 220 kV and 500 kV transmission lines respectively. The faults were successfully cleared but the disturbance caused the loss of 900 MW of solar PV resources in about six PV plants. The majority of inverter trippings was caused by fast transient overvoltages (sub-cycle) and instantaneous protective action at the inverters. A significant number of inverters entered momentary cessation following the fault events. Note that, in this case, no instantaneous tripping occurred due to instantaneous fast frequency changes; the instantaneous tripping was due to transients. The activation of the ride-through function was also a contributing factor as the return to pre-disturbance operation was characterized by a long delay and a slow ramping.

In general, both California events were caused by inverter controls and more specifically, protection settings including instantaneous frequency/transients and ride-through function settings. These cases provide useful information for better design of inverter controls.

2.3 Impact of Inverter-Interfaced Renewable Energy Generators on Distance Protection

The reviewed paper is cited below.

Yu Fang , Ke Jia , Member, IEEE, Zhe Yang , Yanbin Li, and Tianshu Bi, “Impact of Inverter-Interfaced Renewable Energy Generators on Distance Protection and an Improved Scheme”, IEEE Transactions on Industrial Electronics, vol. 66, no. 9, pp. 7078-7088, Sept. 2019

Paper Objectives:

- Inverter interfaced renewable energy generators have different fault characteristics from the synchronous generators.
- This makes the conventional distance protection used in networks with synchronous generators not applicable.
- The objective of this paper is to provide an improved scheme to deal with this adaptability problem based on time delay and zero-sequence impedance.
- Also, validation is done by building a detailed IIREG model and carrying out real-time simulations. Field short circuit tests are also performed in a real wind power plant to examine the practical feasibility of the proposed scheme.

Analysis:

Introduction: Operation of the Conventional grid has little effect on the protection range and sensitivity of distance protection on the other hand renewable energy sources are connected to the grid through converters whose fault characteristics are influenced by control strategies. Due to this difference in characteristics between renewable energy and synchronous generators, conventional protection based on fault characteristics of synchronous generators cannot be used in renewable energy systems.

Inverter interfaced renewable energy Generators (IIREG's) that include type-IV WF's and PV plants, different control strategies and performance of distance protection on renewable energy side was analyzed. An adaptive relay setting principle for distance protection was proposed, this was done by obtaining voltages and flows of all parts of the systems, the trip boundary of the distance relay was reset adaptively. Adaptive scheme required high-performance microprocessors with high penetration level of WF's and these requirements could not be met in some power grids, other methods were utilized like advanced line impedance formula to recognize LLG faults, but this could not accurately be adopted to LL faults due to the lack of zero sequence components.

Analyzing the differential protection relay, the paper says that the deviation of the phase angle of the short-circuit currents on the two terminals caused by control actions after internal faults may cause low sensitivity when large scale WF's are integrated. The current transmission network is equipped with differential protection, distance-based protection and zero sequence overcurrent protection on the IIREG side. Distance protection is blocked sometimes due to the unique fault characteristics of the IIREG's and increased penetration of the IIREG's has resulted in the fact that we cannot only look at the sensitivity of the differential protection anymore. The paper tries to address this issue by proposing a solution to this problem.

Failure Characteristics analysis: In the case of an asymmetric fault in the system, the IIREG suppresses the negative-sequence current and the active and reactive power oscillations by regulating positive and negative sequence current references by adopting a dq synchronous rotating frame.

In short, the low voltage ride through control strategy makes the amplitude of the steady state short circuit current very limited and controls the initial phase angle this is different from the typical synchronous generator.

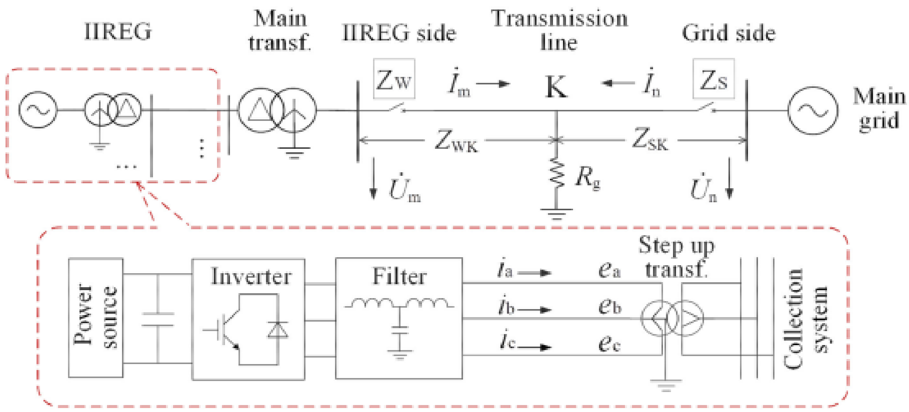

Figure 2.3 Transmission network with inverter interfaced renewable energy generator

Operating performance of distance protection: In this section the characteristics of the failure analysis of the IIREG's is taken from the previous section to analyze the operation of the distance protection under different fault conditions.

When an ungrounded fault occurs on the transmission line due to the lack of zero-sequence path the S.C current in the IIREG is supplied by the inverter. During an asymmetric ground S.C fault the fault location's zero-sequence voltage and the small zero-sequence impedance leads to a significant zero-sequence current on the IIREG side.

In the case of three phase S.C faults and considering the ground impedance relay, the characteristics of the inverter results in the S.C current to be only 1.2-1.5 times the rated current which is much small when compared to the S.C current of the synchronous generator. Thus the grid side impedance is less affected by fault resistance and thus the possibility that the grid side distance relay malfunctions is much less. On the other hand the inverter side impedance gets affected depending on the phase angle of the ratio of the inverter side and the grid side currents(I_{grid}/I_{inv}).If the phase angle is between 0 and 180 degrees the additional impedance is presented as a large inductive impedance and the distance relay will fail to operate for internal faults and if the phase angle is between 180 and 360 degrees it is presented as a capacitive impedance and the relay fails to operate.

In the case of traditional synchronous generator-based systems a quadrilateral distance element is used to offset the impact of the fault resistance on the protection relay, but cannot be used in the case of the IIREG since the additional impedance will lead to being either inductive or capacitive as seen earlier. A mho element is used to understand this purpose in the paper.

Improvement of the protection scheme: A delay element is added to make the inverter side distance relay non operable for a small duration of time. The grid side relay operates reliably and reflects fault, now the IIREG side distance relay can reflect fault accurately. In order to accommodate zero sequence possibilities a zero sequence distance relay and a zero sequence overcurrent relay is connected to the IIREG side.

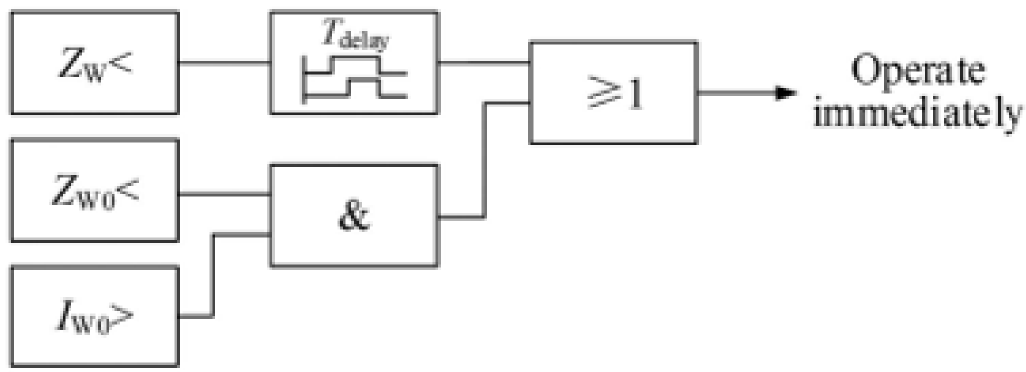

Figure 2.4 Improvements made to the IIREG Protection

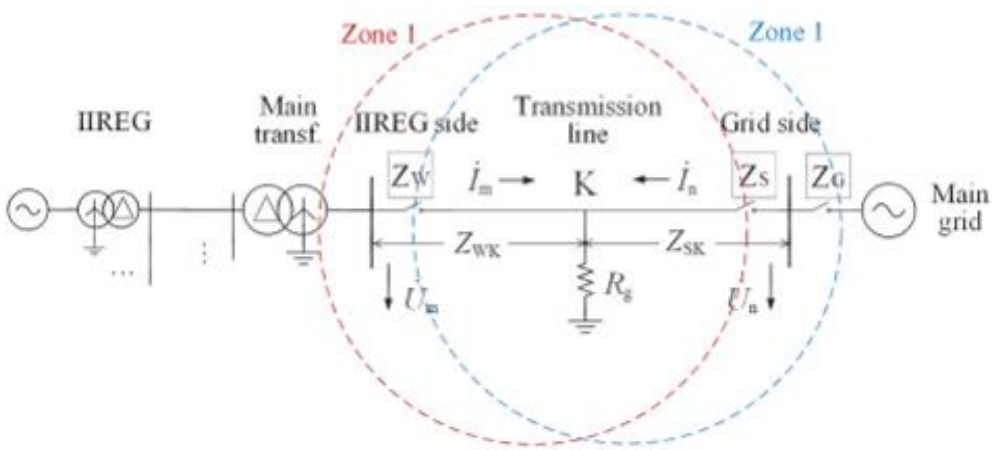

Figure 2.5 Zone protection of the distance relays

Final Remarks: Nice concise and detailed analysis of the effects of the inverter side on the distance protection during faults. The analysis is mostly done on the WF based renewable energy source. Improvements can be made to incorporate solar PV's mainly and other types of traditional renewable energy sources. Also the literature on the faults can be more streamlined and ordered, it is a little confusing for different faults and different relays used and need to be constantly checked for accuracy.

2.4 A Control-Based Solution for Distance Protection of Lines

The reviewed paper is cited below.

Amin Banaiemoqadam , Ali Hooshyar , and Maher A. Azzouz, "A Control-Based Solution for Distance Protection of Lines Connected to Converter-Interfaced Sources During Asymmetrical Faults", IEEE Transactions on Power Delivery, vol. 35, no. 3, pp. 1455-1466, June 2020.

Paper Objectives:

- Converter interfaced renewable energy sources (CIRES) causes mis-operation of distance relays installed near them.
- Several methods have been identified to address this problem. This paper proposes a new approach by regulating the fault currents of CIRES's such that distance relays functions properly without modification. In this method that the paper uses the objective is to mimic certain features of the symmetrical components of synchronous generator's fault currents that affect distance relays.
- It also satisfies the characteristics of the converters such as reducing the phase current magnitude during faults compared to the synchronous generator.
- Some advantages of this method is that it is simple, compatible with most common relays available and is independent of the voltage and the power rating of the CIRES and is cost effective.

Paper Description:

Introduction: Renewable energy sources (RES) have introduced fault ride through (FRT) components into modern grid code operation. The fault characteristics of CIRES are different from that of the SG's and as such the distance relay operating near the CIRES malfunctions. There are several methods to address this issue, one such is the line current differential relays. This requires a high-bandwidth communication channel, which is expensive and thus this method cannot be used as the only solution to the CIRES problem.

This paper proposes a new scheme for current control to prevent distance relays from mis-operating, it focuses on the current control references for the converter control and thus there is no need to modify the relay firmware.

Test system: An IEEE 9-bus system is used for simulation in PSCAD/EMTDC, bus 9 of the original system is replaced by a 13.5 kV, 100 MVA CIRES that is interfaced with bus 9 through a 13.5/230 kV, 120 MVA transformer. The high-voltage (HV) side of the transformer is the point of common coupling (PCC) for the CIRES. Since the fast dynamics of the source, either PV panels or Type IV wind turbine are decoupled from the grid by the DC link capacitor, the energy source along with the source-side converter is modeled by a controllable DC current source. During steady state, the CIRES generates its rated power at unity power factor (PF) at the PCC. The CIRES rides through faults using a breaker chopper circuit. The distance relays are used to protect the line. Different features of the distance elements are modeled like a commercial relay with a quadrilateral characteristic.

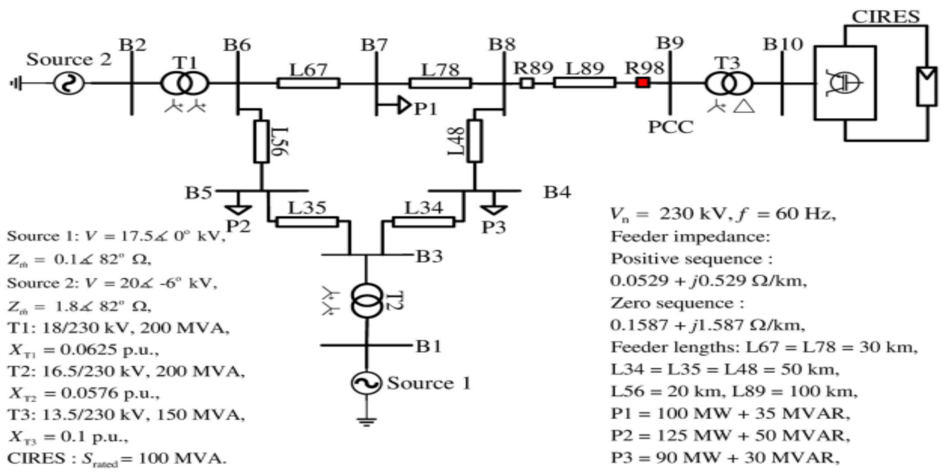

Figure 2.6 Single line diagram of the test system

Problem Statement: Impedance measured by the distance relay deviates from the actual impedance to the fault in the presence of the fault resistance and infeed current at the remote end of the line. For a SG based system, the angle between the fault currents at the two ends of the line is determined by the phase difference between the pre-fault voltage, large angles reduce stability and hence the phase difference is very small. CIRES on the other hand behaves as a current source, the current angle is regulated by the converter's control system such that the host system's GC is satisfied. During fault, the angle of the local current for the relay at the substation of the CIRES can be substantially different from that of the remote-end current. The effect of fault resistance and remote infeed current on the impedance measured by the distance relay is not centered on the resistance axis. This fictitious reactance can cause considerable relay overreach or underreach. It is generally accepted that there should be a small overreach near the sending end terminal where the CIRES is located but instead due to the presence of the inverter there is a small magnitude of the converter fault current which leads to larger fictitious reactance. However, in the case of an intermediate infeed system the relay overreaches instead of underreaches and this creates new issues as the system is designed to handle relay underreach traditionally for a CIRES system.

Proposed Solution: The relay malfunctions due to the phase difference between the infeed and the CIRES fault currents.When the angles between the CIRES fault currents and the SG fault currents is close as possible the phase difference between the local and infeed currents becomes zero and thus the relay operates properly. A feedforward control is used which makes the voltage at the converter side replicate non -idealities of the generator side. CIRES current is a balanced positive sequence current. The converter is open in negative and zero sequence circuits. As a result the control variables are identified as the currents i_d and i_q respectively. And thus by controlling the ratio i_d/i_q we can regulate the current angle.
As soon as the voltage drop is detected, references for i_d and i_q are chosen to control the angle of the local current such that the phase difference between the CIRES and infeed current decreases. These references are i_{d_ref} and i_{q_ref}.

The selection of these two reference currents is done by two strategies:

1. To imitate the pattern of SG's current angles during different fault types, but the problem is that since the magnitude of the fault current on the CIRES still remains small, it can only be used for small infeed circuits.
2. Find proper reference currents for the worst fault condition such that it achieves improved performance of the distance relay for the CIRES.

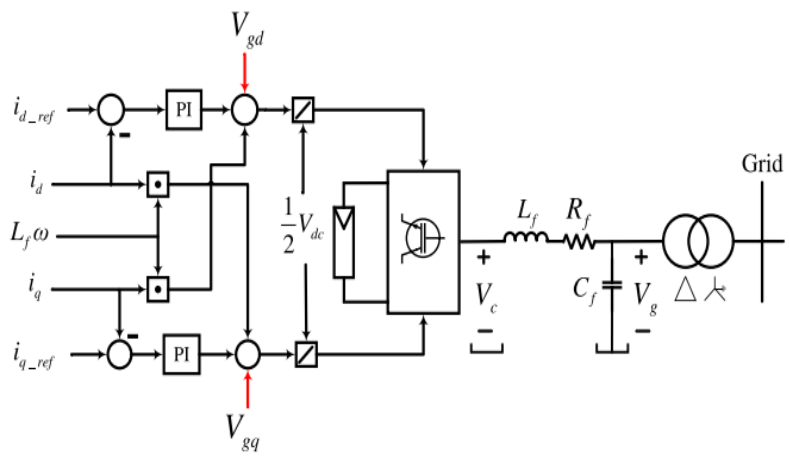

Figure 2.7 Feedforward control of the CIRES system

Final Remarks: Nice, detailed analysis of the improvement scheme of the CIRES current control. Improvements could be made to incorporate a detailed analysis of why the inverter current causes issues, detailed analysis of why different faults such as L-L LLG etc. cause issues instead of clumping them together as two case scenarios and finally depicting a practical and real time scenario of the proposed scheme.

2.5 Adaptive Distance Protection for Lines Connecting Renewable Plants

The reviewed paper is cited below.

Subhadeep Paladhi, and Ashok Kumar Pradhan, "Adaptive Distance Protection for Lines Connecting Converter-Interfaced Renewable Plants", IEEE Journal of Emerging and Selected Topics in Power Electronics, vol. 9, no. 6, pp. 7088-7098, Dec. 2021.

Paper Objectives:

- Fault ride through compliance prevents undesirable disconnection of renewable sources from the network even during fault.
- Various control schemes for the converters modulate the voltage and the current output significantly during a fault.
- This in turn varies the fault characteristics of the renewable sources and therefore affects the performance of the distance relay.
- Distance protection using local data for transmission lines connected to renewable plants is proposed.

- This method calculates the phase angle of the faulted loop current by determining the pure-fault impedance of the renewable plant at every instant following fault detection, irrespective of the control scheme.
- The paper also tests this on a renewable-integrated modified 39-bus New England system using PSCAD/EMTDC.

Analysis:

Introduction: Large Scale Converter interfaced renewable plants (CIRP's) are of interest today to meet the increasing power demand and for environmental reasons. Due to the variability in renewable energy sources, there is a power fluctuation in these plants. An MPPT is used to extract maximum power and to satisfy the grid code utility. Different control schemes are used. One such scheme is the current limiting scheme which ensures the safety of the power electronics components during faults. This however affects the fault currents during fault causing mis-operation of distance relays. There have been several schemes as discussed earlier in the previous papers. This paper proposes a new and improved scheme for mitigating this issue, a distance protection approach is proposed for lines connecting CIRP's mitigating the issue with fault characteristic variation. The method calculates the phase angle of the faulted loop current by determining the pure-fault sequence impedances of the renewable plant with every new samples of voltage and current data available to the relay. Therefore, the proposed adaptive approach uses it to obtain the line impedance up to the fault point from relay bus.

System Description: A 345 kV, 60 Hz, 39 bus New England system is used in PSCAD/EMTDC. The generator connected to bus 33 is replaced by a 300-MW solar PV plant. The solar plant consists of multiple PV units, each connected to the common coupling bus through a dc/ac inverter and transformer. The solar-based CIRP is controlled in the synchronous reference frame, which controls the fault current along with the filter of the converter. Feedforward compensation is provided to decouple the converter operation from the disturbances occurred in the grid side. The solar plant is modeled by satisfying NA-GCs and operates close to the unity power factor. The EU-GC imposes high priority on reactive power support to improve the voltage profile at a common coupling point. The reactive current reference for the purpose is calculated. Performance of the distance protection method is tested.

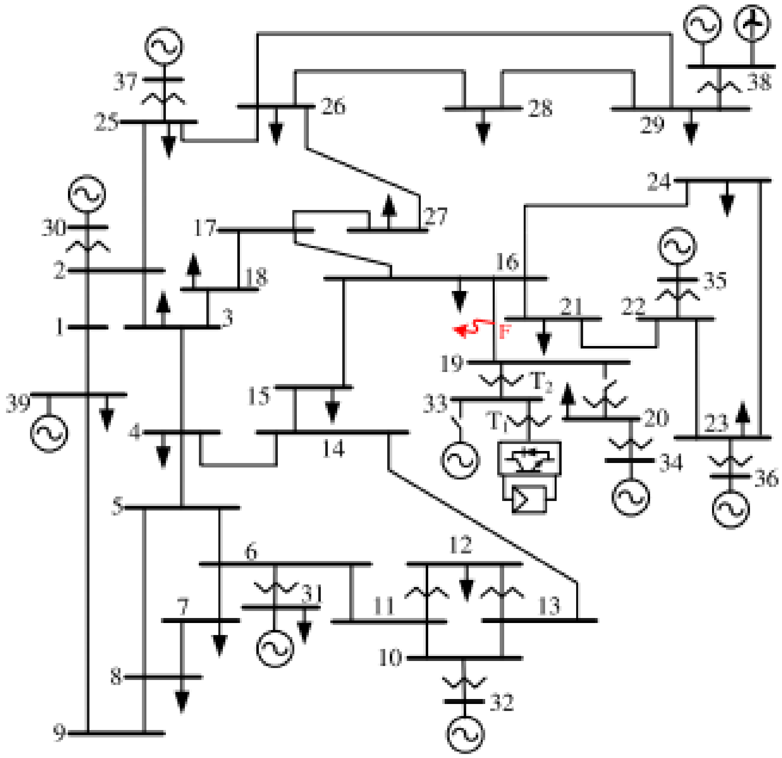

Figure 2.8 39-Bus New England Test System model integrating CIRP

Issue with distance relay for line connecting CIRP: As discussed in the previous papers the control methods utilized by the converter cause the fault currents to be abnormally low and thus the impedance calculation of the relay is very high thus resulting in the relay to mis operate. There is a significant phase difference between the fault currents at the CIRP end and that of the synchronous generator end, this results in a significant shift of the impedance calculated due to the fault and thus there is a huge deviation of the fault impedance to that of the preset value and thus the relay fails to operate for the fault occurring.

Proposed Adaptive Relaying Method: In this section of the paper, it is discussed as to how the phase angle difference between the currents leads to the change in impedance and values and thus requires some correction. First the different fault types are calculated based on the voltage drop principle then they have used alpha as the deviation angle and have used techniques to determine alpha using local data for different fault types using pure fault impedance of solar plant.
In the case of non-available negative sequence current in CIRP during asymmetrical fault the method calculates the deviation angle using negative sequence voltage measured by the relay. This alpha is used with the apparent impedance to determine the line impedance up to the fault point. Thus, considering all measurements and errors the tripping is provided to up to about 80% of the line.

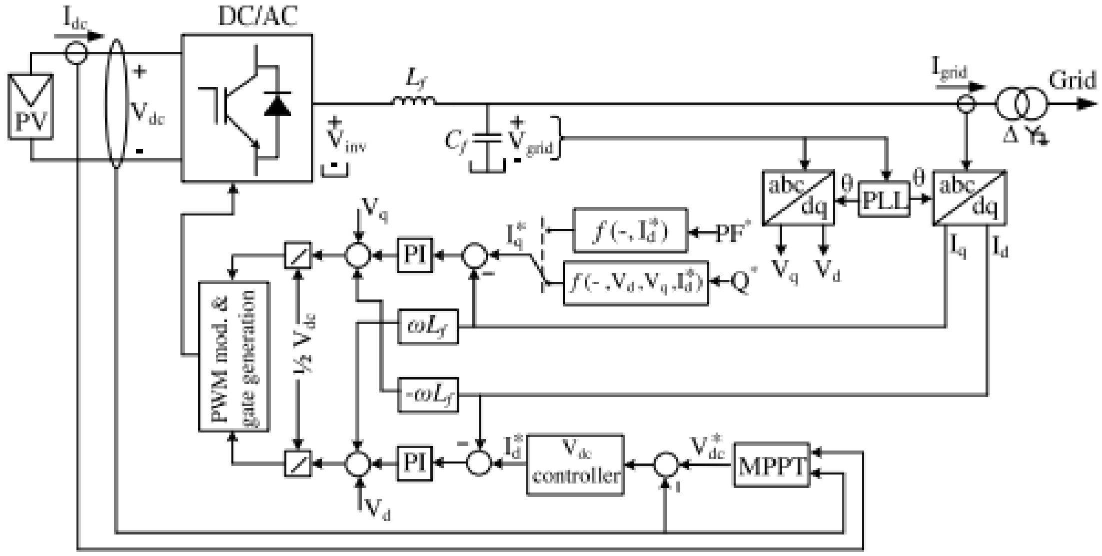

Figure 2.9 Control scheme implemented on the CIRP

Final Remarks: Nice detailed paper about adaptive relaying techniques. The proposed scheme seems plausible but is not backed by real time analysis on real systems and thus remains only in theory.

2.6 Distance Protection of AC Grid with Offshore HVDC-Connected WTS

The reviewed paper is cited below.

Lina He, Chen-Ching Liu, Andrea Pitto, and Diego Cirio, "Distance Protection of AC Grid with HVDC-Connected Offshore Wind Generators", IEEE Transactions on Power Delivery, vol. 29, no. 2, pp. 493-501, April 2014.

Paper Objectives:

- Transmission line close to points of common coupling (PCC) causes the protective relay to mis operate due to short circuit faults and the subsequent fast reactive power control of the voltage source converter-HVDC(VSC-HVDC).
- This paper proposes an apparent impedance calculation method which utilizes the bus impedance matrix to calculate the impedances viewed by the distance relays during the three phase SC fault. It is then used to identify the miscoordination of the zone-2 relays in the combined ac/dc system.
- Thus, the method results in accurate impedances viewed by the distance relay and identifies the protective device setting on the ac grid that needs to be adjusted due to the HVDC control of offshore wind generators.

Analysis:

Introduction: Increasing energy demand has resulted in many countries developing targets to significantly increase the integration of renewable energy sources including wind power. VSC-HVDC is preferred for offshore wind power transmission due to its advantages of fast and independent control of active and reactive power, feasibility of multi-terminal dc-grids and black start capability. The grid side VSC uses constant dc and ac voltage control to independently regulate the transmitted active and reactive power. When the ac side transmission close to the PCC undergoes a SC fault there are technical requirements for the dc side protection as such the PCC voltage is reduced and thus this affects the voltage and current of the ac transmission grid near the PCC. Since the capacity of the VSC station is huge for offshore transmission and thus the impact on the line current and voltage is significant. As a result, the operation of distance protection is also significantly reduced. The basic principle of the distance relay is to measure the apparent impedance using the voltage and current measured by the relay which in turn approximates the distance where the fault occurs. This apparent impedance is then compared with the preset impedance to check whether the fault occurs within the protected zone or not.
Zone-2 relays act as a backup protective function that is usually located on the remote end of line adjacent to the protected line. Due to the impact of VSC fast control on line voltage and current the impedances viewed by Zone-2 relays might fail to locate the fault in the case of SC fault. The error in the fault distance location results in miscoordination, if the fault clearing time exceeds the critical clearing time (CCT) the system becomes unstable and triggers a sequence of cascading events.

Several methods had been identified previously but are limited to ac grids and does not involve an ac grid with HVDC connected offshore wind generators. The paper proposes an apparent impedance calculation method for identification of potential mis coordinated relays, by considering GSVSC's reactive power regulation the proposed method uses Z_{bus} method to calculate impedances viewed by distance relays. It is then applied to the proposed combined ac/dc system to calculate the impedance viewed by a distance relay during a SC fault at the reach of its Zone 2. This result is then compared with the existing Zone-2 settings to identify mis coordinated relays.

System Outline: Two 500 MW offshore wind farms based on double-fed induction generators are connected to an ac grid via H-shaped VSC-HVDC grid. The VSC-HVDC link is automatically set to balance out the real and reactive power of the grid, it does so by utilizing the power-voltage droop control using PI controllers and reference values for the voltage control and uses a feed forward current decoupling controller for the inner current loop. Offshore wind farms have distance relays that are commonly designed for primary and backup protection. Distance relays are arranged to provide two or three protective zones.

Zone-1 comprises 80-90% of the line length and does not have a time delay for operation, it is typically 2 cycles. Zone-2 is required to reach 40-50% of the shortest line emanating from the remote bus with a time delay of 15-30 cycles. The reach of Zone-3 exceeds the adjacent line and has a time delay of 1s.

When the transmission line experiences a fault say between bus 1 and 2 the reduction of bus 1 voltage triggers the VSC to increase the reactive power output to boost the PCC2 voltage. Say there is a relay A near the fault such that the fault lies within its Zone-1 and another relay B such that the fault is in zone-2 of B then the primary protection i.e., relay A fails to operate and clear fault in the zone-1 of relay A since the impedance is increased due to the increase in the voltage levels. The relay B will now try to work as a backup to clear fault with zone-2 time delay.

However, this duration allows the VSC to adjust the reactive power and such the voltage now is further increased more as a resulted the impedance viewed by the relay B is increased and the fault distance viewed also increases. Thus, this overestimation results in the zone-3 of relay B tripping the fault line at its delay time thus resulting in miscoordination.

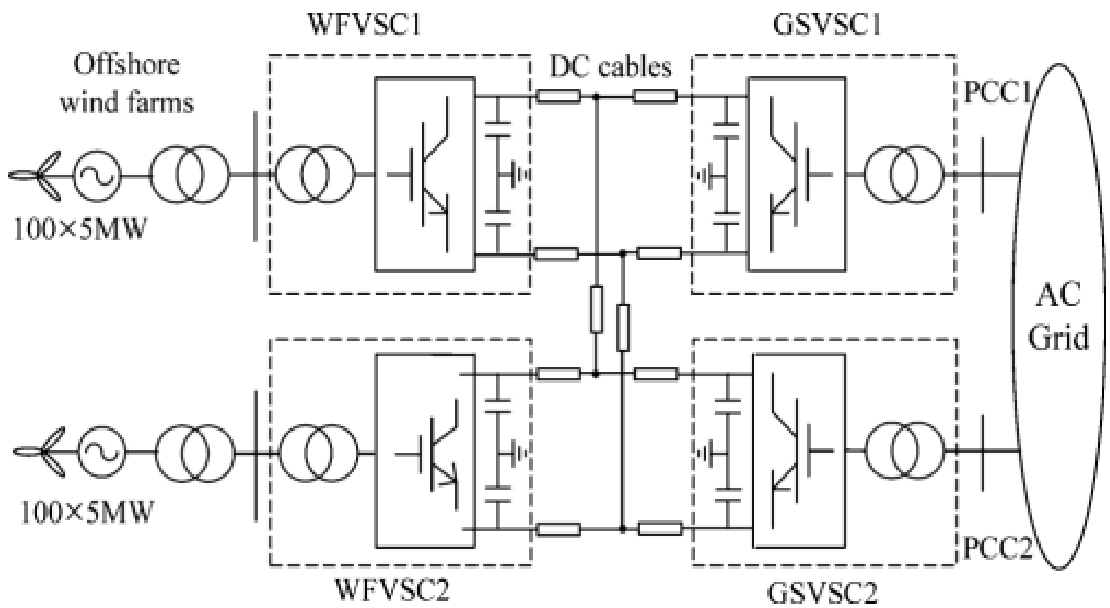

Figure 2.10 System diagram for the AC/DC system

Apparent Impedance Calculation Method: The paper proposes a method to find potential mis coordinated zone-2 relays by doing an apparent impedance calculation method based on Z_{bus}, it is done by:

1. Calculate PCC voltages based on Z_{bus} method during a three-phase SC fault located on 50% of the shortest line emanating from the remote bus of a relay.
2. Consider GSVSCs reactive power control to modify PCC voltages.
3. Use Z_{bus} method to calculate the voltage and current viewed by the relay based on PCC voltages and compare the obtained apparent impedance with the Zone 2 setting of the relay.

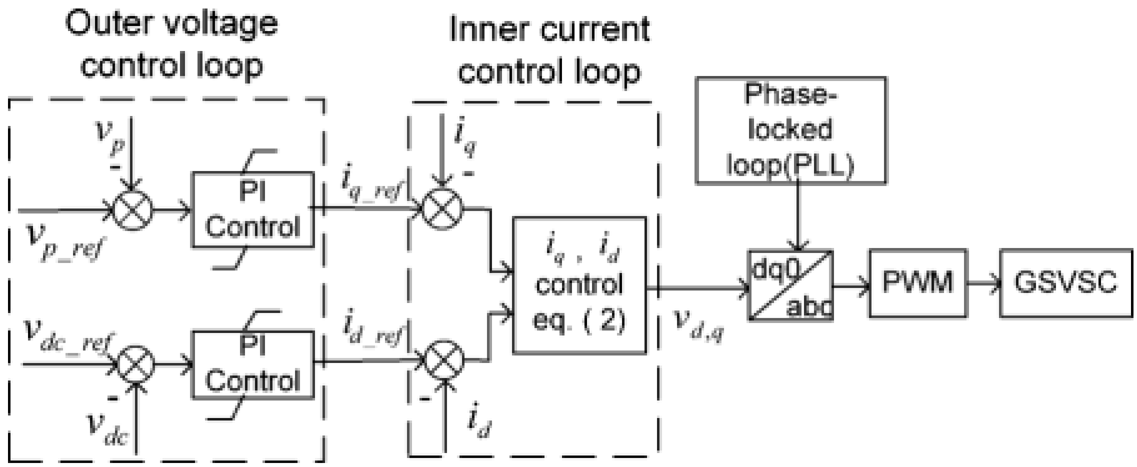

Figure 2.11 Simplified control diagram of VSC

Final Remarks: This paper addresses issues that other papers have just brushed through like the detailed analysis of distance protection function before and during the fault. The proposed method also seems plausible but cannot be implemented for a much more complex system as analysis fails to operate as the no of buses seem to increase and the error margin might increase resulting in the calculation of the PCC voltage difficult.

2.7 Distance Protection of Lines Connected to Induction Generator WTS

The reviewed paper is cited below.

Ali Hooshyar, Maher Abdelkhalek Azzouz, and Ehab F. El-Saadany, "Distance Protection of Lines Connected to Induction Generator-Based Wind Farms During Balanced Faults", IEEE Transactions on Sustainable Energy, vol. 5, no. 4, pp. 1193-1203, Oct. 2014.

Paper Objectives:

- Distance relays are the most used protection relaying for Wind Farms and other renewable sources. The objective of this paper is to reveal some serious defects of distance protection connected to induction generator-based wind farms during balanced fault. A novel modified permissive overreach transfer trip (POTT) scheme along with fault current classification technique is proposed in this paper.

Analysis:

Introduction: Due to environmental concerns, there has been a rapid growth in wind energy technology. Many wind energy technologies utilize induction generators. Squirrel cage Induction generators were the main technology used in early wind farms, they are very cost effective and as such are most commonly used. The new GC's require that WF be connected to power networks during disturbances in order to increase system stability. There were many challenges that were encountered:

1. Protection of IG's during fault

2. Protection of systems that include IG-based WF's

Fault analysis and settings of relays are based upon synchronous generators however the fault behavior of the integrated IG's have a direct impact on the performance of the relays. Impedance based distance relays are used for primary and backup protection of the HV lines. Without a communication channel, distance relays provide non delayed fast tripping over 80%–90% of the line length as well as backup protection for the next lines. If a communication link with minimal bandwidth requirement is in place, fast protection is achieved over the entire length of the line.

The paper addresses the problems of distance protection of the lines connected to IG based WF's during balanced short circuits. A POTT scheme is developed that results in non delayed tripping over the entire transmission line.

Problem Statement: For a squirrel cage Induction generator based WF the fault location changes after a few cycles after a balanced short-circuit occurs, this leads to the malfunctioning of the zone-1 operation of the primary relay and the failure to perform backup operation. In the case of a DFIG based WF it is impossible to measure an accurate impedance as frequencies of the fault current and voltage vary drastically. The impedance when plotted shows a chaotic trajectory which is unreliable even for a short duration of time. Thus, as a result the zone-1 protection malfunctions and the faults are tripped at a delay time.

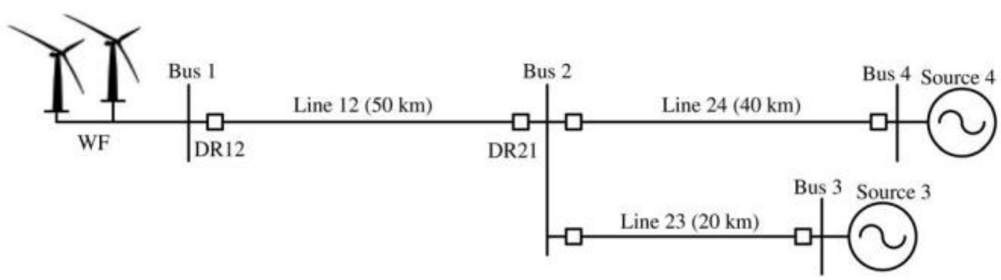

Figure 2.12 Single line diagram of the WF system

Proposed Scheme: A POTT scheme is utilized in this paper that addresses the non-delayed tripping that does not occur in a traditional distance relay over 100% of the line length unless it is connected through a communication channel with the relay on the other end. In this scheme the communication channel has low bandwidth requirement.

Let us consider a distance relay B located next to bus B and protects line AB. If the impedance measured by B falls within the reach of its directional over-reaching zone, there is a fault either on line AB, or on bus A, or inside the WF. The setting of this over-reaching zone is about 150% of the line length. On the other hand, if the impedance measured by A drops below its directional over-reaching zone setting, there exists a fault on line AB or on bus B or on the lines connected to the right of bus B. The only overlap between the A and B relay zones is line AB. As a result, once relay B detects a fault within its over-reaching zone, it sends a trip signal to A. relay A trips line

AB if a trip signal sent by B is accompanied by the detection of a fault within its own over-reaching zone. Relay B also operates based on the same logic. The communication channel over which the data are exchanged requires minimal bandwidth, since each relay transmits only a trip/no-trip signal.

The conventional POTT scheme fails to operate accurately for the lines connected to IG-based WFs during balanced short-circuits, due to incorrect impedance measurement by the distance relay at the WF substation. A modified POTT scheme is developed to tackle this problem. For this modified POTT scheme, the relay is located at the remote end of the line, i.e., Relay B is a regular impedance-based relay with a directional over-reaching zone. The relay located at the WF substation, however, detects faults in its forward direction not based on the measured impedance, but according to the fault current waveshape attributes. The waveshapes of balanced fault currents of IG-based WFs possess distinctive features, which can be utilized to distinguish them from fault currents of bulk HV power systems that the WFs are integrated with. Also, the instantaneous tripping signal of Relay-B is blocked if the fault current features the short circuit behavior of IGs. This strategy prevents maloperation of reverse faults.

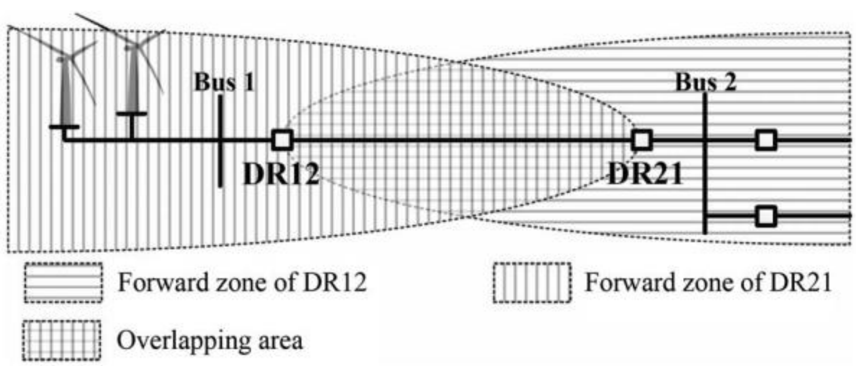

Figure 2.13 POTT scheme diagram

Final Remarks: A nice, detailed analysis of the impact of different types of Wind generators on the mis-operation of the relays, does not include the analysis of inverter-based resources in wind power generation and only includes the effect of IG on the fault characteristics.

2.8 Summary of Literature Survey and Recommendations

The reviewed literature tells us about how different types of inverter-based systems have a consequential effect on the normal operation of the legacy protection systems (relays).The most commonly used relays such as the distance protection relays almost always mis-operate due to the suppression of zero sequence and/or negative sequence components of the fault currents during faults by the inverters, as such it is difficult for the protection functions to identify and eliminate the faults effectively. Most of the papers offer some solutions in mitigating such situations, some of the solutions include addition of a zero-sequence analyzer to the operating relay in order to account for the missing or limited zero sequence fault currents, while others include precision induced tracking of voltages and currents and their frequencies in order to locate fault locations.

While some of the papers do offer clear insight into their methods others are just theoretical and complex and they may not clear of how they can be implemented. In any case, it is clear that we must first understand how legacy protection functions are affected by the operation of inverters. Subsequently, we can devise methods to mitigate the influence of inverters on the protection and control systems.

3. High Fidelity Simulator to Assess Legacy Protection Function Performance

It is important to use a high-fidelity simulator for power systems analysis to investigate the issue of protection systems/inverter interactions. Such precise modeling can be used to assess and predict the response of the system to events that are occurring in inverter dominated power systems.

To illustrate the difference between high fidelity modeling and approximate modeling, we will provide an example and analysis results using two specific computer programs, i.e., the WinIGS which models power system components with high fidelity (i.e. physically based model with the three phases, neutral/shield wires, ground conductors, grounding systems, etc.)s and the program PSCAD that models power system components with approximate models based on symmetrical components, lack of shield/neutral wire representation and other details of the power system. We present the results with these two programs for the same system. The example test system is provided below.

The basic system that we have used to model the software is given below:

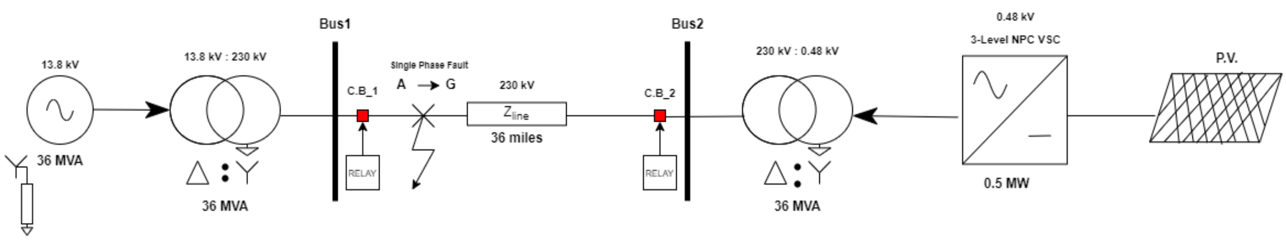

Figure 3.1 Two Bus System P.U diagram

The system consists of a generator on the far right which may be a power plant which is then stepped up by a step-up transformer to 230 kV line-line voltage on the far right is a VSC converter that is connecting the DC source PV to the grid. A line to ground fault occurs in the line and the relays at the buses 1 and 2 are used to protect the line.

3.1 Modeling and Results of the Example Test System with PSCAD

The Two Bus System Model modeled in PSCAD is given in Figure 3.2. The voltage and the current waveforms of the grid are given in Figures 3.4, and 3.5.

A single line to ground(A→G) fault is applied between 0.3 and 0.4 seconds. We can observe that the current in phase A shoots up whereas the voltage goes to zero as expected. However, since there is an inverter in the system the current in phase A should have a lower magnitude than expected due to the characteristics of the inverter to suppress the negative and zero sequence currents in the transmission network (grid).

Relay Waveforms (distance relay used) in PSCAD. The relay model setup is shown in Figure 3-3. The performance of the relay during the fault is shown in Figures 3-7 and 3-8. Note that Figure 3-8 indicates that the relay will trip on zone 1 during the fault.

There are two things we can observe from the waveforms shown in Figures 3-7 and 3-8. There are still some idealities that PSCAD assumes while simulating the system hence there is no accurate characteristic analysis of the relays. PSCAD utilizes trapezoidal method of integration whereas WinIGS uses a more accurate quadratic model which we will see later. PSCAD does not have in-built relay models readily available and the models that do exist are generalized and are not specific hence there is no accuracy while doing analysis.

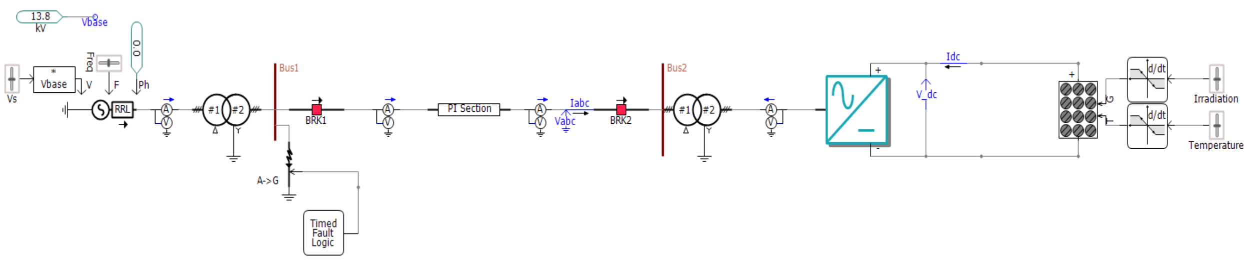

Figure 3.2 Simulation of a Two Bus System PSCAD

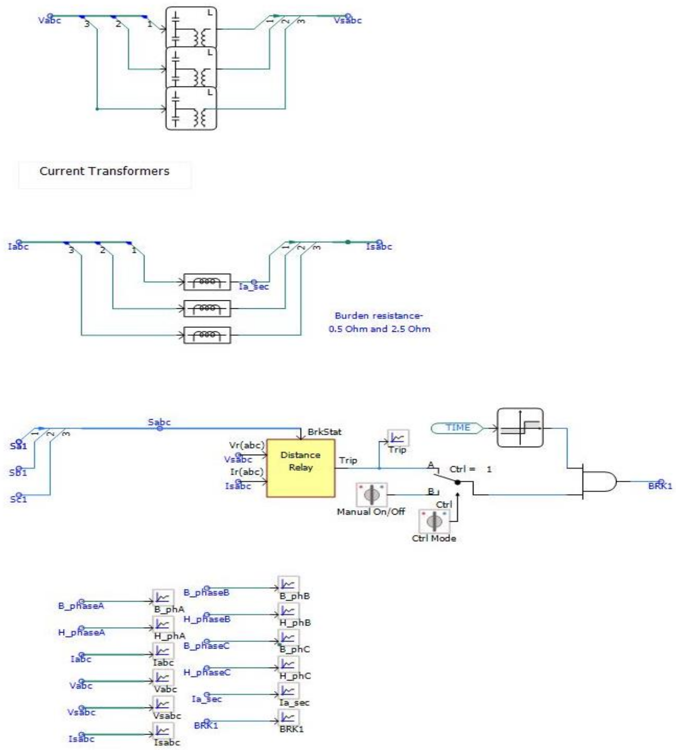

Figure 3.3 Distance Relay Design PSCAD

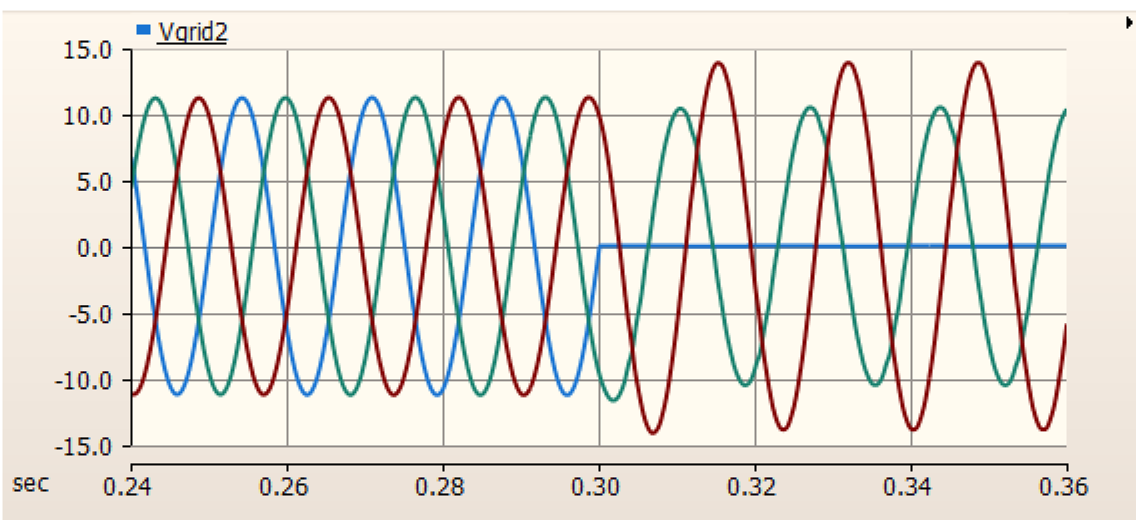

Figure 3.4 V_{grid} Waveform PSCAD

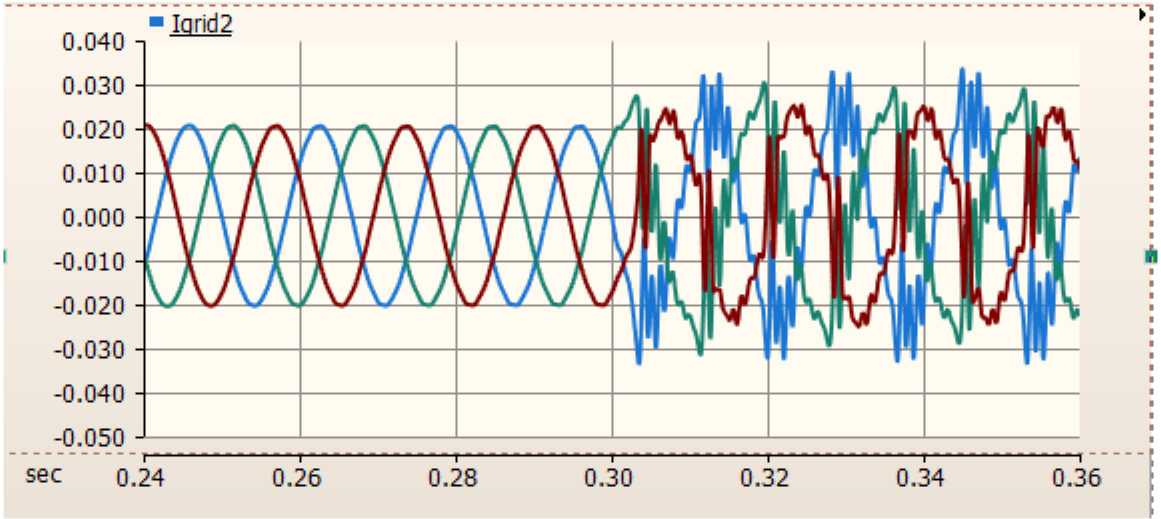

Figure 3.5 I_{grid} Waveform PSCAD

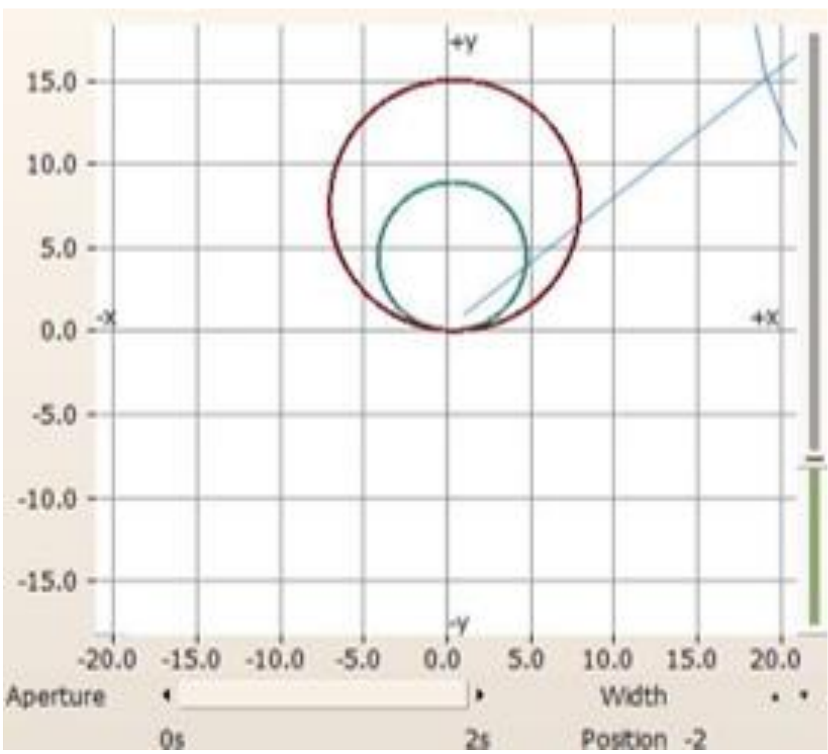

Figure 3.6 Line-Line zone impedance PSCAD

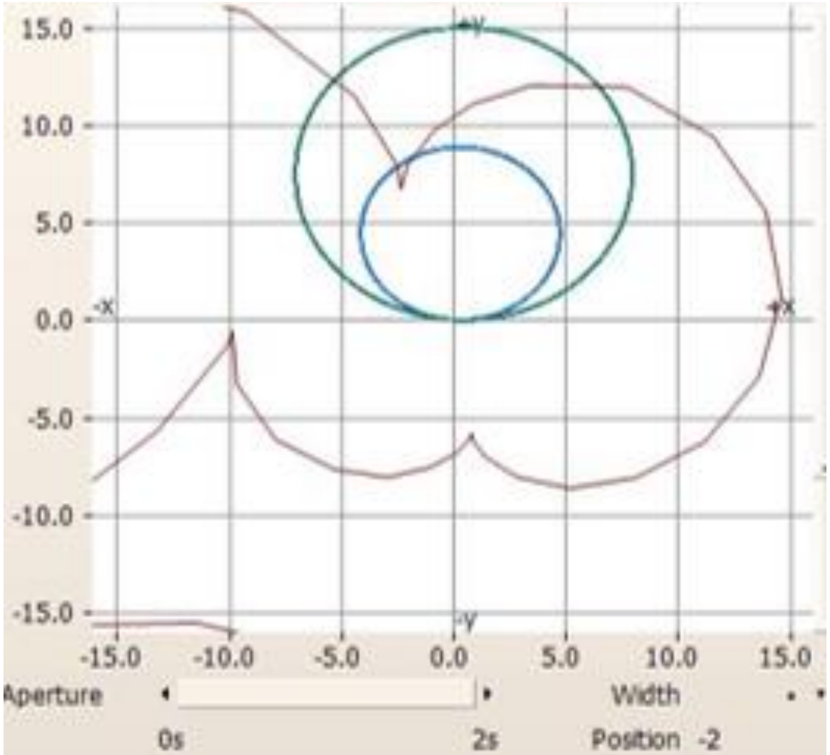

Figure 3.7 Line-Neutral zone impedance PSCAD

3.2 Modeling and Results of the Example Test System with WinIGS

The Two Bus Model in WinIGS is given below:

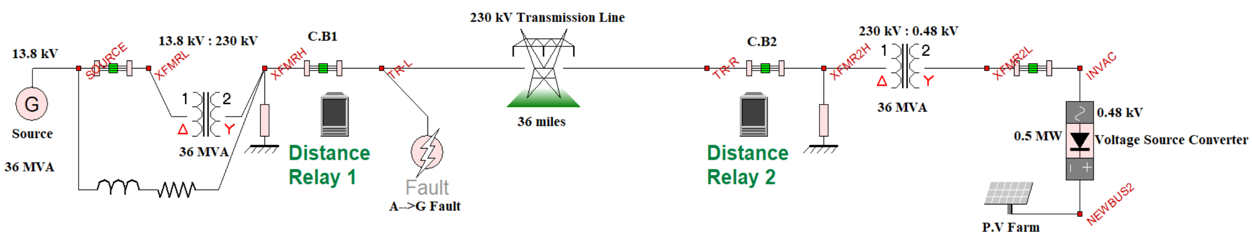

Figure 3.8 Simulation of a Two Bus System WinIGS Q/T

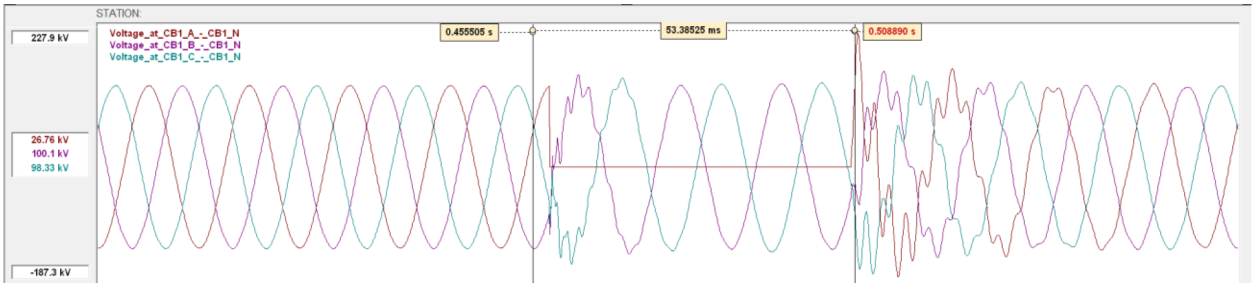

Figure 3.9 Generator side V_{grid} Waveform in WinIGS

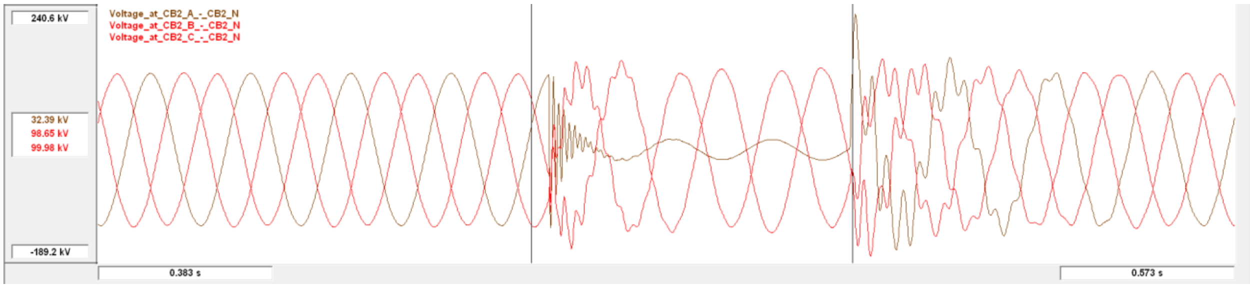

Figure 3.10 Inverter side V_{grid} Waveform in WinIGS

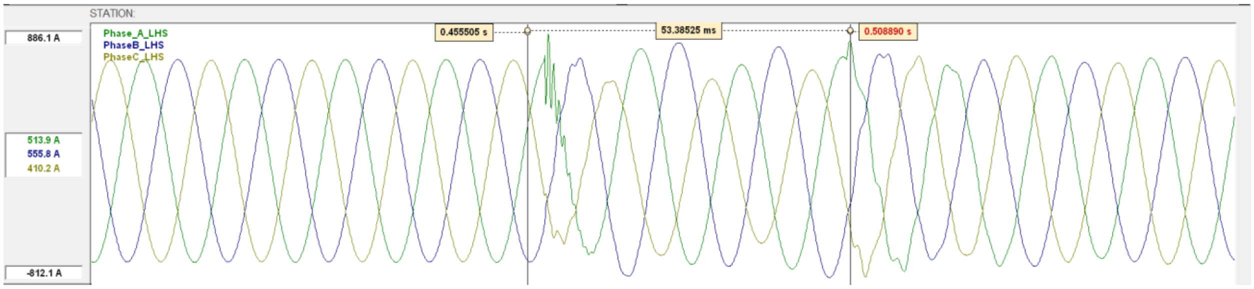

Figure 3.11 Generator side I_{grid} Waveform in WinIGS

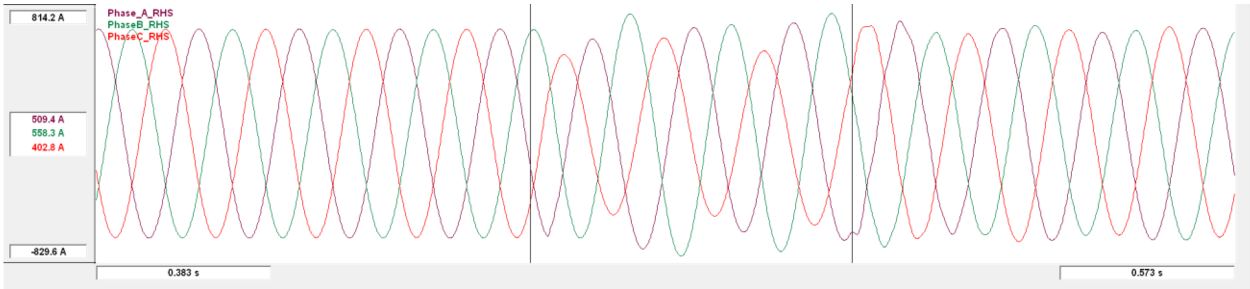

Figure 3.12 Inverter side I_{grid} Waveform in WinIGS

We can notice a significant difference between the waveforms in PSCAD and WinIGS, Due to the A→G fault the voltage on phase A has gone to a small value (ground potential rise) as expected but the difference can be found in the current waveforms, in WinIGS we can see that the current in phase A has significantly reduced instead of increasing during a fault. Thus, we can see the high fidelity in the WinIGS software.

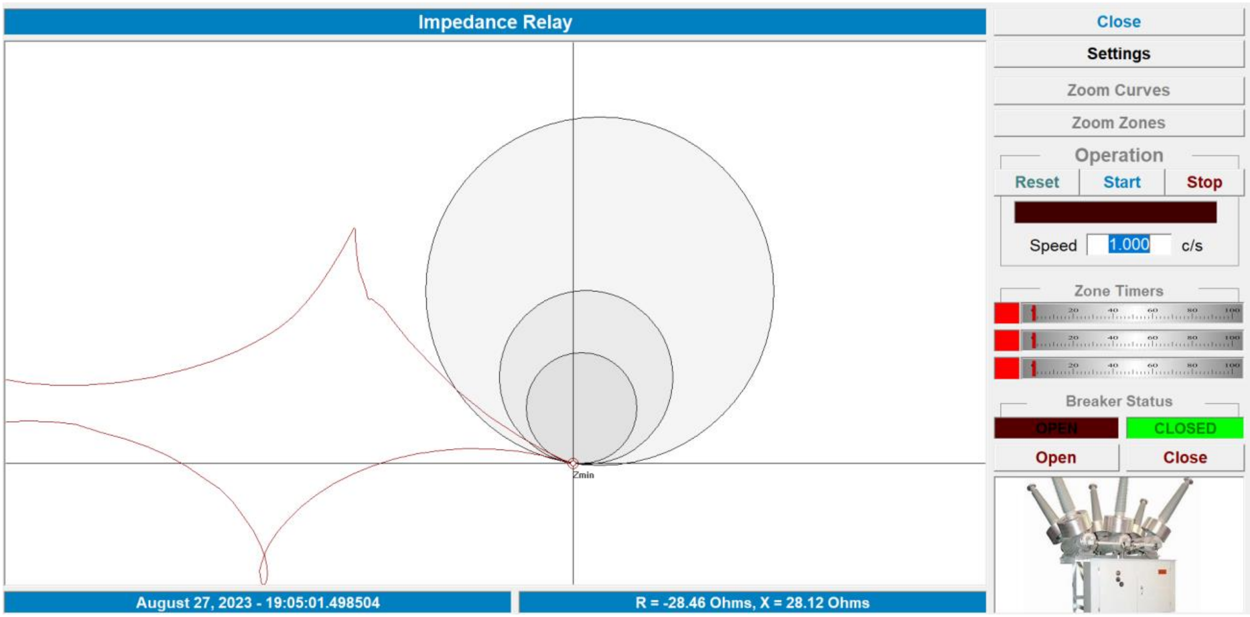

Figure 3.13 Generator side zone impedance for A→G fault in WinIGS

.

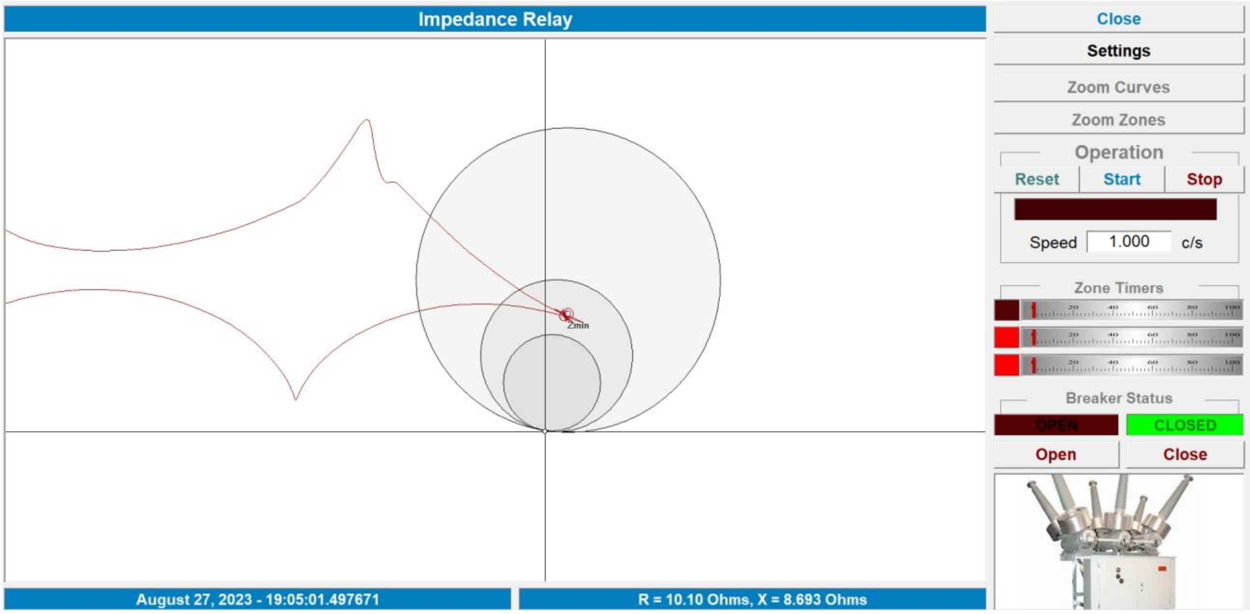

Figure 3.14 Inverter side zone impedance for A→G fault in WinIGS

The distance relay does not trip in WinIGS due to characteristics of the inverter to suppress the negative and zero sequence currents in the transmission network.

3.3 Summary and Comments

We have made such a comparison by taking the common software used for simulation PSCAD and our own software WinIGS and found out that WinIGS is by far the most accurate software as it encompasses real time values and data which cannot be found in PSCAD. Certain features in PSCAD have been assumed as ideal whereas every little detail has been modeled in the WinIGS software.

As discussed in the PSCAD section the disadvantages of PSCAD is that it cannot reproduce the actual fault waveforms in this simple example. In the WinIGS simulation results, we can clearly see that the fault is realistically simulated and the zone impedance trip signals are accurate. The actual fault is in zone 2 and that is what the model predicts. Note also that the PSCAD results indicate that the fault is in zone 1 which is incorrect.

Hence WinIGS software which is a high-fidelity simulator is preferred for simulating and understanding the characteristics of legacy protection in an inverter dominated system.

4. Description of Specific Legacy Protection Functions

This section provides descriptions of specific legacy protection systems. The intent is to investigate the impact of inverters on the performance of these legacy protection functions. Within the scope of the project it is not possible to investigate all the legacy protection functions, for this reason, we limit the work to a number of selected legacy protection functions that are expected to be impacted by inverters the most.

4.1 Legacy Protection Systems

Power Systems consists of three main categories: Generation, Distribution and Transmission. There is a necessity for uninterrupted power supply among these three networks. If the supply is interrupted then it leads to major system damage, for e.g.: if the distribution side is interrupted then major appliances in our houses get damaged. In an ideal scenario, these three networks operate without any problems in them. But in the real world, there are many problems that these networks face such as sagging of the transmission line, duck curve problem etc. But the major problem that these networks have in common is the fault on the line, this causes major abnormalities in the system and introduces new transients in the system that leads to its instability.

To protect the system and to keep it stable, we rely on certain devices to “protect” the system. These devices are called relays and the terminology given to protecting the system results in them being called “protective relays” and the process to be known as “protective relaying”.

Protective relaying is necessary with almost every electrical plant, and no part of the power system is left unprotected. The choice of protection depends upon several aspects such as type and rating of the protected equipment, its importance, location. The protective relaying senses abnormal conditions in a part of the power system and gives an alarm or isolates that part from the healthy system.

The functions of protective relaying include:

- To sound an alarm or to close the trip circuit breaker to disconnect a component during an abnormal condition in the component.
- To disconnect the abnormally operating part to prevent the subsequent faults, e.g.: overload protection of a machine protects the machine and prevents insulation failure.
- To disconnect the faulty part quickly to minimize the damage to the faulty part.
- To localize the effect of the fault by disconnecting the faulty part from the healthy part causing least disturbance to the healthy system.
- To disconnect the faulty part quickly to improve the system stability service continuity and system performance.

The common types of protective relays are:

4.2 Selected Legacy Protection Functions

In this section, we selected a number of the most used legacy protection functions. These functions are defined here and their characteristics as well as the required settings. Then in the next section we use these protection functions to perform performance evaluation within an inverter dominated power systems.

Instantaneous Overcurrent Relay (50)

The fundamental concept of this relay is that it sends trip signals to the circuit breaker once the line current (any phase which we are observing) crosses a certain threshold also known as the pickup value.

This pickup value or I_{pickup} is set by each company having their own designs of the relay.
The equation representing this is given by:

$I_{pickup} = k * I_{sec}$.

This I_{sec} is the secondary current measured by the current transformer which actively measures line current and steps it down so that the A/D converter does not get the full rated line current.

The “k” value also called as the sensitivity value is also determined by each company’s designs, the basic principle is that the value of k is determined by how efficient you want the relay to be in the protection zone. For example, in regions with high motor loads or generators you have a large value of k and for regions with lighting systems you can set the k value to be minimal to be cost efficient. Typical k value ranges from 1.5-2.5 for optimal relay performance.

The diagram of an instantaneous Overcurrent Relay is given below:

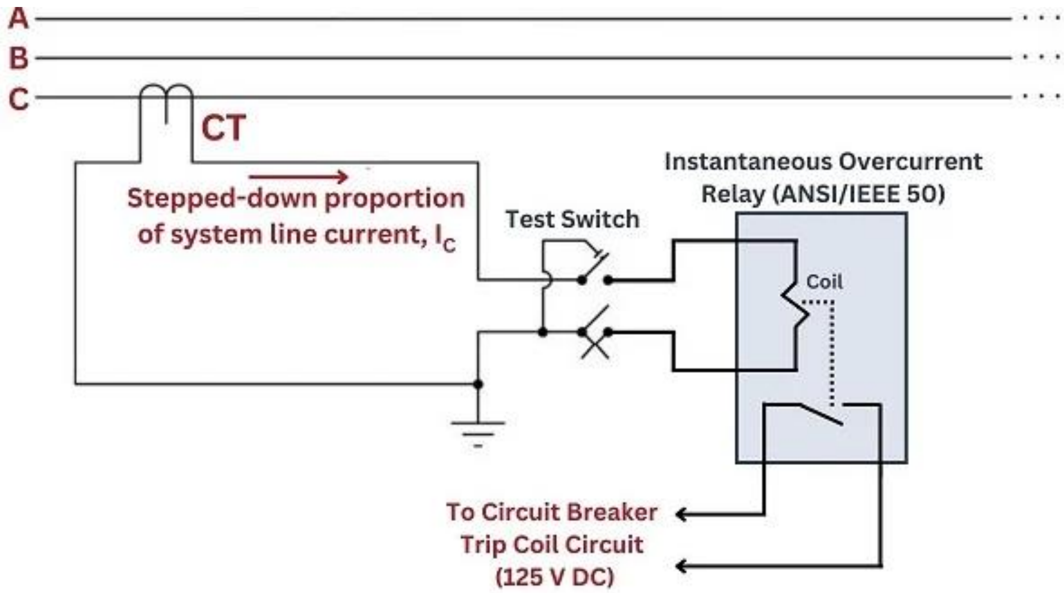

Figure 4.1 Instantaneous Overcurrent Relay

The algorithm for this relay could be explained by the flow chart:

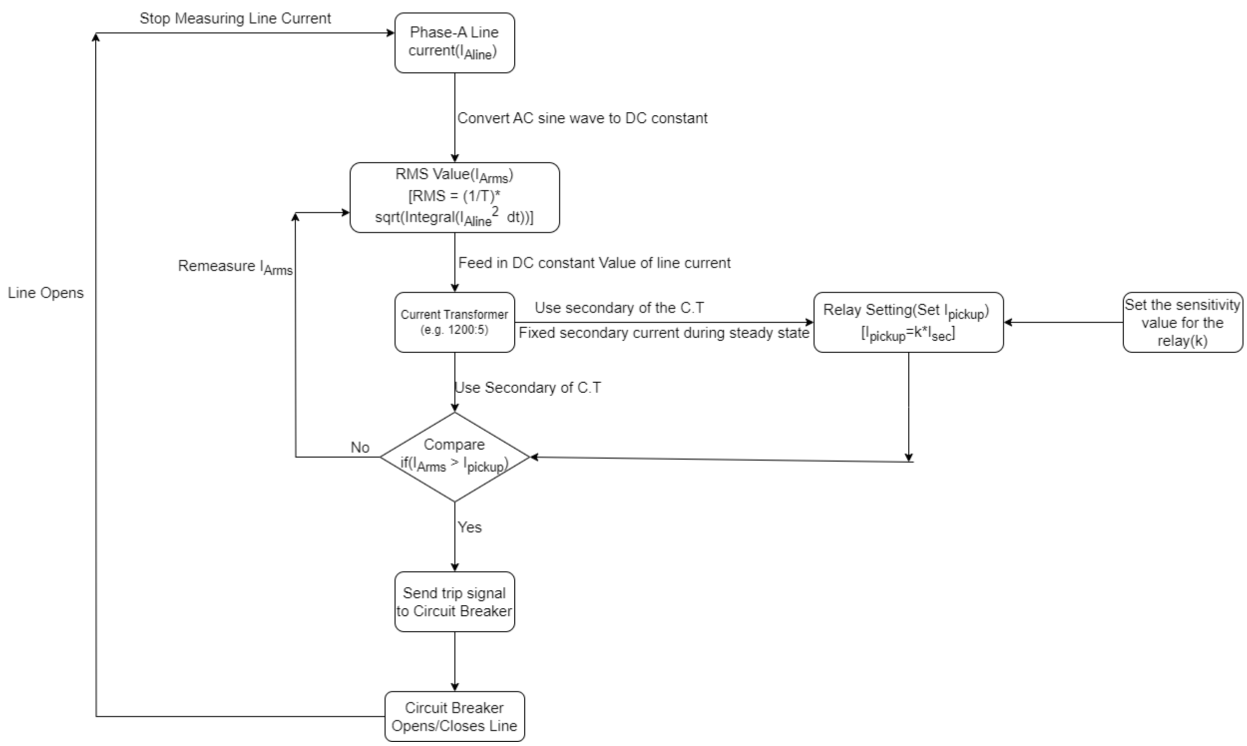

Figure 4.2 Algorithm for an Instantaneous Overcurrent Relay

Time Overcurrent Relay (51)

As we had seen previously that the instantaneous overcurrent relay sends trip signals immediately as soon as the current value exceeds the pickup value. In an ideal case this relay would be very useful but in a real world scenario where we have to protect different types of Zones this function proves to be inefficient, hence we require a certain time delay such that we let the breakers which are downstream from the fault operate first and allow them the chance to isolate only the part of the system that is under fault hereby allowing other parts of the system to operate continuously. In such a scenario we utilize the time over current relay.

In time over current there are two factors to consider.1. The pickup/Plug setting of the relay and 2. The time dial (i.e how much delay we want for the relay).
There are three important things to consider before writing the relay settings:

1. Pickup current value
2. PSM (Plug setting Multiplier)
3. TSM (Time setting Multiplier).

1. Pickup Current:
It is given by the equation:

I_{pickup} = (%of full load current of the CT) x (The current flowing in the line) x (CT Secondary/CT primary)

2. PSM:
It is given by the equation:

I_r = (Measured Value of current in the relay coil)/(pickup current through the relay coil(I_{pickup}))

3.TSM:
This is also commonly called the time dial (t_d) and is a known value given which is the ***ratio of operating time and actual relay operating time.***

With these three values we can write the relay setting for the instantaneous relay:

Condition 1: If ($I>I_{pickup}$) then the relay would trip ; where I is the measured current through the line.
Condition 2: The time to trip is given by:

$$t_0 = \frac{0.14}{I_r^{0.02}-1} * t_d$$ → This is for the standard inverse characteristics.

Similarly,

$$t_0 = \frac{13.5}{I_r-1} * t_d$$ → This is for very inverse characteristics

$$t_0 = \frac{80}{I_r^2-1} * t_d$$ → This is for Extreme Inverse characteristics

Where I_r is the plug setting multiplier of the relay.

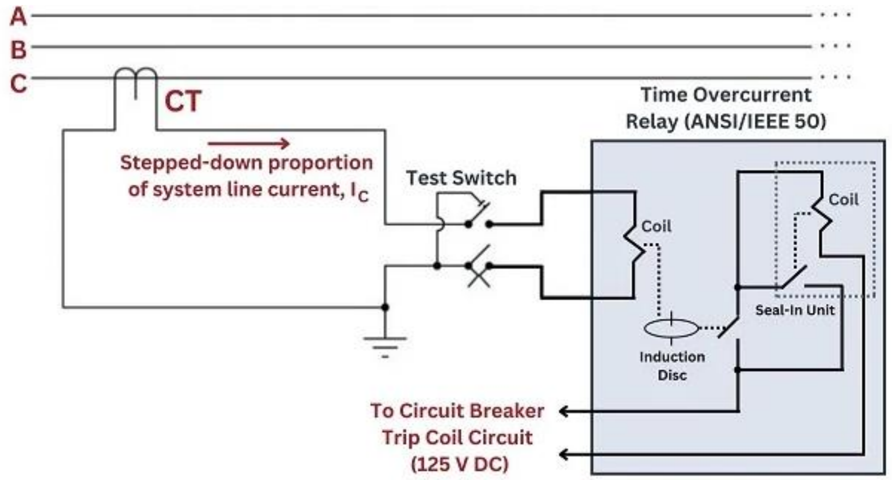

Figure 4.3 Time Overcurrent Relay

The algorithm for the relay is given by:

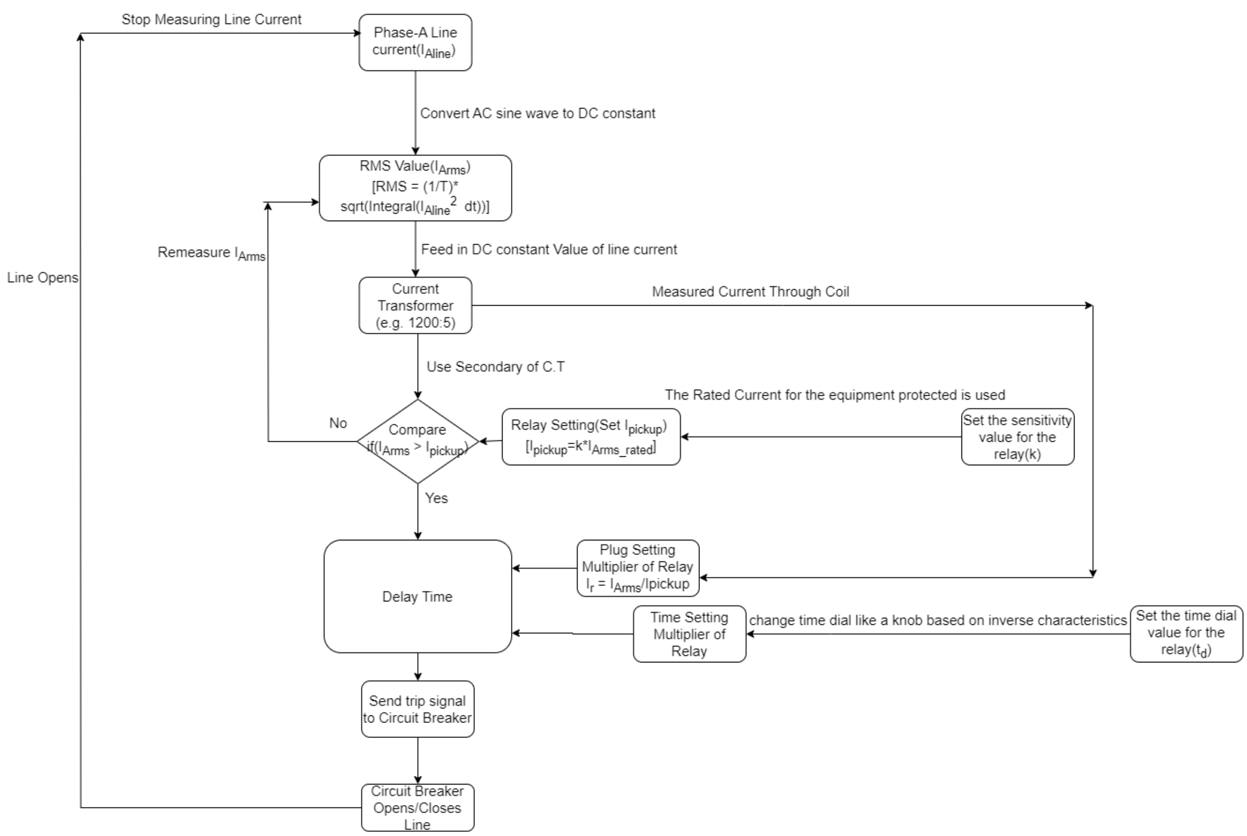

Figure 4.4 Algorithm for Time Overcurrent Relay

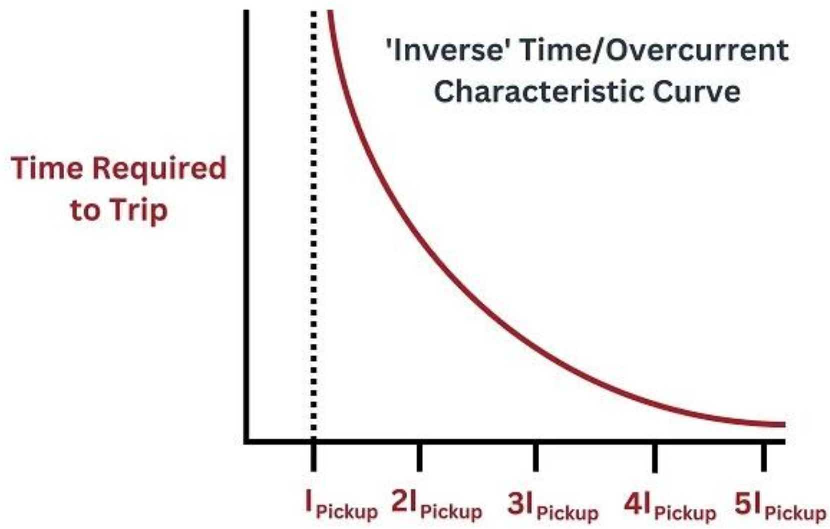

Figure 4.5 Time Overcurrent Relay Inverse Characteristics

Based on the sensitivity that we define we can derive the time inverse characteristics of the Time overcurrent relay as shown above. The time taken to trip decreases as the sensitivity increases.

Directional Overcurrent Relay (67)

Directional Overcurrent Relays are overcurrent relays with a built-in directional setting in it, it has the same characteristics as that of the time overcurrent relay with the delay signal.

These relays are commonly used in systems with multiple sources or feeders where it is important to selectively trip the appropriate circuit breaker or switch to isolate the faulted section of the system while leaving the healthy sections intact. They are also used in systems where fault currents can flow in multiple directions due to interconnected grids, parallel feeders or complex network configurations.

Since these relays can be used in systems with multiple power flow directions and only sends trip signals to the breaker when there is a fault in the direction in which the breaker is set to operate these help in reducing false trips.

The directional characteristics of the directional overcurrent relay is typically achieved using a combination of current magnitude and phase angle comparison. The relay measures the current flowing through the protected circuit and compares it with the set pickup current and time delay settings. If the current exceeds the pickup setting and meets the directional criteria, the relay operates and initiates a trip signal to the appropriate circuit breaker or switch.

The algorithm for the relay is given in Figure 4.7.

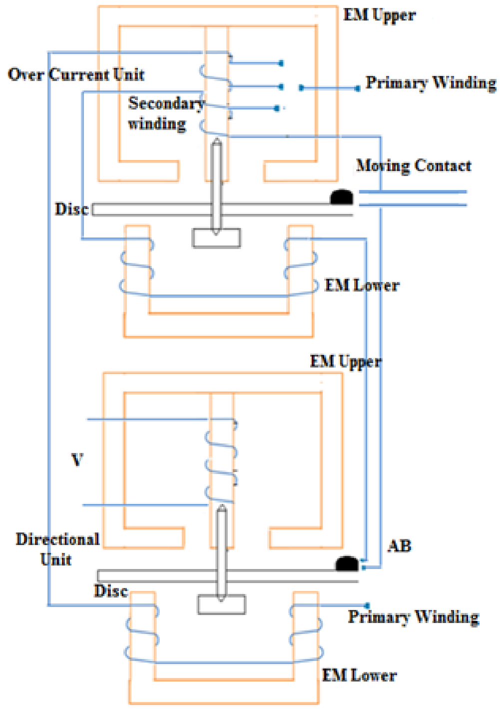

Figure 4.6 Directional Overcurrent Relay

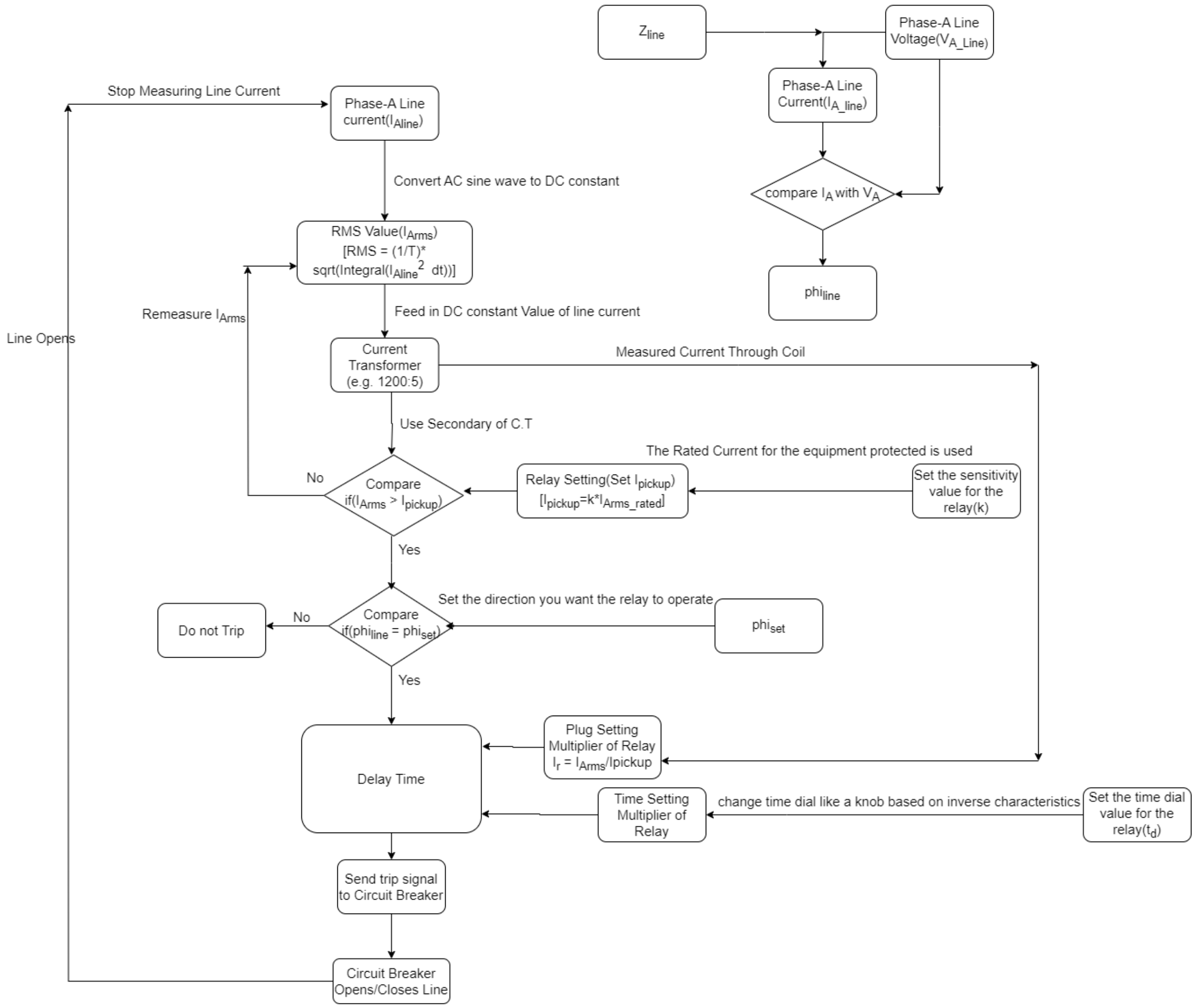

Figure 4.7 Algorithm for Directional Overcurrent Relay

Differential Relay (87)

It is a type of protective relay scheme used in electrical power systems to detect and respond to abnormal current or voltage conditions by comparing the difference between currents or voltages at different points in a system. It is commonly used to protect valuable or critical electrical equipment such as transformers, generators, motors, and busbars.

The basic principle of differential protection is to continuously monitor and compare the currents or voltages at two or more points in the power system. The currents or voltages at these points should be equal under normal operating conditions as they are expected to be part of the same electrical circuit. Any difference between the measured values of currents or voltages beyond a set threshold indicates a potential fault or abnormal condition in the protected equipment and the differential relay operates to initiate a trip signal to disconnect the faulty circuit from the system.

It is of Two Types:

1.Current Differential Protection:
This utilizes CT's and measures the currents at the two ends of the protected equipment.
2.Voltage Differential Protection:
This utilizes PT's and measures the voltages at the two ends of the protected equipment.

We will focus mainly on Current Differential Protection.

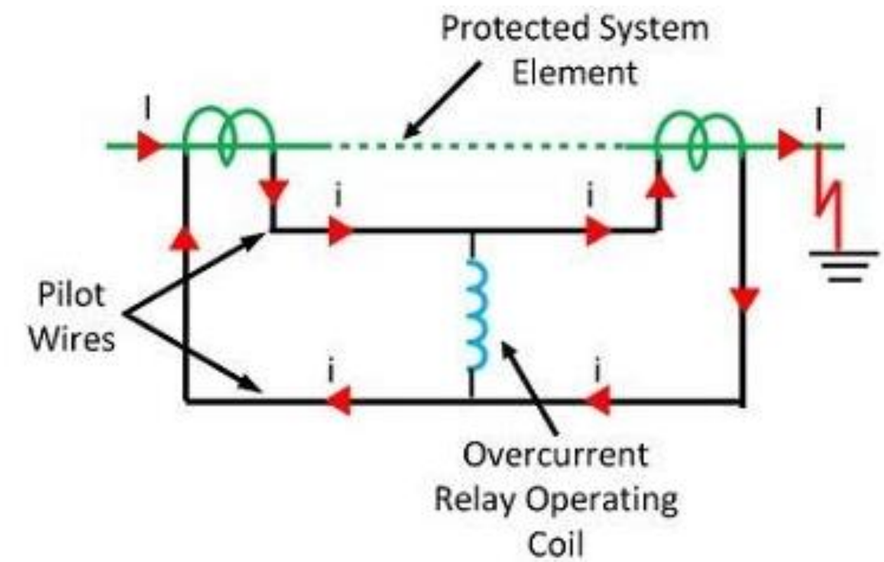

Figure 4.8 Differential Relay

A differential relay responds to the vector difference between two or more similar electrical quantities.

This means that:

- The differential relay has at least two actuating quantities I_1 , I_2
- The two or more actuating quantities must be similar i.e., current/current.
- The relay responds to the vector difference between the two i.e. I_1-I_2 which includes magnitude and/or phase angle difference.

Differential protection is generally unit protection. The protected zone is exactly determined by the location of the CT's or VT''s. The vector difference is achieved by suitable connections of current transformer or voltage transformer secondaries.

The setting of this relay also needs some basic values to be defined:

- **k** is the C.T ratio
- $\mathbf{i_{0,set}}$ operating current setting
- **p** is the percentage setting in p.u

From these base values we can define the conditions of the relay:

Condition 1: Calculate the operating current ($\mathbf{I_0^{\sim}}$):

$$\mathbf{I_0^{\sim} = k * (I_{1,i}^{\sim} + I_{2,i}^{\sim})}$$

Where **i** indicates the phases a, b and c.
Condition 2: Check:
If ($|\mathbf{I_0^{\sim}}| > \mathbf{i_{0,set}}$)
Condition 3: Check:
If $\{|\mathbf{I_0^{\sim}}| > \mathbf{0.5*p*k*(|I_{1,i}^{\sim}| + |I_{2,i}^{\sim}|)}\}$

If the conditions are satisfied the relay trips or else the relay doesn't trip.

The algorithm for the relay is given in Figure 4-9.

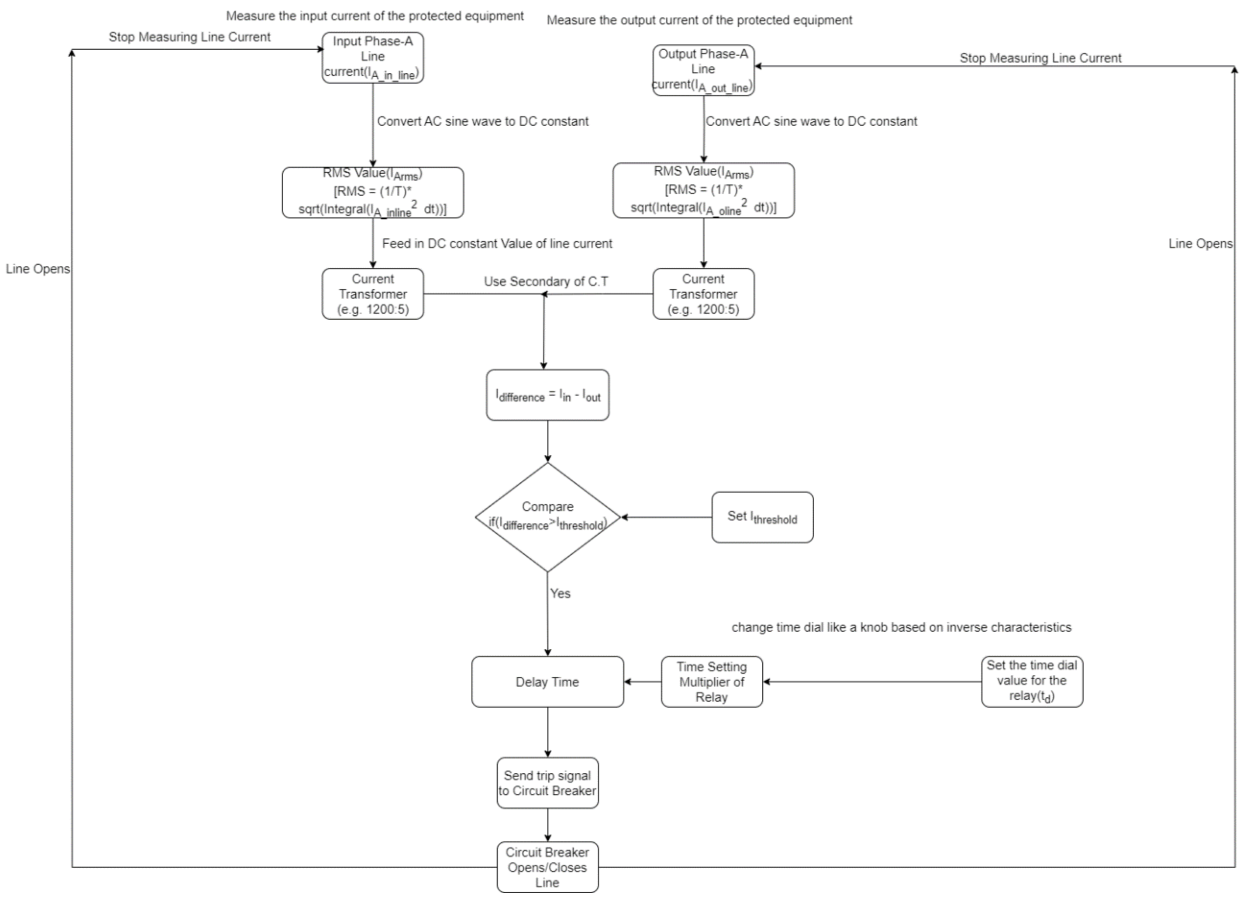

Figure 4.9 Algorithm for Differential Relay

Distance Relay (21)

A distance relay is also known as an impedance relay. It is used to protect power systems and to detect and localize faults or disturbances in transmission lines, distribution lines and or other elements of the power system. It operates based on the measurement of impedance which is the ratio of voltage to current in the power system.

Distance relays are widely used in power systems due to their ability to provide reliable and selective protection for transmission and distribution lines. They are designed to detect and initiate trip signals for faults or disturbances that occur within a specified distance from the relay location. The distance is typically measured in terms of impedance and the relay operates based on predefined impedance characteristics or impedance reach settings.

A distance relay can have multiple zones of protection depending on the manufacturer's design.

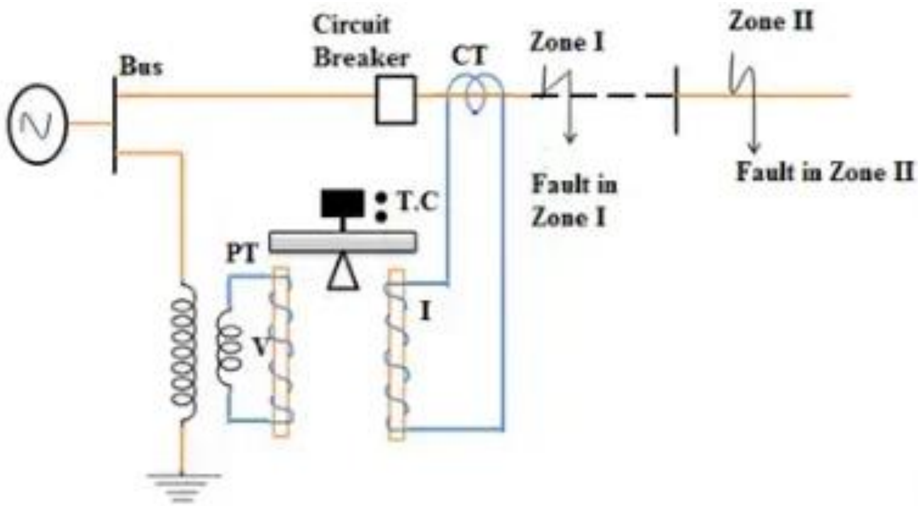

Figure 4.10 Distance Relay

Like the other relays base quantities need to be defined:

1. Z_{zone} is the impedance of the relay; it can have multiple zones.
2. $V^{\sim}$ and $I^{\sim}$ are the voltage and current phasors measured by the CT and the PT respectively.

Based on this we can estimate the conditions for the relay:

Condition 1: Set the value of the distance relay impedance $\mathbf{Z_{zone}}$
Condition 2: Measure the impedance of the line:

$$\mathbf{Z_{line}} = \frac{\mathbf{V^{\sim}}}{\mathbf{I^{\sim}}}$$

Condition 3: If ($\mathbf{Z_{line} < Z_{zone}}$) then the relay trips.

We can have multiple zones of tripping.

In addition to the simple condition 2 the relay computes the following:

If for a positive sequence impedance:

$$\frac{k_1(\tilde{V}_a - \tilde{V}_b)}{k_2(\tilde{I}_a - \tilde{I}_b)}, \quad \frac{k_1(\tilde{V}_b - \tilde{V}_c)}{k_2(\tilde{I}_b - \tilde{I}_c)}, \quad \frac{k_1(\tilde{V}_c - \tilde{V}_a)}{k_2(\tilde{I}_c - \tilde{I}_a)},$$

$$\frac{k_1}{k_2}\left(\frac{\tilde{V}_a}{\tilde{I}_a + m\tilde{I}_0}\right), \quad \frac{k_1}{k_2}\left(\frac{\tilde{V}_b}{\tilde{I}_b + m\tilde{I}_0}\right), \quad \frac{k_1}{k_2}\left(\frac{\tilde{V}_c}{\tilde{I}_c + m\tilde{I}_0}\right)$$

These values are the impedances calculated based on the positive sequence impedance.

The minimum value among the following impedances is actually the $Z_{positivesequenceimpedance}$.

The relay trips :
If ($Z_{positivesequenceimpedance} < Z_{zone}$).

The algorithm for the relay is given by:

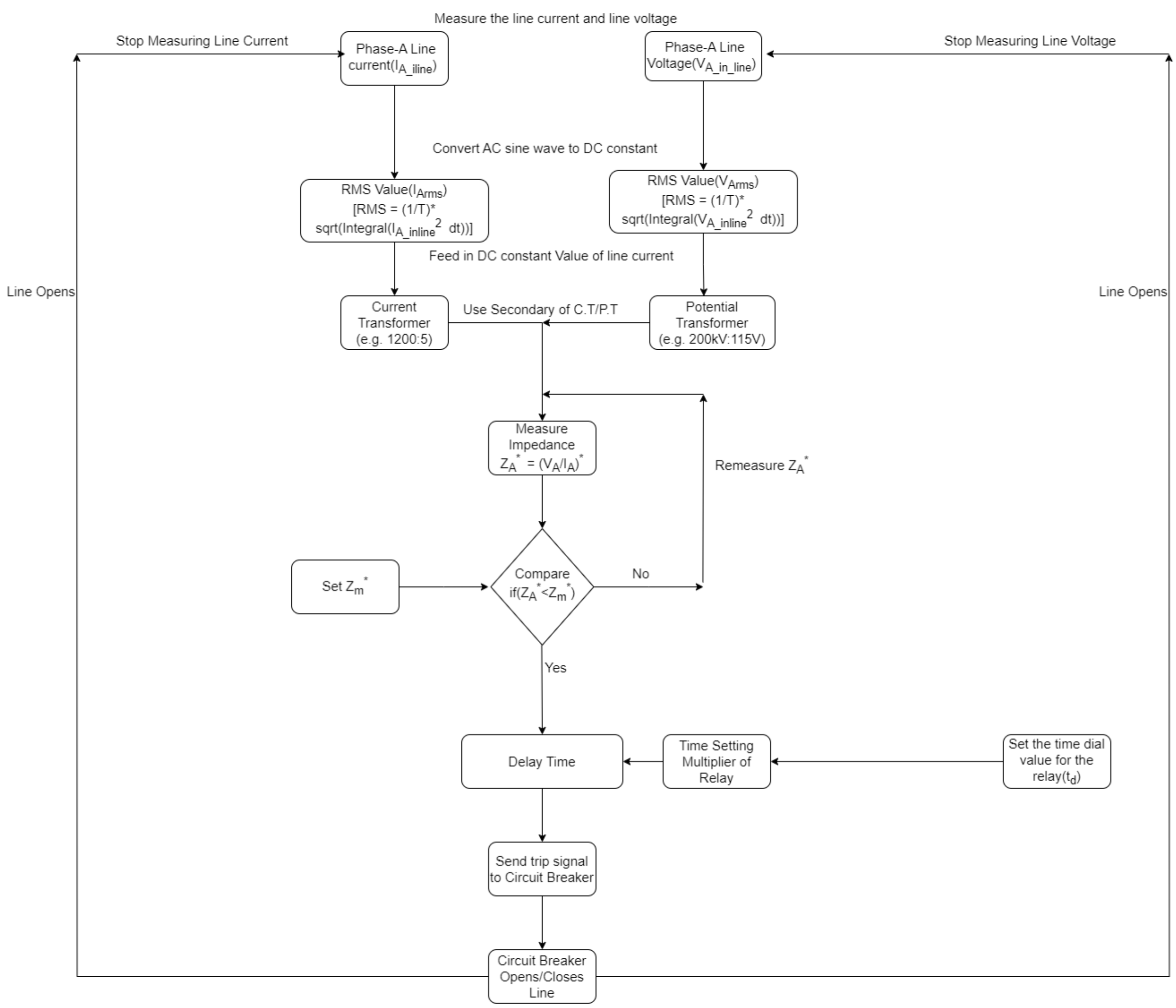

Figure 4.11 Algorithm for Distance Relay

V/f Relay (24)

A V/f relay also known as voltage/frequency relay or an over flux relay is a protective relay used in electrical power systems to detect abnormal voltage and frequency conditions that may indicate a fault or disturbance in the system. It operates based on the measurement of both voltage and frequency and their relationship in a power system.

The V/f relay typically monitors the voltage and frequency at a specific point in the power system such as at the output of a generator, transformer, or distribution line. The relay compares the measured V/f ratio with predefined threshold values or characteristic curves to determine whether the voltage and frequency are within acceptable limits or not.

The algorithm for the V/f relay is given by:

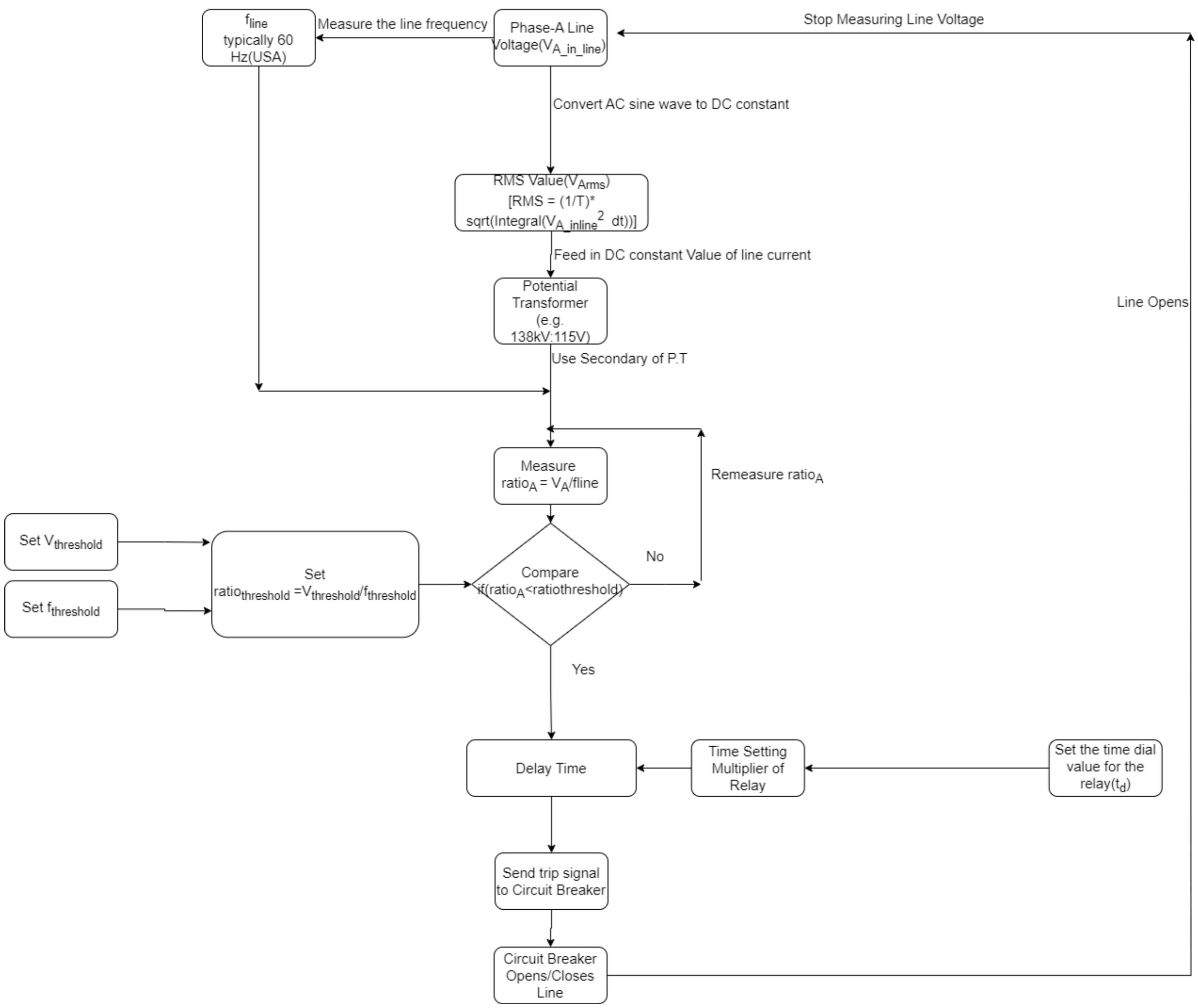

Figure 4.12 Algorithm for V/f Relay

Under/Over-Voltage Relay (27/59)

It is known as a voltage relay and is used in power systems to detect abnormal voltage conditions that may indicate a fault or disturbance in the system. It operates based on the measurement of voltage at a specific point in the power system and compares it with predefined threshold values to determine whether the voltage is within acceptable limits or not.

The under/overvoltage relay typically monitors the voltage at a specific point in the power system, such as at the output of a generator, transformer, or a distribution line. The relay compares the measured voltage with predefined threshold values to determine whether the voltage is within acceptable limits or not.

The algorithm for the relay is given in Figure 4-13.

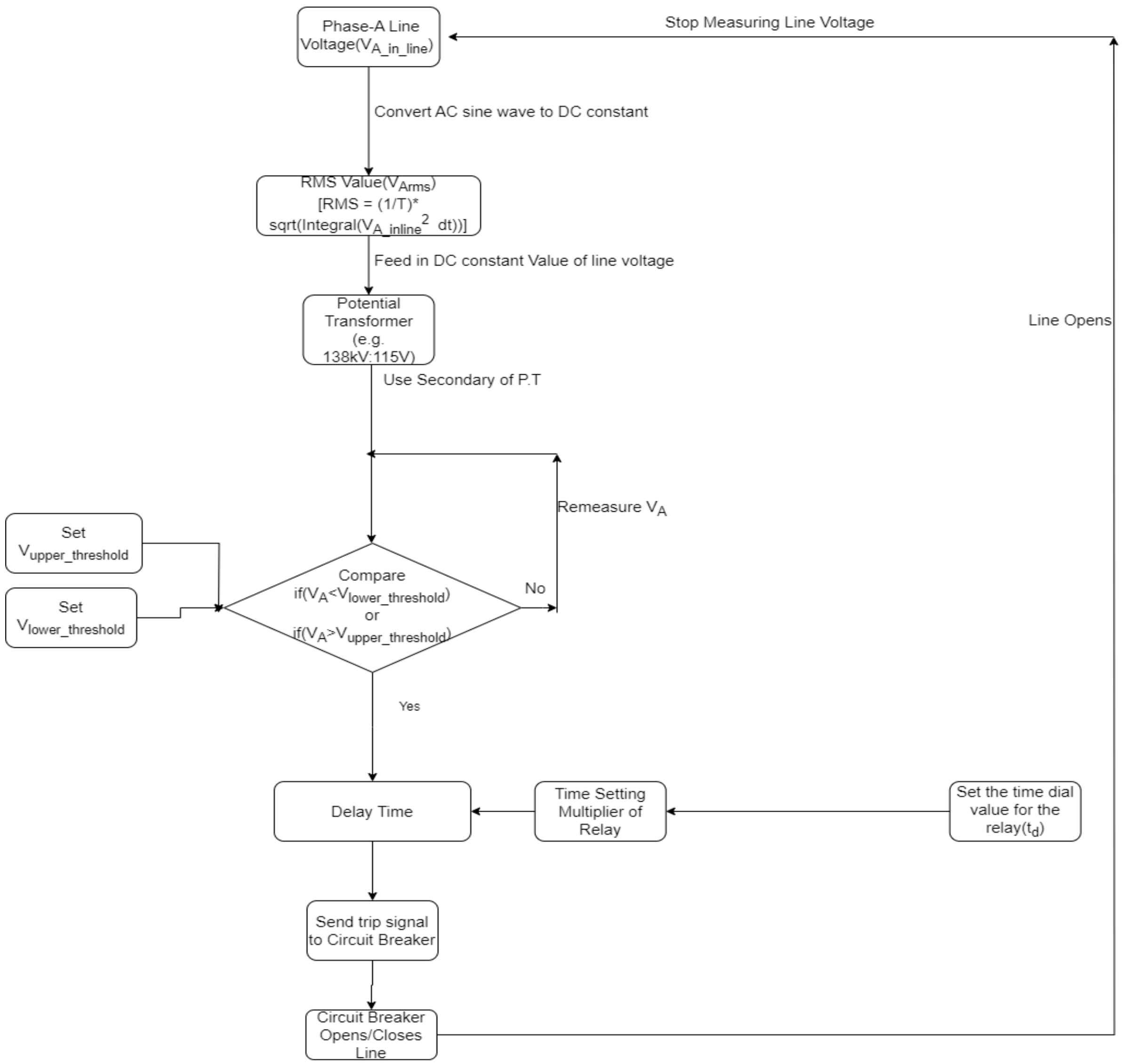

Figure 4.13 Algorithm for Under/Over Voltage Relay

Under/Over Frequency Relay (81)

It is also known as a frequency relay and is used in power systems to detect abnormal frequency conditions that may indicate a fault or a disturbance in the system. It operates based on measurement of frequency at a specific point in the power system and compares it with predefined threshold values to determine whether the frequency is within acceptable limits or not.

Similar to the under/over voltage relays this relay typically monitors the frequency at the outputs of a generator, transformer or a distribution line.

The algorithm for this relay is given by:

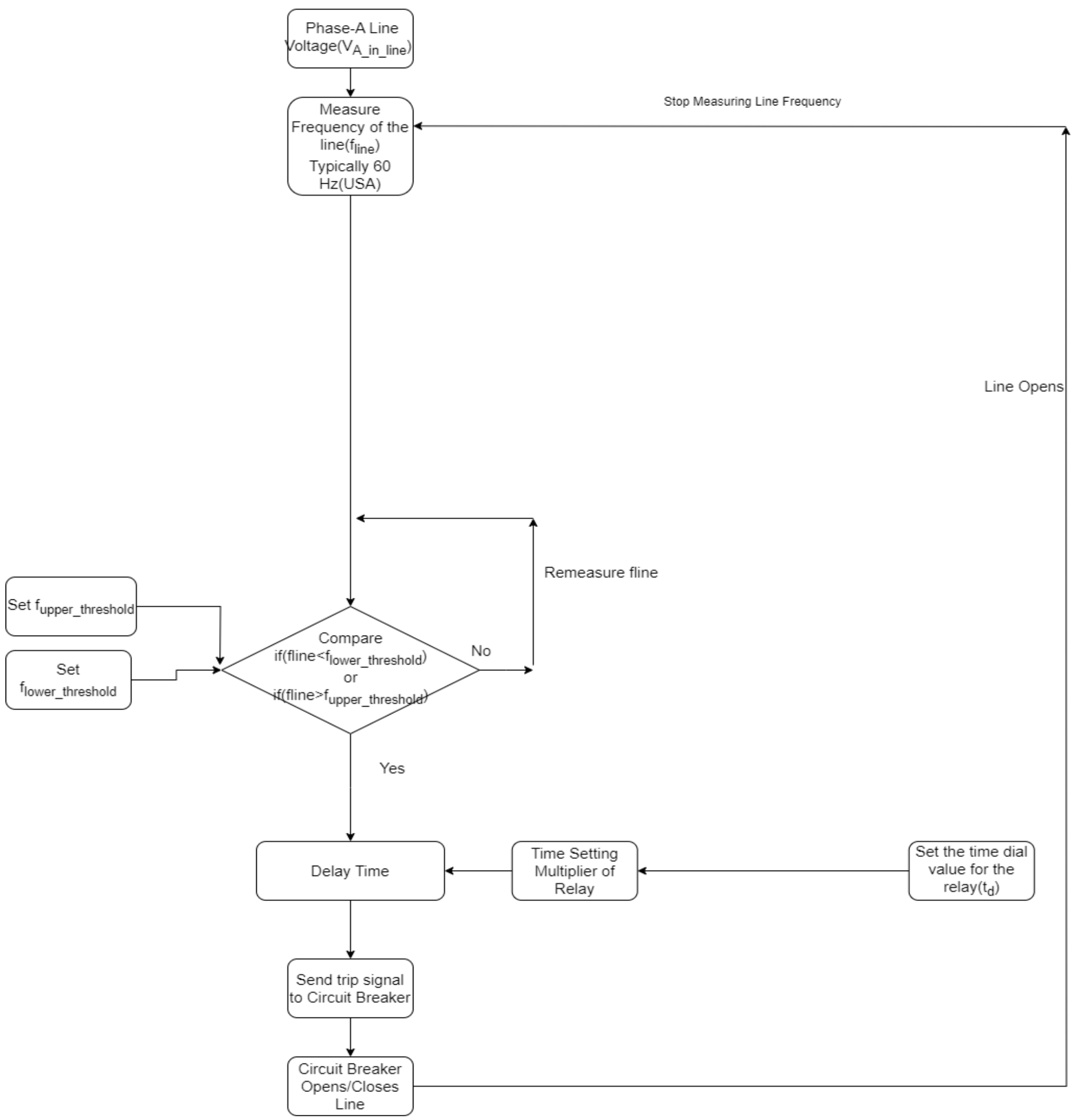

Figure 4.14 Algorithm for Under/Over Frequency Relay

5. Performance Evaluation of Legacy Protection Functions in the Presence of Inverters

Legacy protection function performance in an inverter dominated power system is very important to understand the challenges. In this section we present results of an investigation of the impact of inverters to legacy protection functions. The approach of this investigation is as follows. A system is constructed which consists of a part that is dominated by synchronous machines and another part that is dominated by inverters. We generate several events on this system and observe the response of the legacy relays. The topology of the system also changes for the purpose that the legacy relays will be seeing more of the influence of the inverters. The model has been generated in WinIGS so that the results are realistic.

5.1 Example Test System

The test system used for this investigation is shown in Figure 5.1. A brief description of the system is given below.

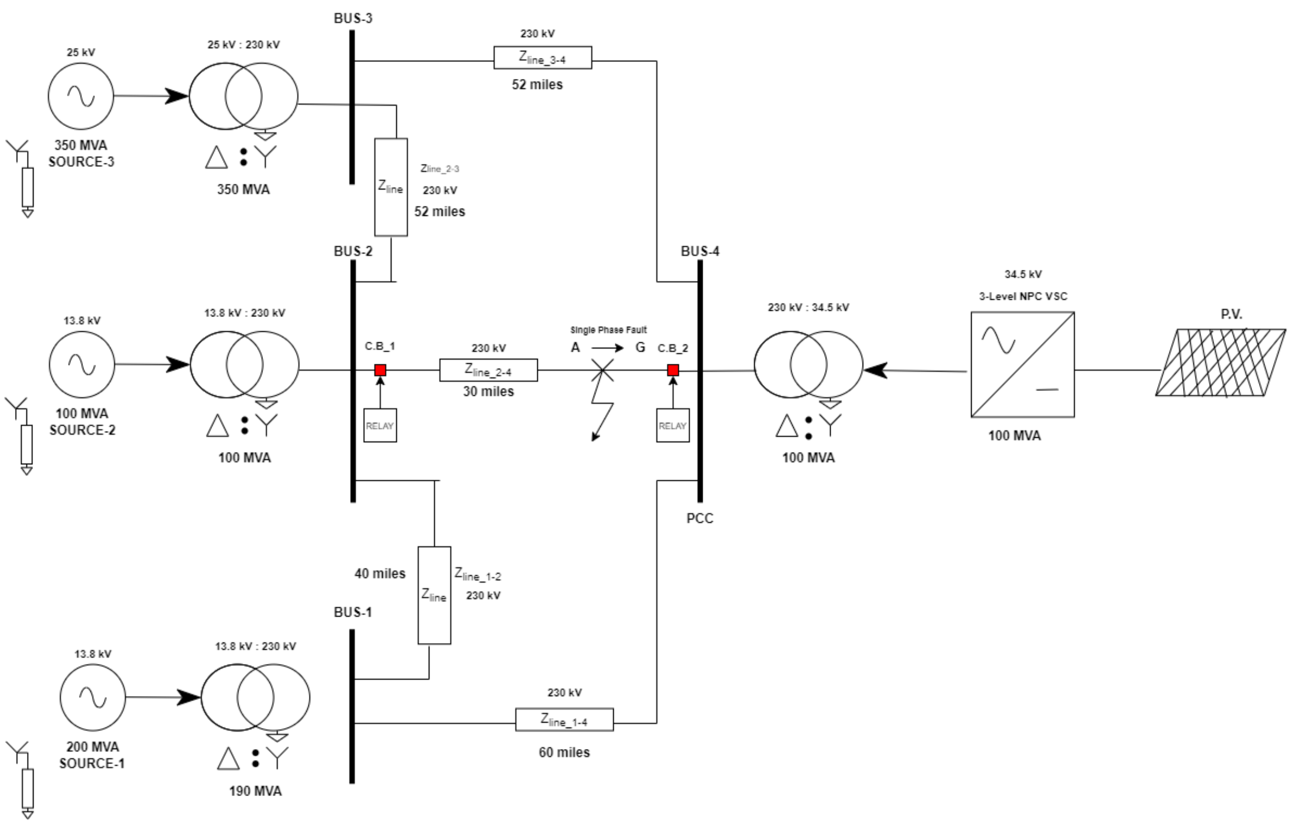

Figure 5.1 Diagram of modified 4-Bus Ring Main System

Generators G1, G2 and G3 are connected to Buses 1, 2 and 3 respectively. G1 and G2 generate at 13.8 kV and are stepped up using a step-up transformer each with individual power ratings as shown. Generator G3 generates at 25 kV and has a power rating of 350 MVA. The system is connected to the Inverter dominated part at the Point of common coupling (PCC) at Bus-4. The inverter also has a rating of 34.5 kV on the AC side and 100 MVA power rating. A suitable step-up transformer is used to step-up the voltage to the grid voltage. The Transmission voltage is at 230 kV. Two relays, as shown in the diagram, protect the transmission line and control the two circuit breakers C.B_1 and C.B_2.

The example test system of Figure 5.1 has been model in WinIGS. The WinIGS model is shown in Figure 5.2.

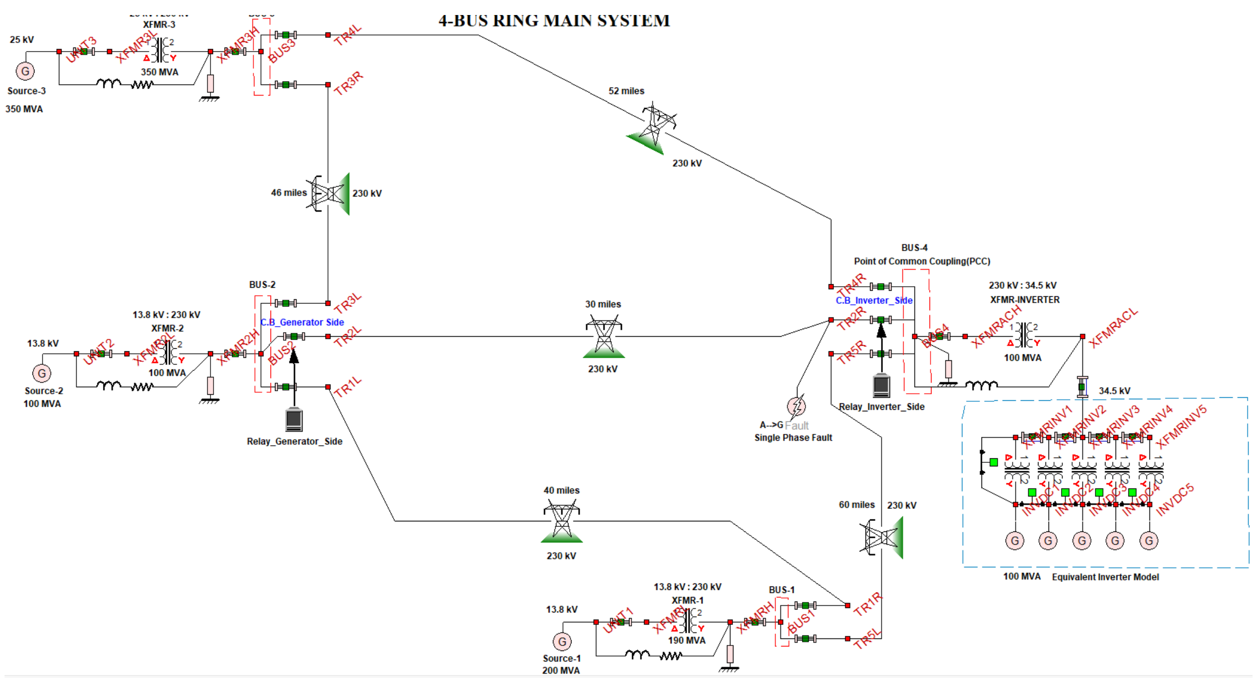

Figure 5.2 Simulation of modified Ring Main System in WinIGS

Two legacy relays are shown in Figure 5.2, as it has been discussed for Figure 5.1 already. Assuming that these relays protect the transmission line, the setting are selected by examining the parameters of the transmission line. Therefore, let's introduce the model of the transmission line to set the relay.

The line parameters are shown in Figures 5.3 and 5.4. The line nominal voltage is 230kV L-L rms voltage. The phase rated voltage is 132.79 kV. The rated current is taken from the conductor rating that is shown in Figure 5.4. The phase conductors of the line are ACSR/FINCH with a rating of 1165 Amperes.

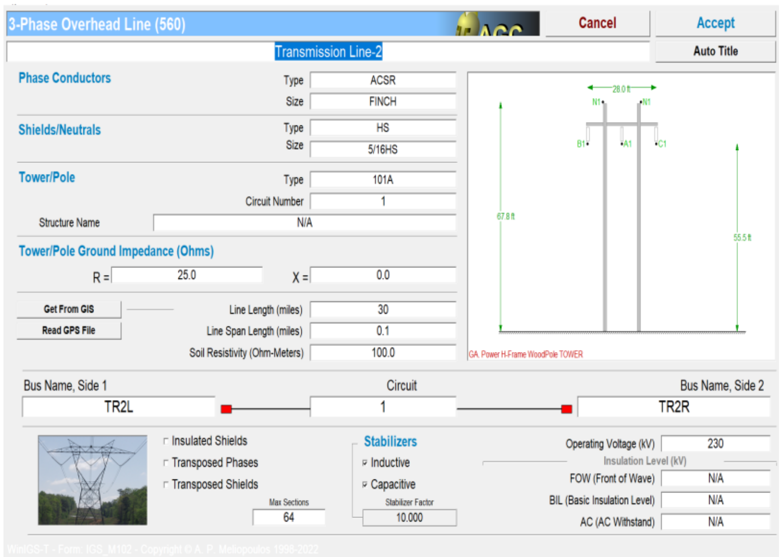

Figure 5.3 Transmission Line overall parameters in WinIGS

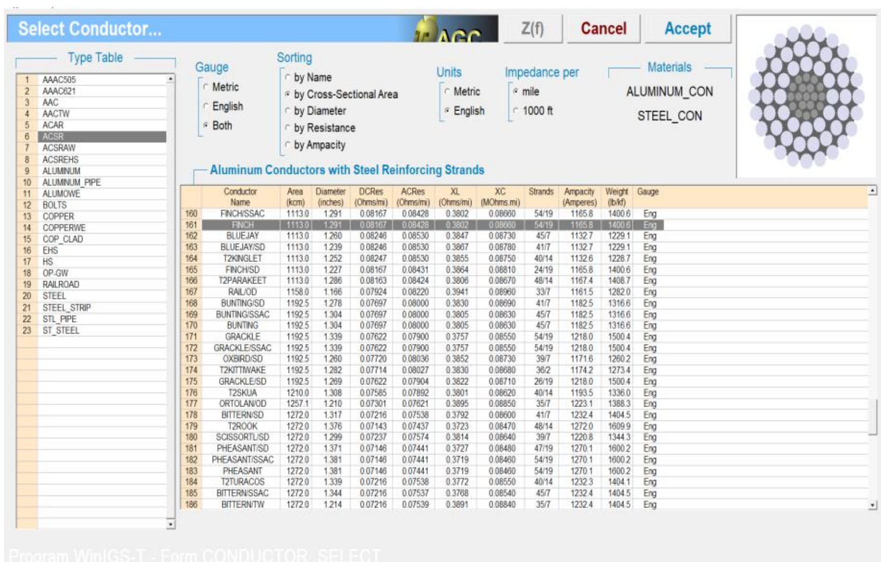

Figure 5.4 ACSR Parameters in WinIGS

The line parameters are computed with the program WinIGS. Figure 5-5 shows the computed parameters of the line.

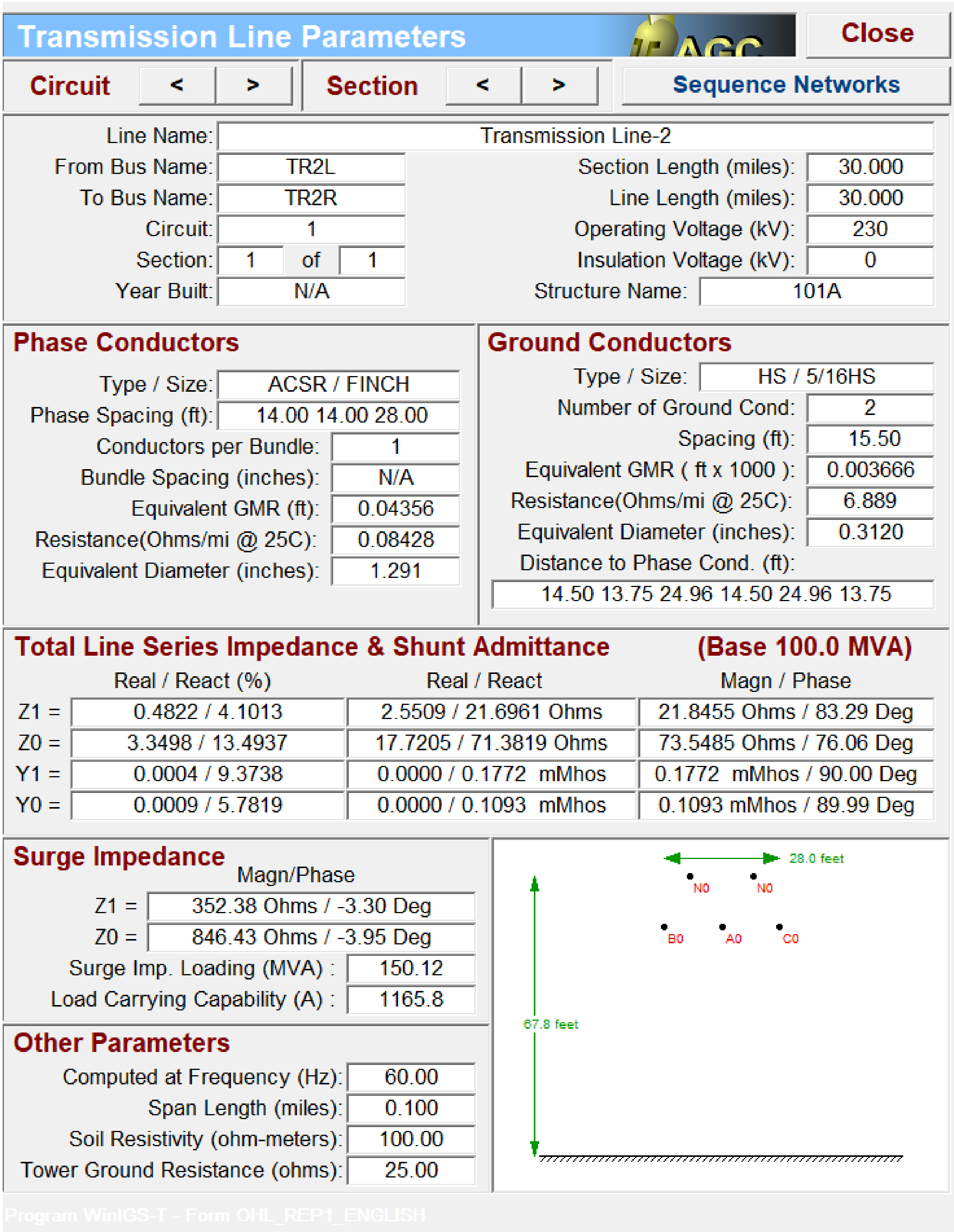

Transmission Line Parameters | Close

Circuit < > | Section < > | Sequence Networks

Line Name:	Transmission Line-2		
From Bus Name:	TR2L	Section Length (miles):	30.000
To Bus Name:	TR2R	Line Length (miles):	30.000
Circuit:	1	Operating Voltage (kV):	230
Section:	1 of 1	Insulation Voltage (kV):	0
Year Built:	N/A	Structure Name:	101A

Phase Conductors

Type / Size:	ACSR / FINCH
Phase Spacing (ft):	14.00 14.00 28.00
Conductors per Bundle:	1
Bundle Spacing (inches):	N/A
Equivalent GMR (ft):	0.04356
Resistance(Ohms/mi @ 25C):	0.08428
Equivalent Diameter (inches):	1.291

Ground Conductors

Type / Size:	HS / 5/16HS
Number of Ground Cond:	2
Spacing (ft):	15.50
Equivalent GMR (ft x 1000):	0.003666
Resistance(Ohms/mi @ 25C):	6.889
Equivalent Diameter (inches):	0.3120
Distance to Phase Cond. (ft):	14.50 13.75 24.96 14.50 24.96 13.75

Total Line Series Impedance & Shunt Admittance (Base 100.0 MVA)

	Real / React (%)	Real / React	Magn / Phase
Z1 =	0.4822 / 4.1013	2.5509 / 21.6961 Ohms	21.8455 Ohms / 83.29 Deg
Z0 =	3.3498 / 13.4937	17.7205 / 71.3819 Ohms	73.5485 Ohms / 76.06 Deg
Y1 =	0.0004 / 9.3738	0.0000 / 0.1772 mMhos	0.1772 mMhos / 90.00 Deg
Y0 =	0.0009 / 5.7819	0.0000 / 0.1093 mMhos	0.1093 mMhos / 89.99 Deg

Surge Impedance

	Magn/Phase
Z1 =	352.38 Ohms / -3.30 Deg
Z0 =	846.43 Ohms / -3.95 Deg
Surge Imp. Loading (MVA) :	150.12
Load Carrying Capability (A) :	1165.8

Other Parameters

Computed at Frequency (Hz):	60.00
Span Length (miles):	0.100
Soil Resistivity (ohm-meters):	100.00
Tower Ground Resistance (ohms):	25.00

Program WinIGS-T - Form OHL_REP1_ENGLISH

Figure 5.5 Line Parameters

From Figure 5-5, the line pos/neg/zero sequence impedances are:

The positive sequence impedance is $Z_1 = 21.8455e^{j83.29^0}$ *Ohms*

The zero-sequence impedance is $Z_0 = 73.5485e^{j76.06^0}$ *Ohms*

Now to understand the operation of the different relays in a system dominated by inverter-based resources let us look at certain different scenarios:

Scenario-1: Three-line system (Connected to the PCC):

Case-A: No fault
Case-B: Fault happening on the 30-mile transmission line 22.5 miles (75%) from the PCC.
Case-C: Fault happening on the 30-mile transmission line 15 miles (50%) from the PCC.

Scenario-2: Two line system (Connected to the PCC):

Case-A: No fault
Case-B: Fault happening on the 30-mile transmission line 22.5 miles (75%) from the PCC.
Case-C: Fault happening on the 30-mile transmission line 15 miles (50%) from the PCC.

Scenario-3: One line system (Connected to the PCC):

Case-A: No fault
Case-B: Fault happening on the 30-mile transmission line 22.5 miles (75%) from the PCC.
Case-C: Fault happening on the 30-mile transmission line 15 miles (50%) from the PCC.

We can therefore study the operation of various relays under inverter-dominated systems by studying the characteristics of said relays in the following scenarios, this will give us an insight into the problems that the protection functions have to face during steady-state operation in systems with inverter domination.

Distance Relay (21) Settings: Now that we have seen the different scenarios in which we want the relays to operate in, we can observe the operation of the distance relay in these following scenarios. But first let us set up the distance relay with three zones.

Zone-1 covers 80% of the line, Zone-2 covers 125% of the line and Zone-3 covers 250% of the line.

From this we can set the zones of the distance relay. Using primary quantities, the settings of the relay are:

Zone-1 = $17.47e^{j83.29^0}$ ohms
Zone-2 = $27.31e^{j83.29^0}$ ohms
Zone-3 = $54.6138e^{j83.29^0}$ ohms

The compensation factor is given by the equation:

$$k = \frac{Z_0 - Z_1}{Z_1};$$

The settings of the distance relay is given below:

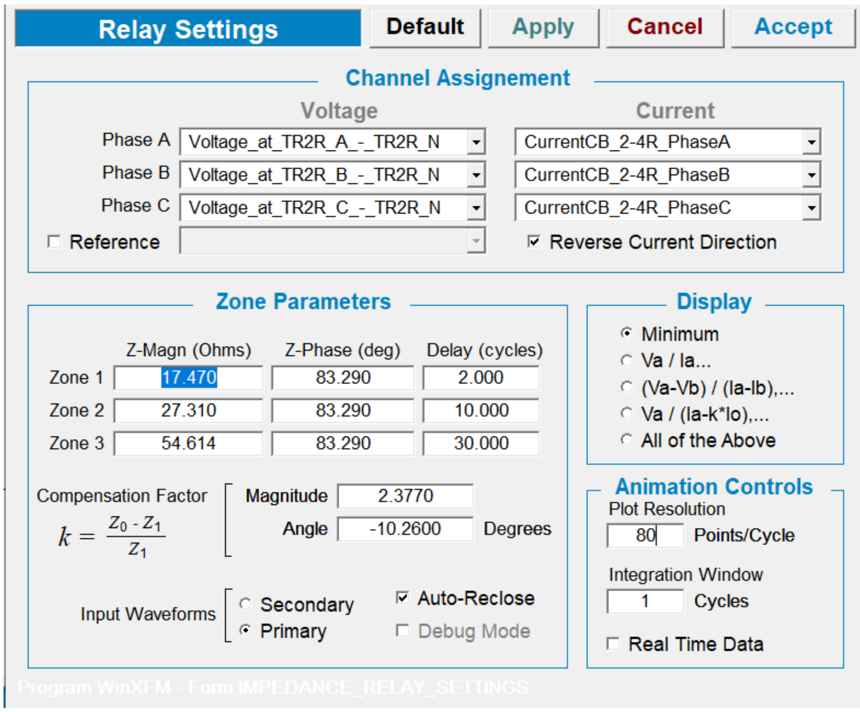

Figure 5.6 Distance relay settings at PCC in WinIGS

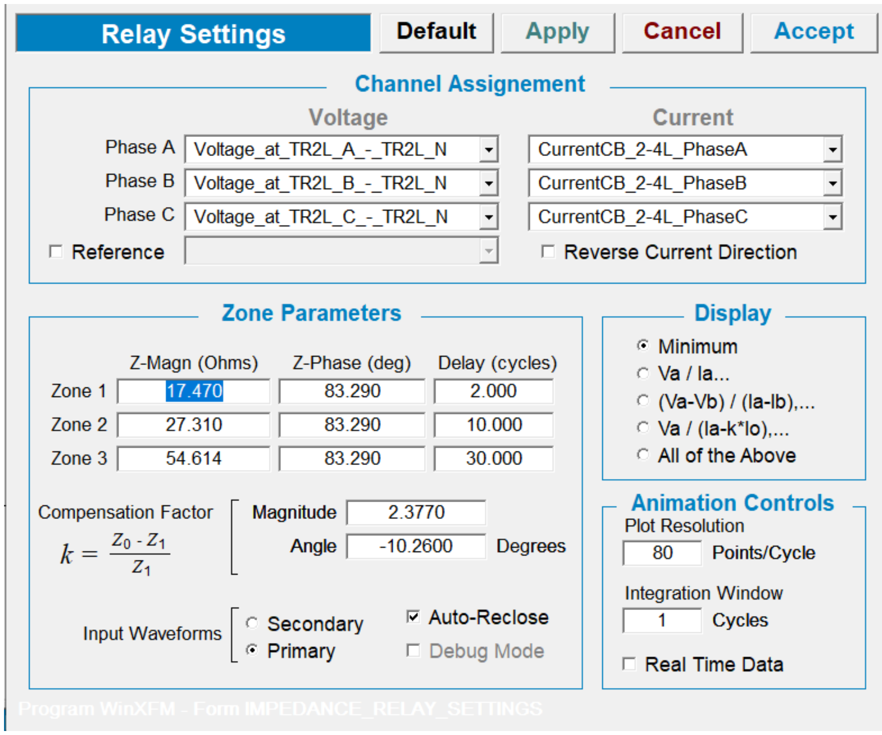

Figure 5.7 Distance relay settings at Bus-2 in WinIGS

5.2 Scenario 1: Contingency 1: All Three Lines Connected

This scenario is where all three lines connected to PCC.
Case-A: No fault in the system.

In this case, the simulation results are shown in Figures 5.9, 5.10, 5.11 and 5.12. The impedance trajectory superimposed on the relay impedance characteristics is given in Figures 5.13 and 5.14.

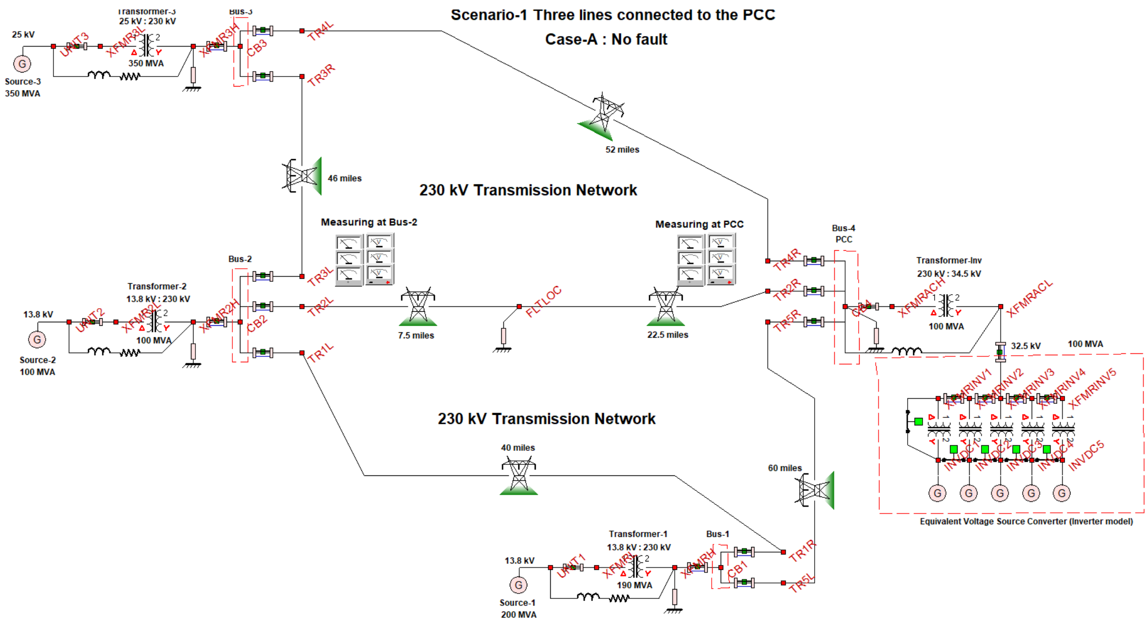

Figure 5.8 Scenario-1 Three Lines Connected to PCC with no Fault

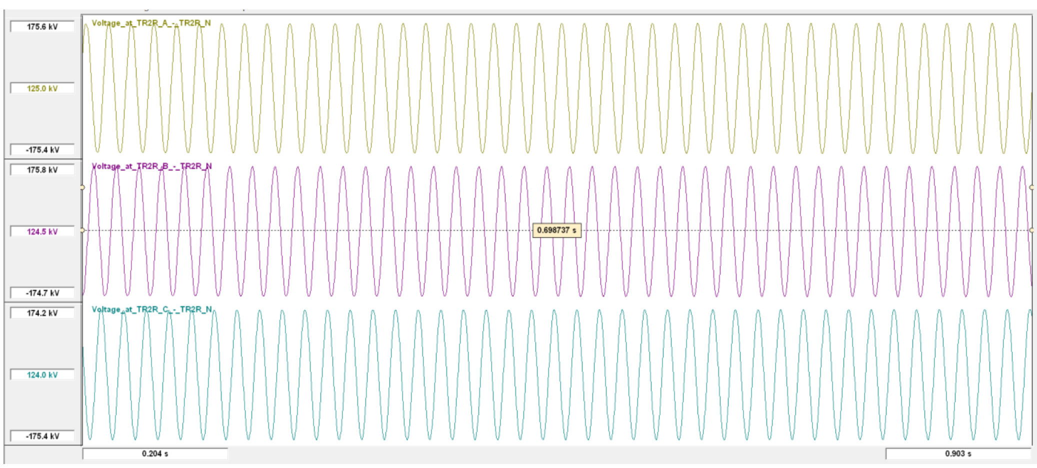

Figure 5.9 Voltage Waveforms at PCC for no fault in scenario-1

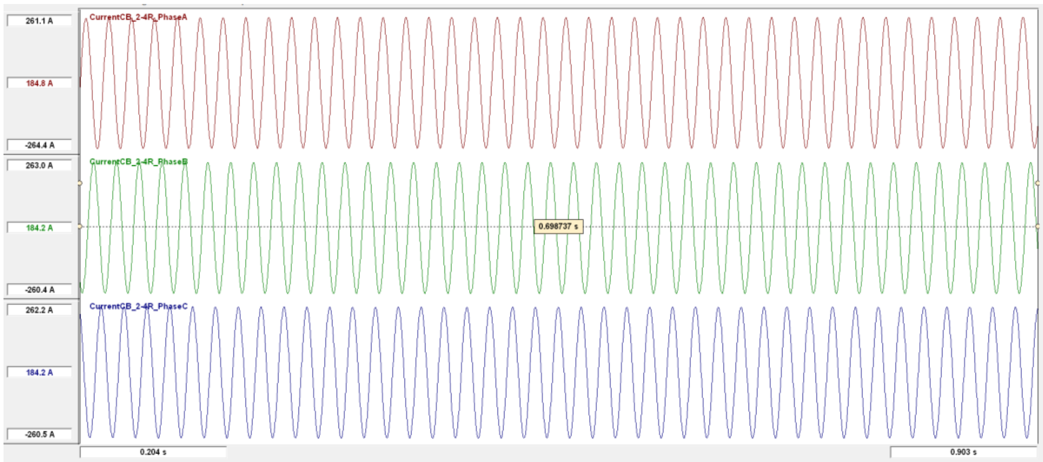

Figure 5.10 Current Waveforms at PCC for no fault in scenario-1

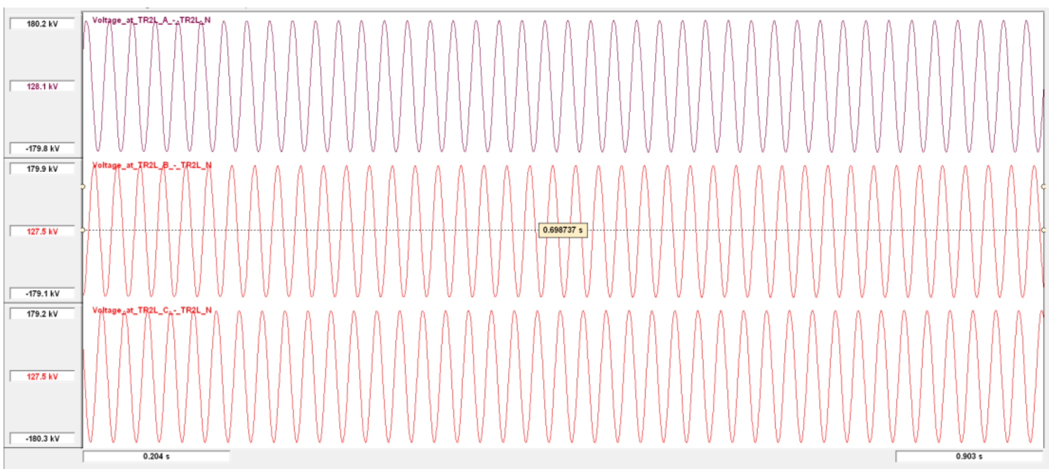

Figure 5.11 Voltage Waveforms at Bus-2 for no fault in scenario-1

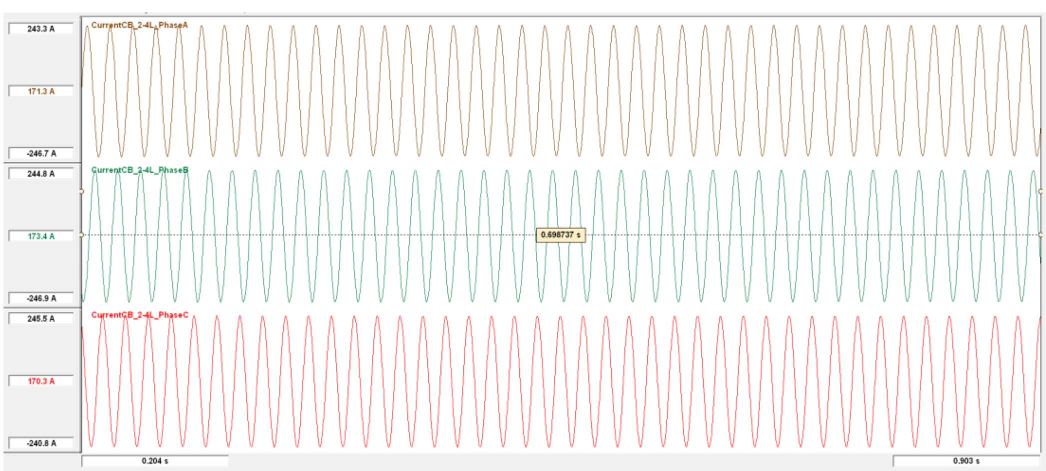

Figure 5.12 Current Waveforms at Bus-2 for no fault in scenario-1

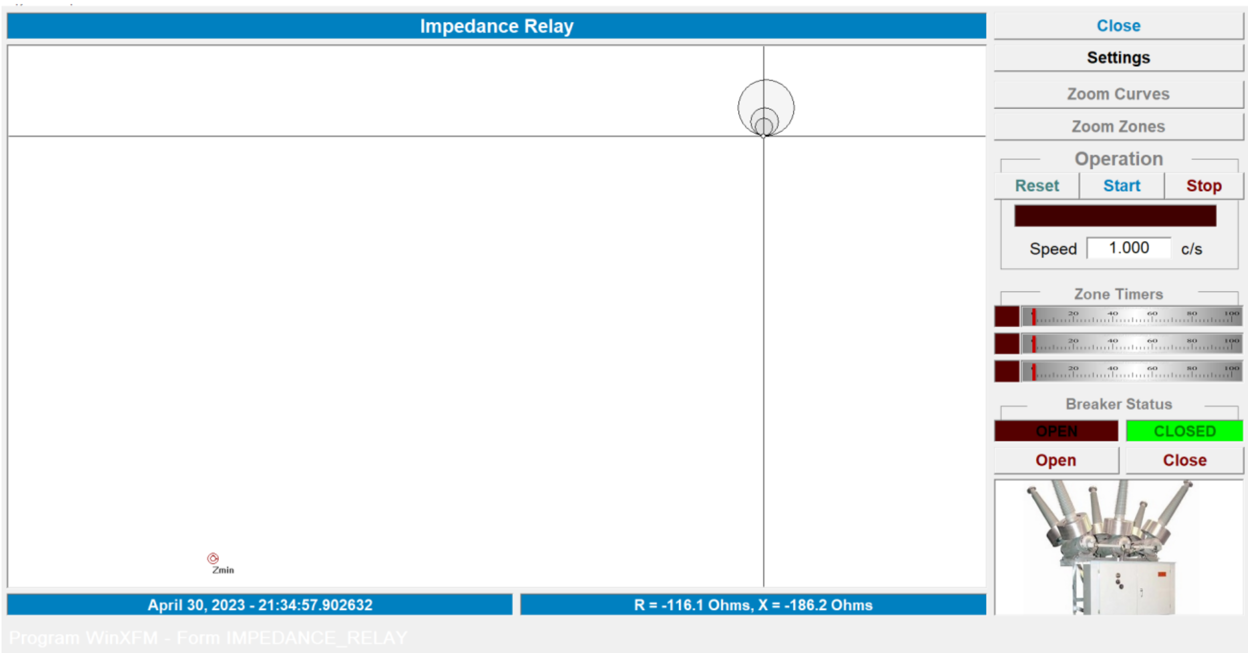

Figure 5.13 Impedance Trajectory Superimposed on Relay Characteristics at PCC

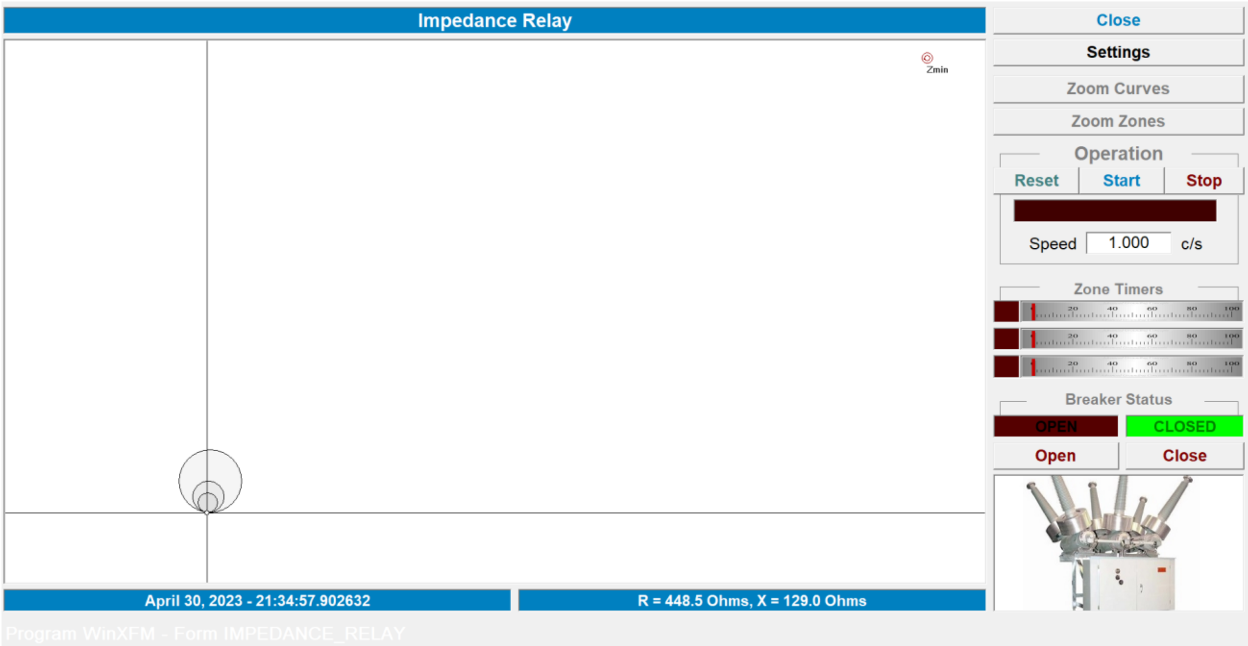

Figure 5.14 Impedance Trajectory Superimposed on Relay Characteristics at Bus-2

Case-B: Fault happening on the 30-mile transmission line 22.5 miles (75%) from the PCC

In this case, several faults occur in the system. Regarding the line under protection, a line fault occurs at 22.5 miles from the PCC at the point FLTLOC indicated in Figure 5-15. The simulated data are provided in Figures 5-16 and 5-17.

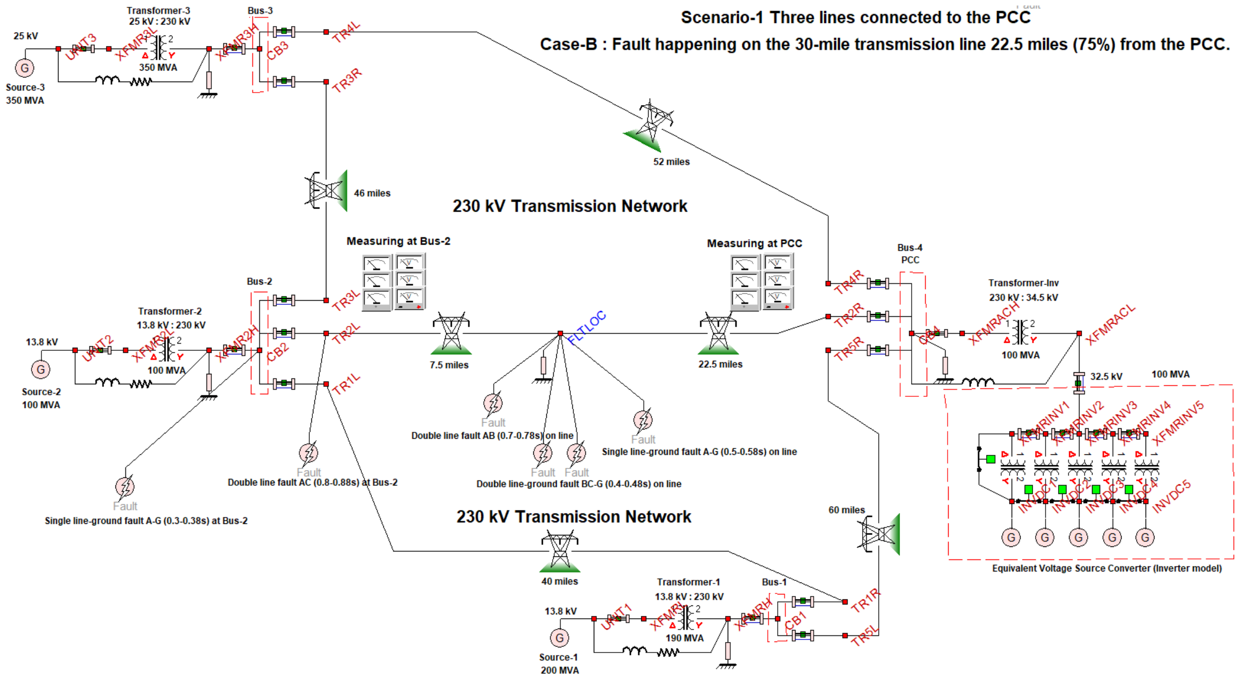

Figure 5.15 Scenario-1 Case-B Fault on Three Lines Connected to PCC at 22.5 miles from PC

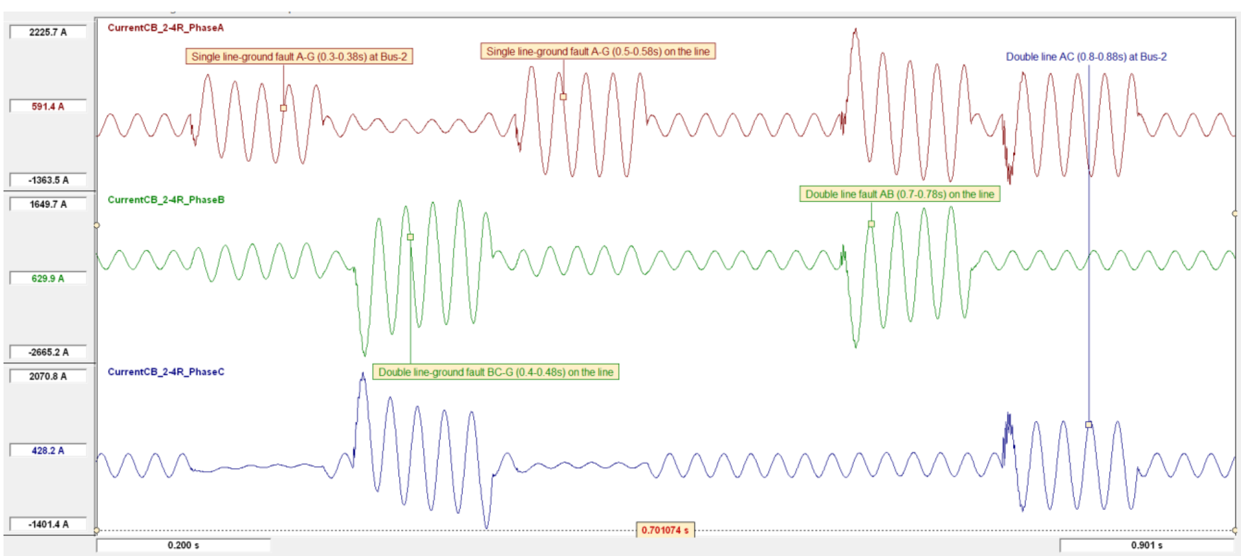

Figure 5.16 Current Waveforms at PCC for Scenario-1 Case-B

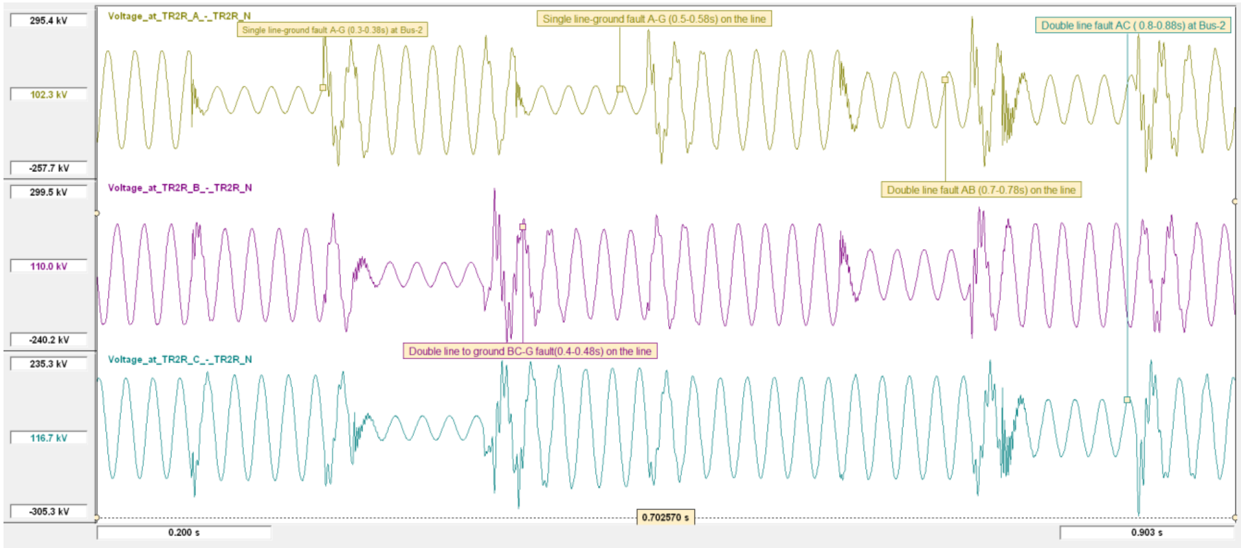

Figure 5.17 Voltage Waveforms at PCC for Scenario-1 Case-B

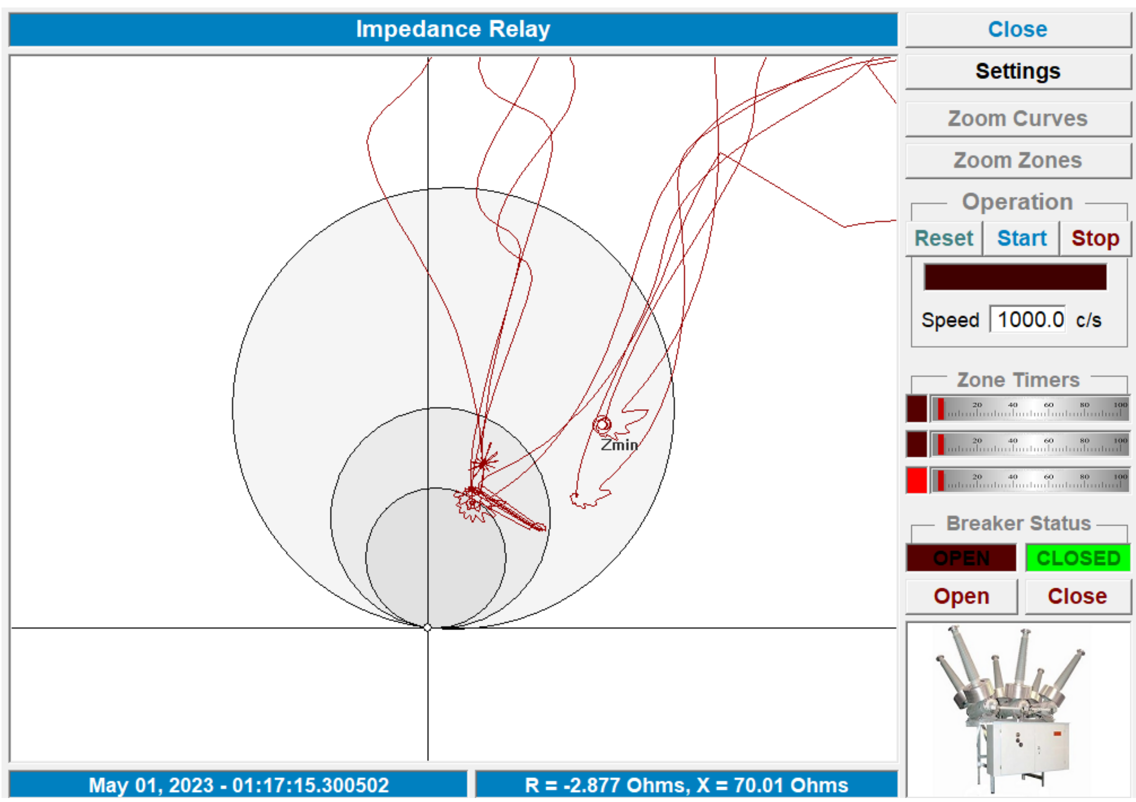

Figure 5.18 Impedance Trajectory Superimposed on Relay Characteristics at PCC for A-G fault at Bus-2

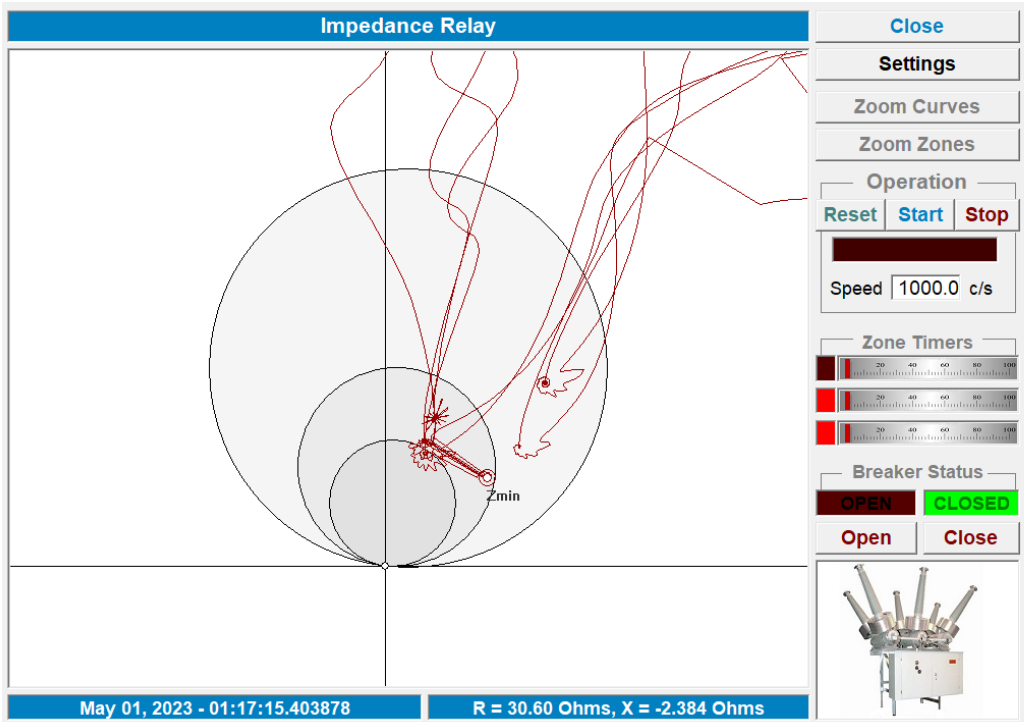

Figure 5.19 Impedance Trajectory Superimposed on Relay Characteristics at PCC for BC-G fault on the line

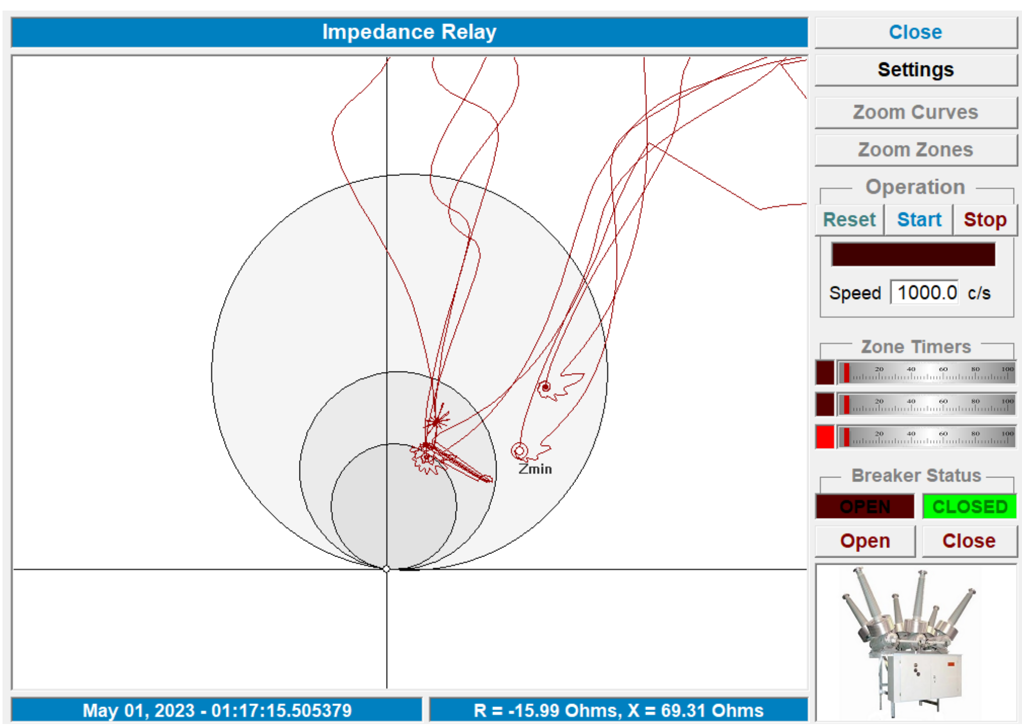

Figure 5.20 Impedance Trajectory Superimposed on Relay Characteristics at PCC for A-G fault on the line

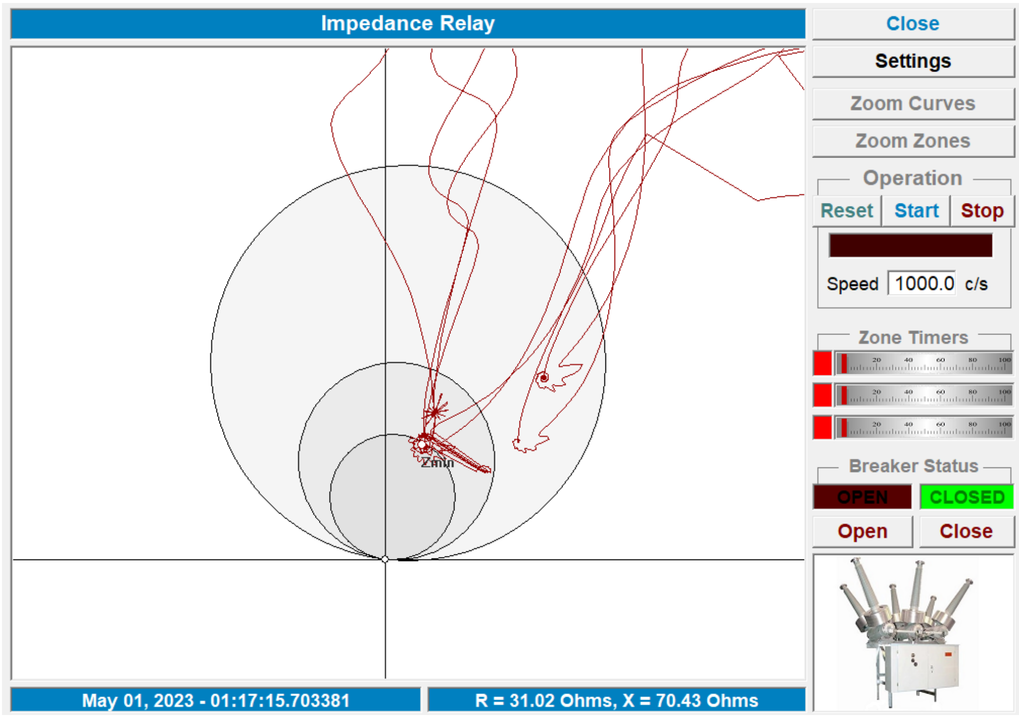

Figure 5.21 Impedance Trajectory Superimposed on Relay Characteristics at PCC for AB fault on the line

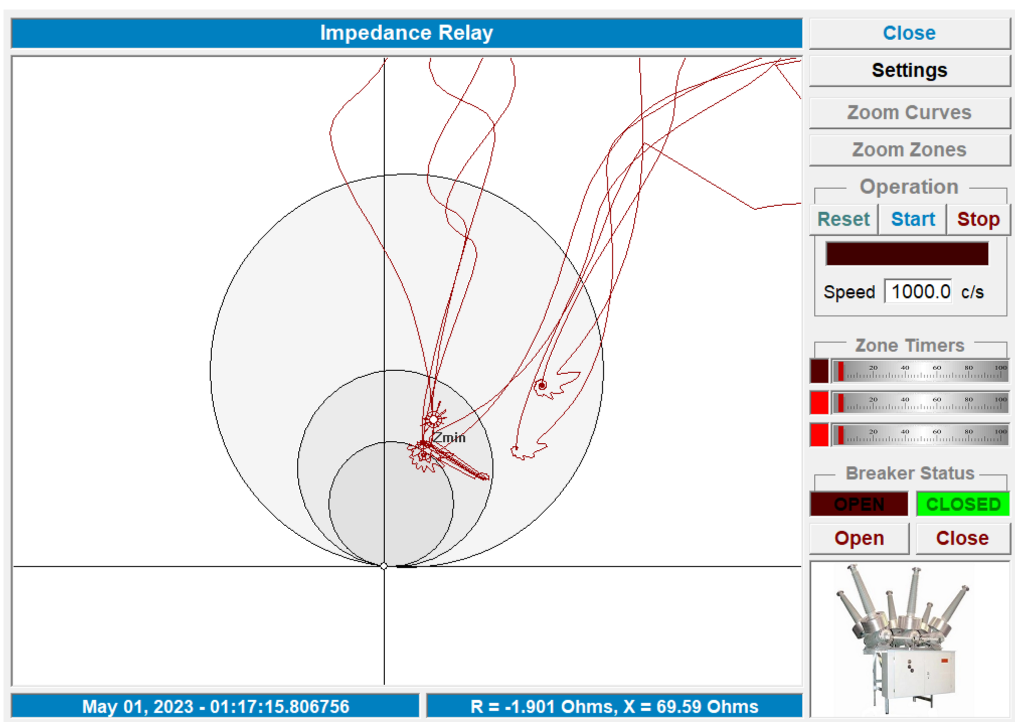

Figure 5.22 Impedance Trajectory Superimposed on Relay Characteristics at PCC for AC fault on Bus-2

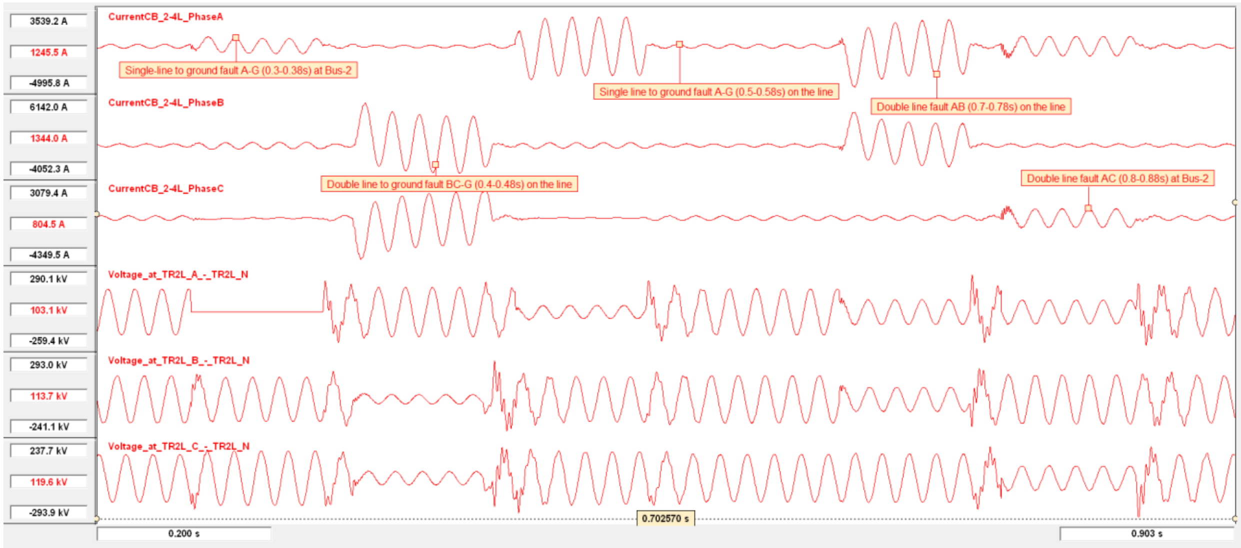

Figure 5.23 Current and Voltage Waveforms at Bus-2 for scenario-1 case-B

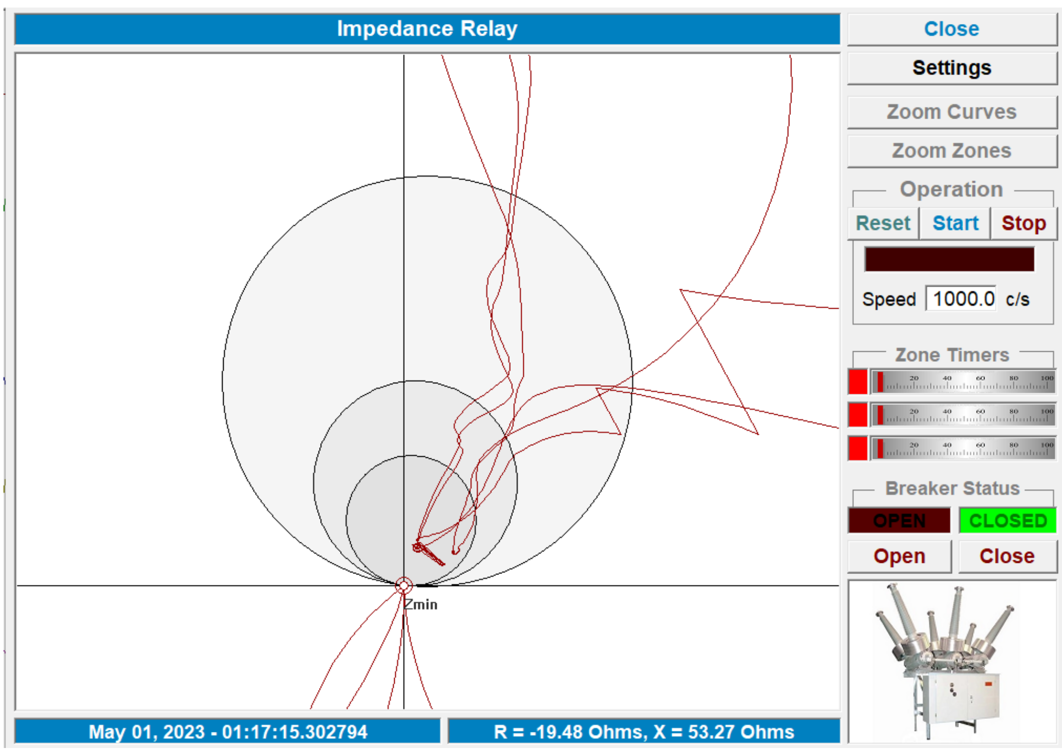

Figure 5.24 Impedance Trajectory Superimposed on Relay Characteristics at Bus-2 for A-G fault on Bus-2

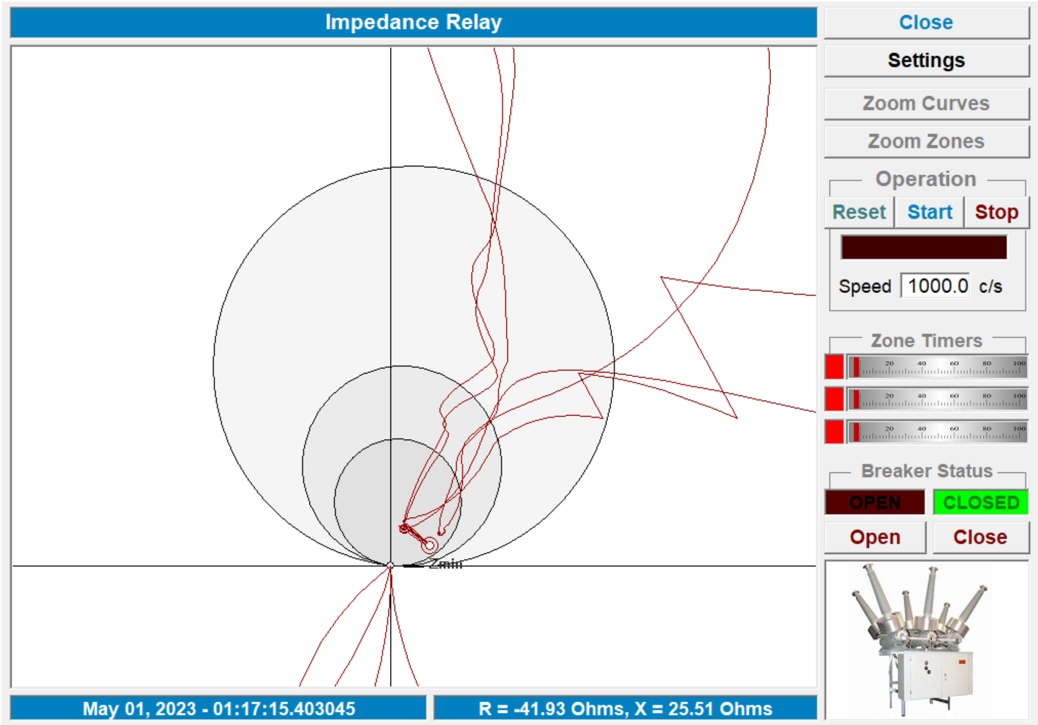

Figure 5.25 Impedance Trajectory Superimposed on Relay Characteristics at Bus-2 for BC-G fault on line

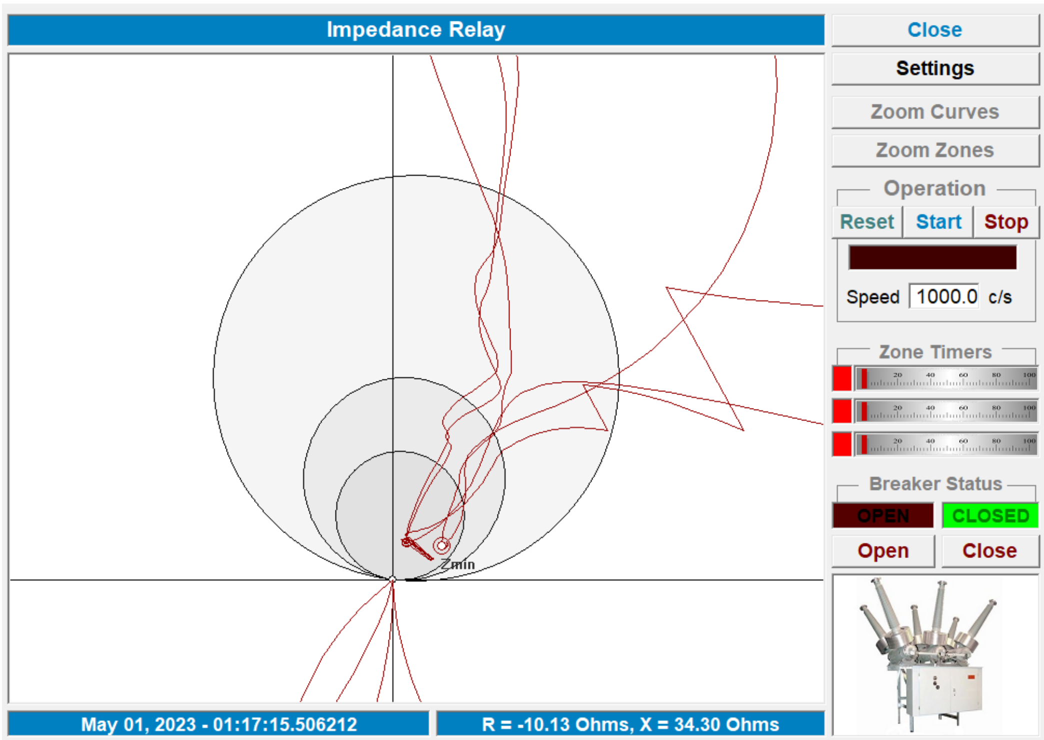

Figure 5.26 Impedance Trajectory Superimposed on Relay Characteristics at Bus-2 for A-G fault on line

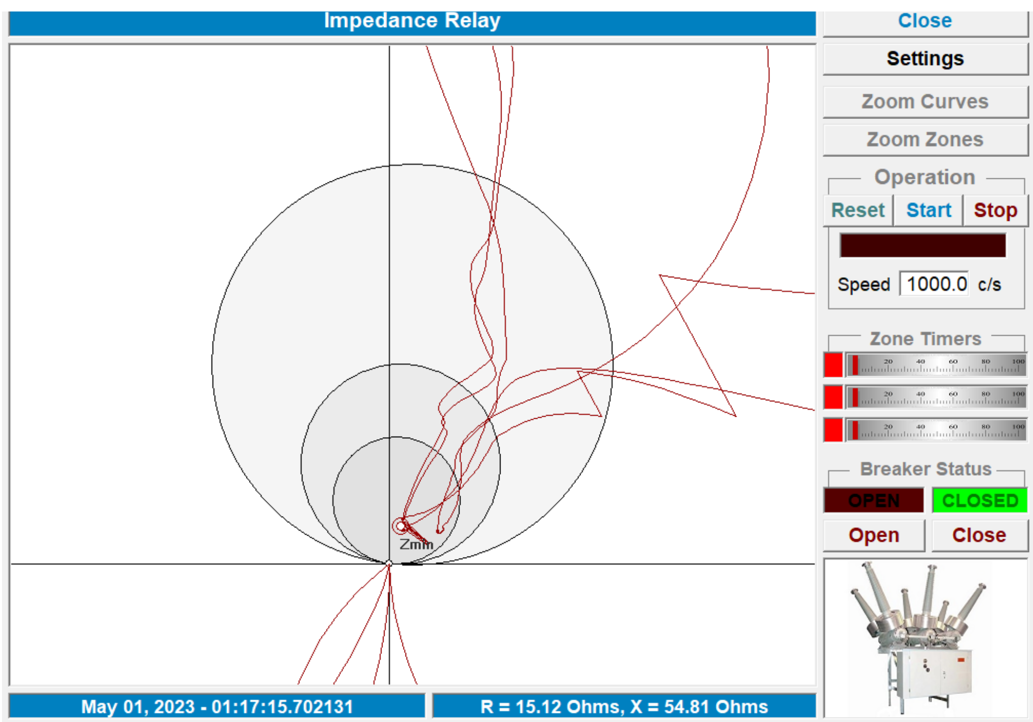

Figure 5.27 Impedance Trajectory Superimposed on Relay Characteristics at Bus-2 for AB fault on line

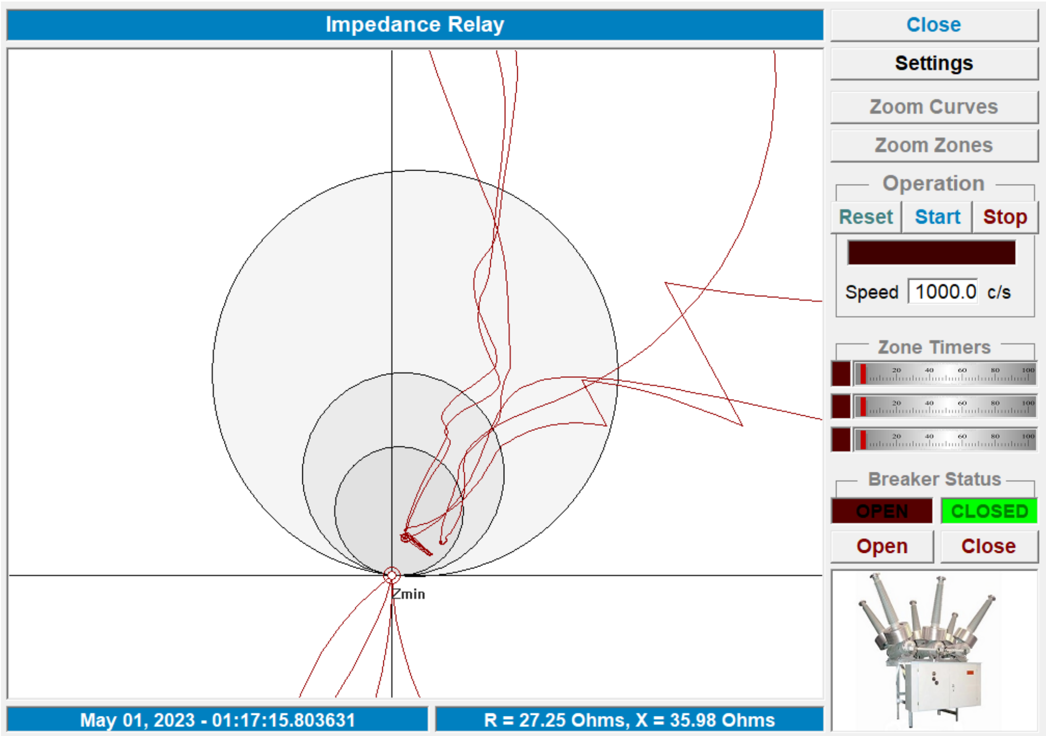

Figure 5.28 Impedance Trajectory Superimposed on Relay Characteristics at Bus-2 for AC fault at Bus-2

Case-C: Fault happening on the 30-mile transmission line 15 miles (50%) from the PCC.

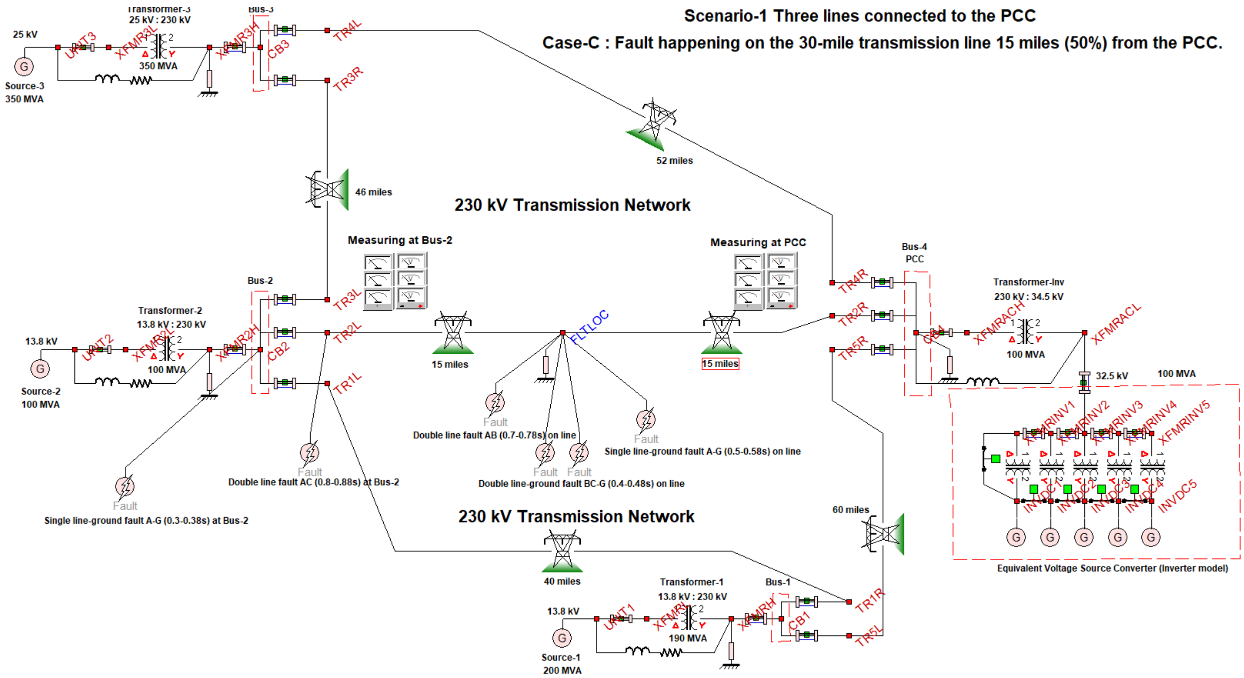

Figure 5.29 Scenario-1 case-C Fault on Three Lines Connected to PCC at 15 miles from PCC

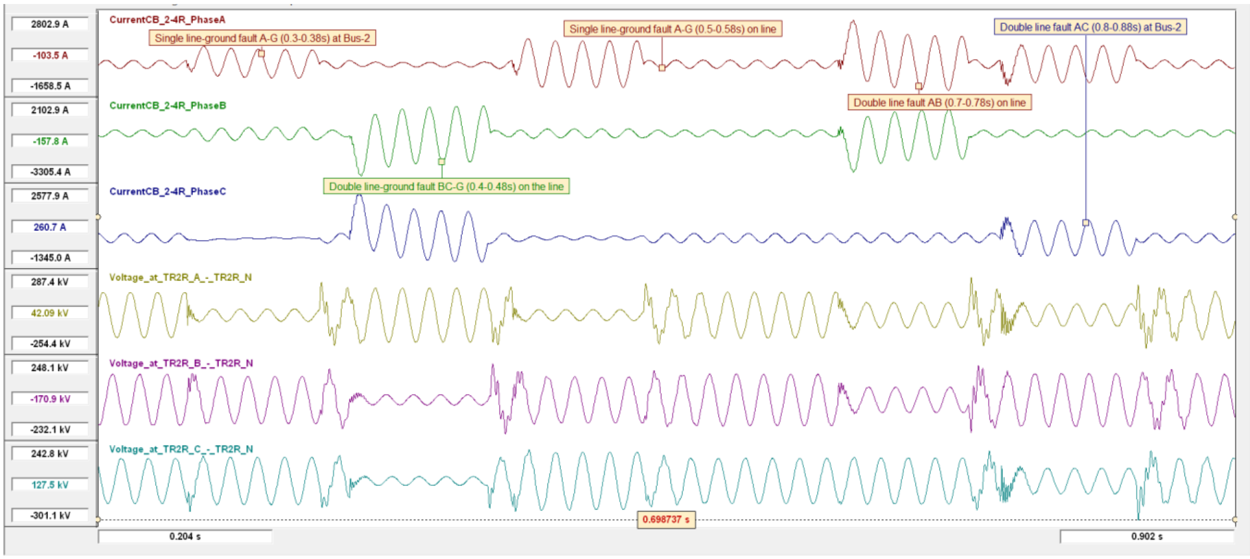

Figure 5.30 Current and Voltage Waveforms at PCC for scenario-1 case-C

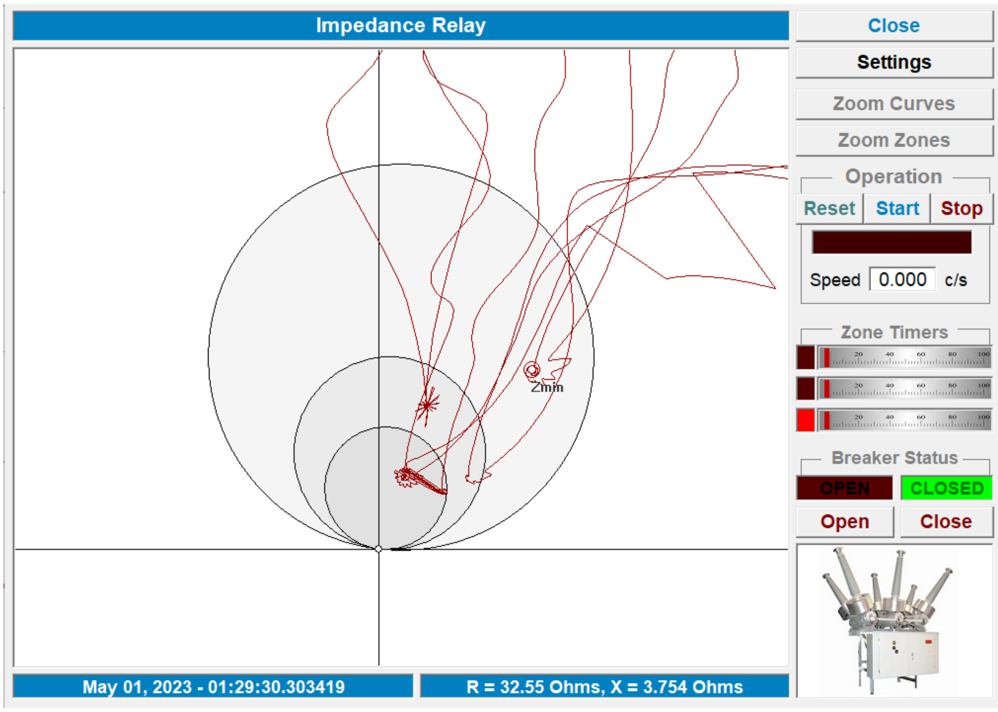

Figure 5.31 Zone impedance characteristics at PCC for A-G fault at Bus-2

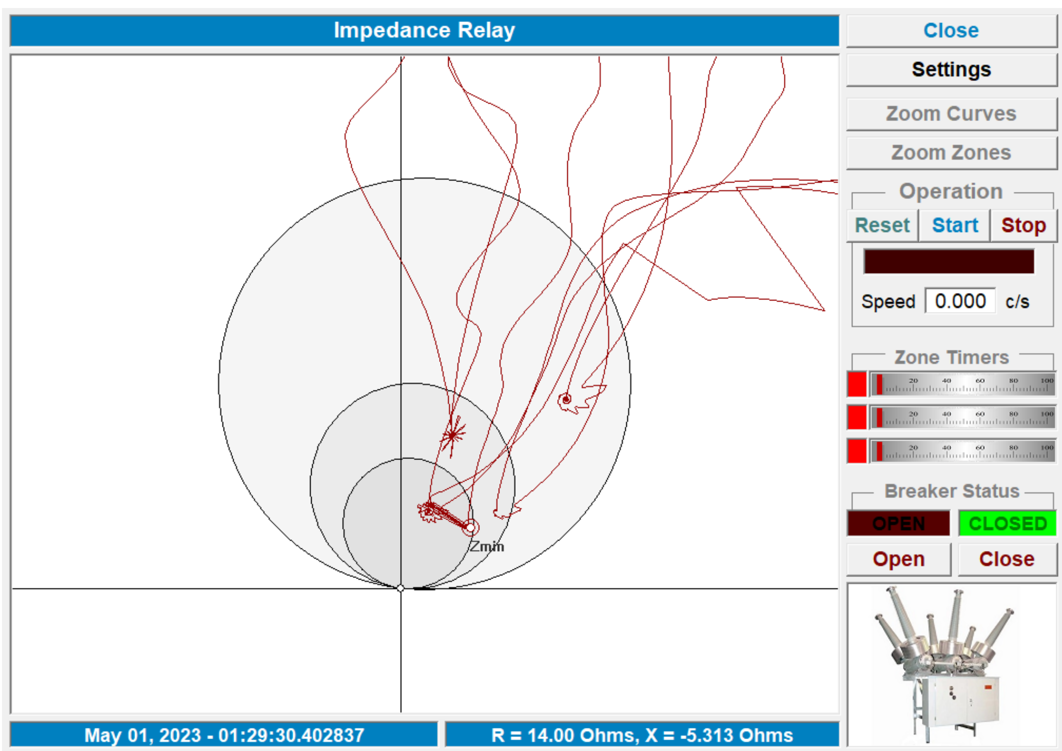

Figure 5.32 Zone impedance characteristics at PCC for BC-G fault on the line

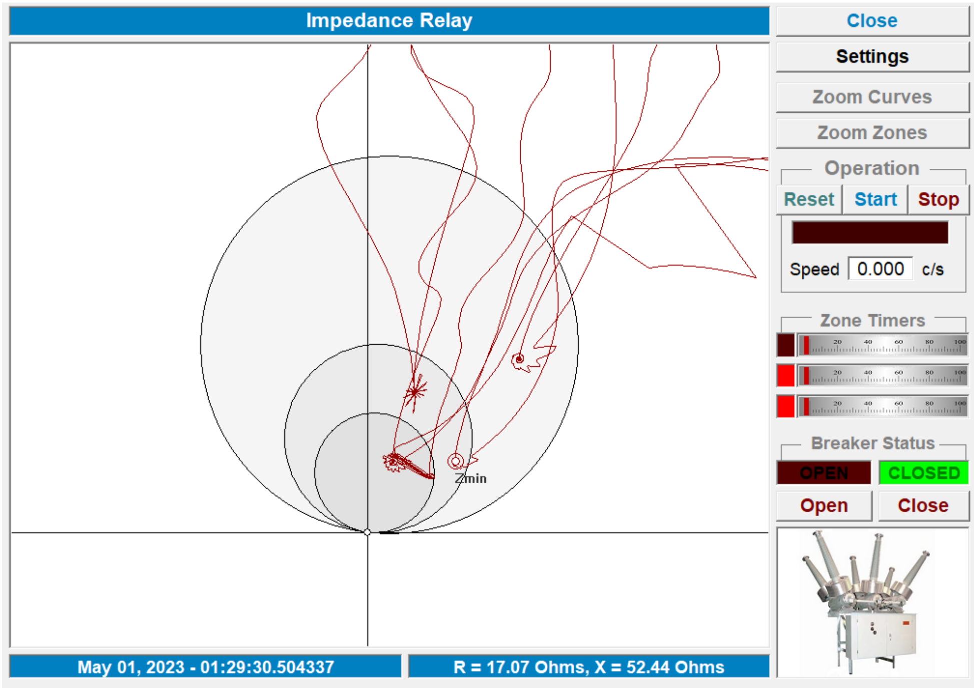

Figure 5.33 Zone impedance characteristics at PCC for A-G fault on line

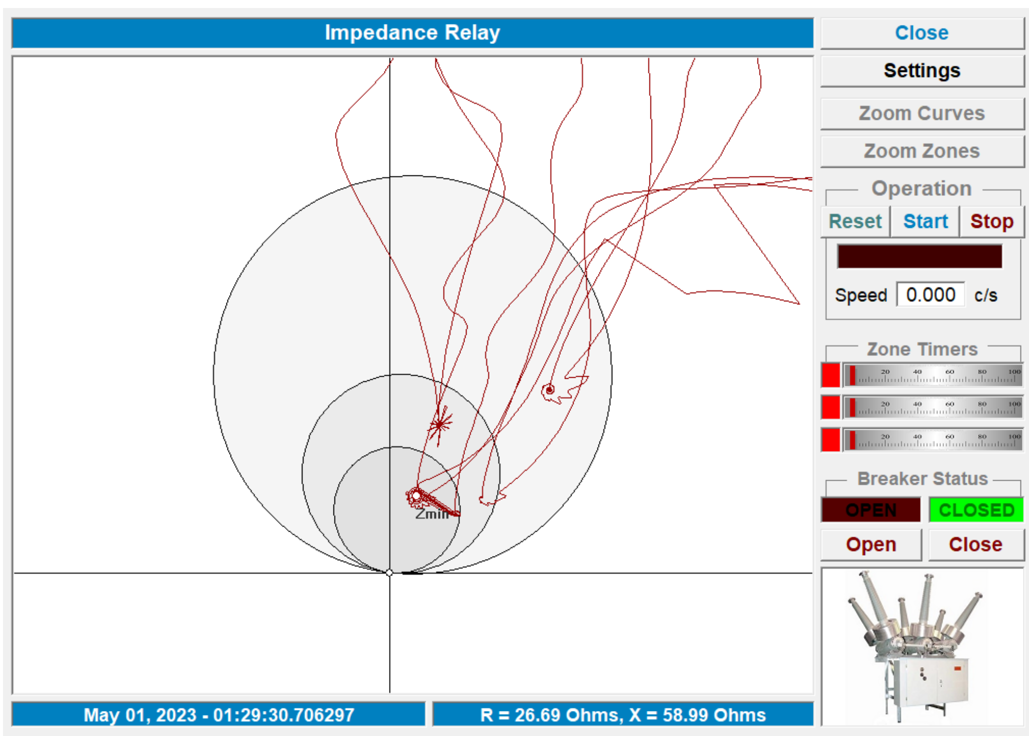

Figure 5.34 Zone impedance characteristics at PCC for AB fault on the line

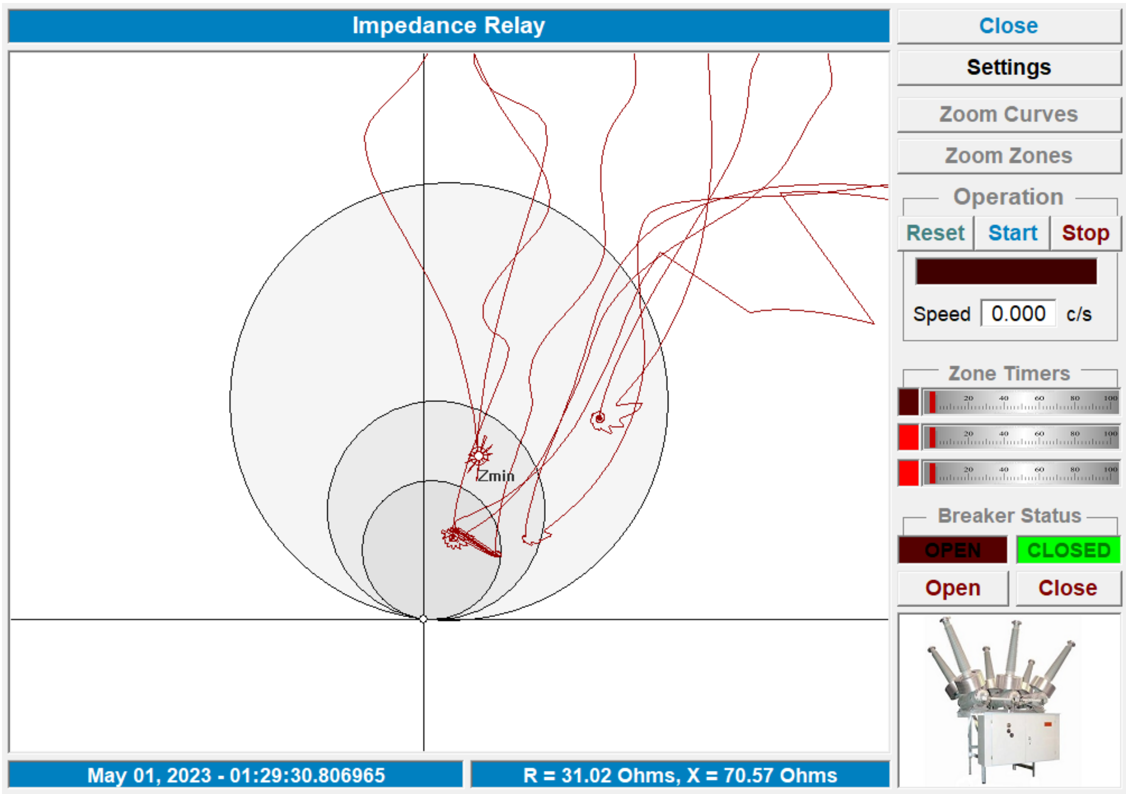

Figure 5.35 Zone impedance characteristics at PCC for AC fault at Bus-2

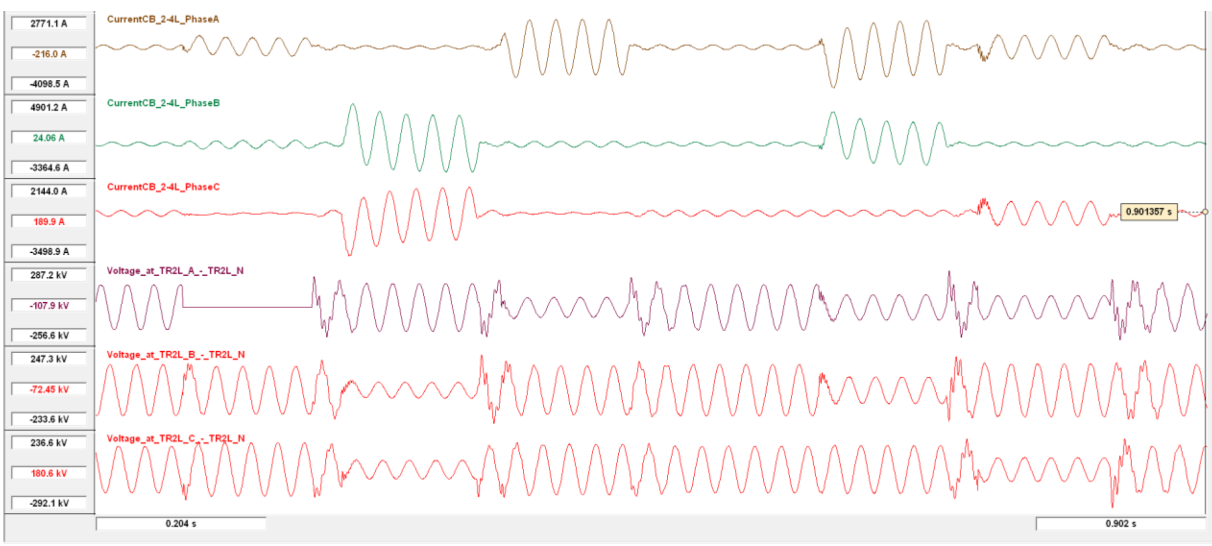

Figure 5.36 Current and Voltage Waveforms at Bus-2 for scenario-1 case-C

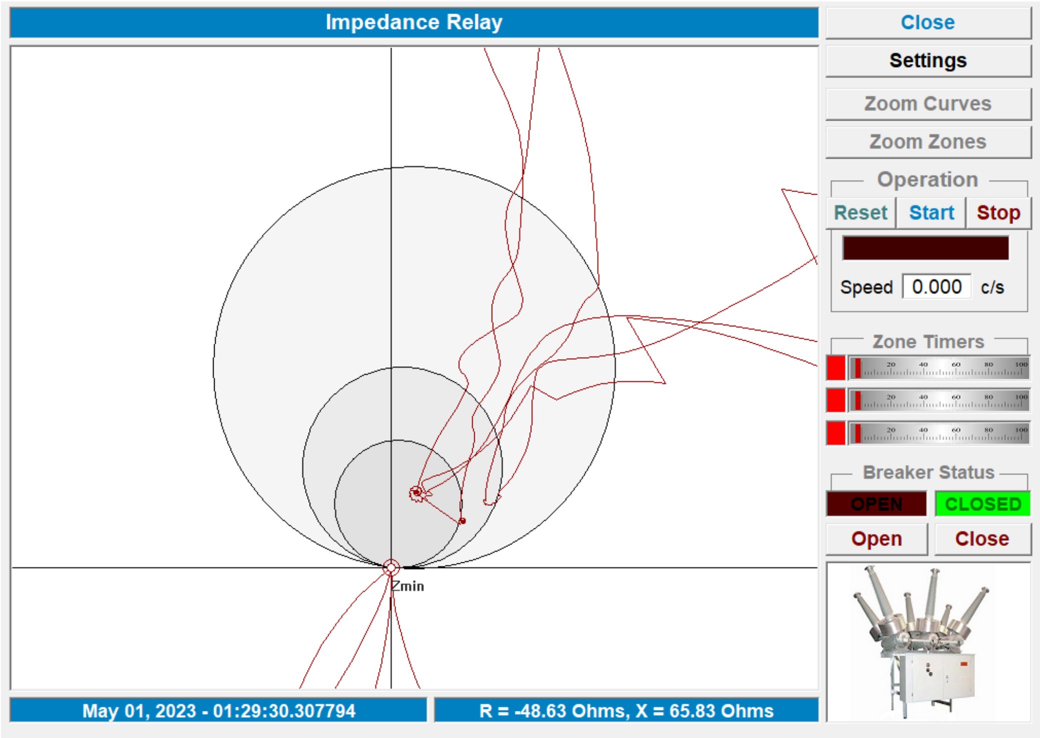

Figure 5.37 Zone impedance characteristics at Bus-2 for A-G fault at Bus-2

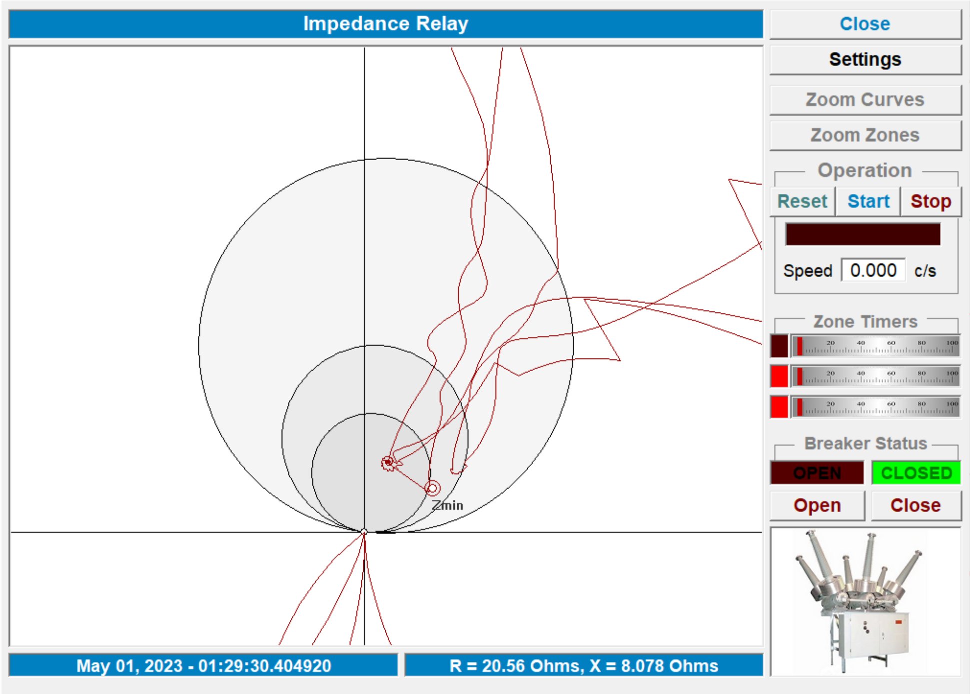

Figure 5.38 Zone impedance characteristics at Bus-2 for BC-G fault on line

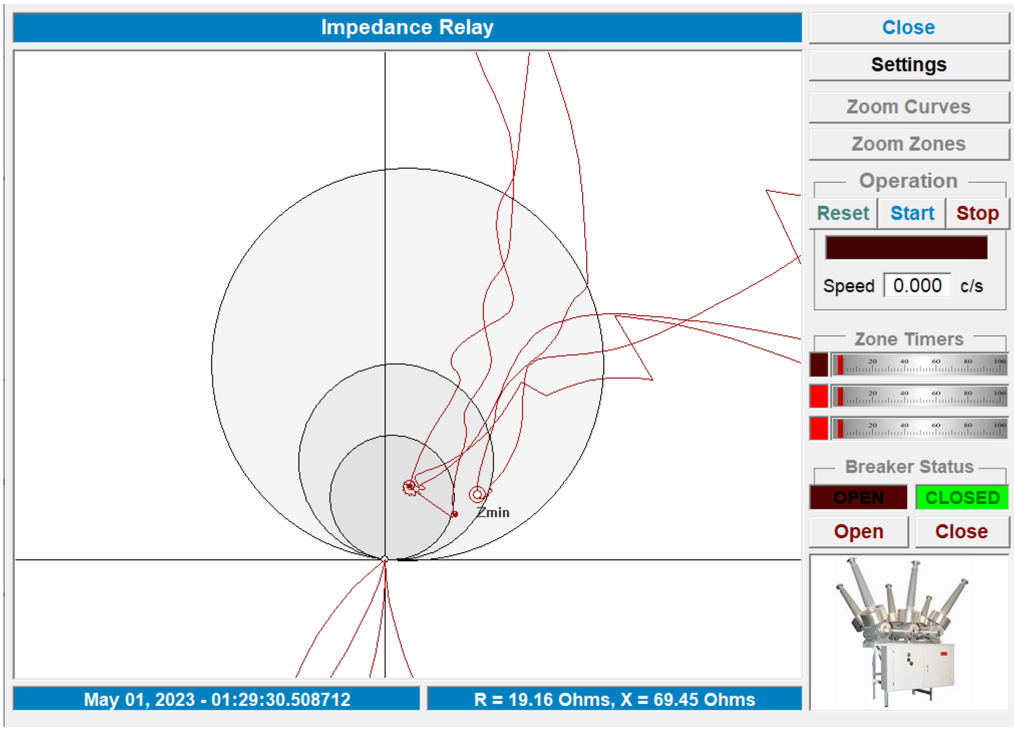

Figure 5.39 Zone impedance characteristics at Bus-2 for A-G fault on line

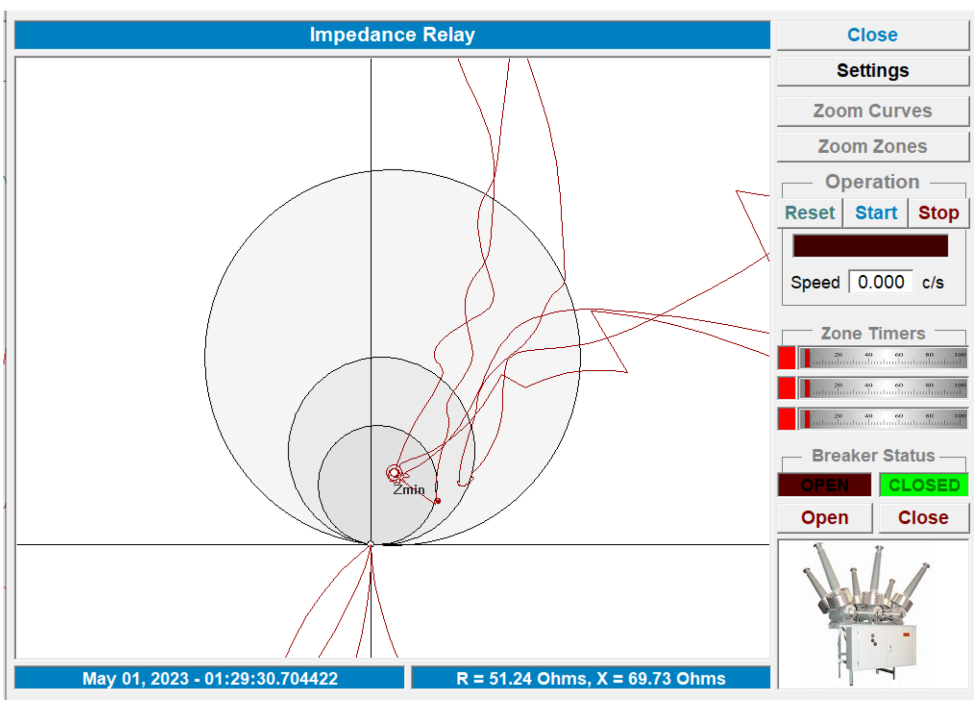

Figure 5.40 Zone impedance characteristics at Bus-2 for AB fault on line

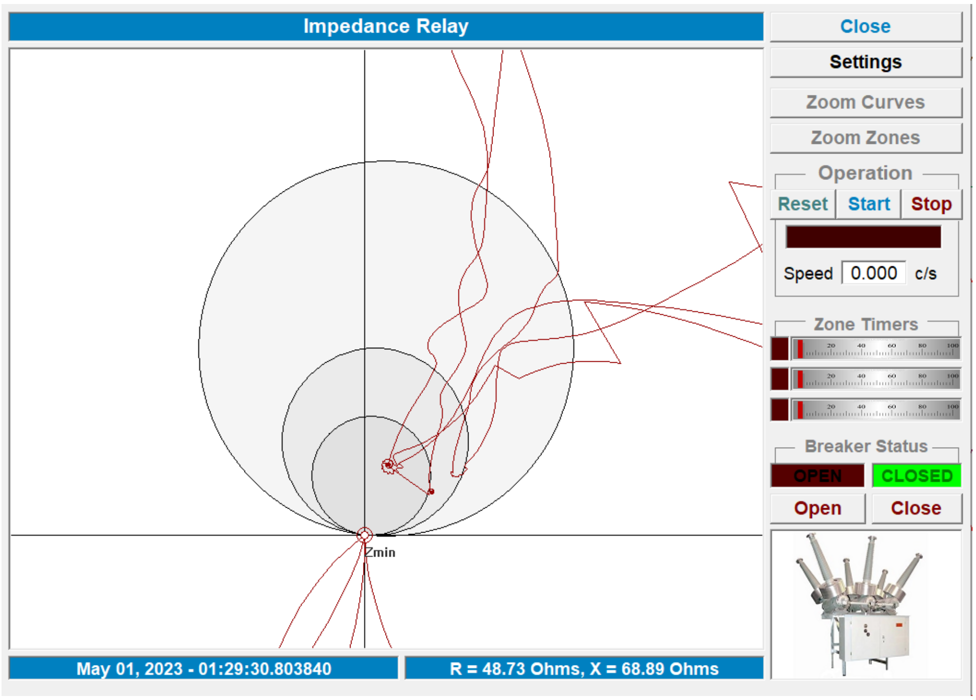

Figure 5.41 Zone impedance characteristics at Bus-2 for AC fault at Bus-2

5.3 Scenario 2: Contingency 2: Two Lines Connected, One Out

Case-A: No fault in the system.

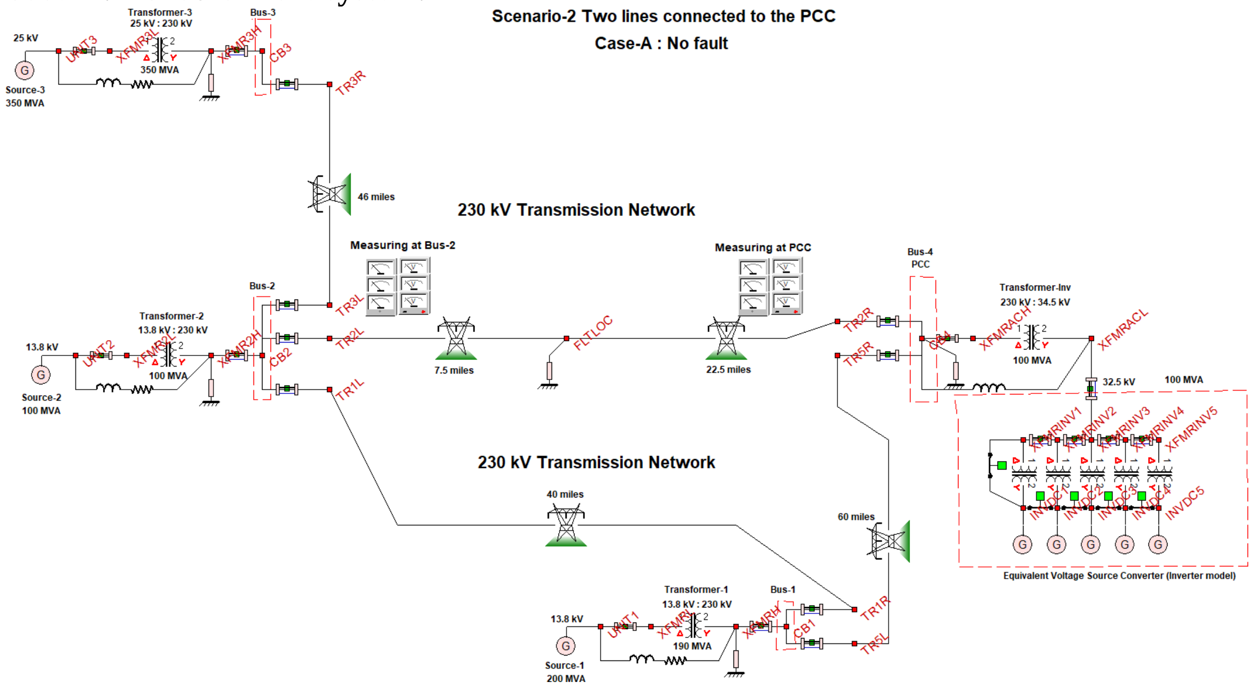

Figure 5.42 Scenario-2 Two Lines Connected to PCC With no Fault

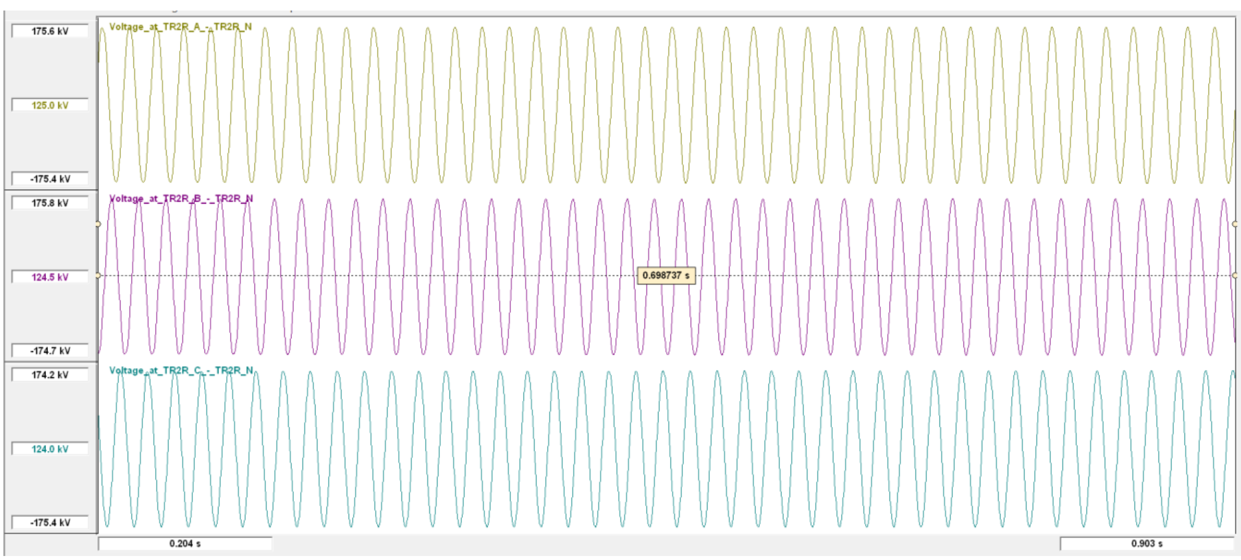

Figure 5.43 Voltage Waveforms at PCC for no fault in scenario-2

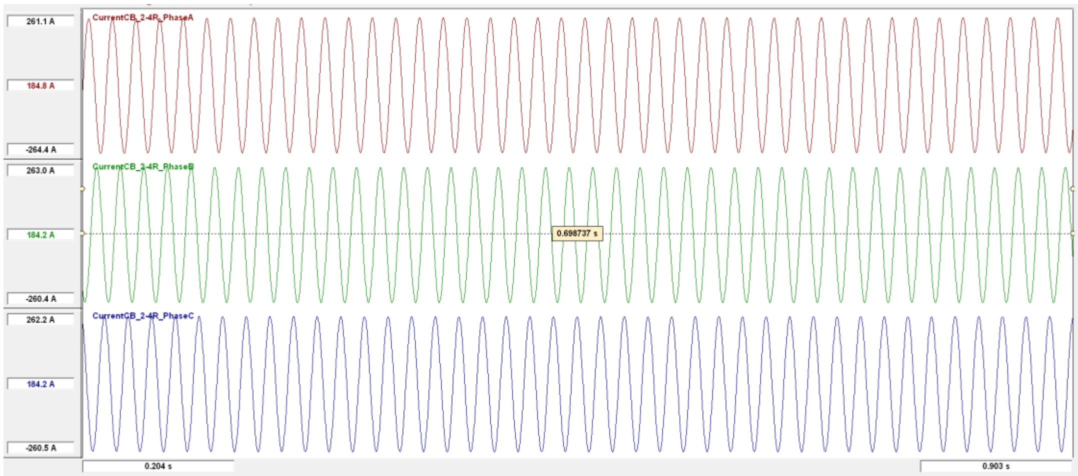

Figure 5.44 Current Waveforms at PCC for no fault in scenario-2

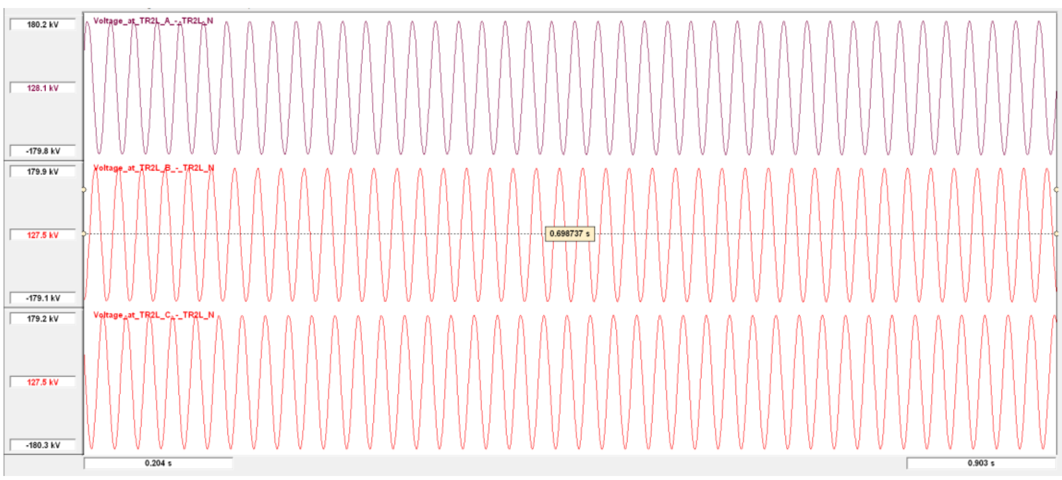

Figure 5.45 Voltage Waveforms at Bus-2 for no fault in scenario-2

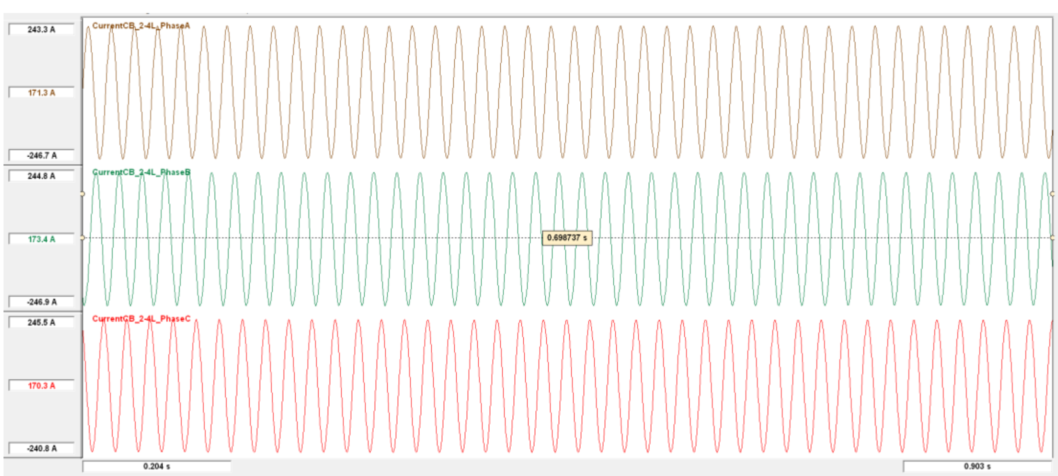

Figure 5.46 Current Waveforms at Bus-2 for no fault in scenario-2

The zone impedance characteristics is given by:

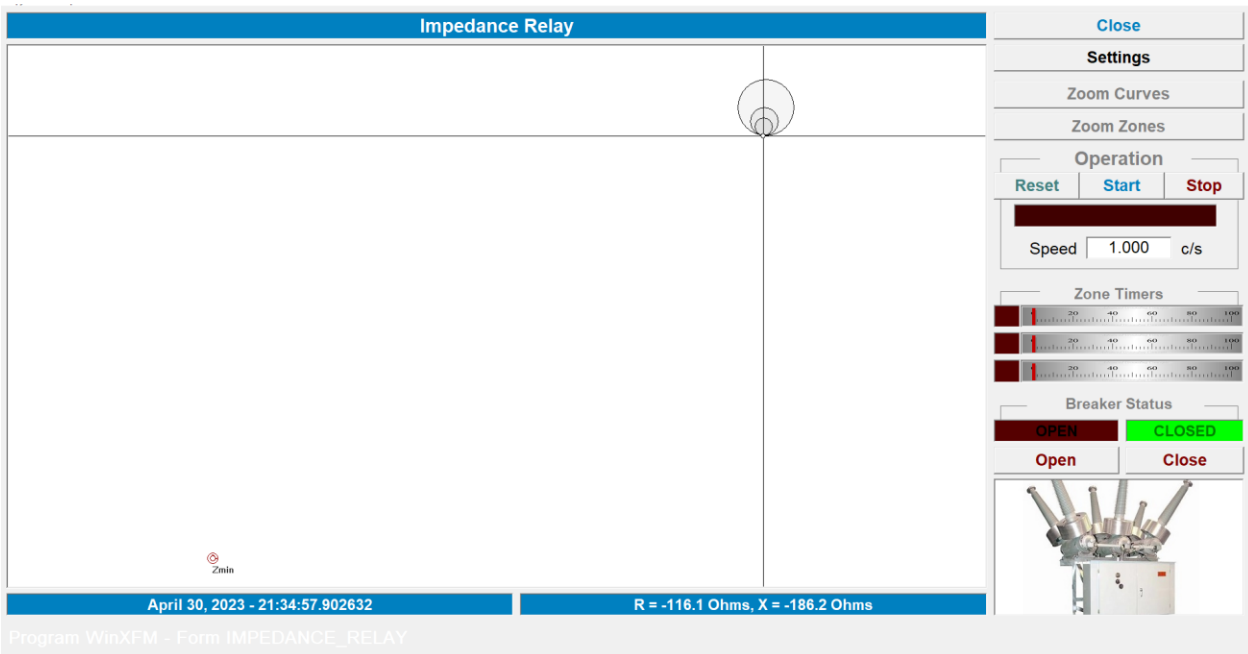

Figure 5.47 Zone impedance characteristics at PCC

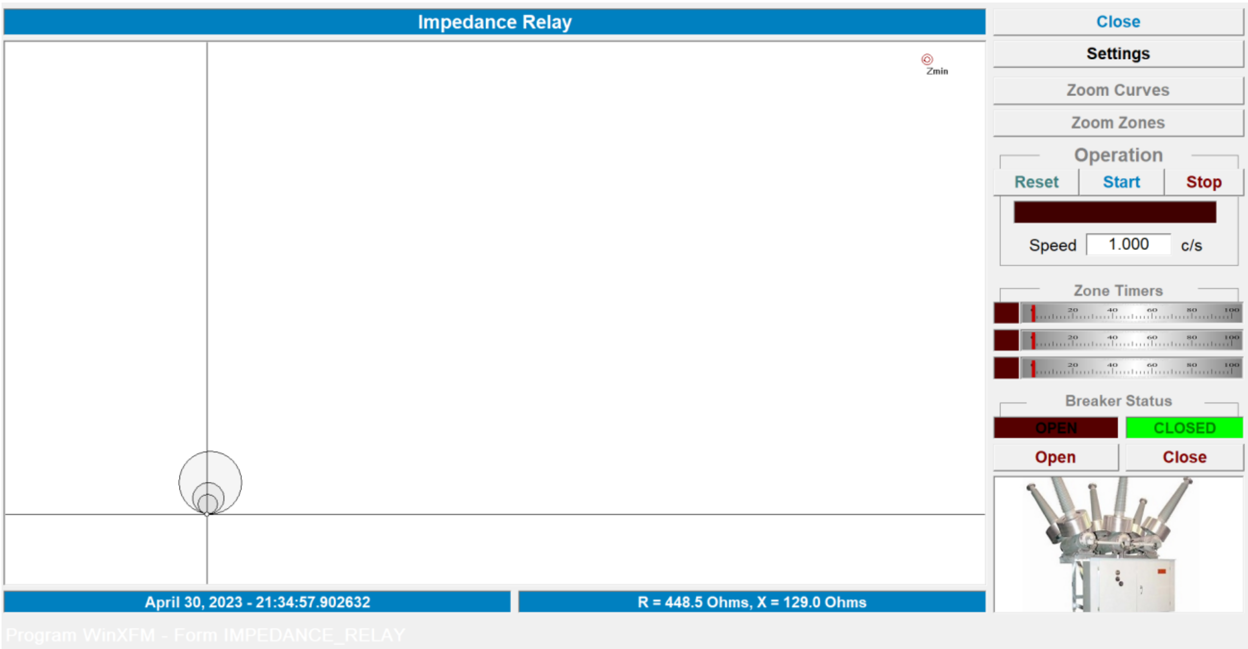

Figure 5.48 Zone impedance characteristics at Bus-2

Case-B: Fault happening on the 30-mile transmission line 22.5 miles (75%) from the PCC.

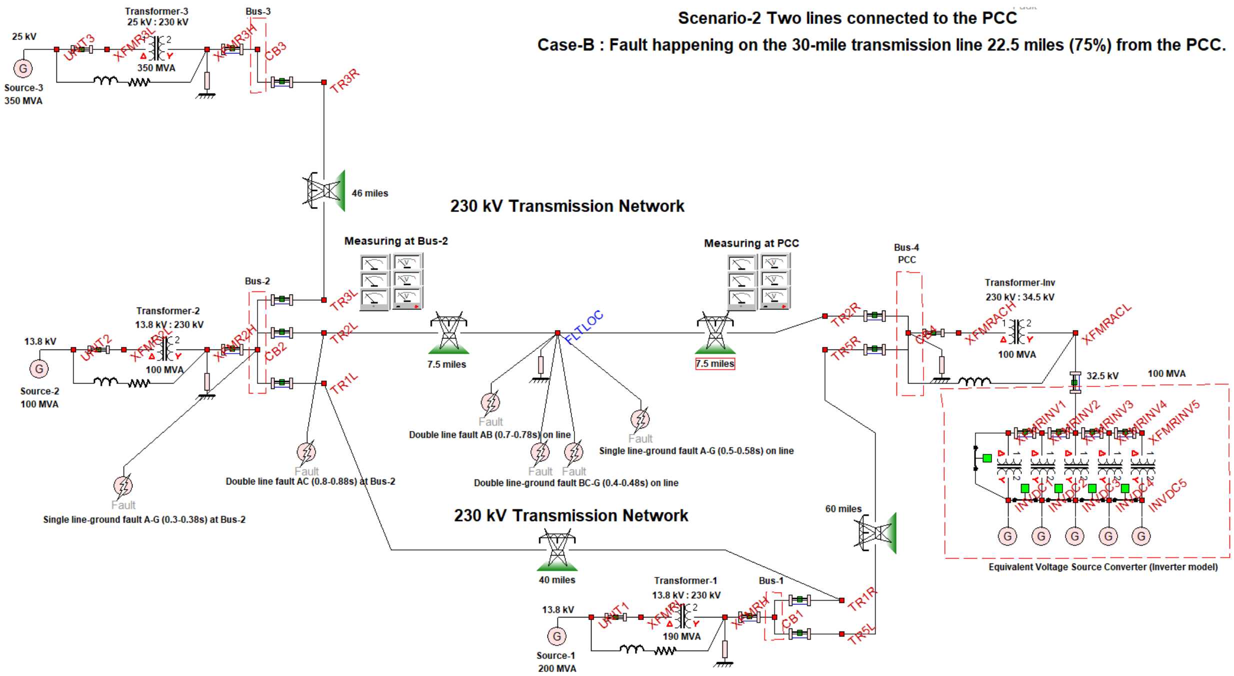

Figure 5.49 Scenario-2 case-B Fault on Two Lines Connected to PCC at 22.5 miles from PCC

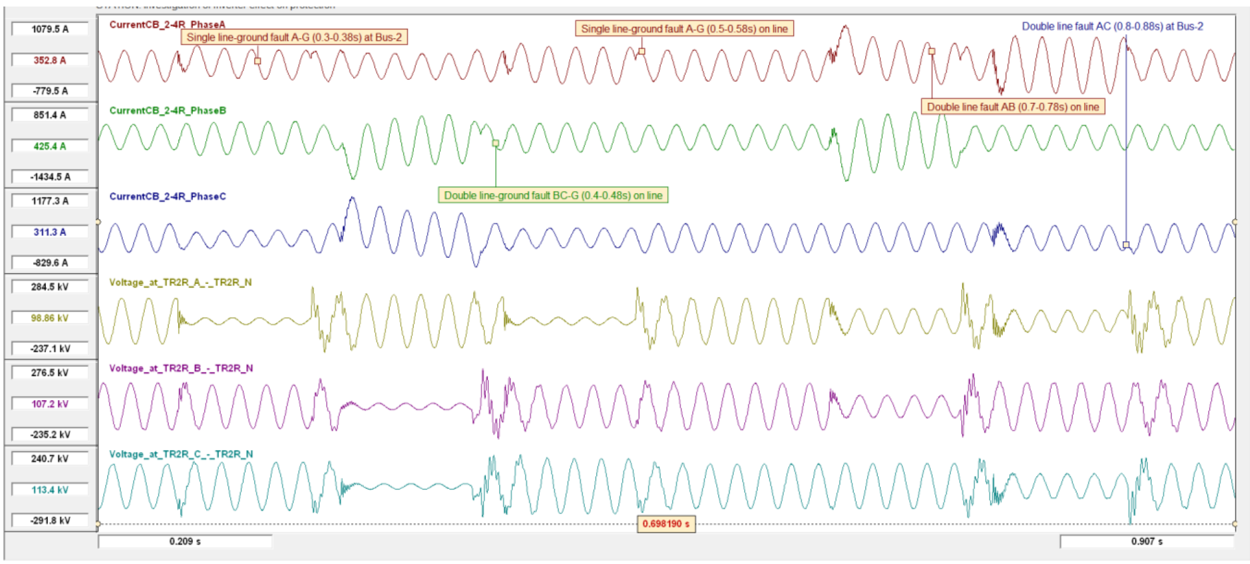

Figure 5.50 Current and Voltage Waveforms at PCC for scenario-2 case-B

The relay characteristics are given:

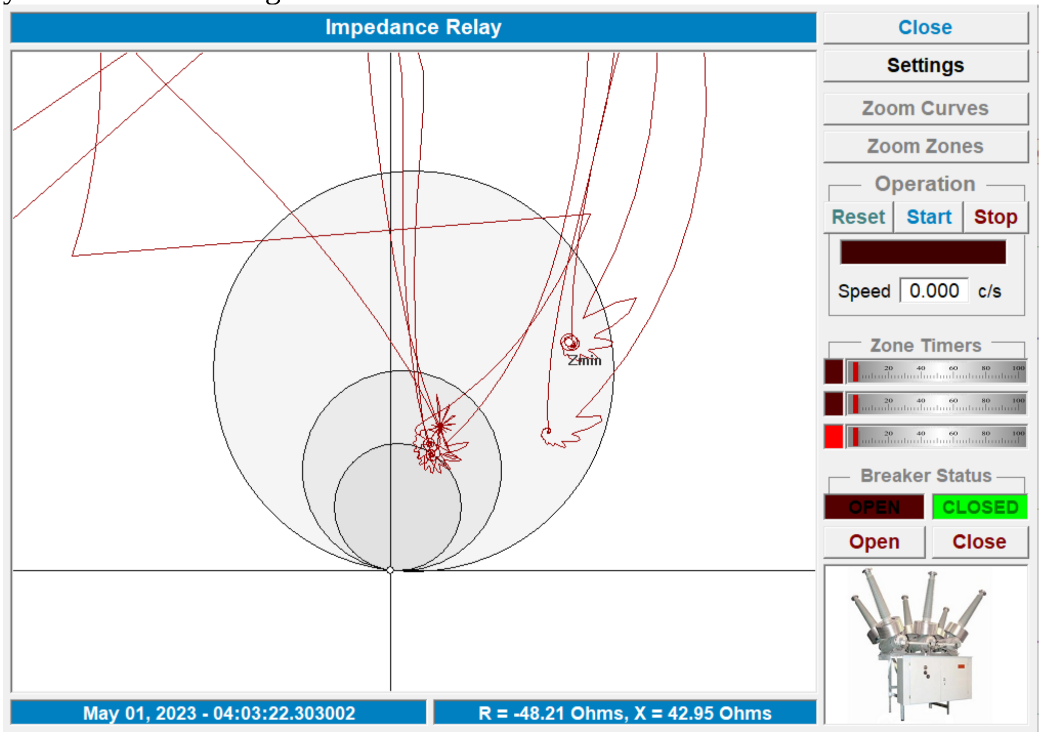

Figure 5.51 Zone impedance characteristics at PCC for A-G fault at Bus-2

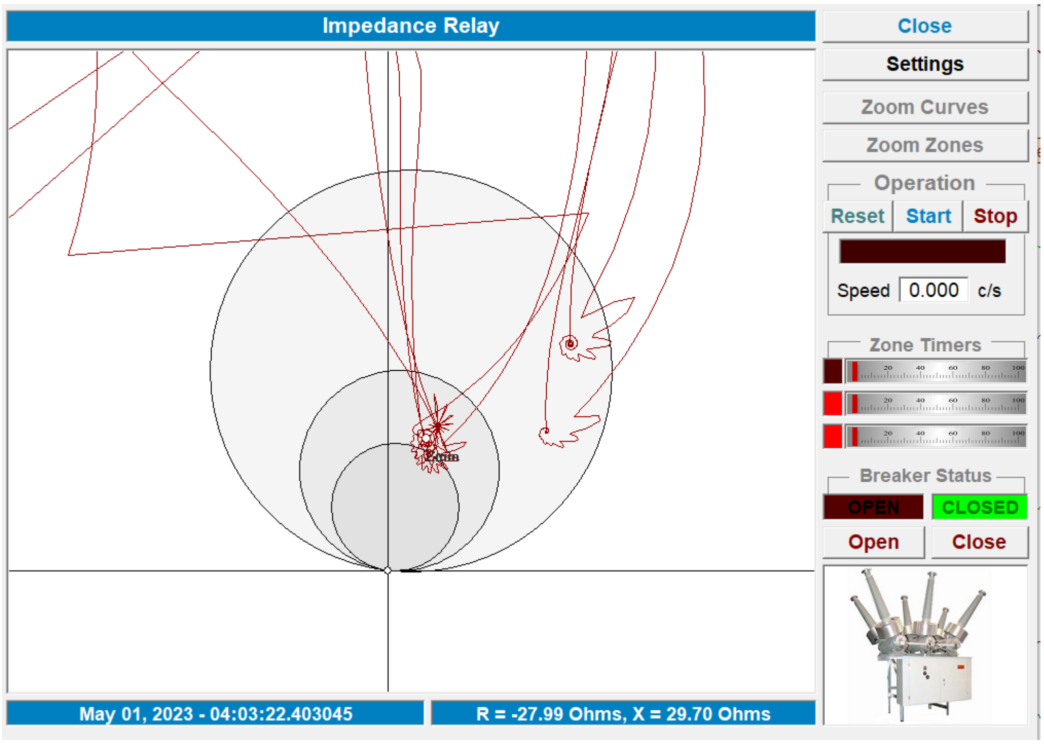

Figure 5.52 Zone impedance characteristics at PCC for BC-G fault on the line

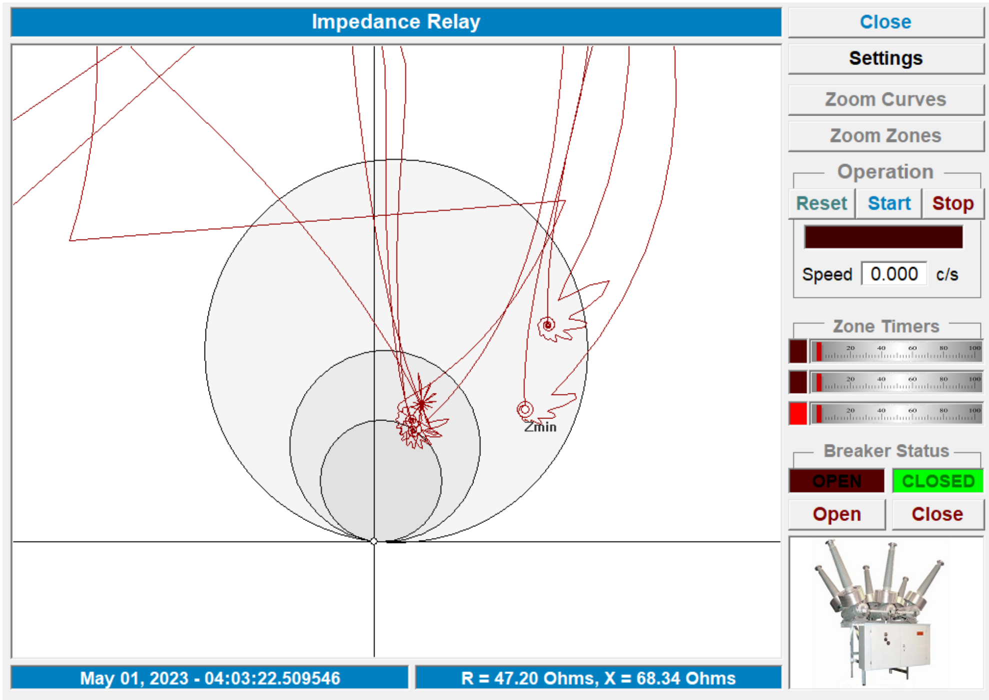

Figure 5.53 Zone impedance characteristics at PCC for A-G fault on the line

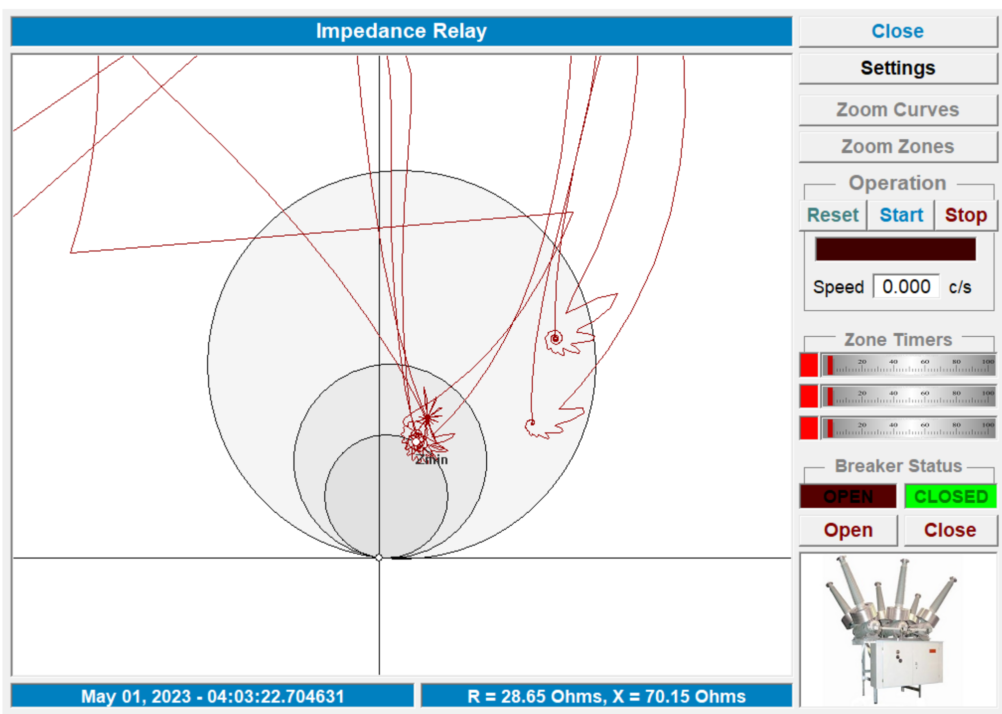

Figure 5.54 Zone impedance characteristics at PCC for AB fault on the line

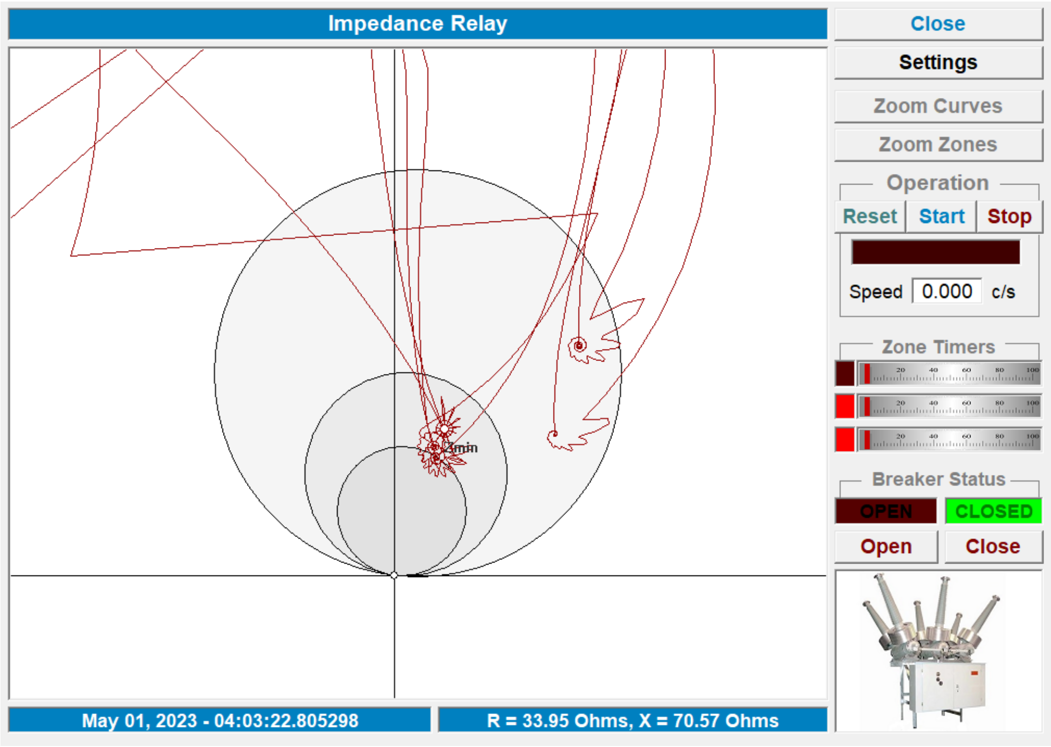

Figure 5.55 Zone impedance characteristics at PCC for AC fault on Bus-2

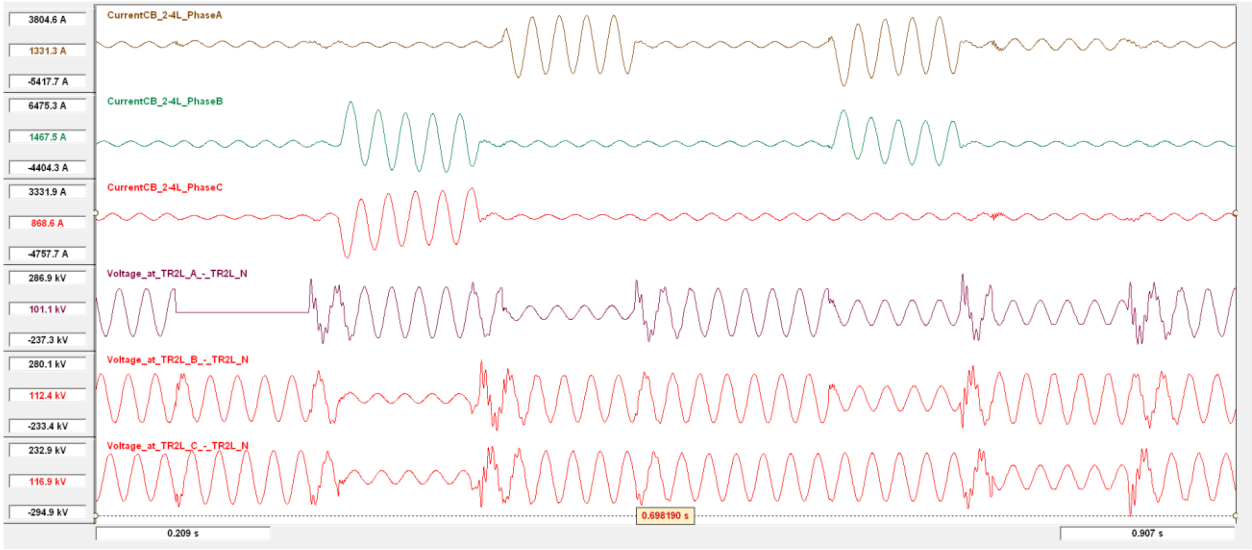

Figure 5.56 Current and Voltage Waveforms at Bus-2 for scenario-2 case-B

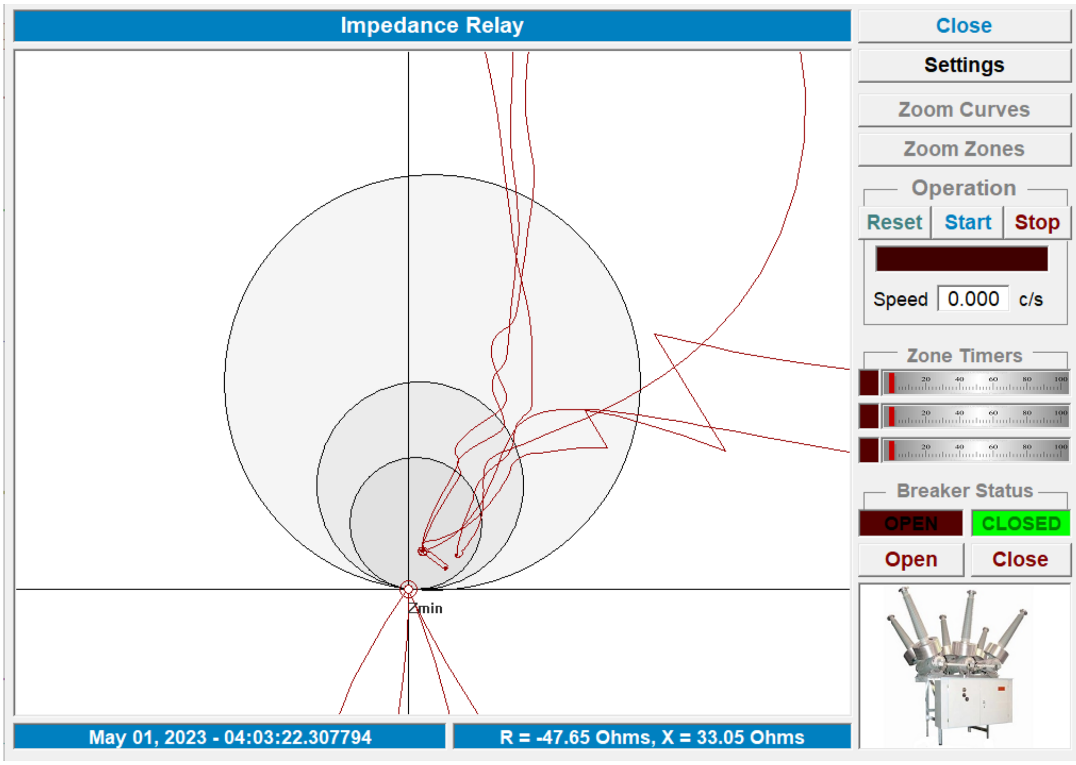

Figure 5.57 Zone impedance characteristiscs at Bus-2 for A-G fault on Bus-2

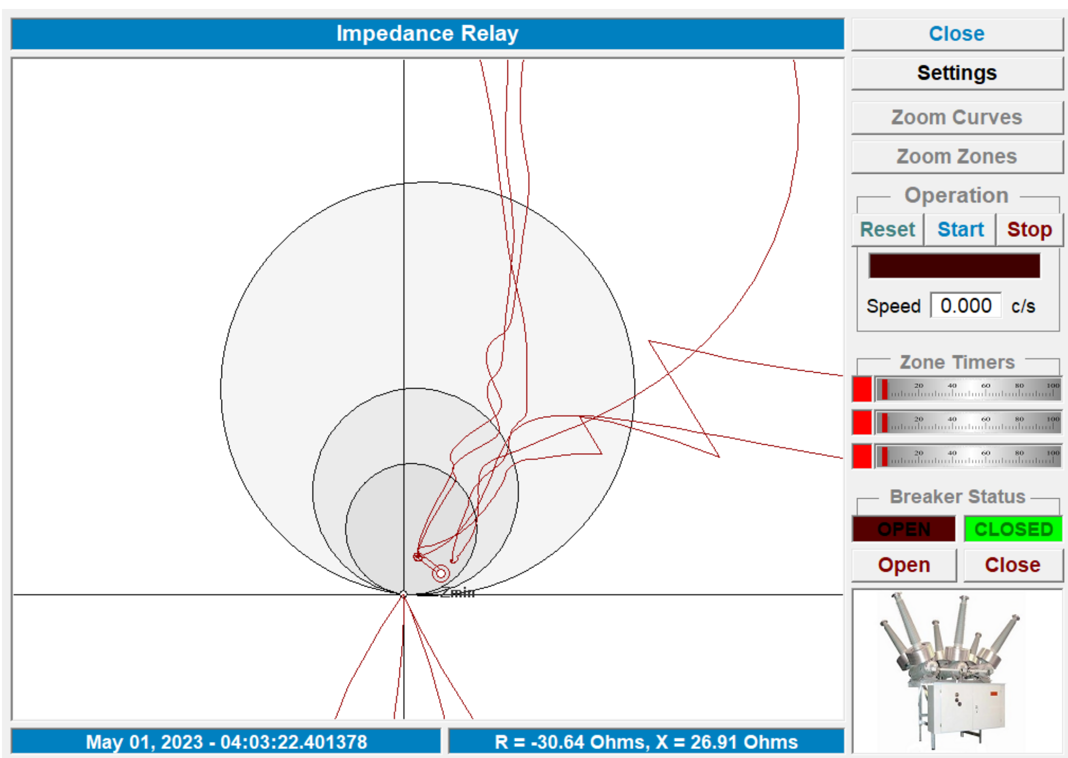

Figure 5.58 Zone impedance characteristics at Bus-2 for BC-G fault on line

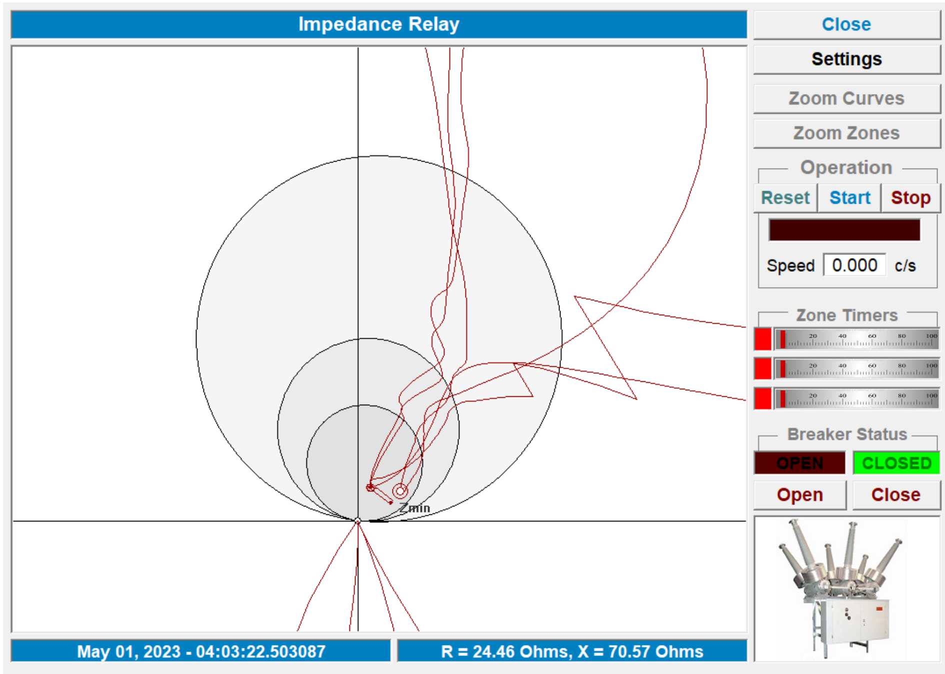

Figure 5.59 Zone impedance characteristics at Bus-2 for A-G fault on line

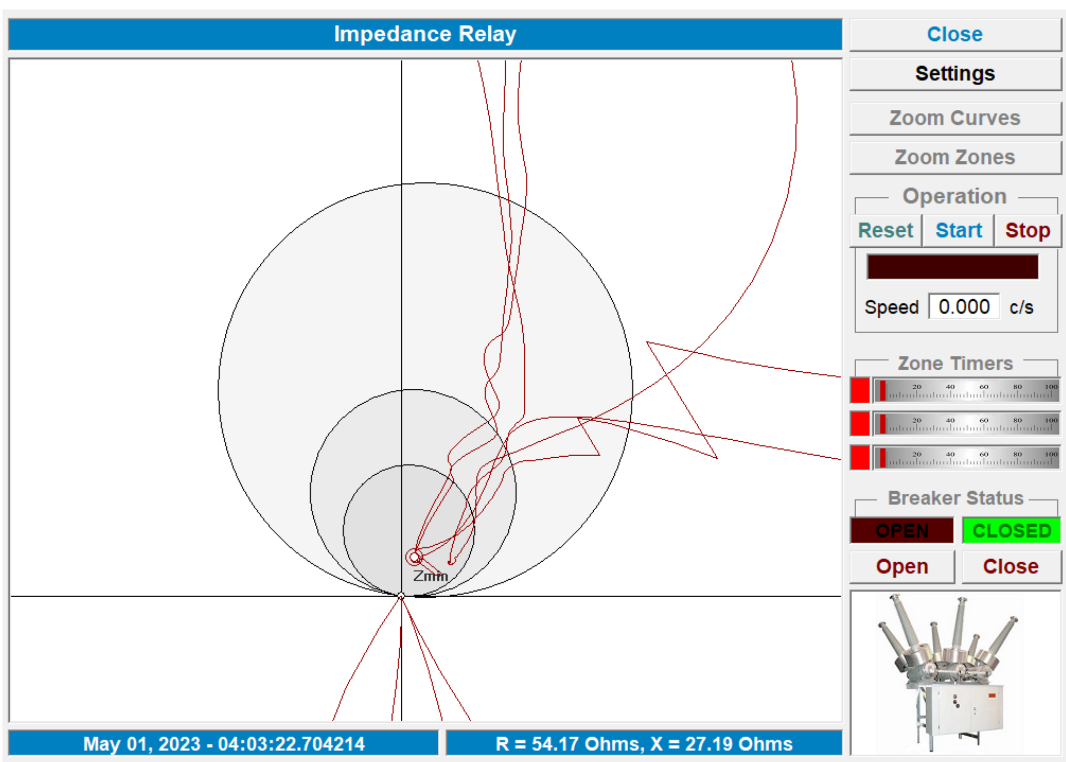

Figure 5.60 Zone impedance characteristics at Bus-2 for AB fault on line

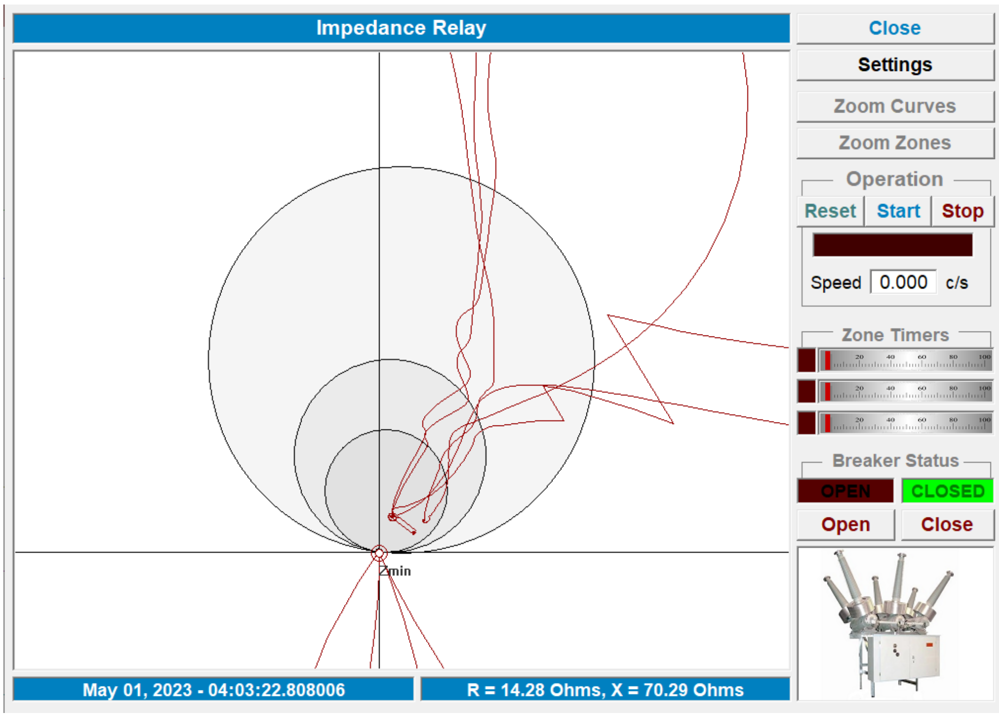

Figure 5.61 Zone impedance characteristics at Bus-2 for AC fault at Bus-2

Case-C: Fault happening on the 30-mile transmission line 15 miles (50%) from the PCC.

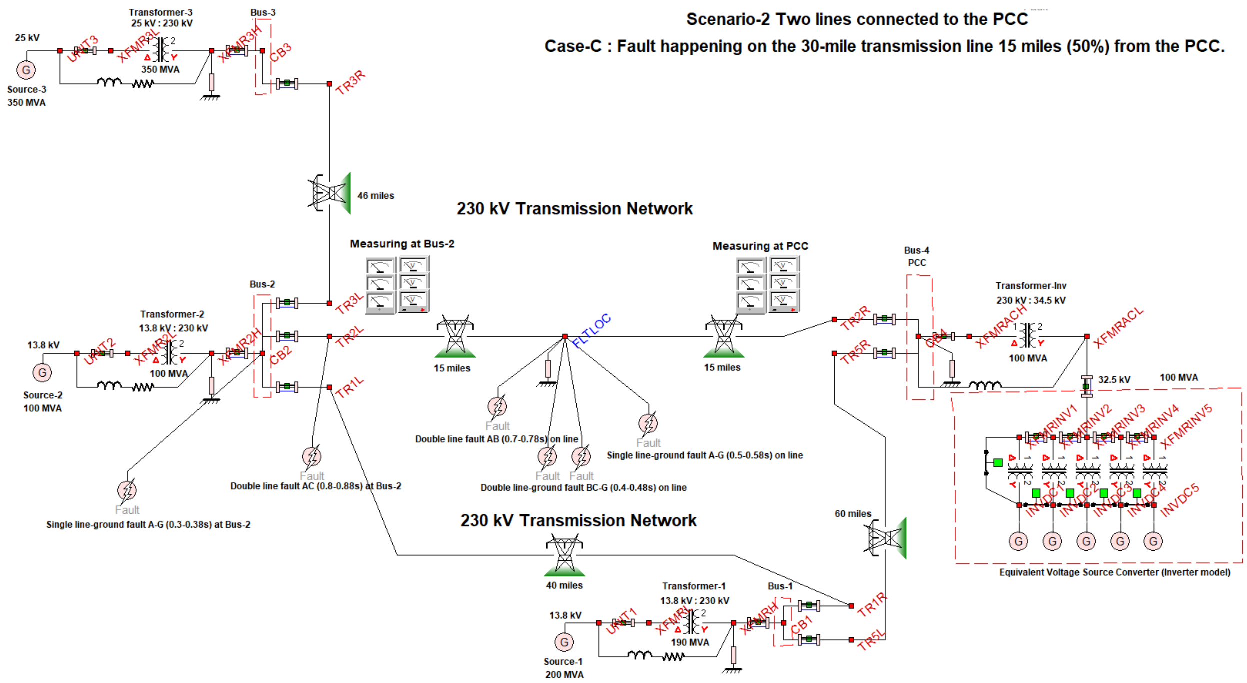

Figure 5.62 Scenario-2 Case-C Fault on Two Lines Connected to PCC at 22.5 miles from PCC

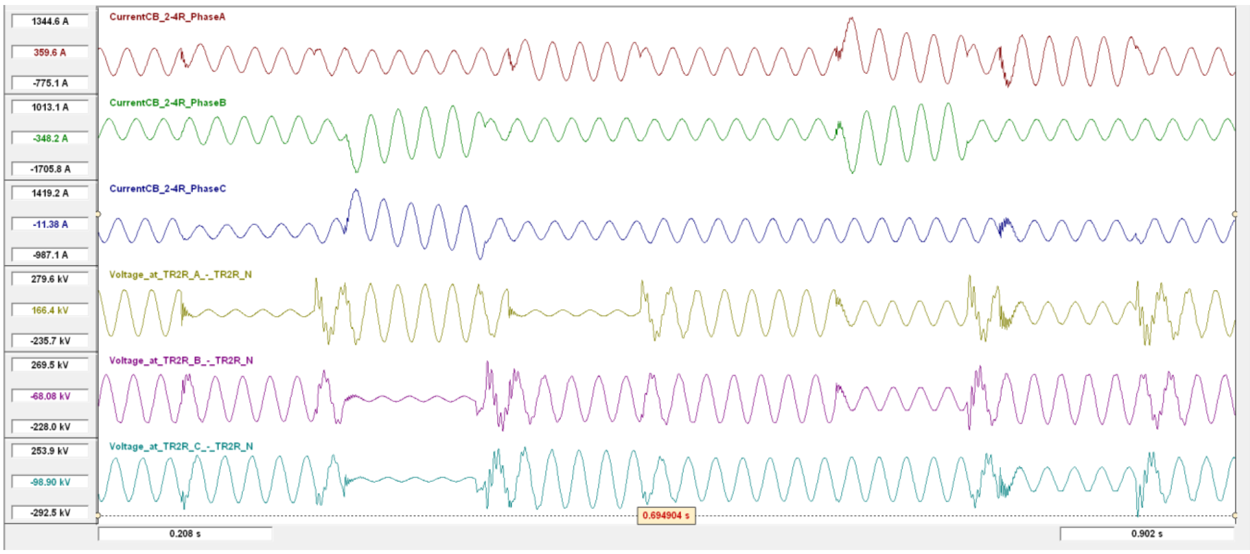

Figure 5.63 Current and Voltage Waveforms at PCC for scenario-2 case-C

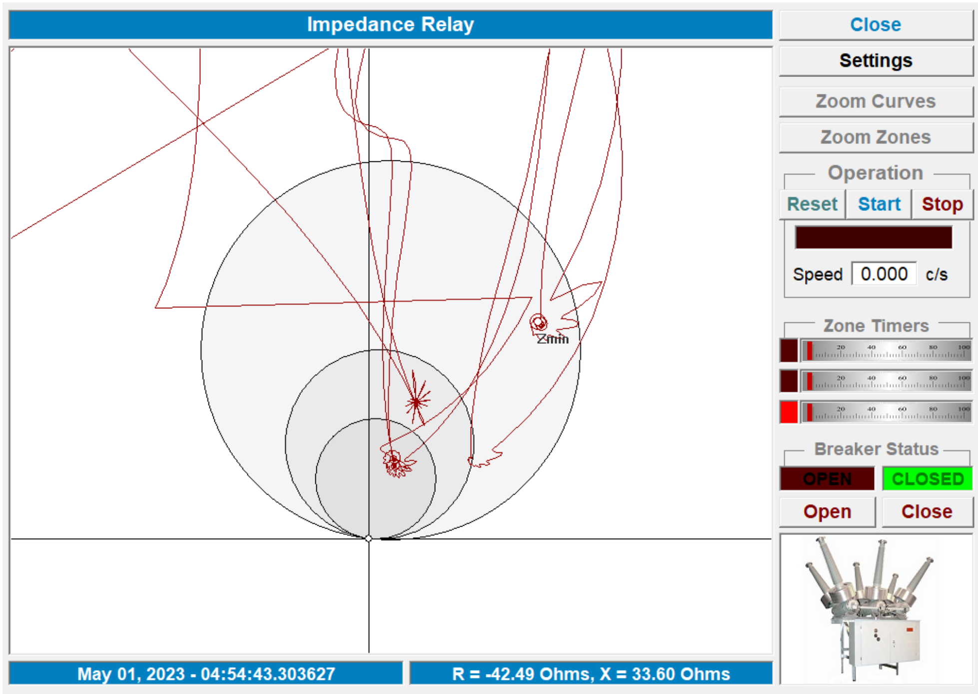

Figure 5.64 Zone impedance characteristics at PCC for A-G fault at Bus-2

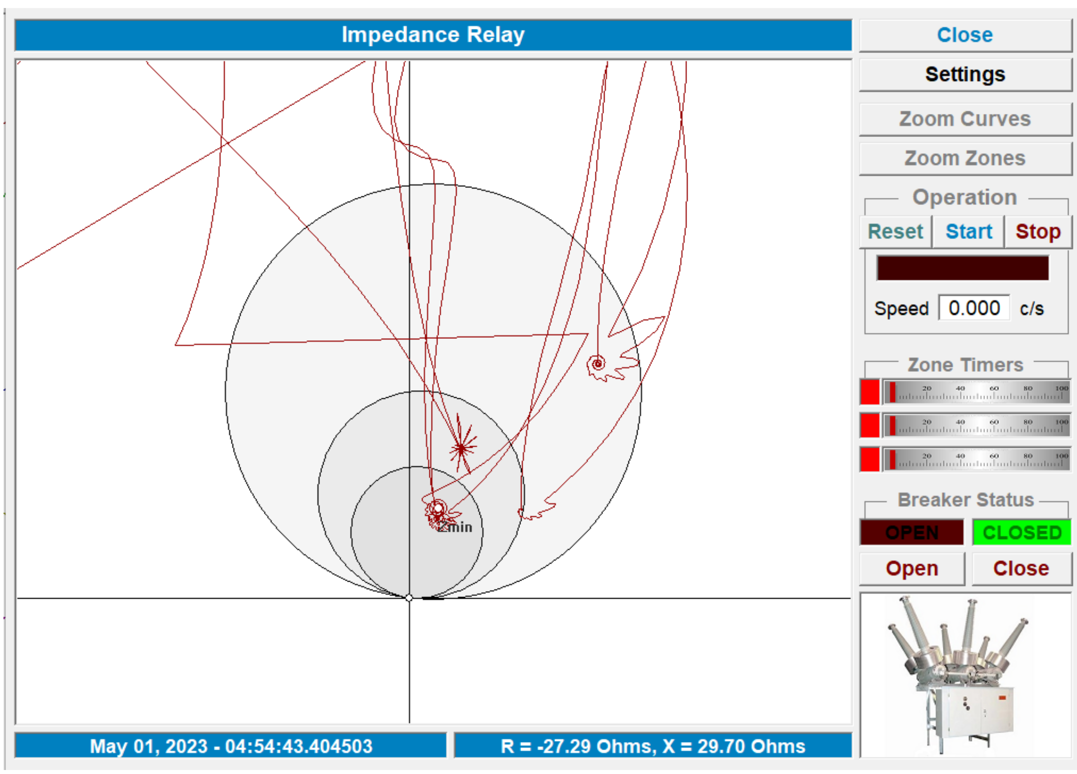

Figure 5.65 Zone impedance characteristics at PCC for BC-G fault on the line

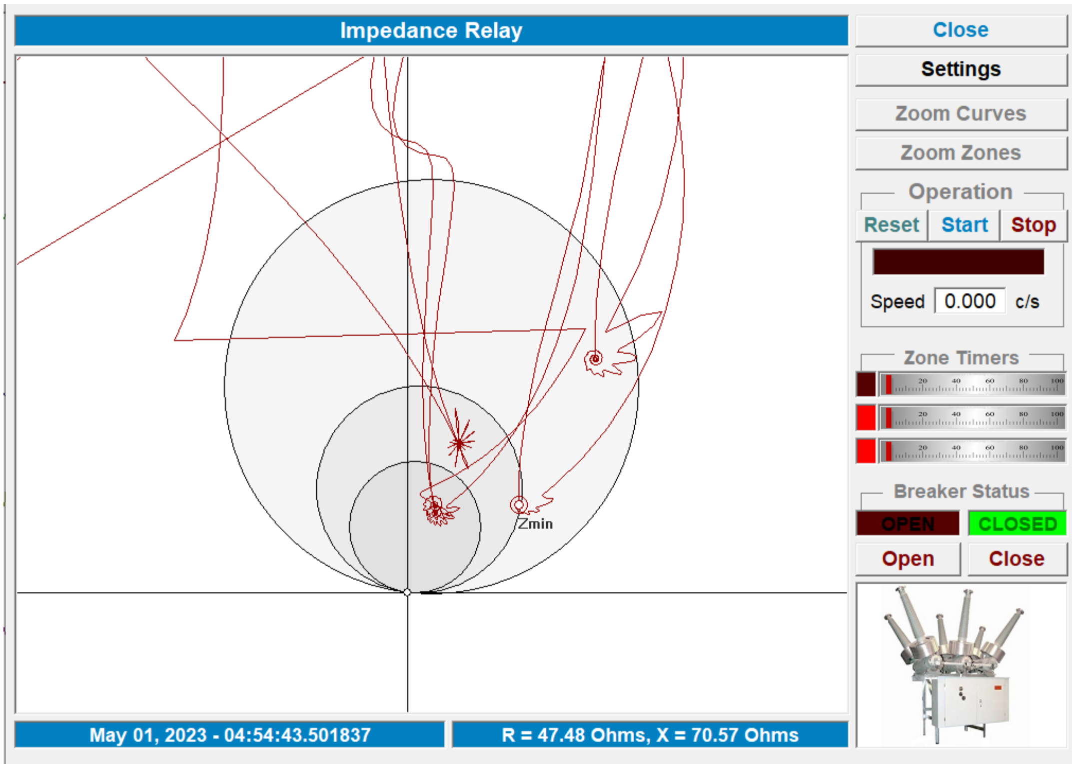

Figure 5.66 Zone impedance characteristics at PCC for A-G fault on line

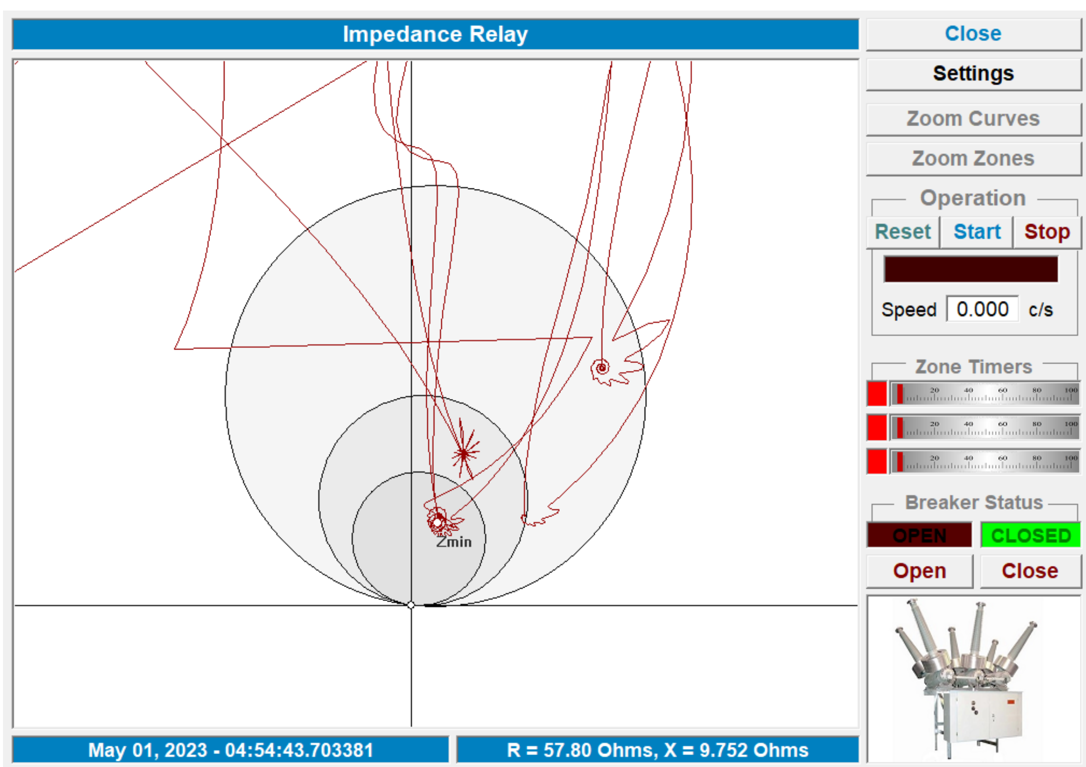

Figure 5.67 Zone impedance characteristics at PCC for AB fault on the line

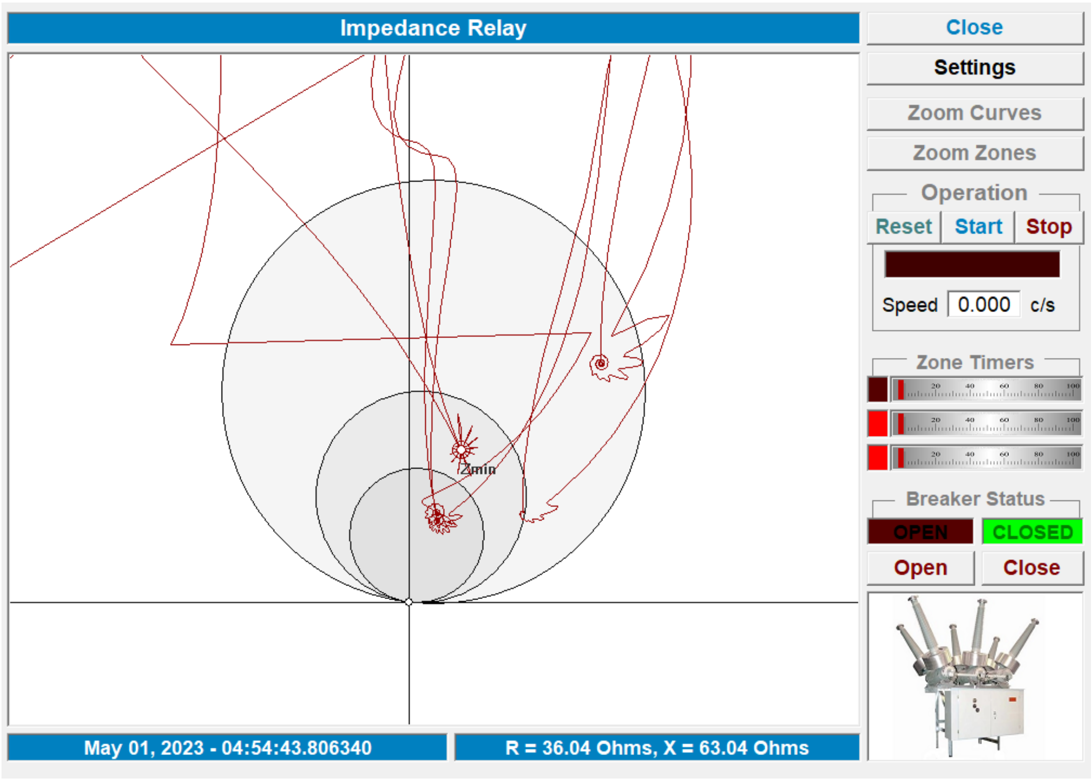

Figure 5.68 Zone impedance characteristics at PCC for AC fault at Bus-2

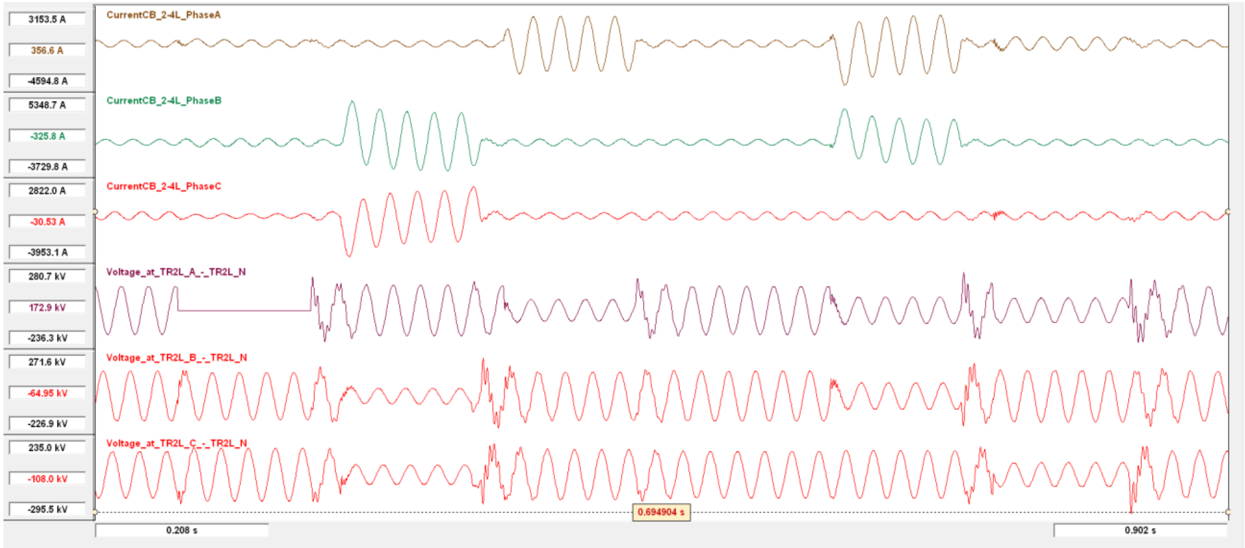

Figure 5.69 Current and Voltage Waveforms at Bus-2 for scenario-2 case-C

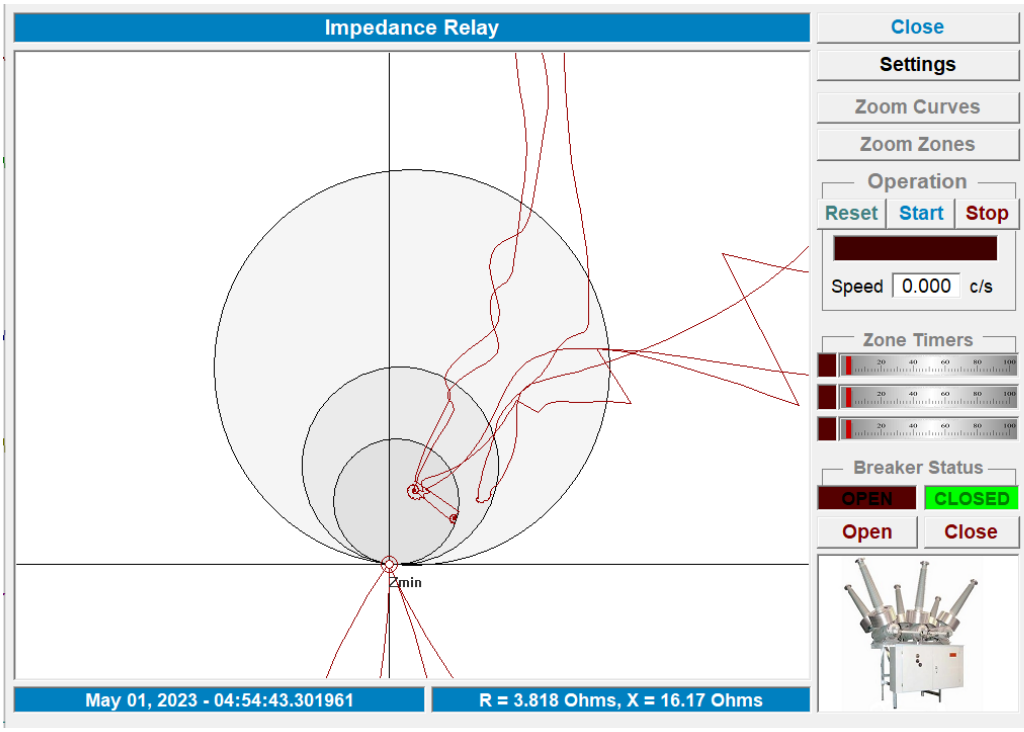

Figure 5.70 Zone impedance characteristics at Bus-2 for A-G fault at Bus-2

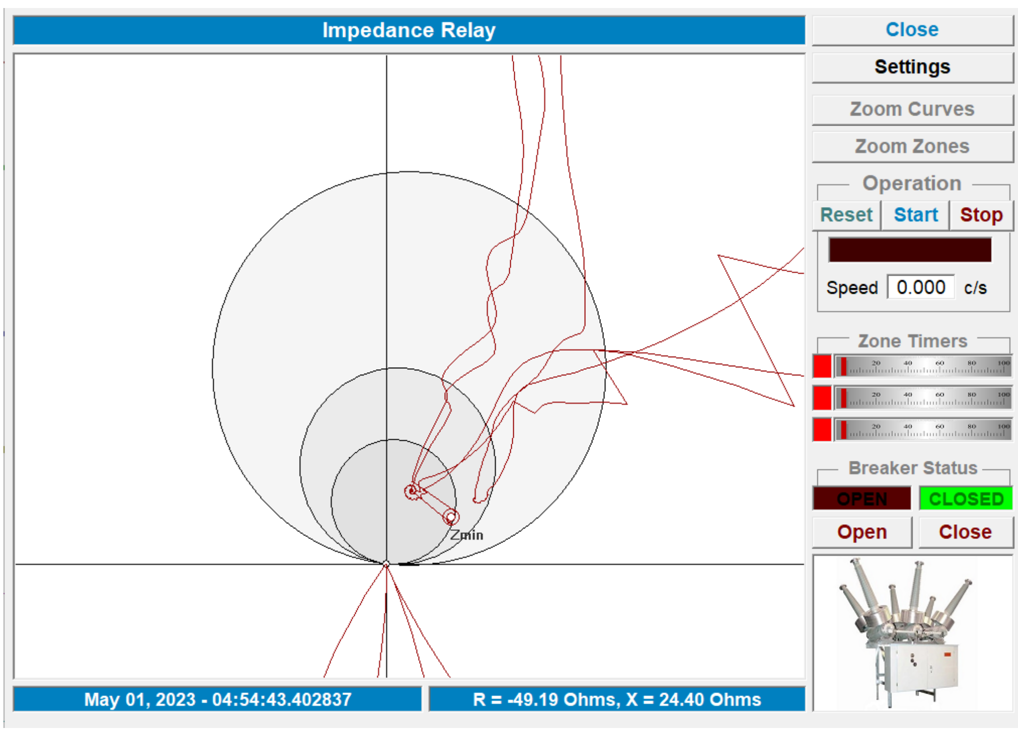

Figure 5.71 Zone impedance characteristics at Bus-2 for BC-G fault on line

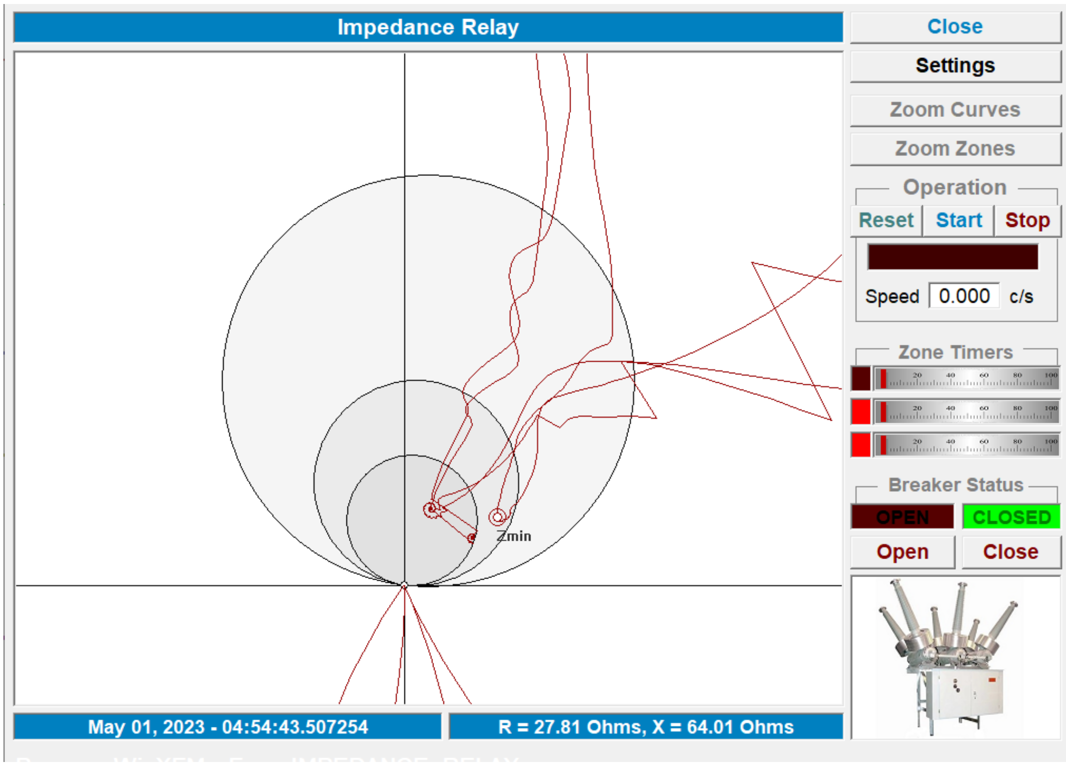

Figure 5.72 Zone impedance characteristics at Bus-2 for A-G fault on line

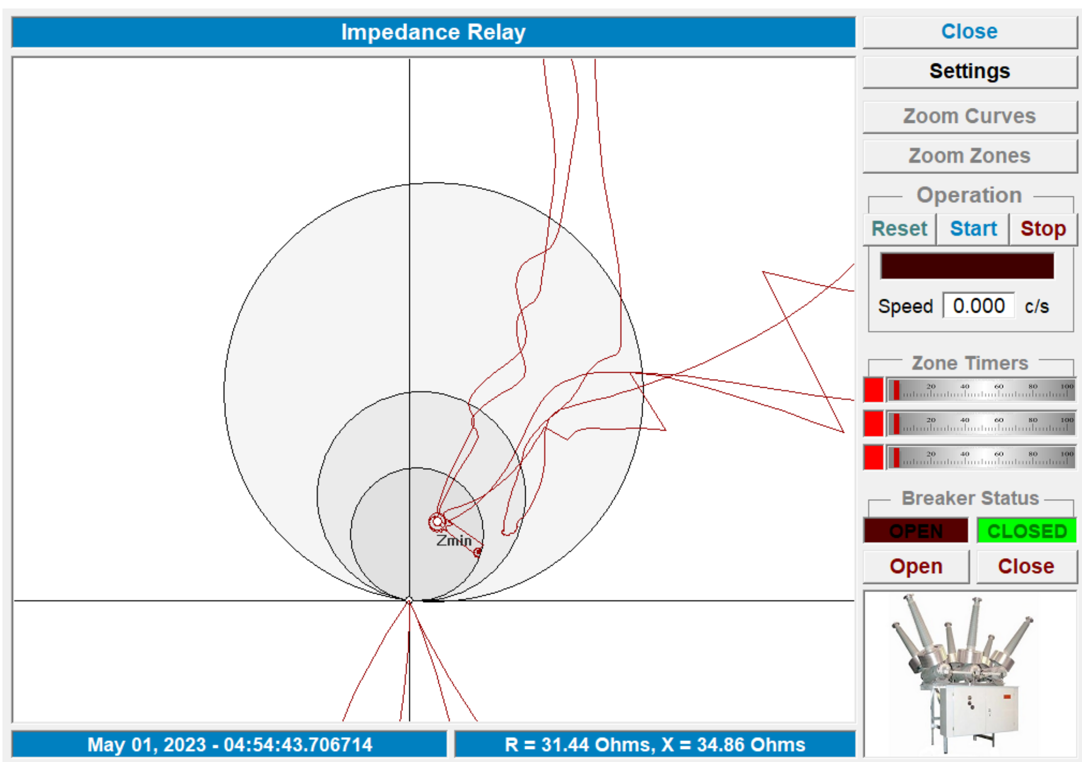

Figure 5.73 Zone impedance characteristics at Bus-2 for AB fault on line

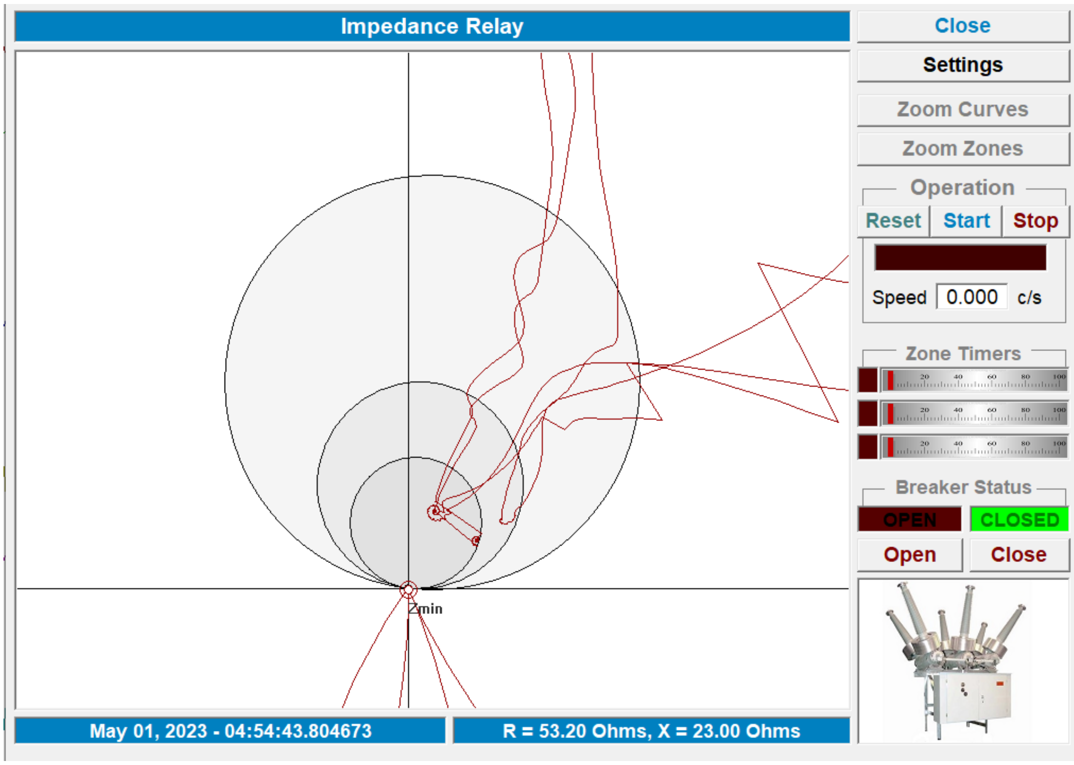

Figure 5.74 Zone impedance characteristics at Bus-2 for AC fault at Bus-2

5.4 Scenario 3: Contingency 3: One Line Connected, Two Lines Disconnected

This scenario is characterized with the outage of two transmission lines.
Case-A: No fault in the system.

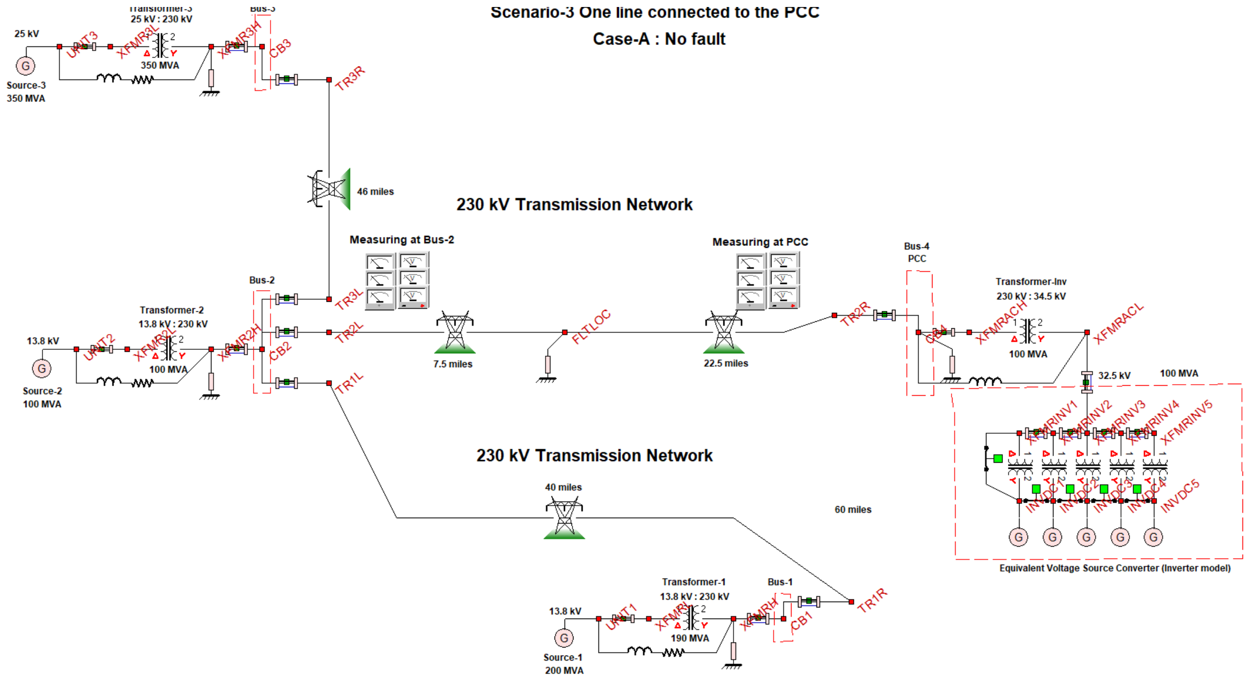

Figure 5.75 Scenario-3 One Line Connected to PCC With no Fault

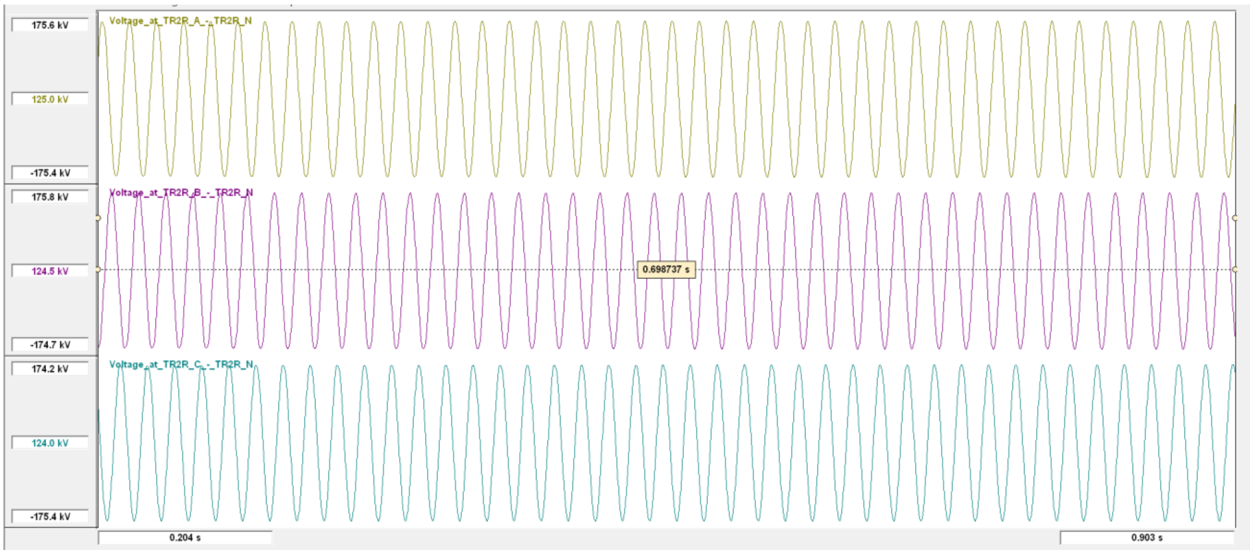

Figure 5.76 Voltage Waveforms at PCC for no fault in scenario-3

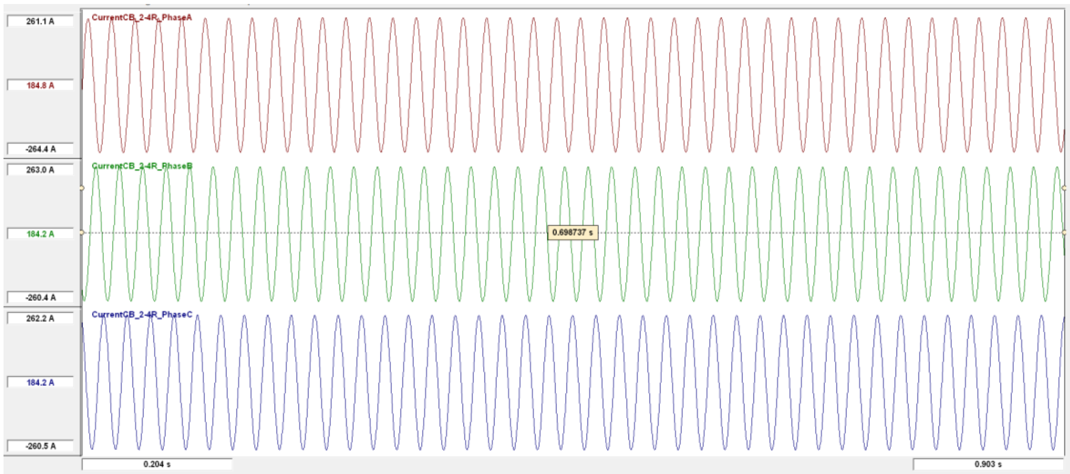

Figure 5.77 Current Waveforms at PCC for no fault in scenario-3

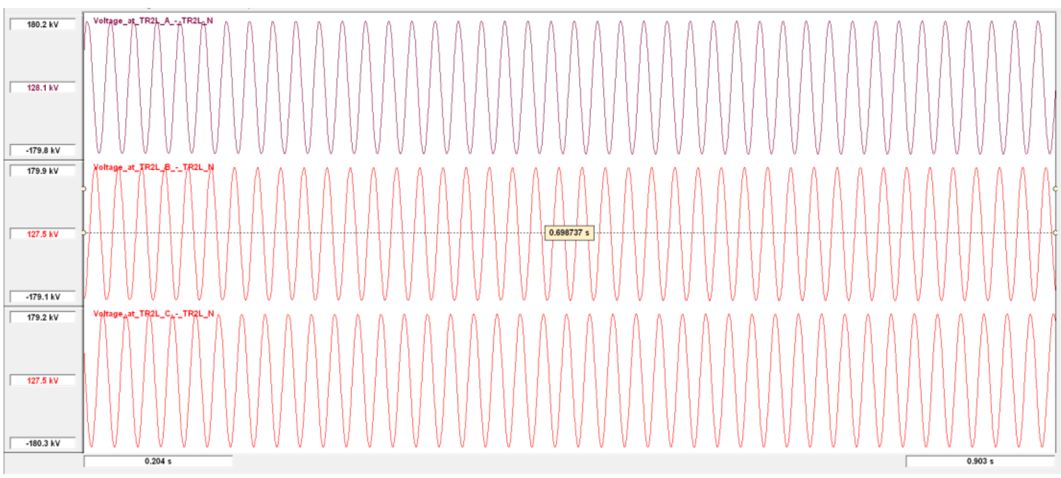

Figure 5.78 Voltage Waveforms at Bus-2 for no fault in scenario-3

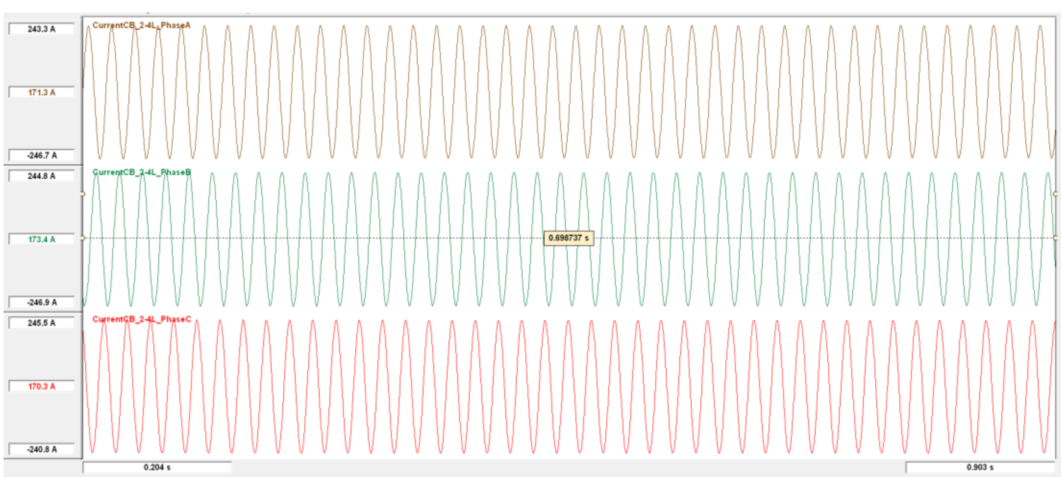

Figure 5.79 Current Waveforms at Bus-2 for no fault in scenario-3

The zone impedance characteristics is given by:

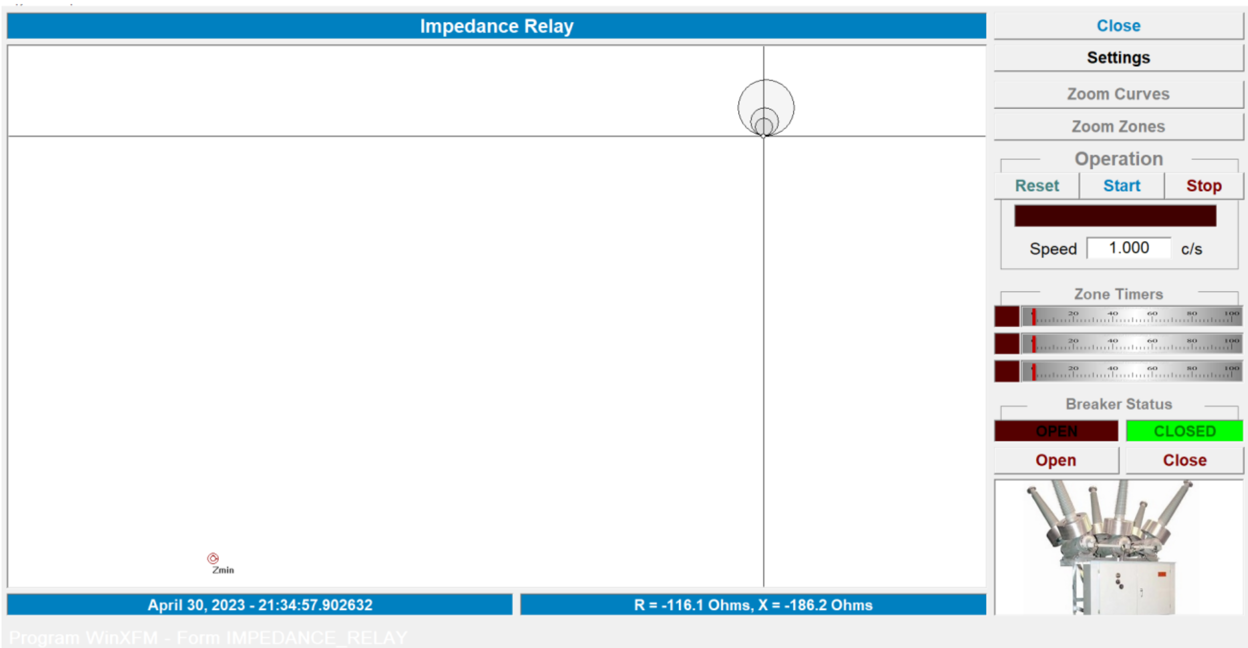

Figure 5.80 Zone impedance characteristics at PCC

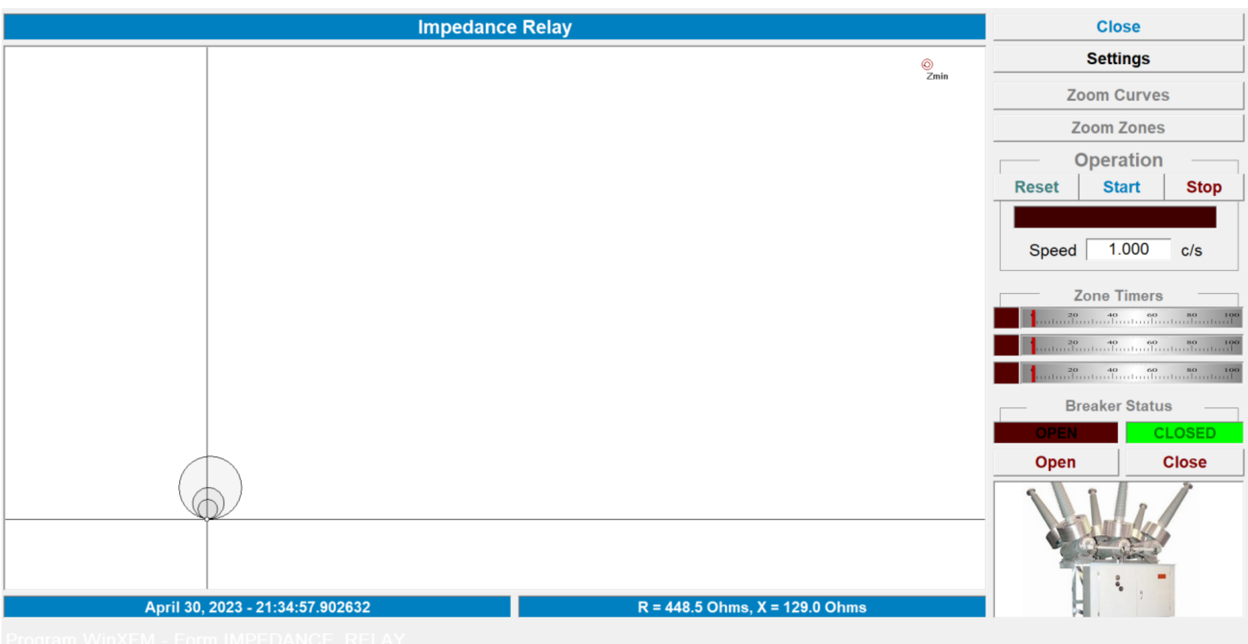

Figure 5.81 Zone impedance characteristics at Bus-2

Case-B: Fault happening on the 30-mile transmission line 22.5 miles (75%) from the PCC.

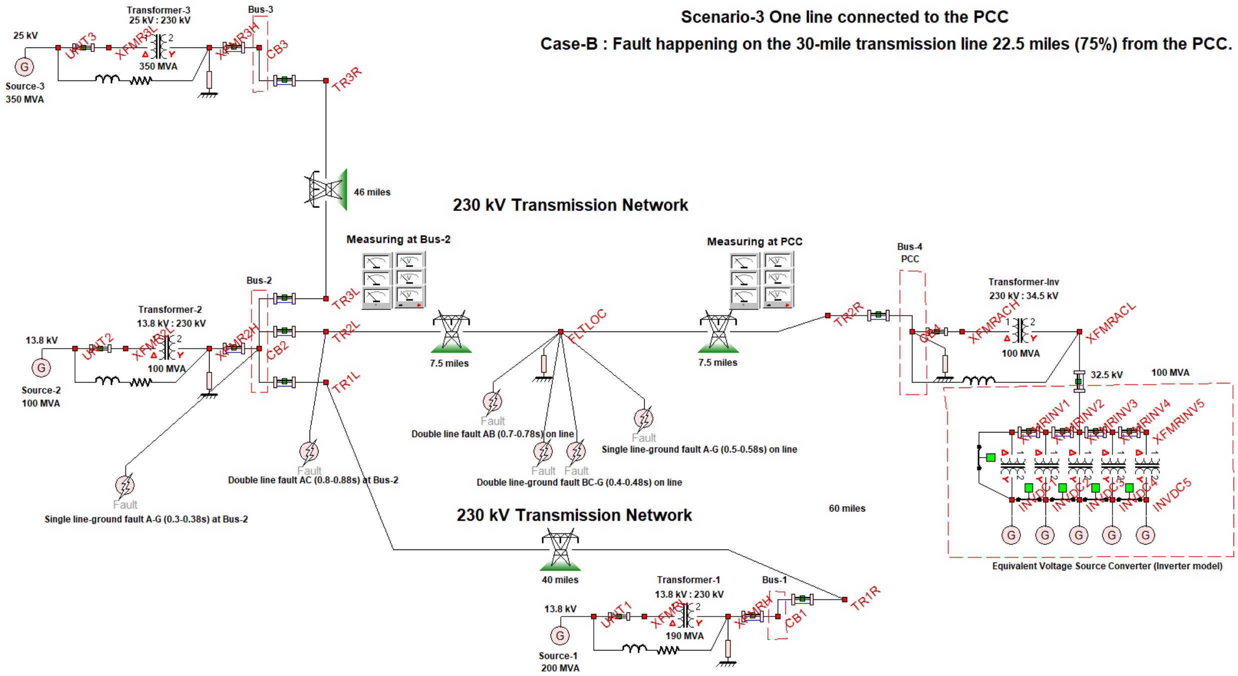

Figure 5.82 Scenario-3 case-B Fault on One Line Connected to PCC at 22.5 miles from PCC

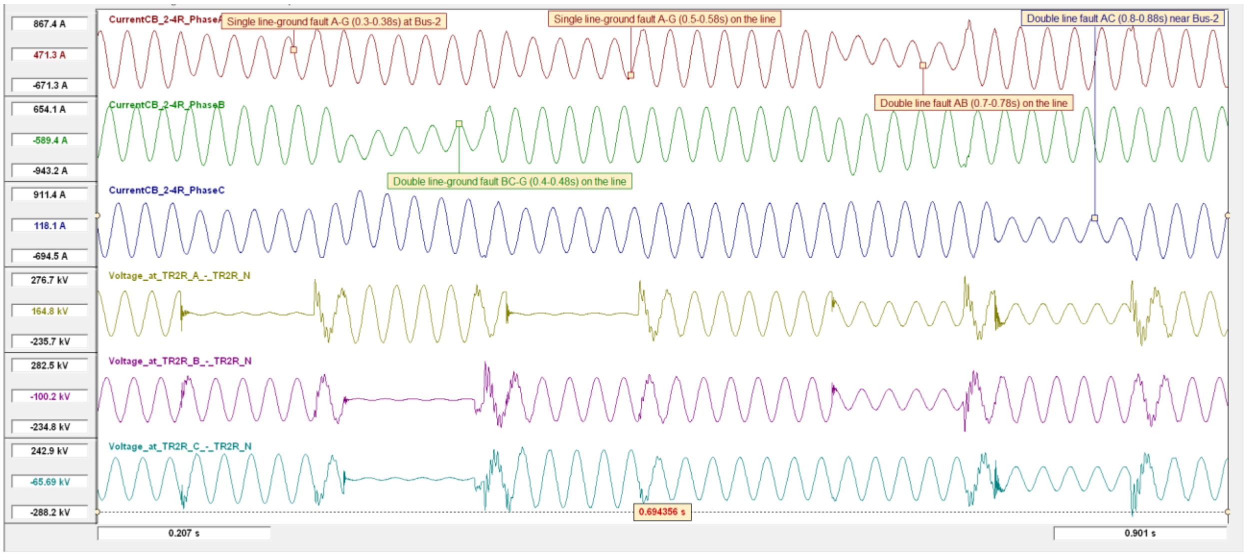

Figure 5.83 Current and Voltage Waveforms at PCC for scenario-3 case-B

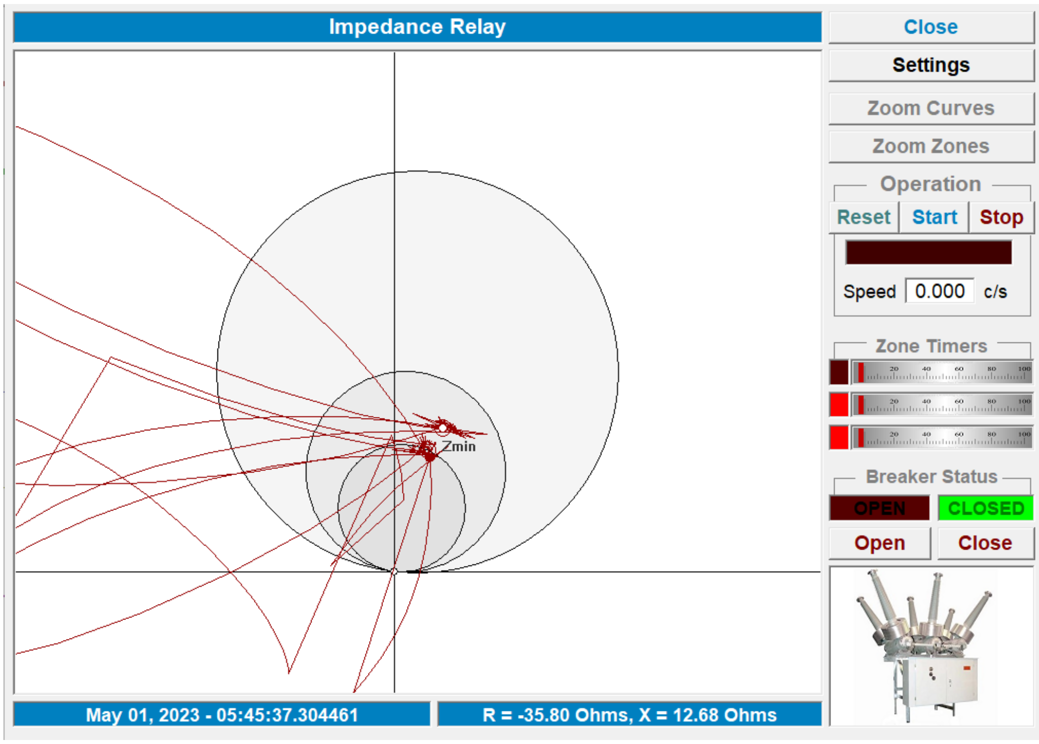

Figure 5.84 Zone impedance characteristics at PCC for A-G fault at Bus-2

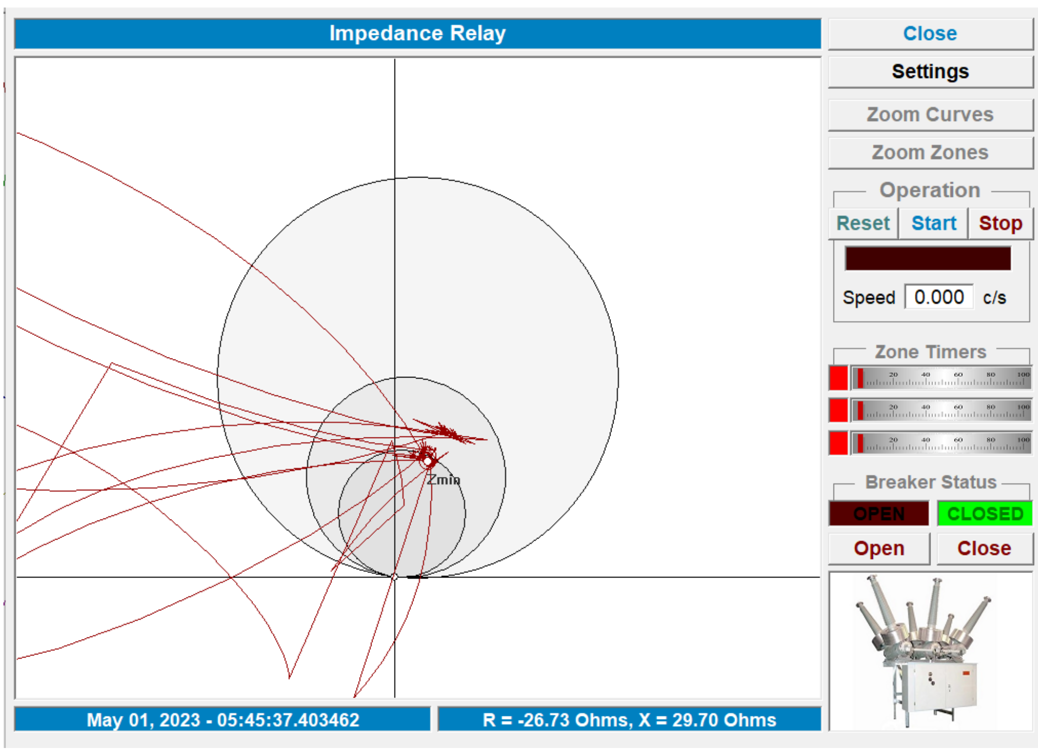

Figure 5.85 Zone impedance characteristics at PCC for BC-G fault on the line

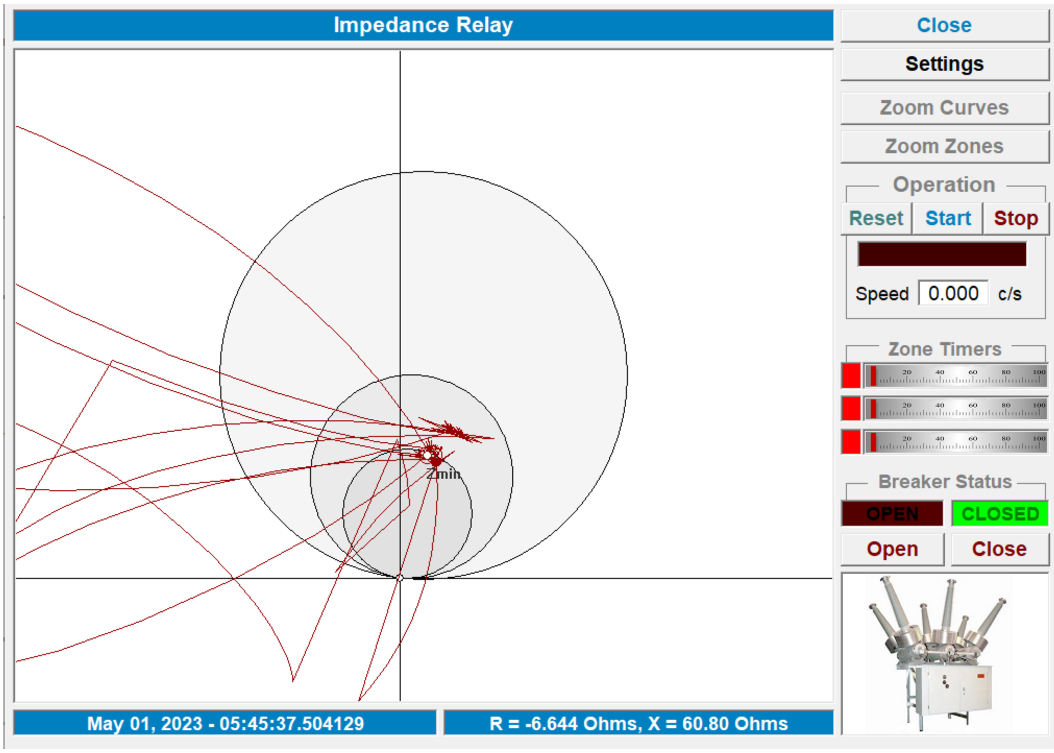

Figure 5.86 Zone impedance characteristics at PCC for A-G fault on the line

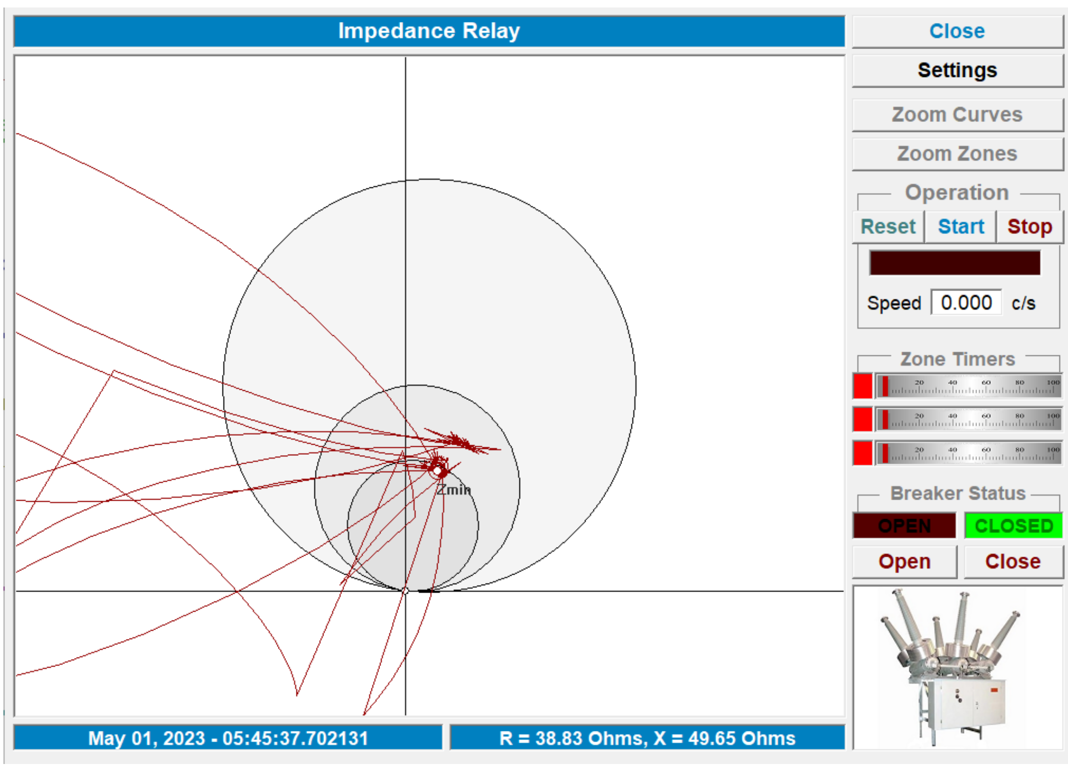

Figure 5.87 Zone impedance characteristics at PCC for AB fault on the line

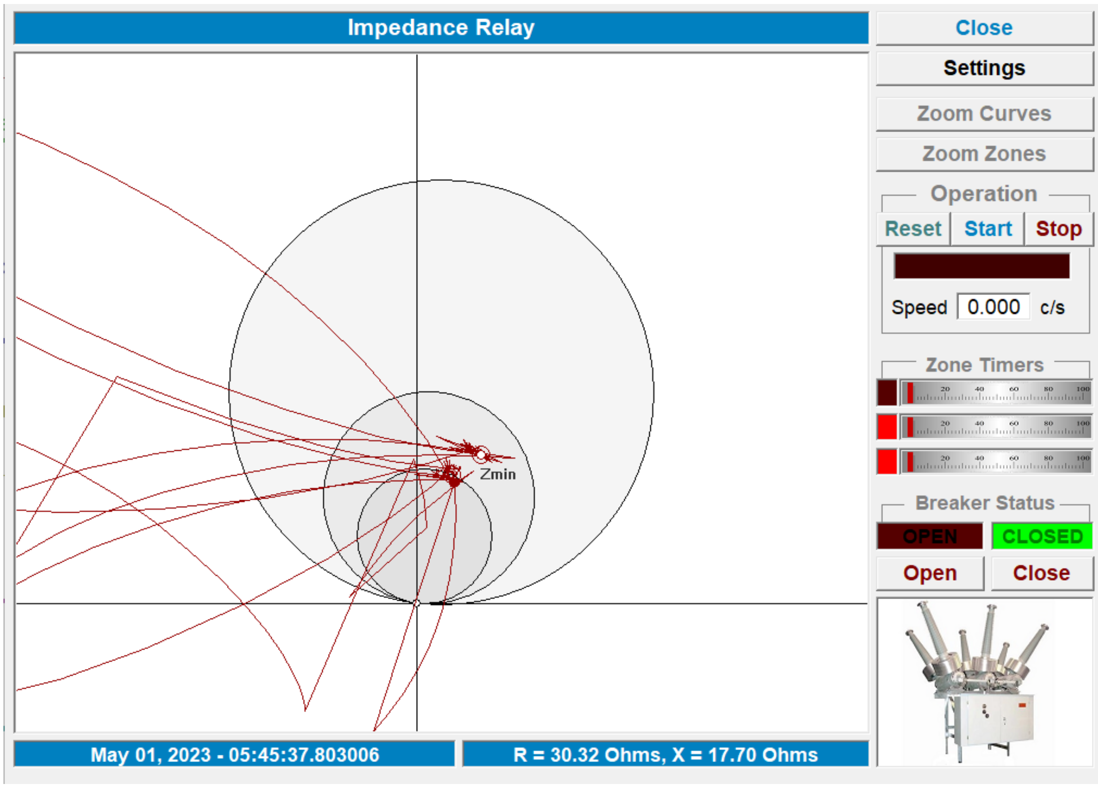

Figure 5.88 Zone impedance characteristics at PCC for AC fault on Bus-2

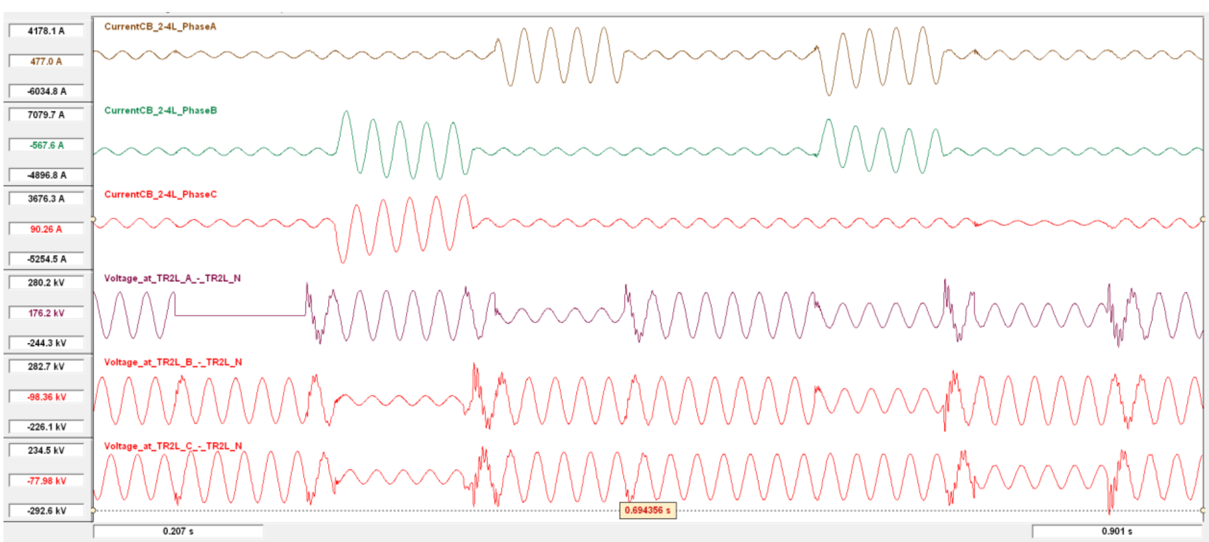

Figure 5.89 Current and Voltage Waveforms at Bus-2 for scenario-3 case-B

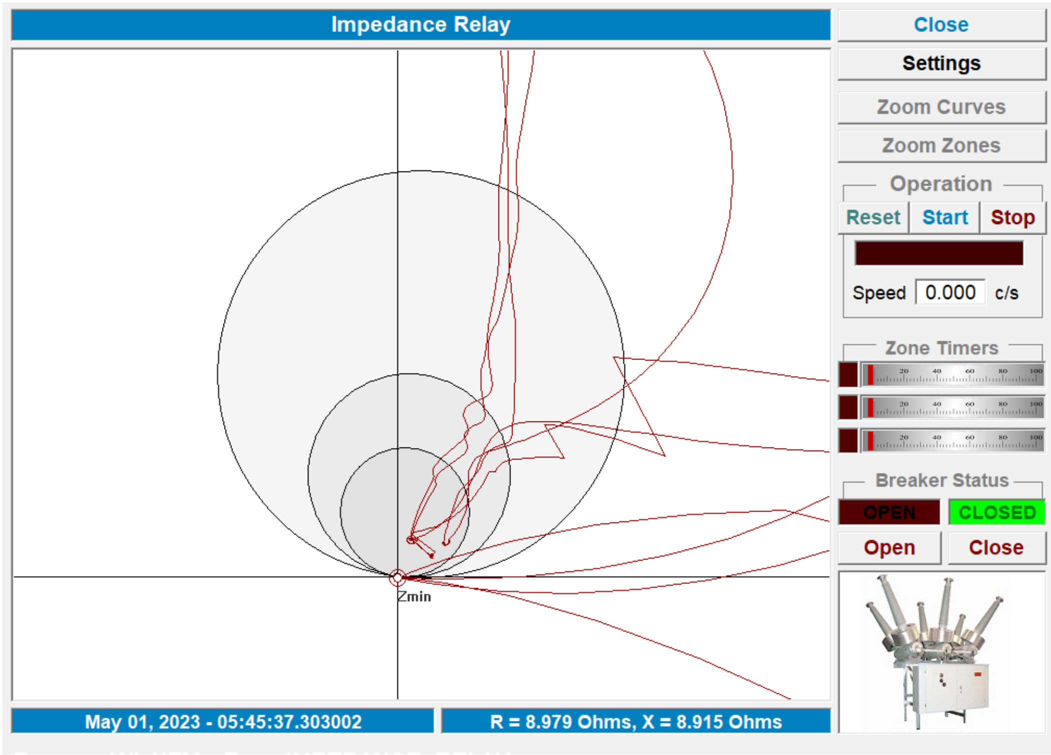

Figure 5.90 Zone impedance characteristics at Bus-2 for A-G fault on Bus-2

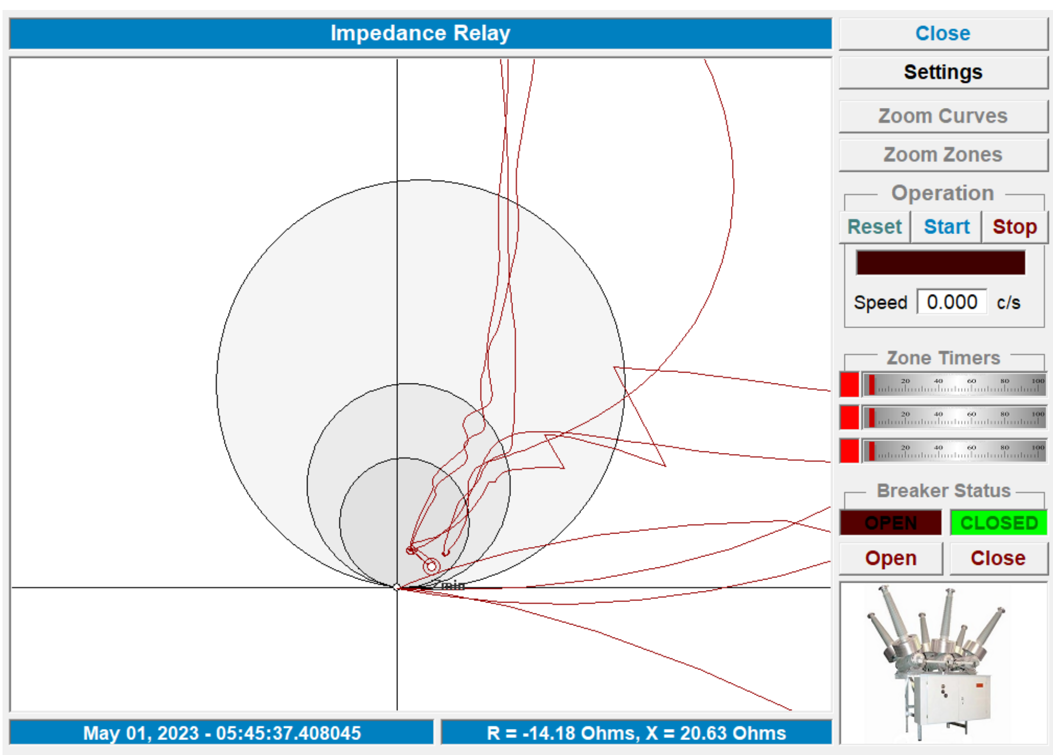

Figure 5.91 Zone impedance characteristics at Bus-2 for BC-G fault on line

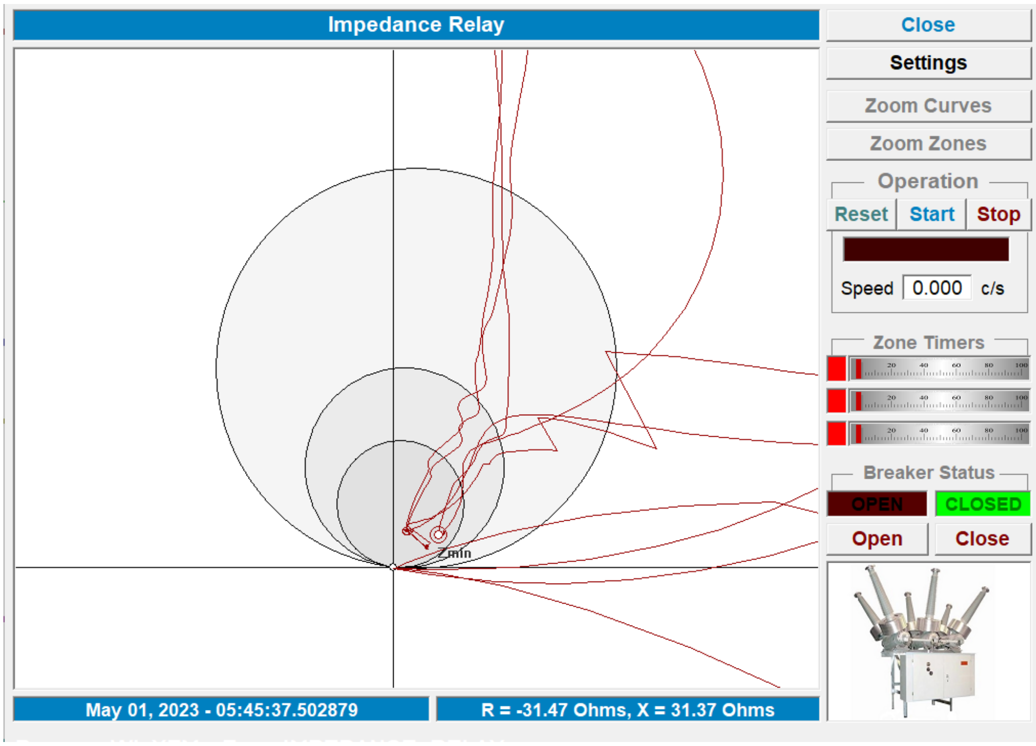

Figure 5.92 Zone impedance characteristics at Bus-2 for A-G fault on line

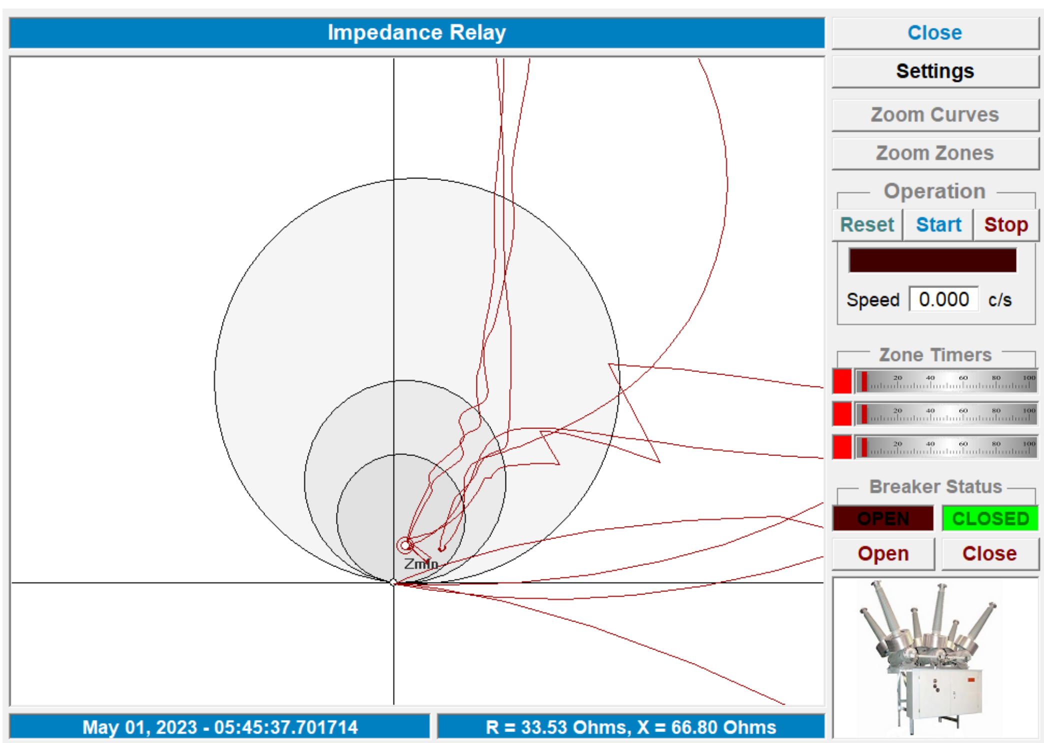

Figure 5.93 Zone impedance characteristics at Bus-2 for AB fault on line

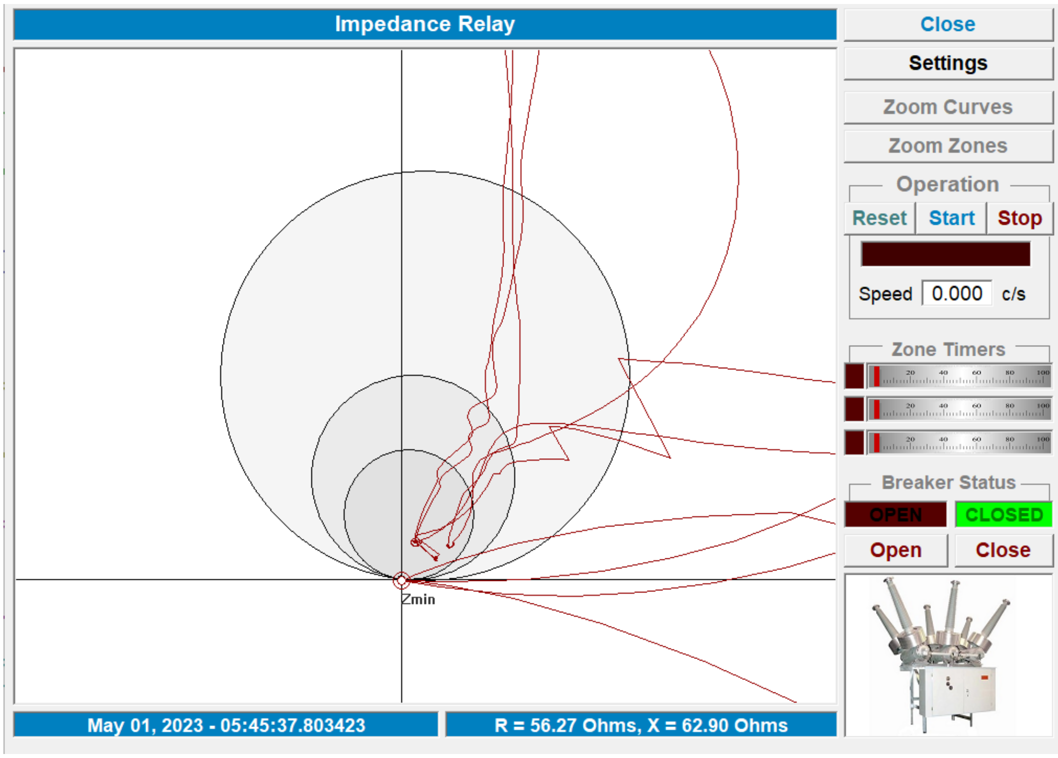

Figure 5.94 Zone impedance characteristics at Bus-2 for AC fault at Bus-2

Case-C: Fault happening on the 30-mile transmission line 15 miles (50%) from the PCC.

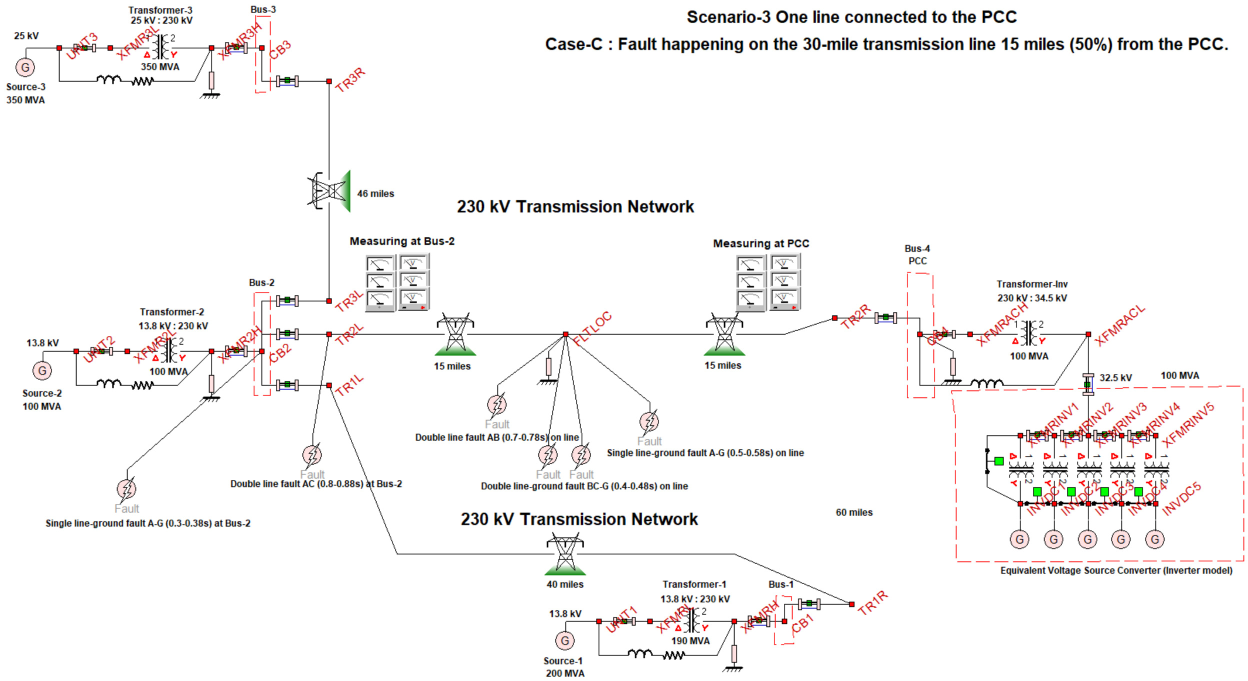

Figure 5.95 Scenario-3 case-C Fault on One Line Connected to PCC at 15 miles from PCC

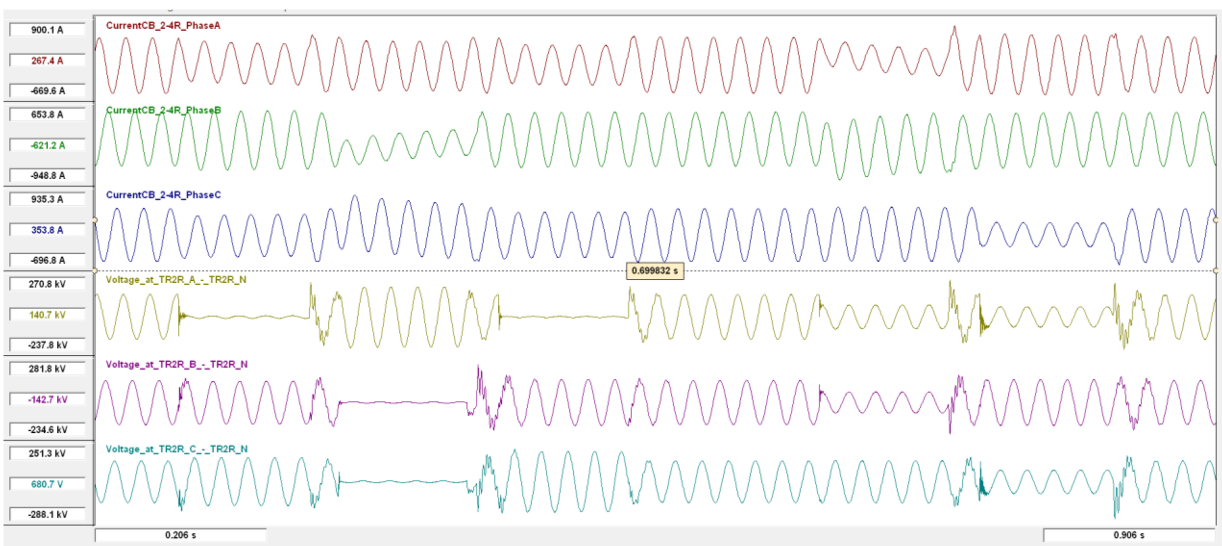

Figure 5.96 Current and Voltage Waveforms at PCC for scenario-3 case-C

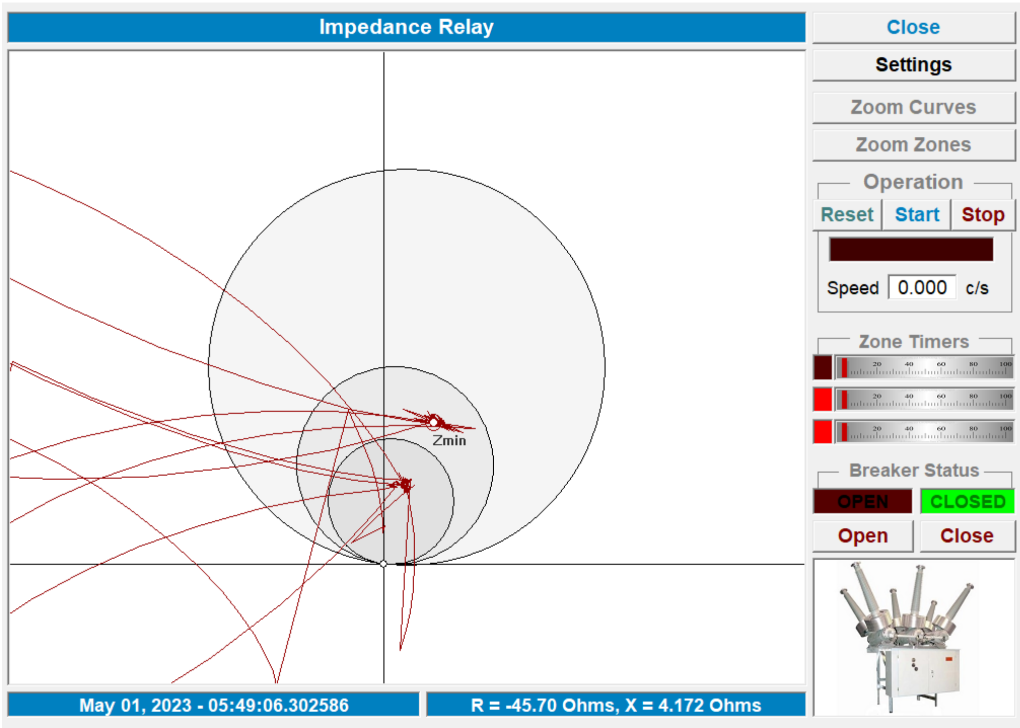

Figure 5.97 Zone impedance characteristics at PCC for A-G fault at Bus-2

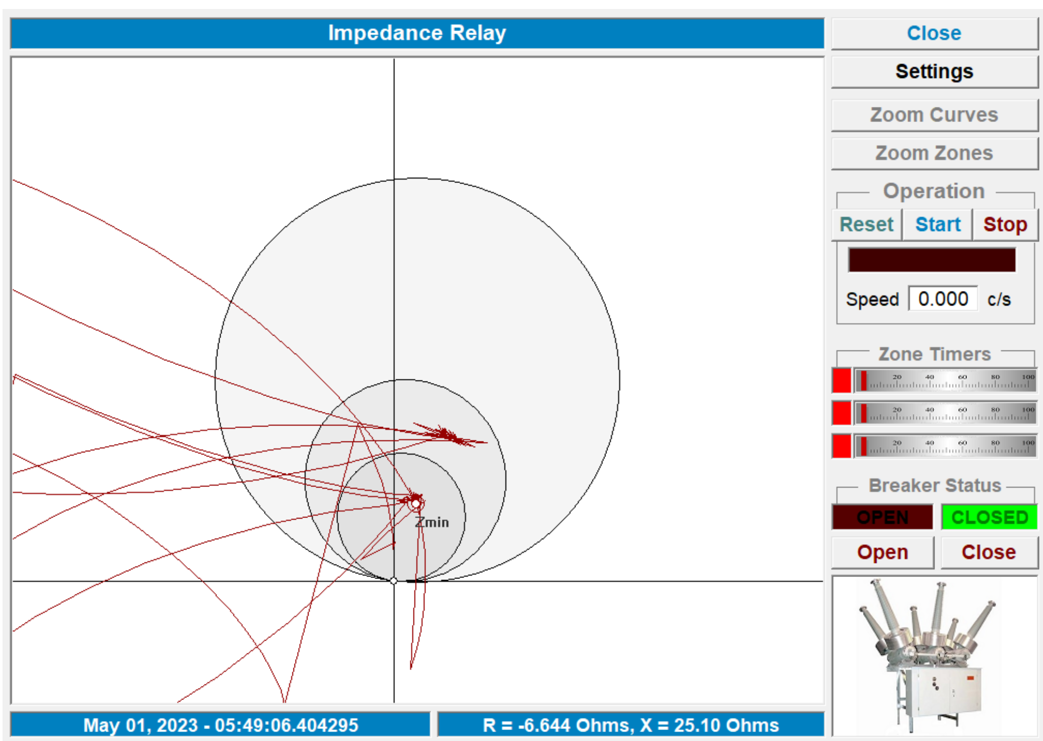

Figure 5.98 Zone impedance characteristics at PCC for BC-G fault on the line

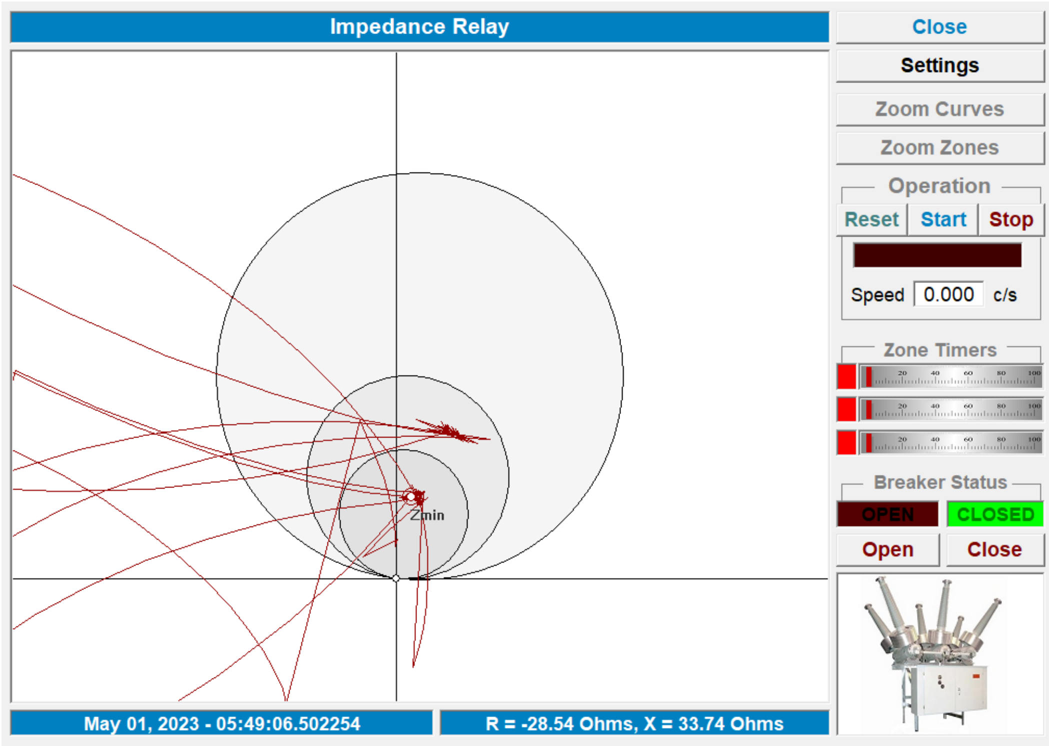

Figure 5.99 Zone impedance characteristics at PCC for A-G fault on line

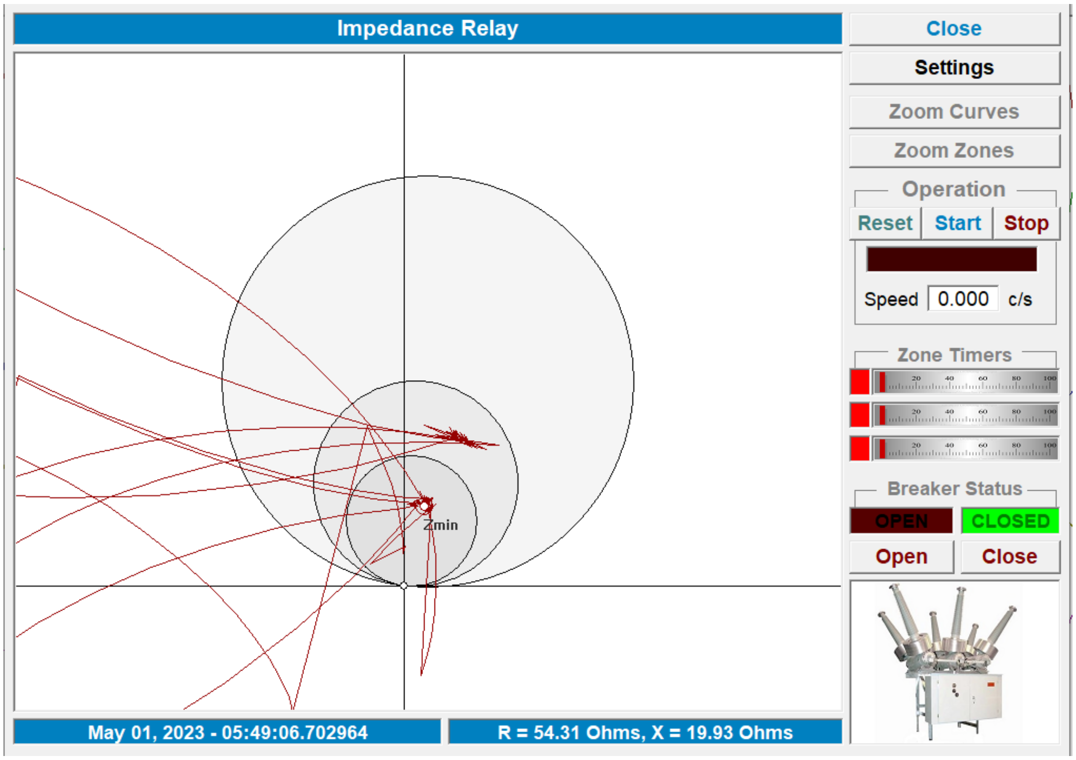

Figure 5.100 Zone impedance characteristics at PCC for AB fault on the line

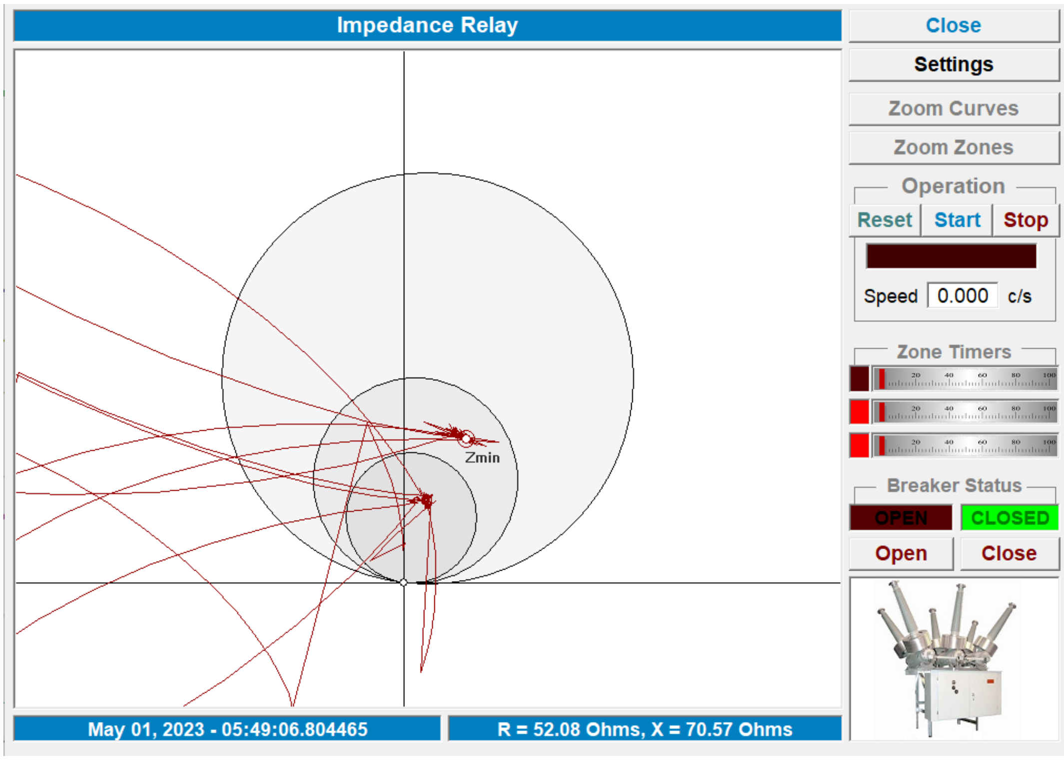

Figure 5.101 Zone impedance characteristics at PCC for AC fault at Bus-2

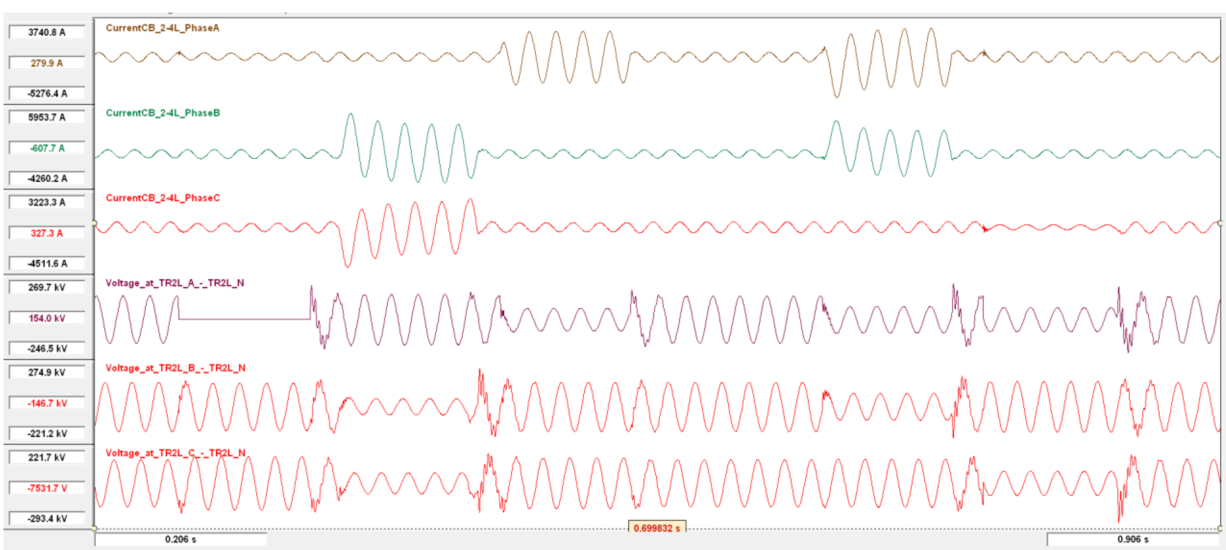

Figure 5.102 Current and Voltage Waveforms at Bus-2 for scenario-3 case-C

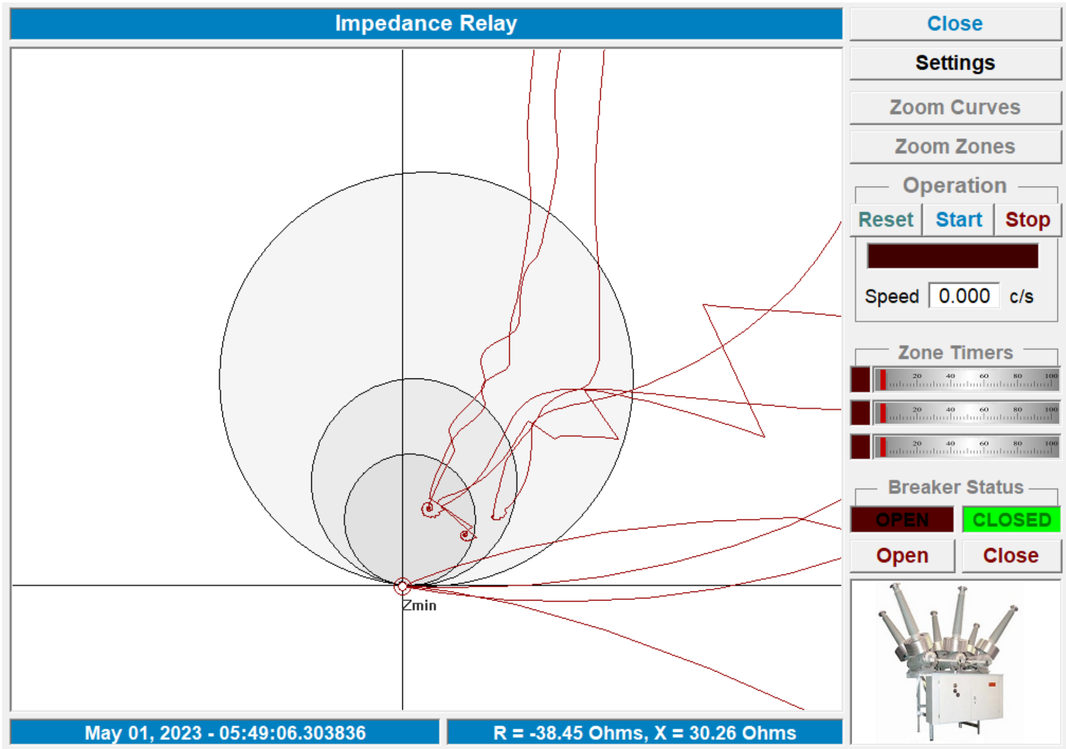

Figure 5.103 Zone impedance characteristics at Bus-2 for A-G fault at Bus-2

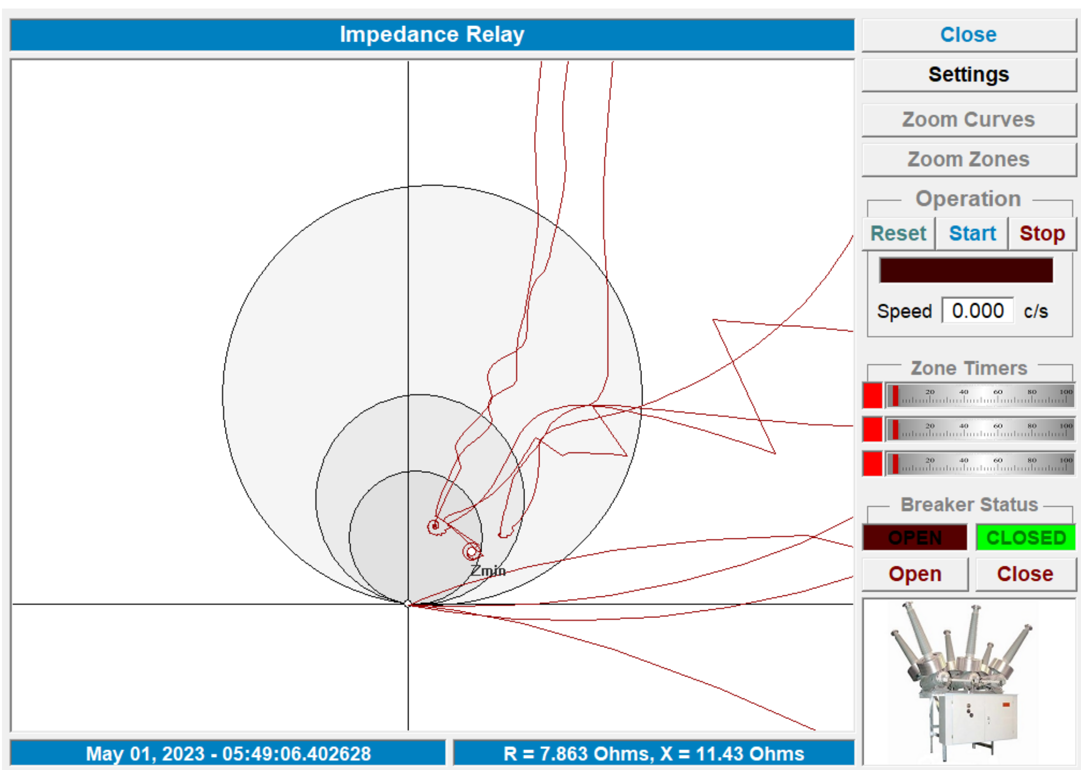

Figure 5.104 Zone impedance characteristics at Bus-2 for BC-G fault on line

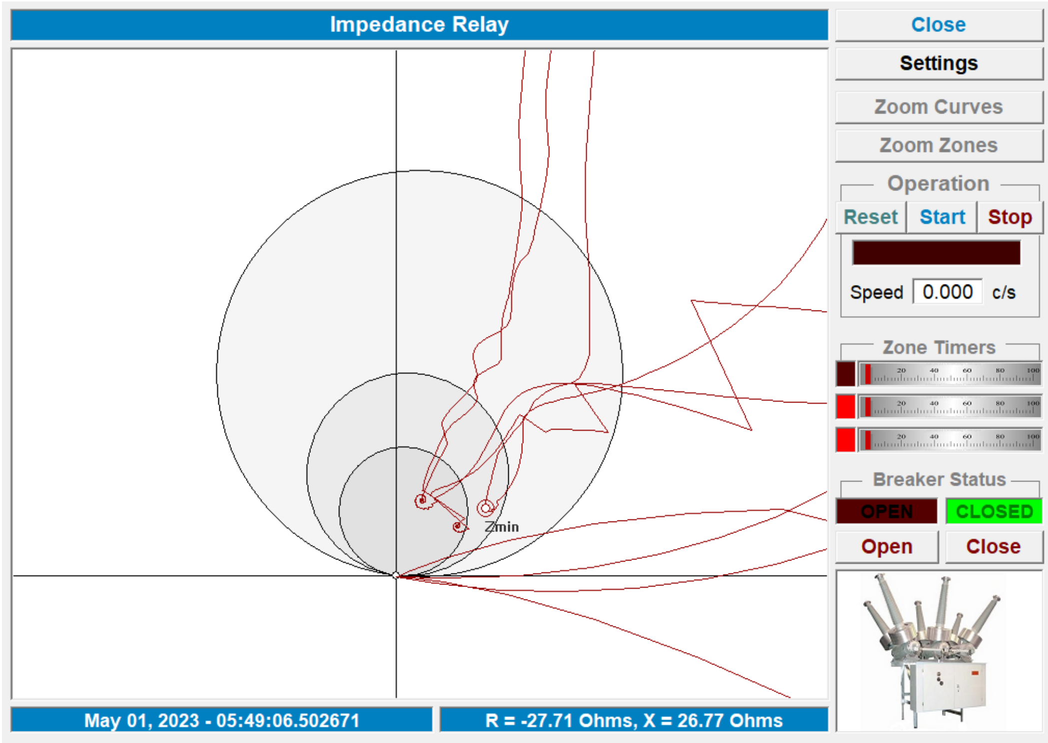

Figure 5.105 Zone impedance characteristics at Bus-2 for A-G fault on line

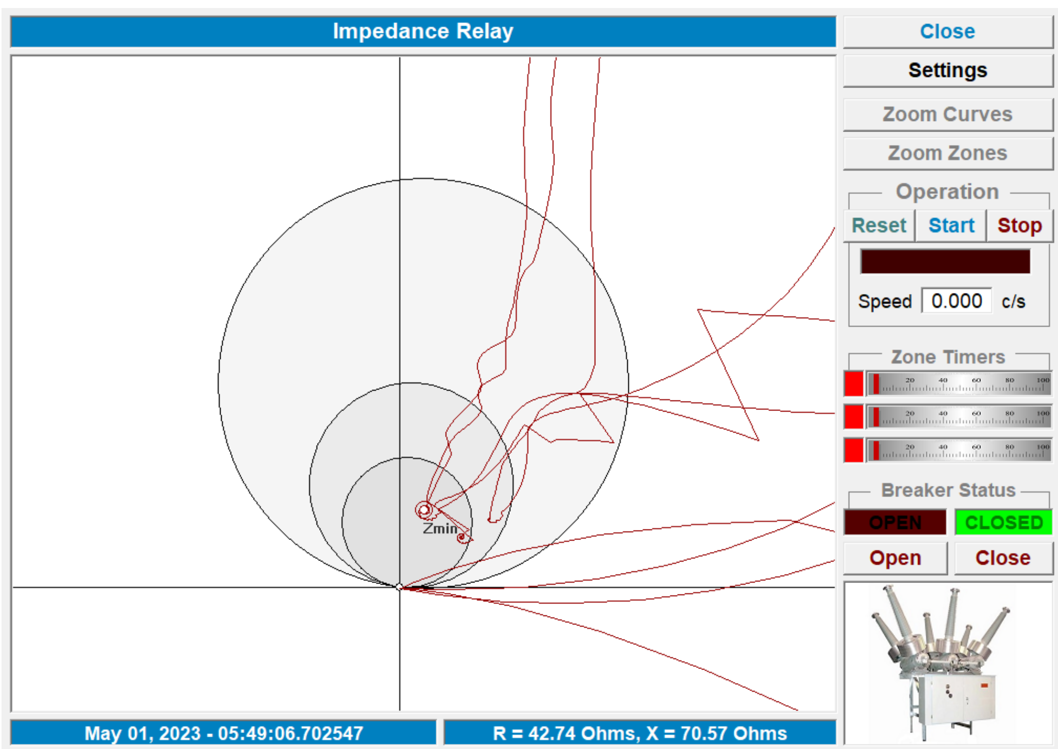

Figure 5.106 Zone impedance characteristics at Bus-2 for AB fault on line

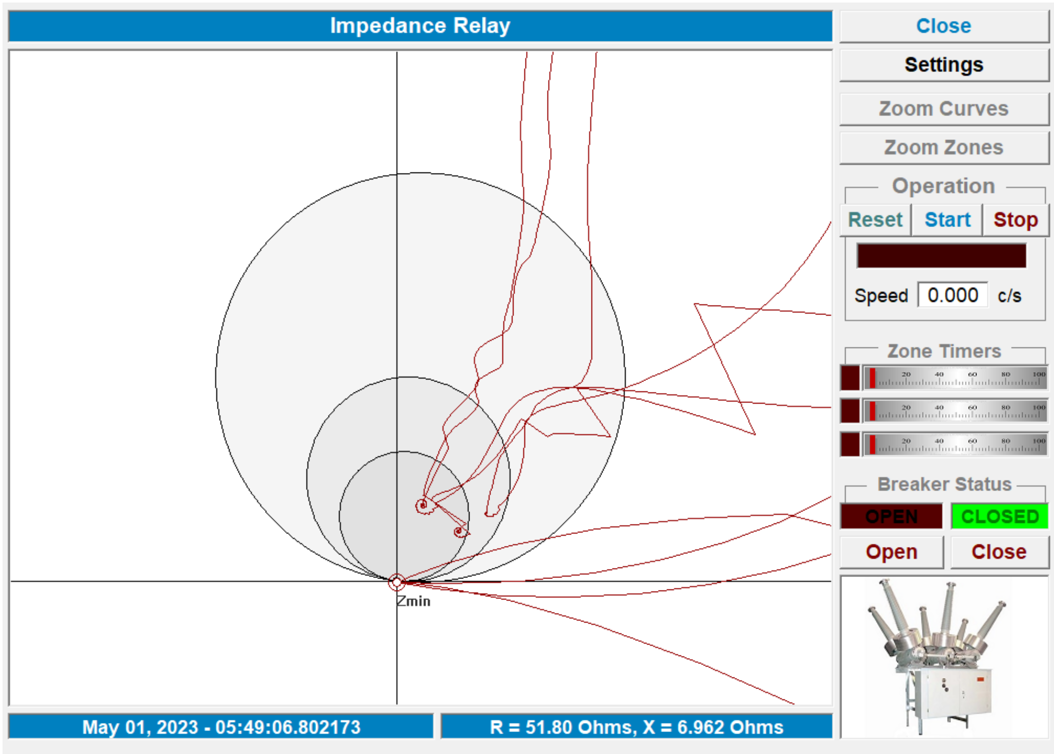

Figure 5.107 Zone impedance characteristics at Bus-2 for AC fault at Bus-2

6. Laboratory Testing with Hardware in the Loop

This section describes work that was performed in the laboratory to verify the response of legacy protection and control systems when they are presented with inputs (voltages and currents) coming from simulation of system with high penetration of inverters.

6.1 Introduction

Laboratory testing enables the testing of the protection and control system whether it is a legacy protection system or estimation based protection system (setting-less relay) with hardware in the loop. For this purpose, simulated data are streaming into a bank of digital to analog converters, the output of the converters are next fed into a bank of amplifiers to bring the analog signal to typical levels encountered in an actual protection system. These signals are connected to the inputs of legacy protective relays or to the inputs of merging units. In the case of merging units, the output of the merging units is fed into a computer that acts as the process bus that receives the sample values and the computer performs the protection functions.

This section describes the experiment set-up and provides example results. It is organized as follow: Section 6.2 describes the laboratory circuitry that enables experiments with hardware in the loop; Section 6.3 describes the simulated events and the associated data used for these experiments; Section 6.4 explains the detailed setup for how to send simulation data to the merging units; Section 6.5 describes the data received from merging unit; Section 6.6 combines the simulation data (input) and merging unit data (output) and calculates their differences; Section 6.7 analyzes the differences between input and output.

6.2 Experiment Circuit Description

The connection diagram between various equipment is illustrated in Figure 6.1. Basically, the experiment consists of three parts: 1) simulator; 2) process bus; 3) setting-less protection relay.
In the simulator part, the user interface generates digital streaming waveforms representing the terminal voltages and currents of the protection zone (power system component) to the NI 32 channel DC/AC converter. It is emphasized here that the source for the digital streaming waveforms can be simulated voltages and currents of the power system component, or field collected measurements from the CTs/PTs in the COMTRADE format. Omicron amplifiers receive the analog signals from the NI DC/AC converter and amplify these signals to a range which is very similar to real output of electronic CTs/PTs (for voltages around 50V and for currents around 5A). In this manner, the electrical output (voltages and currents) of the Omicron amplifiers are treated as the secondary electrical quantities from the CTs/PTs in this lab implementation.

In the process bus part, two merging units from Reason and GE are connected to the output terminals of the Omicron amplifier, and a cross connect panel or Ethernet hub routes the data from the output of merging units.

The Setting-less protection relay, which is implemented as another user interface, receives the data sampled by each merging unit and feed the data to dynamic state estimator.

As a summary, the simulator sends COMTRADE file to the experiment circuit (called input COMTRADE file), and the relay receives streamlined data from the experiment circuit, the relay has the option to feed the data directly into the protection algorithm, or simply store all data into COMTRADE file (called output COMTRADE file) for future use.

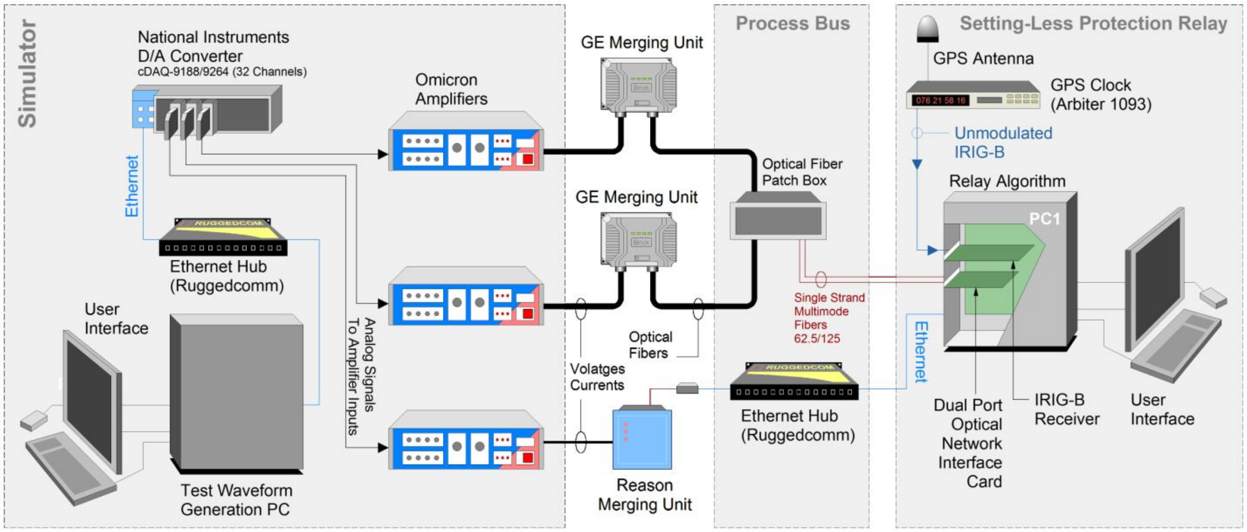

Figure 6.1 Experiment Setup – Connection Diagram

In this document, only the data from REASON merging unit is used. A detailed wiring diagram between the amplifier and the REASON merging unit is illustrated in Figure 6.2. The CMS 156 amplifier has three phase voltage channels and one neutral voltage channel, three phase current channels and one neutral current channel. All the outputs are connected to the inputs of the REASON MU via a panel where banana type plugs are used. The wiring cable from amplifier to the panel is AWG #10, and the wiring cable from the panel to the MU is AWG #16. The amplifier has 1V/50V amplification over voltage channels, and 1V/5A amplification over current channels.

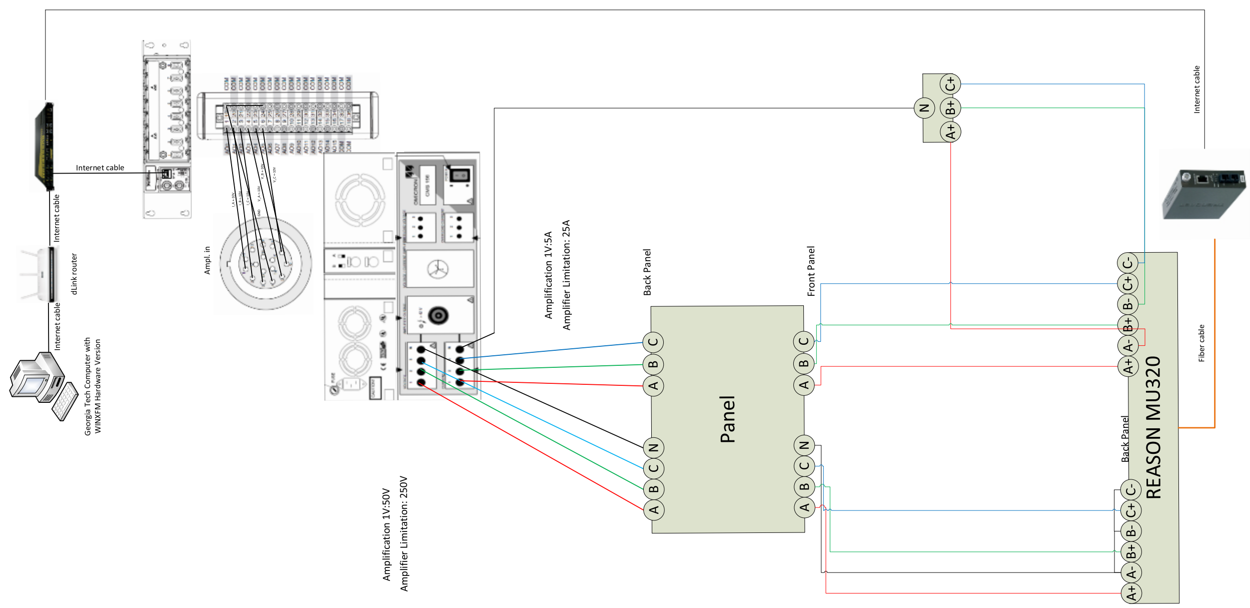

Figure 6.2 Wiring Diagram between Amplifier and Reason MU

6.3 Simulation Events

The test system that WINXFM uses to generate simulation data to the amplifier is illustrated in Figure 6.3. The transmission line framed by the blue dashed line, from node YJLINE1 to node YJLINE2, is under protection. The loading current on the line is around 420A. There are three voltage meters and three current meters on node YJLINE1 and another three voltage meters and three current meters on node YJLINE2. However, since the merging unit can only sample dataset from one amplifier, the voltage and current measurements on node YJLINE1 is chosen.

The simulation time is 2 seconds, where the transmission line works in normal operation. No external/internal events simulated.

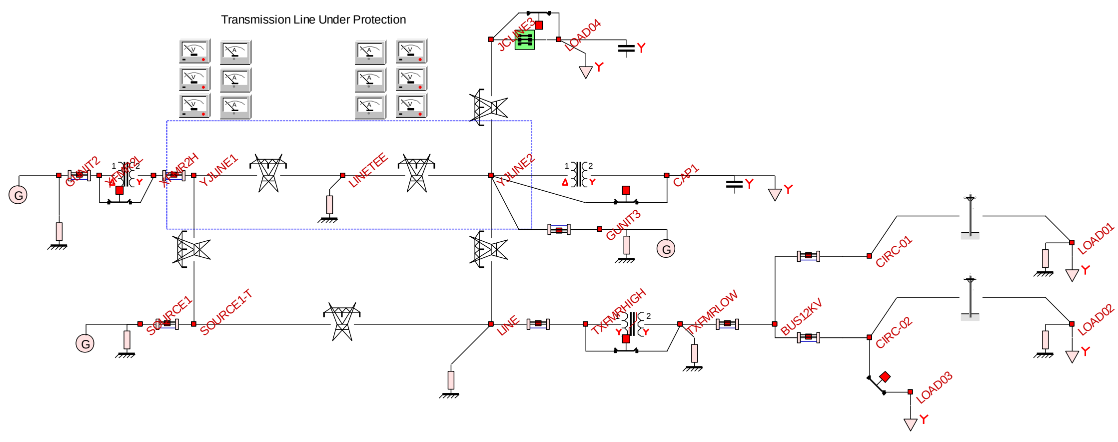

Figure 6.3 Test System for Generating Simulation Data

A snapshot of the voltage and current measurements on node YJLINE1 is in the Figure 6.4. Here, Voltage_A_SIM stands for simulated phase A to neutral voltage on node YJLINE1.

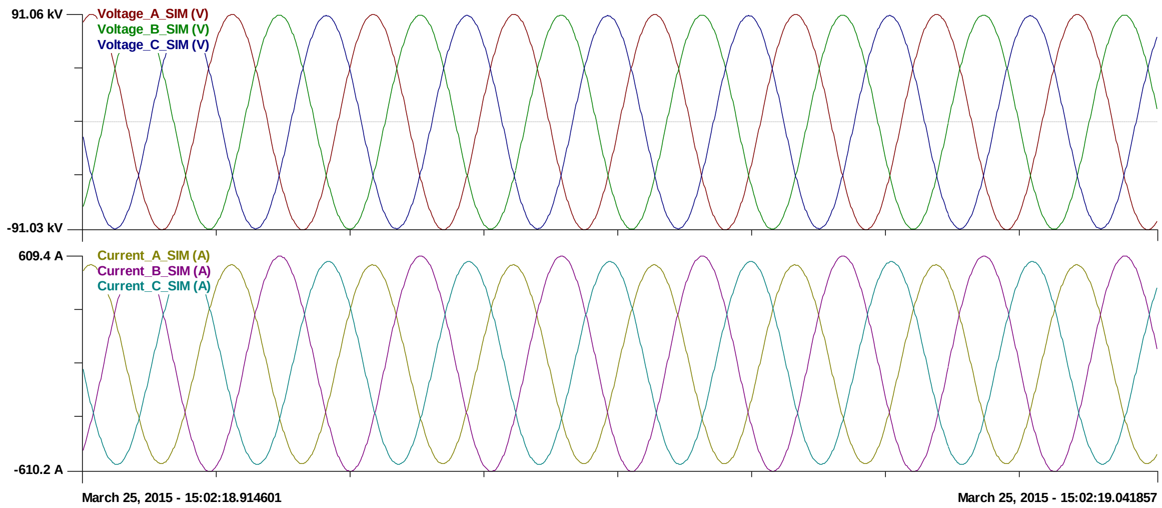

Figure 6.4 Test System Simulation Results

6.4 Experiment Setup

To run the experiment, the user needs to setup two user interfaces.

The first user interface sets up the transformation ratio of the amplifier. Since PT/CT are not available at this moment, the amplifiers transform the simulation data which are in primary electrical level to a range which is very similar to real output of electronic CTs/PTs (for voltages around 50V and for currents around 5A). In this manner, the electrical output (voltages and currents) of the Omicron amplifiers are treated as the secondary electrical quantities from the CTs/PTs in this lab implementation. Figure 6.5 to Figure 6.10 shows the setup for each channel. In Figure 6.5, the source peak is 569A for phase A current, and set the transformation ratio to 500:1, so that the amplifier output peak is 1.138A. Note that 5A peak is usually used but for the sake of safety we set the peak around 1A. The same ratio is set for phase B and C current in Figure 6.6 and Figure 6.7. In Figure 6.8, the source peak is 91kV for phase A voltage, and set the transformation ratio to 100kV:66.7V, so that the amplifier output peak is 60V. The same ratio is set for phase B and C voltage in Figure 6.9 and Figure 6.10. Figure 6.11 is used to check all the amplifier channels. Only 6 channels are active at this moment. The data are played back repeatedly so that a discontinuity happens every 2 seconds.

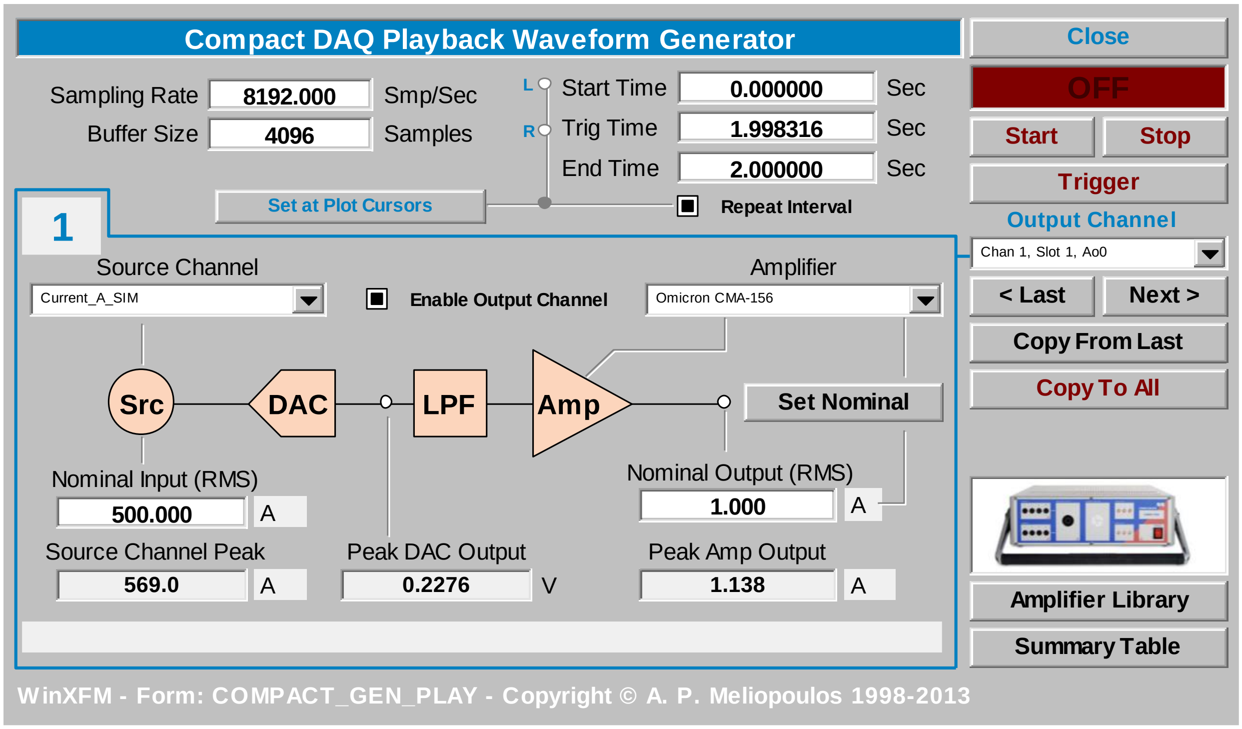

Figure 6.5 Amplifier Setup for Transformation on Phase A Current

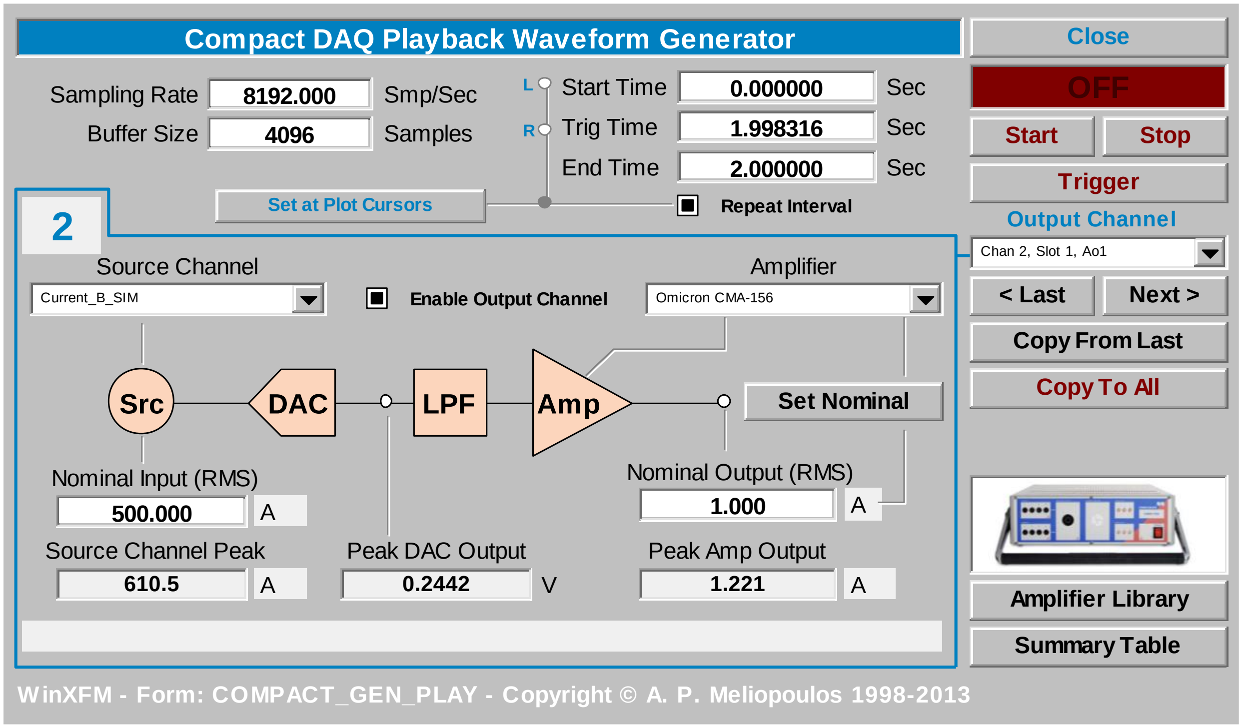

Figure 6.6 Amplifier Setup for Transformation on Phase B Current

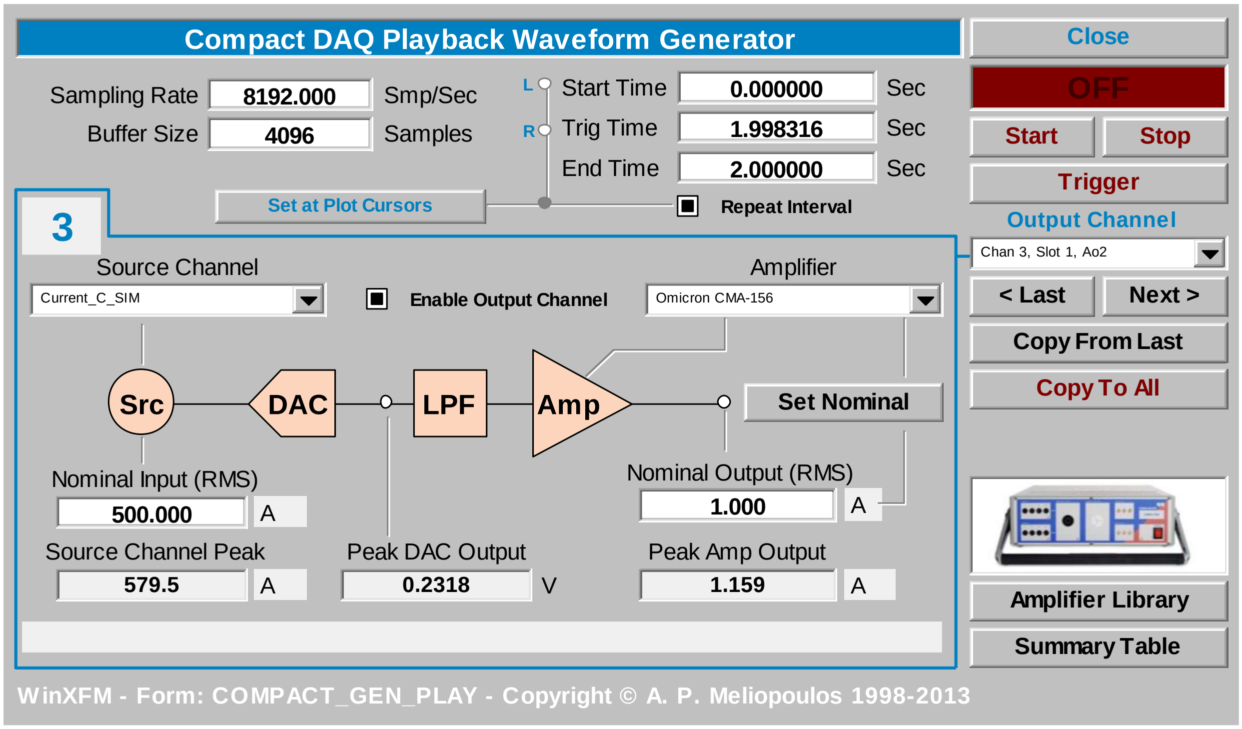

Figure 6.7 Amplifier Setup for Transformation on Phase C Current

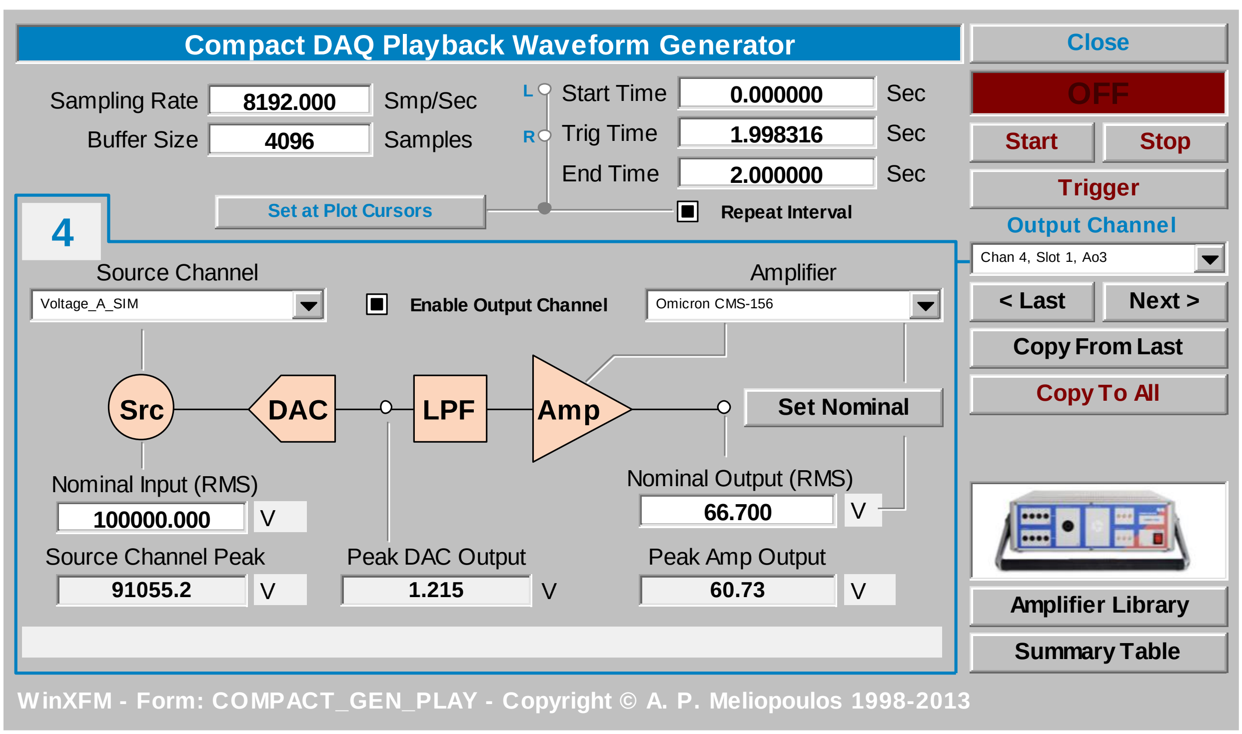

Figure 6.8 Amplifier Setup for Transformation on Phase A Voltage

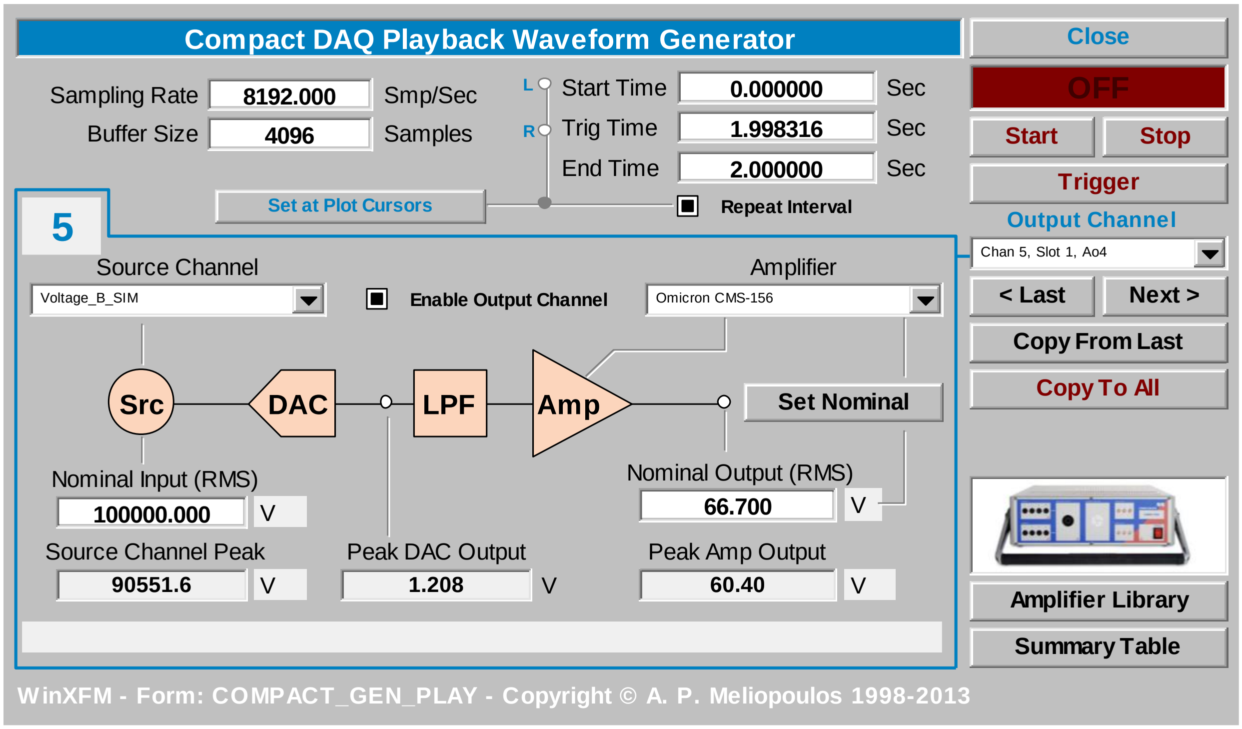

Figure 6.9 Amplifier Setup for Transformation on Phase B Voltage

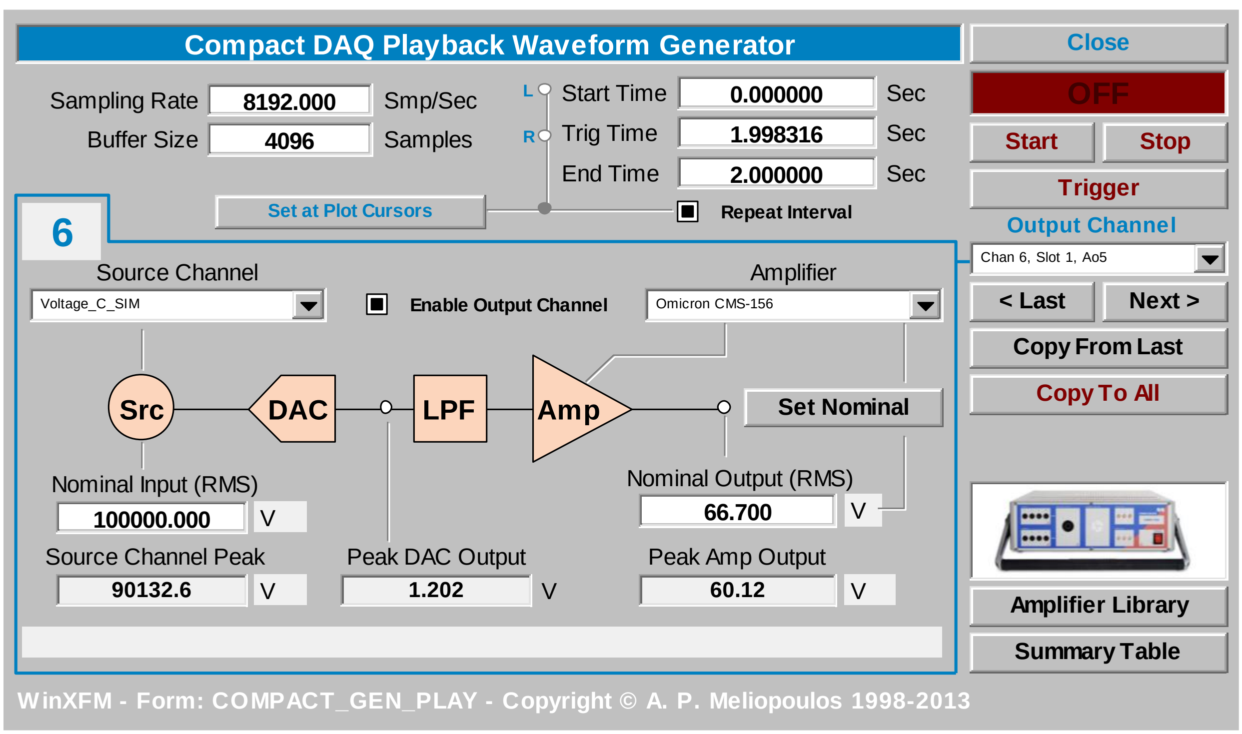

Figure 6.10 Amplifier Setup for Transformation on Phase C Voltage

Compact DAQ Playback Waveform Generator Setup Summary

Close

Sampling Rate 8192.000 Hz | Start Time 0.000000 sec | End Time 2.000000 sec

Buffer Size 4096 | Trig Time 1.998316 sec | Repeat Yes

Amplifier Library

	Pin/Slot	Active	Type	Source Chan	Amplifier	Src Nominal	Src Peak	Out Nominal	Out Peak
1	1/0	1	Current	Current_A_SIM	Omicron CMA-156	500.0 A	569.0 A	1.000 A	1.138 A
2	1/1	1	Current	Current_B_SIM	Omicron CMA-156	500.0 A	610.5 A	1.000 A	1.221 A
3	1/2	1	Current	Current_C_SIM	Omicron CMA-156	500.0 A	579.5 A	1.000 A	1.159 A
4	1/3	1	Voltage	Voltage_A_SIM	Omicron CMS-156	100000.0 V	91055.2 V	66.70 V	60.73 V
5	1/4	1	Voltage	Voltage_B_SIM	Omicron CMS-156	100000.0 V	90551.6 V	66.70 V	60.40 V
6	1/5	1	Voltage	Voltage_C_SIM	Omicron CMS-156	100000.0 V	90132.6 V	66.70 V	60.12 V
7	1/6	0	Current	Current_A_SIM	Omicron CMA-156	500.0 A	569.0 A	2.000 A	2.276 A
8	1/7	0	Current	Current_A_SIM	Omicron CMA-156	500.0 A	569.0 A	2.000 A	2.276 A
9	1/8	0	Current	Current_A_SIM	Omicron CMA-156	500.0 A	569.0 A	2.000 A	2.276 A
10	1/9	0	Current	Current_A_SIM	Omicron CMA-156	500.0 A	569.0 A	2.000 A	2.276 A
11	1/10	0	Current	Current_A_SIM	Omicron CMA-156	500.0 A	569.0 A	2.000 A	2.276 A
12	1/11	0	Current	Current_A_SIM	Omicron CMA-156	500.0 A	569.0 A	2.000 A	2.276 A
13	1/12	0	Current	Current_A_SIM	Omicron CMA-156	500.0 A	569.0 A	2.000 A	2.276 A
14	1/13	0	Current	Current_A_SIM	Omicron CMA-156	500.0 A	569.0 A	2.000 A	2.276 A
15	1/14	0	Current	Current_A_SIM	Omicron CMA-156	500.0 A	569.0 A	2.000 A	2.276 A
16	1/15	0	Current	Current_A_SIM	Omicron CMA-156	500.0 A	569.0 A	2.000 A	2.276 A
17	2/0	0	Current	Current_A_SIM	Omicron CMA-156	500.0 A	569.0 A	2.000 A	2.276 A
18	2/1	0	Current	Current_A_SIM	Omicron CMA-156	500.0 A	569.0 A	2.000 A	2.276 A
19	2/2	0	Current	Current_A_SIM	Omicron CMA-156	500.0 A	569.0 A	2.000 A	2.276 A
20	2/3	0	Current	Current_A_SIM	Omicron CMA-156	500.0 A	569.0 A	2.000 A	2.276 A

WinXFM - Form: COMPACT_GEN_PBACK_TABLE - Copyright © A. P. Meliopoulos 1998-2013

Figure 6.11 Summary Table of All the Channels Setup in the Amplifier

The second user interface sets up the data concentrator, which is demonstrated in Figure 6.12. According to IEC 61850-9-2 light, the first four channels are currents and the second four channels are voltages. So that the MU order is 1, 2, 3 for currents, and 4, 5, 6 for voltages. Also, the PT transformation ratio is set to be 100kV/66.7V which is the same as that of the first user interface. The CT transformation ratio is set to be 500A/1A which is the same as that of the first user interface. Here, Voltage_A_MU stands for phase A to neutral voltage captured from merging unit.

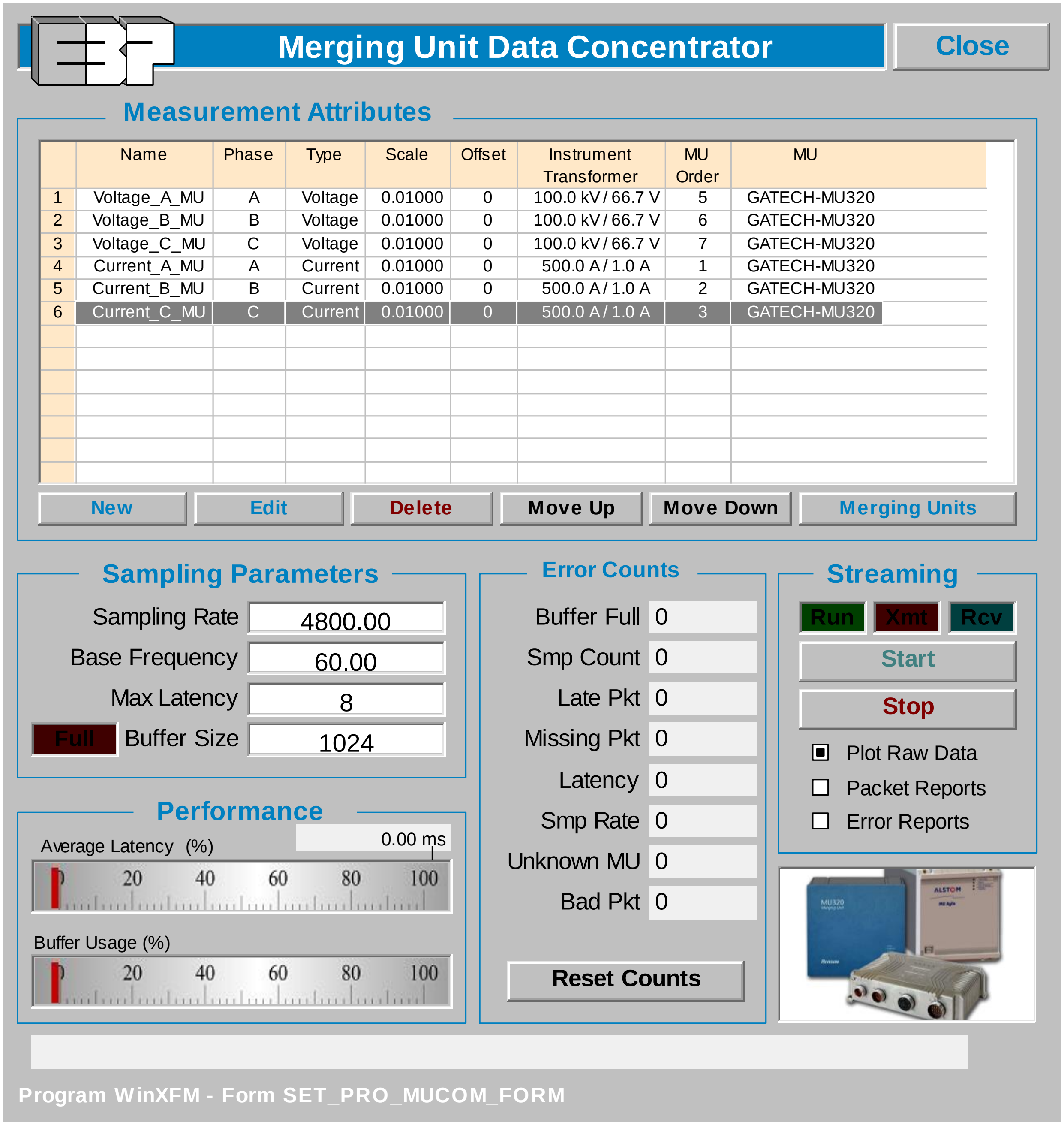

Figure 6.12 Data Concentrator Setup

6.5 Data from Merging Units

A snapshot of the data captured from merging unit is in Figure 6.13. The data is stored in output COMTRADE file for analysis.

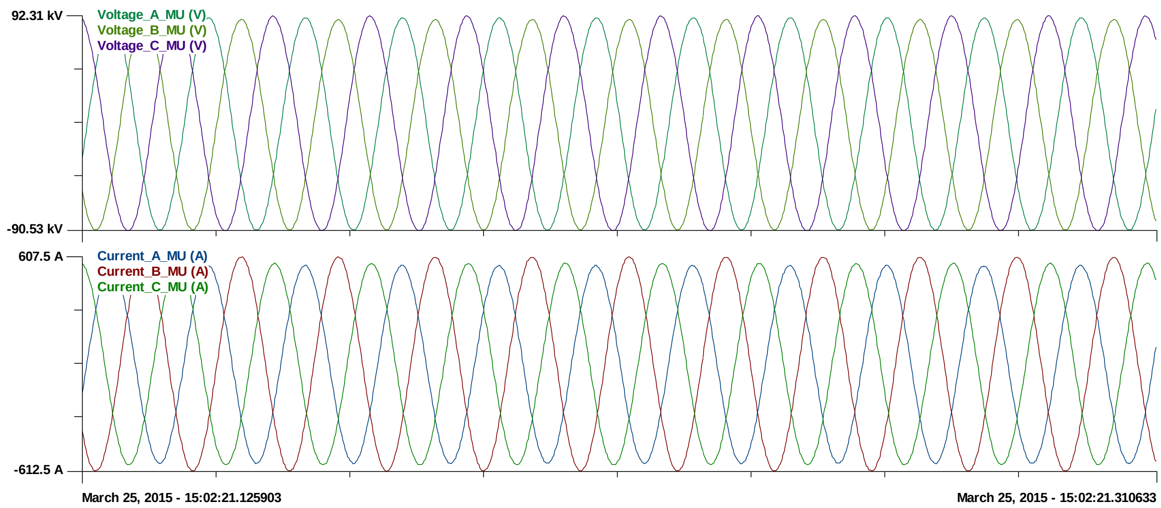

Figure 6.13 Data Captured from Merging Unit

6.6 Combined Results for Input and Output of the Experiment

As illustrated, the input and output of the experiment are stored in COMTRADE file for analysis. The first study is to compare the input and output, and ideally the two should be identical, however they're not due to channel noises, timing issues, etc.

In order to compare the two, firstly the output needs to be aligned to the input. The reason is that the data are played back repeatedly every playback cycle (one playback cycle is 2 seconds), so that if the merging unit records 10 seconds of data, there would be 5 playback cycles of output, however only 1 cycle of input. The starting point of a single playback cycle of the output needs to be aligned with the starting point of the cycle of the input. Figure 6.14 shows the time alignment point. At the alignment point, one cycle of the playback is finished, and a new cycle is started. It is easy to observe that discontinuity of waveforms exists between two cycles.

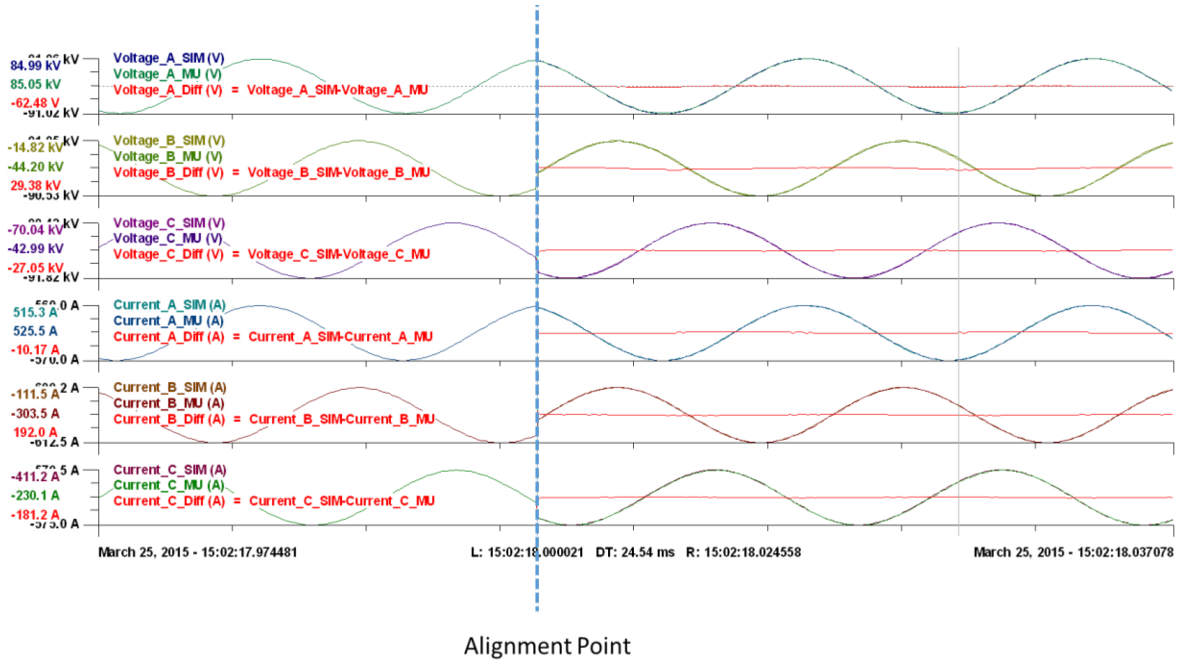

Figure 6.14 Alignment Point between Input and Output

The comparison between input and output for a whole playback cycle (2 seconds) is illustrated in Figure 6.15.

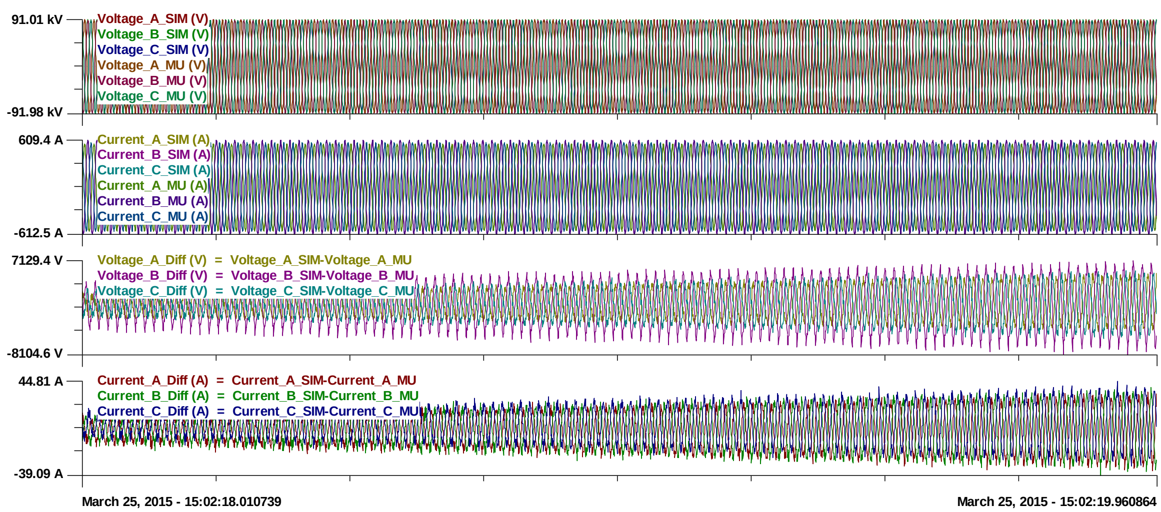

Figure 6.15 Comparison between Input and Output of the Experiment

From Figure 6.15 it is seen that the magnitude of the error increases over time.

7. In search of Protection and Control to Inverter Characteristics

It is evident that the interaction of protection and control systems with the new characteristics of the power system created by the proliferation of inverter interfaced resources is and will continue to be a major issue of concern. In this environment, we should try to develop protection and control systems that are immune to these new characteristics. The estimation based protection (aka setting-less protection) provides such a solution. This technology is described in this section.

7.1 Protection and control for systems with high levels of CIG

The characteristics of systems with high penetration of grid interfaced inverters, GFL or GFM, are substantially different from conventional systems with primarily synchronous generators both in terms of fault current levels and fault current components, i.e., DC offset, negative and zero sequence components and duration. Specifically: (a) significant differences exist between fault currents contributed by synchronous generators and inverter based resources which present obstacles in coordinating overcurrent relays; (b) fault current contributions from inverters do not include, or produce, much lower negative and zero sequence currents; many legacy relays use the negative sequence component as a polarizing quantity to detect fault direction; these relays may malfunction under these conditions; and (c) many grid interfaced inverters connect variable amount of renewable energy resources to the grid resulting in frequent configuration changes altering the network topology; this reality makes the process of coordinating legacy relays very challenging and many times unsolvable resulting in compromised coordination schemes.

To address the above issues, the dynamic state estimation based protection (EBP) method (a.k.a. setting-less protection, see Fig. 44) has been introduced in [84]. It does not need complicated settings and no coordination is required with other protection functions. The EBP examines the consistency between the measurements and the dynamic model of the protection zone. The EBP has been inspired from differential protection which simply monitors Kirchoff’s current law of a protection zone. EBP extents this concept to monitor all physical laws obeyed by the protection zone, and therefore will not be affected by external variations such as frequent changes of sources, level of fault currents, content of fault currents and/or loads. Therefore, it is immune to the characteristics of inverter interfaced generation.

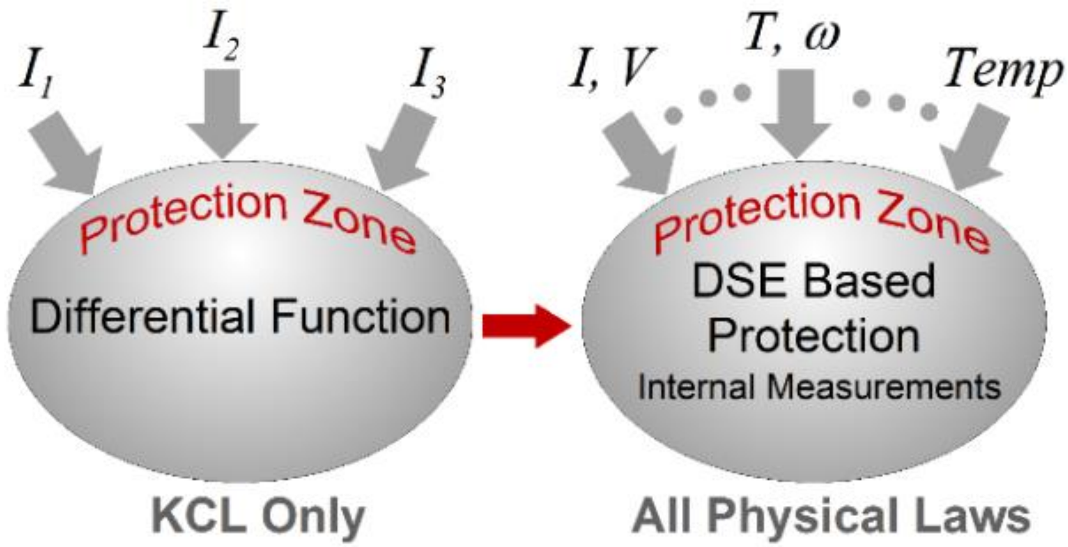

Figure 7.1 Conceptual Illustration of the Dynamic State Estimation Based Protection (EBP).

In dynamic EBP protection, all existing measurements in the protection zone are utilized (currents and voltages at the terminals of the protection zone, as well as voltages and currents inside the protection zone (as in capacitor protection) or speed and torque in case of rotating machinery or other internal measurements including thermal measurements). These measurements should obey the physical laws for the protection zone (for example, physical laws such as KCL, KVL, motion laws, thermodynamic laws). This principle means that the measurements should satisfy the dynamic model of the protection zone as long as the protection zone is free of faults. When there is a fault within the protection zone, the measurements would not satisfy the dynamic model of the protection zone. This distinction is a powerful, secure and reliable method to identify internal faults and block any external faults. A systematic approach to verify that the measurements satisfy the mathematical model is a dynamic state estimation procedure. The resulting method is a dynamic EBP. When an internal fault occurs, even high impedance faults or faults along a coil, for example, the dynamic state estimation reliably detects the abnormality and a trip signal is issued. This basic approach has been presented for specific cases.

The EBP method requires a high-fidelity mathematical model of the protection zone, the measurements and the dynamic state estimation algorithm.

The dynamical model of the protection zone is a set of differential and algebraic equations. In general, it will be a multi-physics model, for example, for transformer protection, the model will be the electro-thermal model of the transformer. The proposed method starts with this model and utilizes a *quadratization* procedure which reduces any higher order nonlinearities to no more than second order by the introduction of additional variables, if necessary (if model is linear or quadratic this process is not needed). This transformation does not change the model. We refer to this model as the quadratized dynamic model of the protection zone (QDM). The form of the QDM is given below in matrix format:

Protection zone quadratized model:

$$\begin{aligned} i(t) &= Y_{eqx1}\mathbf{x}(t) + D_{eqxd1}\frac{d\mathbf{x}(t)}{dt} + C_{eqc1} \\ 0 &= Y_{eqx2}\mathbf{x}(t) + D_{eqxd2}\frac{d\mathbf{x}(t)}{dt} + C_{eqc2} \\ 0 &= Y_{eqx3}\mathbf{x}(t) + \begin{Bmatrix} \vdots \\ \mathbf{x}(t)^T\langle F^i_{eqxx3}\rangle\mathbf{x}(t) \\ \vdots \end{Bmatrix} + C_{eqc3} \end{aligned} \tag{1}$$

The first matrix equation expresses the through variables (i(t)) of the protection zone; note that in a case of an electrical system the through variables are simply the currents at the terminals of the protection zone, for rotating machines it may also include torque, and for electro-thermal models it may include heat flow. The variables contained in the array $\mathbf{x}(t)$ represent the state of the protection zone; for a purely electrical system, the state variables are the voltages at the various nodes of the system and the matrix Y_{eqx1} the resistive admittance matrix. The dynamics of inductors, capacitors, rotating mass and other such components are represented with the differential terms. Note also the states for rotating machines may include speed and for electro-thermal models will include temperatures. The second matrix equation represents the internal equations of the system; in case of an electrical system, these equations would be KCL and KVL for internal electrical nodes and/or electrical loops of the system. Finally, the third matrix equation represents the nonlinear relationships among the states of the protection zone. Detailed information can be found in [86] through [90].

The measurements are expressed as functions of the protection zone state, $\mathbf{x}(t)$. These functions may include linear, quadratic and/or differential terms:

$$\mathbf{z}(\mathbf{x}) = Y_{mx}\mathbf{x}(t) \begin{Bmatrix} \vdots \\ \mathbf{x}(t)^T\langle F^i_{mx}\rangle\mathbf{x}(t) \\ \vdots \end{Bmatrix} + D_{mx}\frac{d\mathbf{x}(t)}{dt} + C_m \tag{2}$$

where $\boldsymbol{z}(t)$ are the measured quantities. These measurements may represent any measurable quantity of the system, for example voltage, current, speed, temperature.

Any protection zone model can be cast into the above syntax. Models of transformers, lines, capacitor banks, motors, generators units have been developed using the QDM syntax. This syntax enables a full object orientation in all subsequent computations.

Using the protection zone and measurement model in QDM syntax, the dynamic state estimation is performed by an algorithm that is identical for any protection zone (i.e., it is object-oriented). Three alternate approaches have been implemented and tested for the dynamic state estimation algorithm: (a) extended Kalman filter, (b) constrained optimization method where the constraints are the second and third matrix equations in (1), and (c) unconstrained optimization method where the above mentioned constraints are relaxed and enforced via penalty functions.

To illustrate the method and exemplify the merits of the approach, an example protection system is presented here. The example compares the performance of a high-end protective relay to the performance of the EBP for a circuit in a microgrid that includes many inverters and it is designed as a five-wire system (there phases, neutral and ground). The microgrid is shown in Fig. 7.2. The circuit under protection is the circuit between buses I and II. The circuit cross section is also given in the figure, showing the three phases, the neutral and the ground in the form of the conduit.

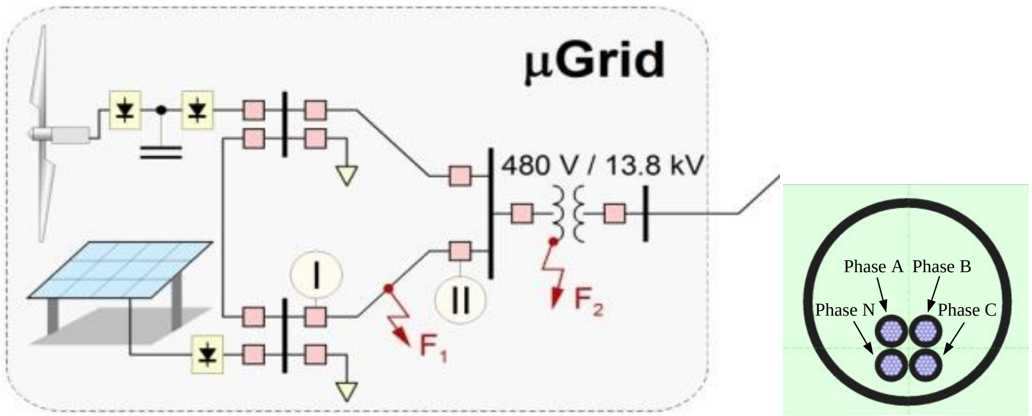

Figure 7.2 Example microgrid and circuit under protection

Assuming that two distance relays protect the indicated circuit at the two ends of the circuit, we simulate a single-phase to ground fault in the middle of the circuit and observe the response of the relays. The response is illustrated in Fig. 7.3. Note that, even if the fault is in the middle of the circuit, the distance relay "sees" the impedance way outside the relay characteristics (red star). This wrong performance is the result of the inverter characteristics and the grounding design of the five-wire system. Note that if the model is simplified and symmetrical components are used, then the relay will see the impedance at zone 2 characteristic (blue star). This performance is still wrong since the fault is in the middle of the circuit and the relay should have seen the fault inside the zone 1 characteristic.

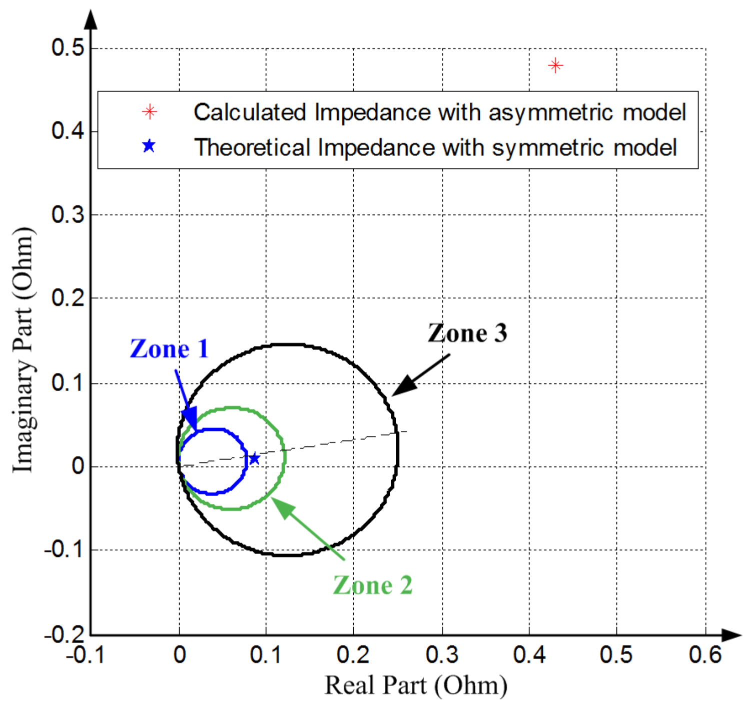

Figure 7.3 Performance of distance relay for a fault in the middle of the circuit I-II (see Fig. 7.2)

Now we simulate the operation of the EBP for the same circuit and the same fault. The results are shown in Fig. 7.4. The figure illustrates the electric current waveforms (top two traces), the residuals computed by the dynamic state estimation (mid traces) and the confidence level (bottom trace, probability that the measurements fit the dynamic model). Note once the fault occurs the confidence level drops to zero indicating an internal fault. Once the fault is detected the EBP relay uses user directives to trip the circuit (user defined delays and transfer trip if required). Note also in this case, the fault current before and after the fault are not very different as the inverters limit the fault current.

This example illustrates that in the presence of inverters, legacy protection may mis-operate (in this case will not trip a fault in the middle of the circuit under protection) while the estimation-based protection will reliably detect the fault and trip the circuit, even if the fault current levels are quite low.

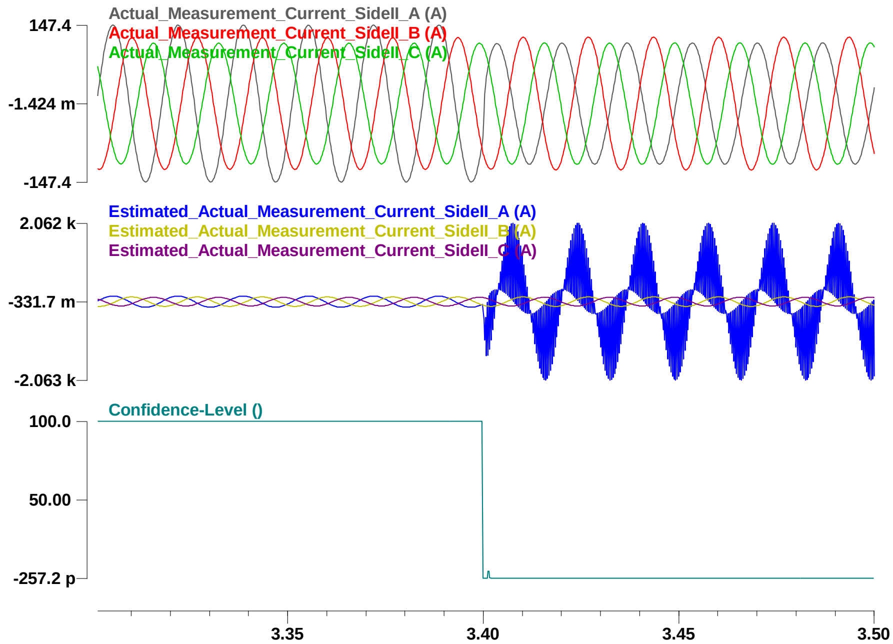

Figure 7.4 EBP Results: fault in the middle of circuit I-II (see Fig. 7.2)

7.2 Observations on Estimation Based Protection

Looking at all the drawbacks we can propose our own solution to the problem. After the 2003 North-East blackout researchers have come up with a pretty niche concept called the setting-less relays. This kind of protection scheme does not implement settings or uses very little number of settings and as such is independent of the major effects of the grid. Some of its advantages include:

- Simplified settings/settings not required.
- Can differentiate between internal faults within the device/network from un-faulted conditions. For example, it identifies the high inrush currents of a transformer and considers it under normal operation.
- It is based on dynamic state estimation which takes in real time data and measurements.
- Coordination between different relays is not required.

Setting-less relays have had a significant impact on today's power systems. These relays provide more accurate and reliable protection of electrical equipment and systems, which helps to improve system stability, minimize damage from faults, and reduce downtime.

One of the key advantages of setting-less relays is their ability to adapt to changing system conditions. As power systems become more complex and dynamic, it is increasingly difficult to predict fault conditions and adjust traditional relays accordingly. Setting-less relays use advanced algorithms and digital signal processing to analyze system behavior in real-time and automatically adjust their protective settings to match the system conditions.

This ability to adapt to changing conditions has made setting-less relays an essential component of modern power systems. These relays are used to protect a wide range of equipment including transformers, generators, motors, etc. By providing more accurate and reliable protection these relays help to prevent equipment damage, reduce downtime, and improve overall system reliability and safety. These relays are designed to quickly detect and isolate fault conditions, which helps to prevent cascading failures and minimize the risk of widespread blackouts like the northeast blackout of 2003. The use of digital technology has further improved the fidelity of such devices to detect faults and reduced the risk of false trips.

Overall, the setting-less relays have a significant impact on modern power systems and would likely evolve in the future to meet the demands for a more complex protection for a complex network.

8. Conclusions

We can summarize the project in the following points:

Understood the need for high-fidelity modelling.
Learned about different kinds of legacy protection devices.
Performed an evaluation of Legacy protection devices in systems with IBR penetration.
Proposed a possible future solution with minimalistic drawbacks.

We saw that with high penetration of IBR's the numerical relays mis-operate during faults due to the characteristics of the IBR to suppress negative and zero sequence currents in the system, this in turn results in the settings of these numerical relays to be obsolete. These relays now must be manually tuned to accommodate for this characteristic. This is a tedious task and can be expensive and laborious as the numerical relays need to be "pre-set" every time a renewable energy source is added to the grid since these sources most commonly the wind energy and solar P.V's utilize inverters for transmission of their energy.

A solution was proposed by researchers and industry experts in the papers at the start of the report, this included the addition of negative and zero sequence components into the algorithm of certain numerical relays, modifying the controller design of the inverter (Voltage source converter) etc. but there were a lot of drawbacks in the solutions proposed such as:

Most solutions are proposed with Wind farm technology in mind, the solar P.V has different characteristics that need to be incorporated such as MPPT, average insolation etc. which can further cause changes in the VSC control algorithm.

Numerical relays must coordinate between each other, the concept of coordination was introduced during electromechanical relays, it provided a time delay for the relays upstream so that they do not trip for faults downstream and instead the relays near the faults trip first. Nowadays numerical relays have most of the older relays designed but still have the concept of coordination time inbuilt. These solutions do not accurately describe the effect of coordination time (time delay) on the protection of the network.

As stated earlier the grid is ever expanding and more and more renewables are added every day, this results in having to "pre-set" the relays every time a new renewable is added as it incorporates inverters.

Most of the existing solutions are unique and as such cannot be implemented in the network as certain solutions do not work for certain applications. Therefore, incorporating unique solutions makes it harder to track them.

Finally, these solutions may sometimes be expensive as the numerical relays need to be modified or the VSC controller needs to be modified (2 most general cases), it may seem that we can just implement the logic within the relays, but we need to do that for the existing relays and modifying several relays every time a new renewable is added is economically expensive and non-feasible.

References

[1] Y. Fang, K. Jia, Z. Yang, Y. Li and T. Bi, "Impact of Inverter-Interfaced Renewable Energy Generators on Distance Protection and an Improved Scheme," in IEEE Transactions on Industrial Electronics, vol. 66, no. 9, pp. 7078-7088, Sept. 2019, doi: 10.1109/TIE.2018.2873521.

[2] A. Banaiemoqadam, A. Hooshyar and M. A. Azzouz, "A Control-Based Solution for Distance Protection of Lines Connected to Converter-Interfaced Sources During Asymmetrical Faults," in IEEE Transactions on Power Delivery, vol. 35, no. 3, pp. 1455-1466, June 2020, doi: 10.1109/TPWRD.2019.2946757.

[3] S. Paladhi and A. K. Pradhan, "Adaptive Distance Protection for Lines Connecting Converter-Interfaced Renewable Plants," in IEEE Journal of Emerging and Selected Topics in Power Electronics, vol. 9, no. 6, pp. 7088-7098, Dec. 2021, doi: 10.1109/JESTPE.2020.3000276.

[4] L. He, C. -C. Liu, A. Pitto and D. Cirio, "Distance Protection of AC Grid With HVDC-Connected Offshore Wind Generators," in IEEE Transactions on Power Delivery, vol. 29, no. 2, pp. 493-501, April 2014, doi: 10.1109/TPWRD.2013.2271761.

[5] A. Hooshyar, M. A. Azzouz and E. F. El-Saadany, "Distance Protection of Lines Connected to Induction Generator-Based Wind Farms During Balanced Faults," in IEEE Transactions on Sustainable Energy, vol. 5, no. 4, pp. 1193-1203, Oct. 2014, doi: 10.1109/TSTE.2014.2336773.

[6] H. Lund and B. V. Mathiesen, “Energy system analysis of 100% renewable energy systems—The case of Denmark in years 2030 and 2050,” Energy, vol. 34, no. 5, pp. 524–531, 2009.

[7] Z. Shuai, C. Shen, X. Yin, X. Liu, and Z. J. Shen, “Fault analysis of inverter-interfaced distributed generators with different control schemes,” IEEE Trans. Power Del., vol. 33, no. 3, pp. 1223–1235, Jun. 2018.

[8] H. M. Hasanien, “An adaptive control strategy for low voltage ride through capability enhancement of grid-connected photovoltaic power plants,” IEEE Trans. Power Syst., vol. 31, no. 4, pp. 3230–3237, Jul. 2016.

[9] Y. Wang and B. Ren, “Fault ride-through enhancement for grid-tied PV systems with robust control,” IEEE Trans. Ind. Electron., vol. 65, no. 3, pp. 2302–2312, Mar. 2018.

[10] K. Jia, Z. Yang, Y. Fang, T. Bi, and M. Sumner, “Influence of inverter-interfaced renewable energy generators on directional relay and an improved scheme,” IEEE Trans. Power Electr., vol. 34, no. 12, pp. 11843–11855, Dec. 2019.

[11] https://spectrumlocalnews.com/nys/rochester/weather/2022/08/09/a-brief-look-back-at-the-northeast-power-outage-of-2003.

[12] EPRI Report, "Grid Transformation Workshop Results," April 2012

[13] E. Farantatos, G. K. Stefopoulos, G. J. Cokkinides, and A. P. S. Meliopoulos, "PMU-based dynamic state estimation for electric power systems," in Proc. IEEE PES General Meeting, 2009.

[14] R. Huang, E. Farantatos, G. J. Cokkinides, and A. P. S. Meliopoulos, "Substation based dynamic state estimator - numerical experiment," in Proc. IEEE PES Transmission and Distribution Conference and Exposition, New Orleans, 2010.

[15] A. P. S. Meliopoulos, G. J. Cokkinides, F. Galvan, B. Fardeanesh, and P. Myrda, "Delivering accurate and timely data to all," IEEE Power and Energy Magazine, vol. 5, pp. 74-86, May 2007.
[16] A. P. S. Meliopoulos, G. J. Cokkinides, C. Hedrington, and T. L. Conrad, "The supercalibrator - A fully distributed state estimator," in Proc. IEEE PES General Meeting, 2010.
[17] F. C. Schweppe,R. D. Masiello, "A Tracking Static State Estimator," Power Apparatus and Systems, IEEE Transactions on, vol. PAS-90, pp. 1025-1033, 1971.
[18] G. Stefopoulos, G. J. Cokkinides, and A. P. S. Meliopoulos, "Expert symbolic transient simulator based on quadratic integration method," in Proc. the 13th International Conference on Intelligent Systems Application to Power Systems, 2005, pp. 347-353.
[19] G. K. Stefopoulos, G. J. Cokkinides, and A. P. S. Meliopoulos, "Quadratized model of nonlinear saturable-core inductor for timedomain simulation," in Proc. IEEE PES General Meeting, 2009.
[20] A. P. Meliopoulos, G. J. Cokkinides, and G. K. Stefopoulos, "Quadratic Integration Method," in Proceedings of the 2005 International Power System Transients Conference (IPST 2005), Montreal, Canada, 2005.
[21] https://control.com/textbook/electric-power-measurement-and-control/instantaneous-and-time-overcurrent-5051-protection/
[22] https://circuitglobe.com/differential-protection-relay.html
[23] https://www.electrical4u.com/distance-relay-or-impedance-relay-working-principle-types/
[24] A. P. S. Meliopoulos, G. J. Cokkinides, Z. Tan, S. Choi, Y. Lee and P. Myrda, "Setting-Less Protection: Feasibility Study," 2013 46th Hawaii International Conference on System Sciences, Wailea, HI, USA, 2013, pp. 2345-2353, doi: 10.1109/HICSS.2013.628.
[25] S. Vejdan and A. P. Meliopoulos, "The impact of instrumentation errors on dynamic state estimation-based protection," 2017 IEEE Power & Energy Society General Meeting, Chicago, IL, USA, 2017, pp. 1-5, doi: 10.1109/PESGM.2017.8274263.
[26] C. Zhang, G. Song, A. P. S. Meliopoulos and X. Dong, "Setting-Less Nonunit Protection Method for DC Line Faults in VSC-MTdc Systems," in IEEE Transactions on Industrial Electronics, vol. 69, no. 1, pp. 495-505, Jan. 2022, doi: 10.1109/TIE.2021.3050380.
[27] O. Vasios, S. Kampezidou and A. P. S. Meliopoulos, "A Dynamic State Estimation Based Centralized Scheme for Microgrid Protection," 2018 North American Power Symposium (NAPS), Fargo, ND, USA, 2018, pp. 1-6, doi: 10.1109/NAPS.2018.8600675.
[28] G. I. Maldonado, "The performance of North American nuclear power plants during the electric power blackout of August 14, 2003," IEEE Symposium Conference Record Nuclear Science 2004., Rome, Italy, 2004, pp. 4603-4606 Vol. 7, doi: 10.1109/NSSMIC.2004.1466907.
[29] https://ietresearch.onlinelibrary.wiley.com/doi/full/10.1049/smt2.12016
[30] https://www.prioritywire.com/specs/ACSR.pdf
[31] A. M. El-Hadidy and C. Rehtanz, "Early detection of tree faults," 22nd International Conference and Exhibition on Electricity Distribution (CIRED 2013), Stockholm, 2013, pp. 1-5, doi: 10.1049/cp.2013.0913.
[32] S. Nuchprayoon and A. Chaichana, "Performance Comparison of Using ACSR and HTLS Conductors for Current Uprating of 230-kV Overhead Transmission Lines," 2018 IEEE International Conference on Environment and Electrical Engineering and 2018 IEEE

Industrial and Commercial Power Systems Europe (EEEIC / I&CPS Europe), Palermo, Italy, 2018, pp. 1-5, doi: 10.1109/EEEIC.2018.8493888
[33] NERC Disturbance Report, "1,200 MW Fault Induced Solar Photovoltaic Resource Interruption Disturbance Report", June 2017.

Part III

Load and Inverter Based Resources Dynamic Response Analysis

Venktataramana Ajjarapu
Aditya Shankar Kar, Graduate Student

Iowa State University

For information about this project, contact

Venkataramana Ajjarapu
Iowa State University
Department of Electrical and Computer Engineering
Ames, Iowa, USA 50011-3060
Phone: 515-294-7687
Fax: 515-294-4263
Email: vajjarap@iastate.edu

Power Systems Engineering Research Center

The Power Systems Engineering Research Center (PSERC) is a multi-university Center conducting research on challenges facing the electric power industry and educating the next generation of power engineers. More information about PSERC can be found at the Center's website: http://www.pserc.wisc.edu.

For additional information, contact:

Power Systems Engineering Research Center
Arizona State University
527 Engineering Research Center
Tempe, Arizona 85287-5706
Phone: 480-965-1643
Fax: 480-727-2052

Notice Concerning Copyright Material

PSERC members are given permission to copy without fee all or part of this publication for internal use if appropriate attribution is given to this document as the source material. This report is available for downloading from the PSERC website.

© 2023 Iowa State University. All rights reserved

Table of Contents

List of Figures

List of Tables

1. Introduction

1.1 Background

Historically, dynamic load modeling in power systems has evoked very high attention from transient, long-term, and small-signal stability studies. In [1], a variety of load models that can be used for performing transient studies is presented. Induction motors consume a significant portion of the total load power [2] [3], and hence their behavior has critical impacts on the power system dynamics. In combination with static ZIP load components, it forms the substation load model that is both simple and commonly used. An aggregated induction motor model is summarized in [2]. Studies using such aggregated load modeling and parameter estimation using measurement data have been presented in [4] [5] [6] [7] [8]. In [9], a probabilistic model of the load with many induction motors is presented to study the cascading stall of a power system.

When an induction motor stall following a severe disturbance, it can draw 5 to 8 times its normal reactive power requirement [10], which may delay the voltage recovery and may lead to the tripping of loads and rapid collapse of an area power system [11]. This phenomenon is the cause of the Fault Induced Delayed Voltage Recovery (FIDVR), and therefore, it is very important to study the dynamics, using a model that includes not only a dynamic model based on the induction motor state variables but also its stalling, tripping and reconnecting characteristics which can vary from the type and size of the motors.

Considering the significant impact of induction motor dynamics, Western Electricity Coordinating Council (WECC) load modeling task force included equivalent induction motors. along with the trip and reconnect characteristics to the existing ZIP load models. Single-phase air conditioner (A/C) model with stalling characteristics has also been added to this aggregated model and is known as the Composite Load Model (CLM).

The WECC CLM shown in Figure 1 is discussed in detail in [12] [13]. The load types are classified under 3 main categories: static load, induction motor load, and electronic load. Along with the loads, distributed photo voltaic resources in distribution system are represented by an aggregated distributed energy resource (DER) model. Static load is represented by the load that is exponentially dependent on the load bus voltage. Typically, these exponents correspond to the conventional ZIP model. Induction motors are further classified into 3 types of 3-phase induction motors (A, B, C) depending upon their application and one single-phase induction motor (D), which represents the motors used in A/C compressors. The lumped feeder impedance and the feeder shunt compensation are represented by $\mathrm{R_f}\,,\ \mathrm{X_f}\ and\ \mathrm{B_f}$, respectively. Complete CLM which includes DER consist of 175 parameters where the number of parameters in DER model are 132.

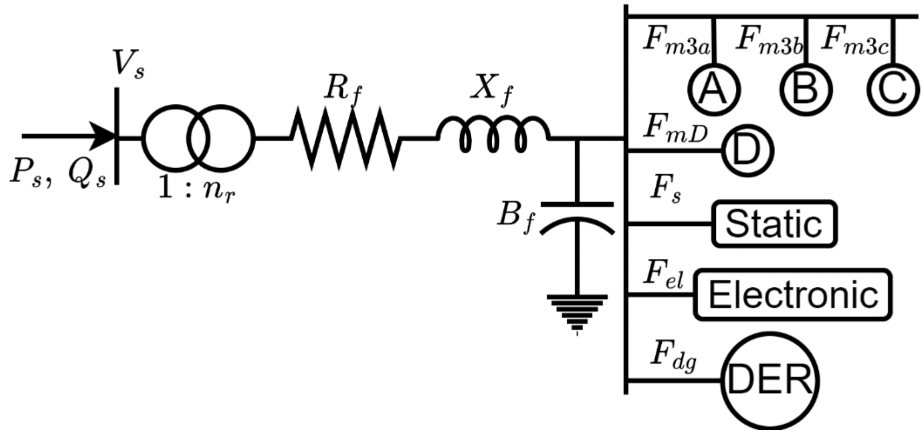

Figure 1 The WECC aggregated Composite Load Model (CLM) [12]

1.2 Motivation

A great challenge lies in tuning this CLM represented by 175 parameters. In reality, there are numerous individual loads of various types, it is a very complex task to determine the parameters of such a load model and ascertain the dynamic performance of the system under study [14]. In [15] [16], the challenges of the sensitivities in model parameter estimation are discussed. Due to the lack of a systematic approach to determine the parameter values, most often, only generic values are used for the parameters. Several efforts have been undertaken by WECC, various National Labs and Electric Power Research Institute (EPRI) towards enhancing the adoption of the CLM by the utilities. [14] describes a bottom-up approach to identify the overall CLM load compositions from the individual loads in the DS. [17] discusses the process to generalize the load model calibration methodology developed for WECC to address the FIDVR phenomenon in planning studies. However, none of these studies explicitly utilize the full DS model with dynamics for individual loads.

With the increasing use of data-analysis tools by utilities on DS measurements, new sensors (μPMUs [18], continuous point-on-wave [19], etc.) and the increasing penetration of DERs, we believe that the distribution system operators (DSOs) will have information about the downstream DS dynamics soon. The importance to the transmission system (TS) and distribution system (DS) co-simulation is also growing after the NERC and FERC, USA reported that the netting of DERs for bulk power systems in not recommended to accurately capture the impact of DERs on bulk grids, especially when they provide ancillary services [20] [21]. But, integrating many DS dynamic models with the TS model in a single simulation will lead to an unwieldy and impractical model, and higher computational time. It is beneficial to reduce the DS models size and retain the full DS dynamics for the faster simulations.

The increasing number of distribution generation (DG) connected via smart inverters in the distribution system is also fundamentally altering the overall dynamics of the load, as seen by the bulk transmission grid. It is now necessary to consider the dynamic behavior of the DGs and inverters in the distribution grid and their interaction with other loads, such as motors, after an event (fault, etc.) in the bulk grid. Furthermore, these devices have many control parameters that can drastically alter the behavior of the dynamics. Hence, it is important for the grid operators/owners to identify and estimate the critical parameter values to ensure system stability over a wide range of operating conditions.

1.3 Objective

The objective of the current research is to develop a reduced order distribution system model (RDSM) in the lines of the WECC Composite Load Model (CLM) which is one of the most comprehensive aggregated load models used in transmission system dynamic studies. Parameters of the composite load models in reduced distribution systems will be optimally selected to match the terminal characteristics of full distribution system. The proposed Reduced Distribution System Model (RDSM) will facilitate the simulation of large power system with improved distribution system details. This will also have an added advantage of solving the optimization problem faster as the number of nodes is reduced from the original system. Apart from the RDSM, we will also identify the critical settings of inverter-based resources such as grid forming inverter (GFM) using the global sensitivity analysis. This sensitivity analysis of the parameters can be utilized for the tuning of the control parameters and for the estimation of the GFM inverter parameters to match their dynamic responses.

2. Development of Reduced Order Distribution System Models

2.1 Distributed load model Vs Aggregated load model

Distributed load model comprises of a CLM representation of each load in a distribution system. In contrast to the aggregated CLM, which consists of one big motor of each type, the distributed load model comprises numerous actual real-size motors. In the CLM, if there is an under-voltage trip or a thermal trip, either a fraction is considered as tripped (in the case of three-phase induction motors) or the entire motor trips (in the case of single-phase induction motors). If a fraction trips, then the CLM assumes a part of the motor load is dropped and so the motor operates at a different operating point on the Torque-Speed curve. And when a fraction reconnects, the load is correspondingly increased. The Combined Transmission-Distribution System (CoTDS) co-simulation-based distributed load model shown in Figure , on the other hand, captures the behavior of motors tripping and reconnecting to start from zero or very low speed.

Table 1 Key differences between aggregated CLM and distributed load model

	Aggregated CLM	**Distributed Load Model**
Load	Aggregated at one node	Distributed across the feeder
No. of IMs	One of each type	Numerous
No. of fractions of 3-ϕ IM	Two of each type	Flexible
No. of fractions of 1-ϕ IM	One	Flexible
Under-voltage trip of 3-ϕ IM	Fraction of load drops and speed increases.	Fraction of motors disconnect and speed drops
Reconnection of 3-ϕ IM	Fraction of load increases and speed drops	Motors reconnect and their speed increases
Stalling of 1-ϕ IM	Entire motor stalls	Only fraction of motors stall
Behaviour capture	Average	Detailed

All the parameters of the CLM, as provided by WECC load modeling, are important for conducting transient studies. Many of the parameters need to be changed from their default value in accordance with the load system under study. The individual fraction of each of the load types determines the overall composition of the load and plays a vital role in the dynamic behavior. The equivalent feeder impedance significantly influences the voltage dip and duration of recovery.

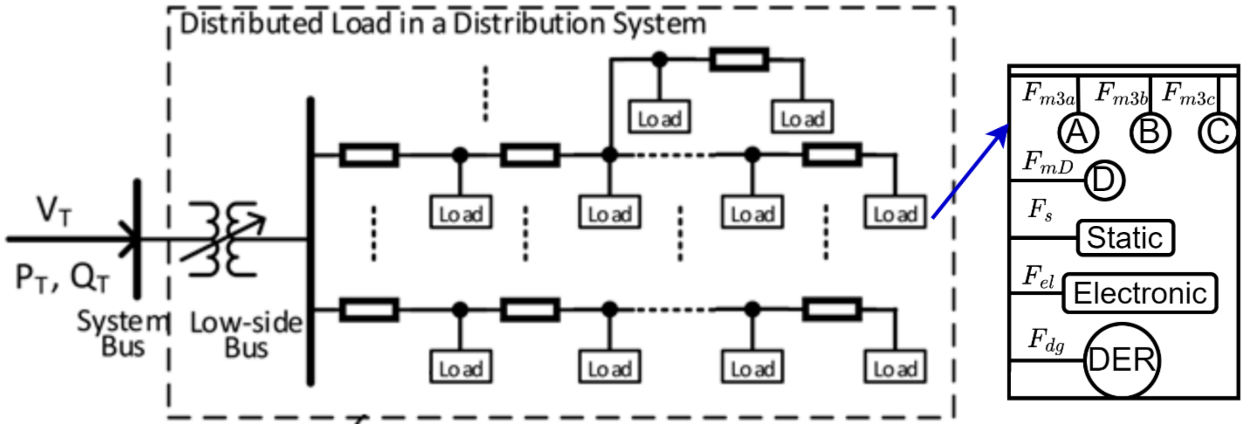

Figure 2 The Distributed Load Model

Therefore in this study, the parameters of load fractions, $F_{mA}, F_{mB}, F_{mC}, F_{mD}, F_{el}$ and the equivalent feeder impedance, $R_f + jX_f$ are identified as those which needs to be calculated to equivalently represent the distribution system as shown in Figure 3. The procedure for determining these identified parameters is now described. First, the CoTDS co-simulation is run until a steady state is reached. The interface variables provide the values for the transmission system bus voltage, V_T and the distribution system source power P_T, Q_T . The load at node, n is given by (pn, qn) for a total of N nodes in the distribution system. The distribution system power ow gives the node voltages at all the load nodes V_n for n = 1 to N. The sum total of the entire load power given by the terms, P_L and Q_L, is determined by the following equation.

$$P_L = \sum_{n=1}^{N} p_n \,; Q_L = \sum_{n=1}^{N} q_n$$

The load on each of the distribution system nodes is classified into the load types similar to the CLM, i.e., static, electronic, 3-phase induction motors (Type A, B, and C) and single-phase A/C motor load (Type D). It is assumed that the fraction of load type given by $f_n^S, f_n^E, f_n^A, f_n^B, f_n^C, f_n^D, f_n^{DG}$ is known on each node and their sum total to 1.

$$f_n^S + f_n^E + f_n^A + f_n^B + f_n^C + f_n^D = 1$$

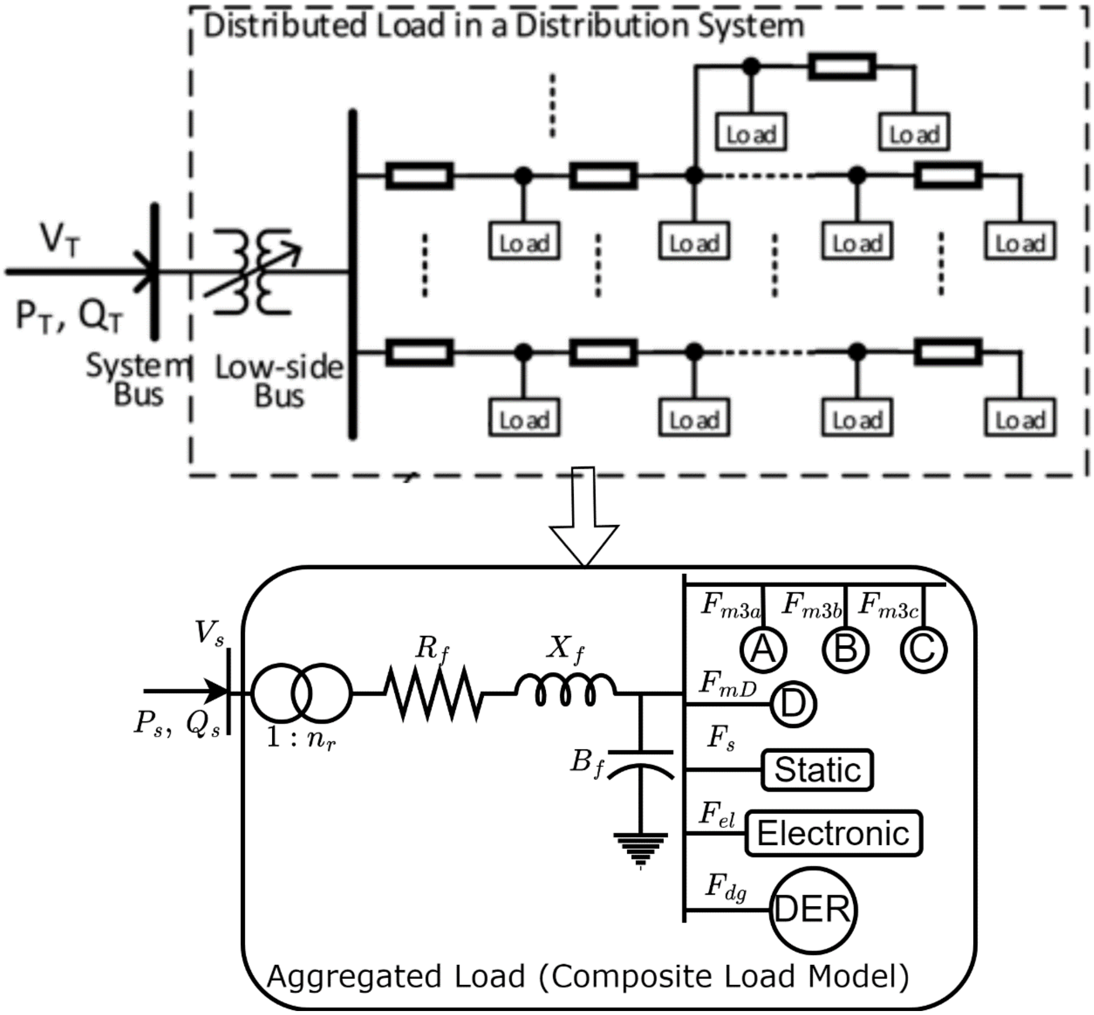

Figure 3 CLM representation of the distribution system.

2.2 FIDVR behavior using distributed load models and aggregated CLM.

The CoTDS dynamic simulation is set up with a test case as shown in Figure 4 using a WECC 9-bus transmission system interfaced at Bus 6 with a distribution system feeder comprising of 40 sub-systems. The total load on each sub-system is 2.5MW, 0.75MVar.

The objective is to study the FIDVR behavior using the distributed load model and compare it with the conventional aggregated CLM. In this study, the distribution system load in each of the nodes consists of load fractions, $f_n^S = 0.1, f_n^E = 0.1, f_n^A = 0.2, f_n^B = 0.1, f_n^C = 0.1, f_n^D = 0.4$. The system is subjected to a 3-phase to GND fault for 83ms (5 cycles) on Bus 5 of the transmission system. This leads to a FIDVR phenomenon due to the stalling of the single-phase A/C motors.

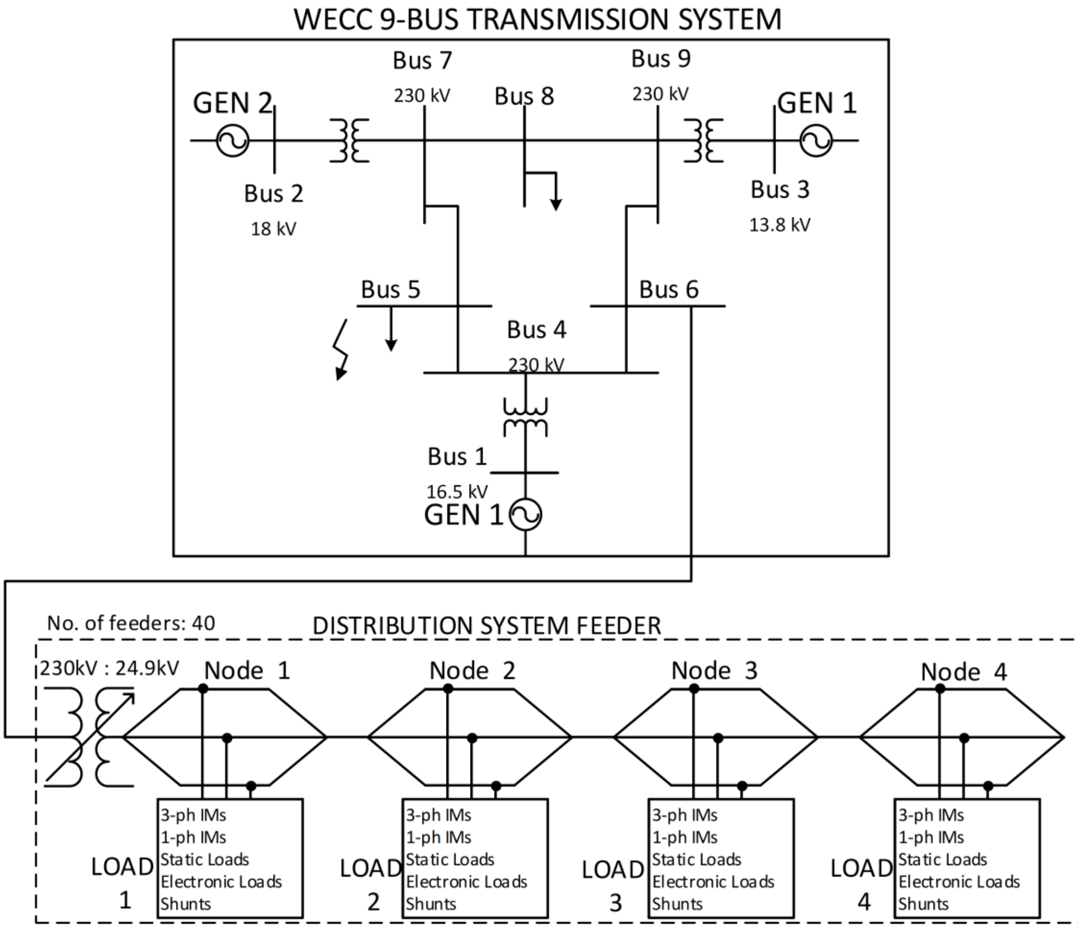

Figure 4 WECC 9-bus system and 40 sub-systems of a 4-node distribution system feeder.

Figure shows the evolution of the distribution system node voltages during the delayed voltage recovery using the distributed load model. These plots are compared to the load bus voltage obtained by setting nominal load fractions of $f_n^E = 0.1, f_n^A = 0.2, f_n^B = 0.1, f_n^C = 0.1, f_n^D = 0.4$. The feeder impedance is kept at the default value of $R_f = 0.04$ and $X_f = 0.04$. The following inferences can be made by observing these voltage recovery plots.

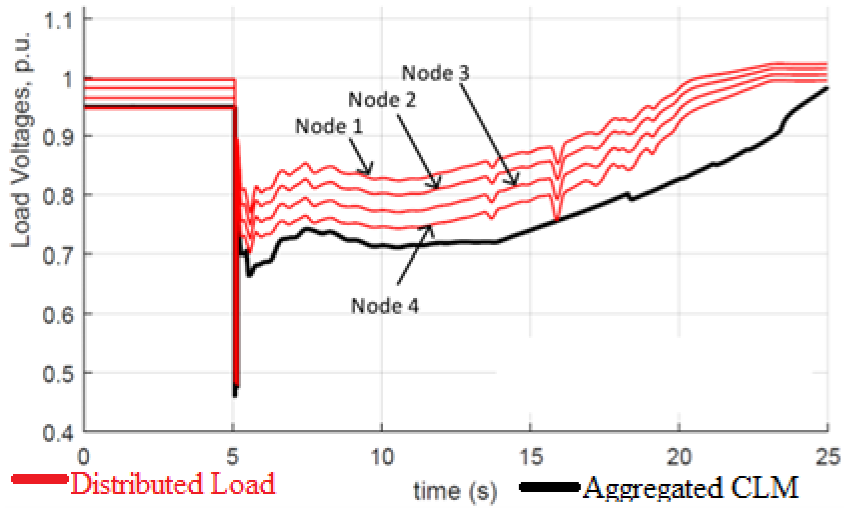

Figure 5 Load bus voltage evolution of CLM at Bus 6 using CLM and node voltages of the distribution system at Bus 6 using distributed load model.

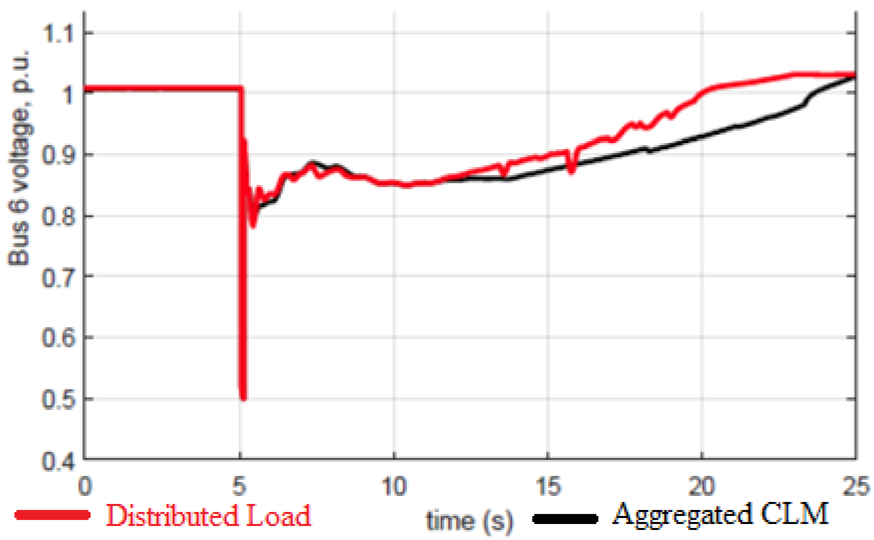

Figure 6 Bus 6 voltage using CLM and aggregated CLM

The load bus plot using the default parameters is not representing the average plot of the distribution system node voltages, and hence the recovery time is also not the same. This is because the default equivalent feeder impedance is larger than that of the distribution system, and so the load voltage is lower, to begin with. This causes the stall power in the single-phase A/C motor to be lower, and therefore the thermal tripping is slower, which in turn causes a longer recovery time. The distribution system node voltages in Figure with the distributed load model show sharp dips, whereas the equivalent load voltage with the CLM is smoothly recovering. This shows that the distributed load model is capturing behavior that is not seen using the CLM. Upon further examination of the distributed load model results, the 3-Φ induction motors that trip during the fault due to U/V, drop their speed. It is evident that the parameters of the CLM model needs proper tuning and use of default parameters leads to inaccurate representation of the distribution system. It is also known fact that the detailed representation of the distribution systems is complex and leads to higher computational burden. We present the development of reduced order distribution system models to retain the dynamics of full distribution systems by optimally selecting the parameters of the CLMs in the reduced order model.

2.3 Reduced distribution system modelling.

2.3.1 Identification of load area

Consider a radial distribution system shown in Figure with several nodes, with each node comprising static, electronic motor loads (3-φ and 1-φAC motors) and DG inverters. Measurement devices such as µPMUs measure load voltage and power in the distribution lines/loads at sub-second intervals. The objective is to reduce the number of nodes and represent the load at each measurement node using an aggregated dynamic model that captures the overall dynamic behavior of the full model. The placement of µPMUs is a problem that is beyond the scope of this work. Here it is assumed that they are placed at nodes where secondary feeders and large loads are connected to the primary feeder. Figure displays the resulting reduced order model (ROM) of the distribution system, with each cluster represented as a sub-model (composite load model).

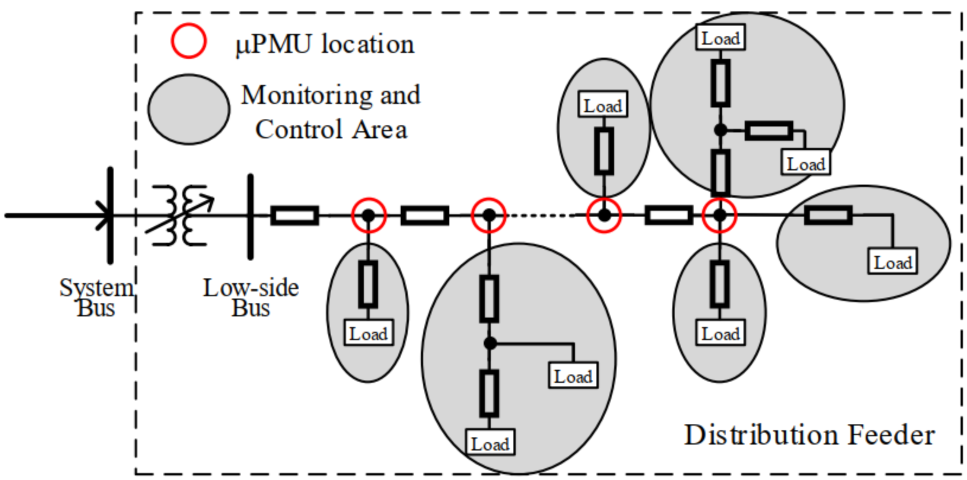

Figure 7 Radial distribution system with µPMUS installed in some nodes

2.3.2 Sub-Model based on Load Areas

The proposed RDSM is made up of several sub-models connected in a structure similar to the original topology, as shown in Figure . The sub-model is analogous to the CLM described previously with selected parameters to represent relevant portions of the DS with an equivalent feeder impedance, a load tap changing transformer and a load block. The load block includes static load, IM loads, and PV inverter. The static load parameters correspond to the conventional ZIP model. The electronic loads are absorbed into the constant power parameters of the ZIP load. The

3-φ IM (A, B, C type motors of the CLM) are lumped into one motor, and the 1-φ IM (Type D of the CLM) represents the motors used in residential A/C compressors. Table I shows the relevant parameters of the sub-model that would represent the portion of the DS network. Here, Fs, Fm1, and Fm3 are the fractions of the corresponding loads, and Fdg is the fraction of the equivalent DG in that portion of the network. Rf, Xf, Bf, and nr are the parameters of the equivalent feeder impedance. The static load, the 3-φ IM, and the 1-φ IM and DG inverter are represented by the parameters in the respective columns in Table I and these parameters are defined in the WECC CLM specifications [5].

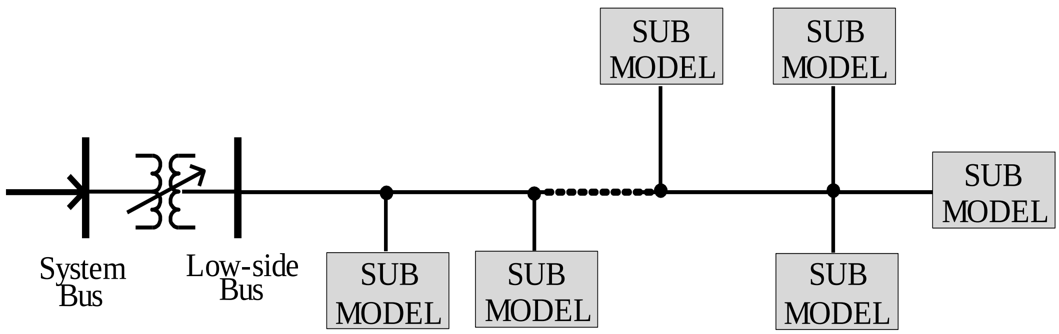

Figure 8 Resulting ROM structure of the distribution system

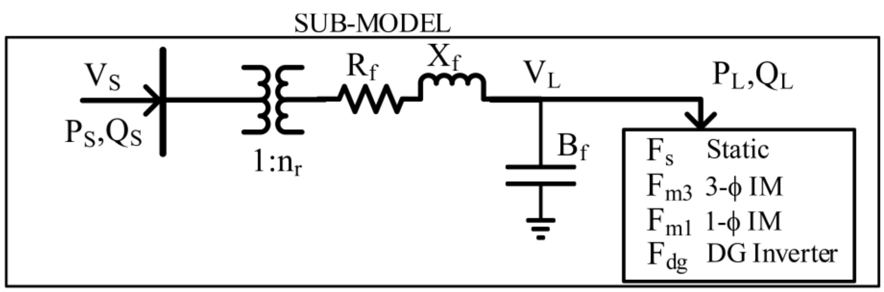

Figure 9 Components of sub model

Table 2 Parameters of the sub-model of the RDSM

Load Fraction	**Equiv. Feeder**	**Static (ZIP)**	**3ϕ IM.**	**1ϕ IM**	**DERs**
Fs	Rf	Pz0	Rs	Vstall	Fdg
Fm1	Xf	Qz0	Xls	Tstall	GFM/GFL
Fm3	Bf	Pi0	Xm	Rstall	Volta-Var
Fpv	nr	Qi0	Rr1	Xstall	F-Control
		Pp0	Xlr1	T_{th}	

		Qp0	Rr2	θ_1	
		Qsh0	Xlr2	θ_2	
			H		

2.4 RDSM Parameter Estimation

The dynamic data that is required is obtained by performing a Gridlab-D simulation on a system comprising a single generator or a substation connected to the distribution system under study. The substation can either be a test system or an equivalent of a large transmission system under study. Since the purpose here is to generate a large amount of surrogate data from the distribution system, it is not necessary to consider the entire transmission system. The entire system becomes necessary at a later stage when studying or validating the FIDVR control and mitigation scheme.

The sub-model parameters are classified into steady-state network parameters and dynamic load parameters. The steady-state network parameters correspond to the equivalent feeder impedance, and the dynamic parameters correspond to the load component parameters, as given in Table I. The fraction of each of the load types and DGs is estimated based on the load composition and available data.

In the absence of real measured data, surrogate data obtained from a Gridlab-D simulation is used. The steps to determine these parameters are [22]:

1. The CoTDS simulation is run using a single generator and a single-line transmission system, and the distribution system needs to be reduced.
2. The steady-state data of the sub-station voltage, the active power, reactive power, and the voltage data at all the nodes of the distribution feeder are used to determine the equivalent feeder parameters.
3. The dynamic data of the voltage, the active power, and the reactive power at the transmission side are recorded. This represents the actual data from the actual load.
4. The values of the parameter set λ of the sub-model are determined using an optimization routine to minimize the error between the time series of the measured data, D, and the calculated values, C(λ).

The objective function of the optimization that needs to be minimized, η(λ), is the sum of squares of the difference between the two-time series and is given by:

$$\eta(\lambda) = [D \; - \; C(\lambda)]^T . [D - C(\lambda)]$$

where C(λ) is the corresponding calculated values of the data set, D, for a given λ. The calculated values C(λ) are obtained by solving the dynamic equations of the sub-model, including the effects of the stalling and thermal tripping of the 1-φ induction motor.

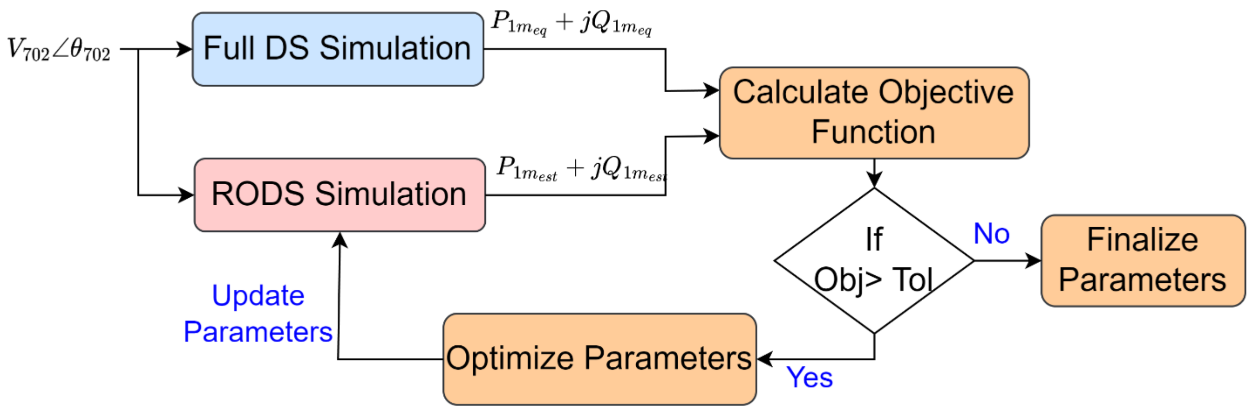

Figure 10 Block diagram of methodology for RDSM parameters determination

2.5 Parameter Estimation of IEEE 37-Node Distribution System

Fig. 5 shows the IEEE 37-node system [6]. This feeder is an actual feeder located in California. The figure shows the node locations where the μPMUs are installed for measuring the voltages and power entering each load area. The load areas, represented by the shaded regions, are required to be reduced to the sub-models. All the sub-models, together with the interconnecting network impedances, will form the RDSM representation of the IEEE 37-node distribution system.

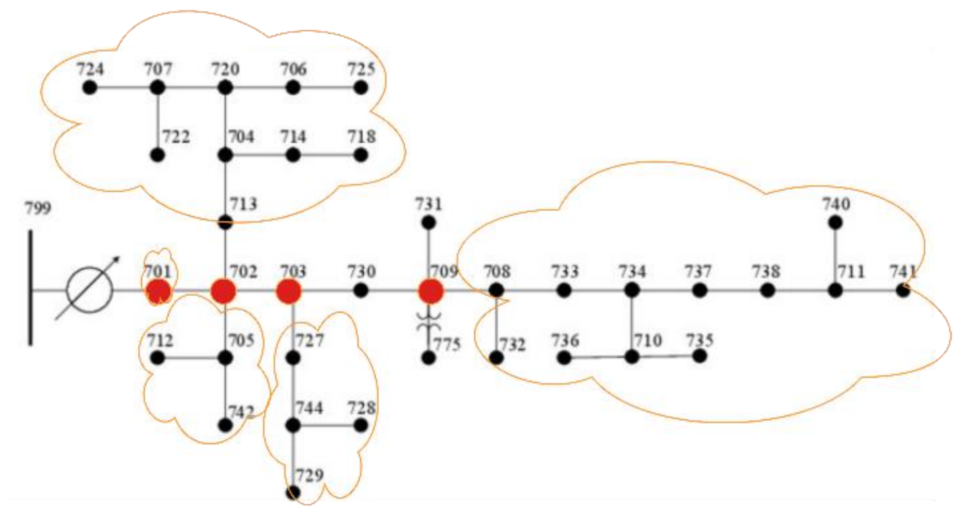

Figure 11 IEEE 37-node system for RDSM parameter estimation [6].

Each of the distribution system loads in the IEEE 37-node feeder is separated into the composite load model components, including static, electronic, 3-φ IM, and 1-φ A/C IM. In order to simulate a realistic scenario, the fraction of loads of each type (Fs, Fm3, and Fm1) is assigned according to a normal distribution around a mean value which is estimated based on the type of loads present in each location [17]. In addition, each of the motor load types which have its own set of parameters to characterize them and has variability included by connecting several motors with a normal distribution of parameters. Along with the dynamic load models in the DS, CLM also consist of aggregated DER model to consider the penetration of distributed resources in DS. In this study we consider 30% penetration of DERs in the DS. Dynamic model of DERs is grid forming with real and reactive power control capabilities [23]. Parameters of DER also included in the development of RDSM.

2.6 Results

Dynamic responses of the detailed distribution system and ROM model are tested in an unbalanced case with the 40% dip in the substation voltage as disturbance. Full distribution stems with each load represented as a composite load consisting of DER is shown in Figure for the 37-node distribution system at Node 702 and further (Area-3). Reduced order model of Area-2 with the composite load model is shown in Figure . Parameters of ROM are estimated suing the methodology presented in Figure .

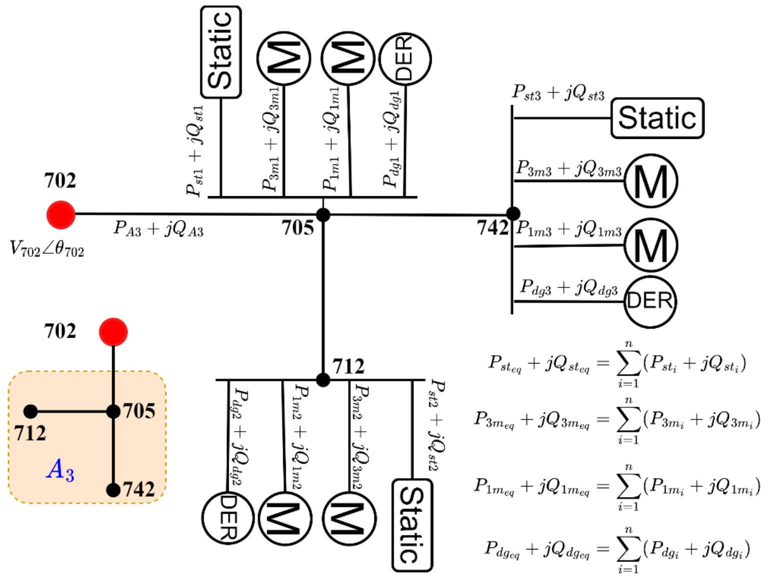

Figure 12 Full distribution system with composite load models at node 702 in 37 bus system

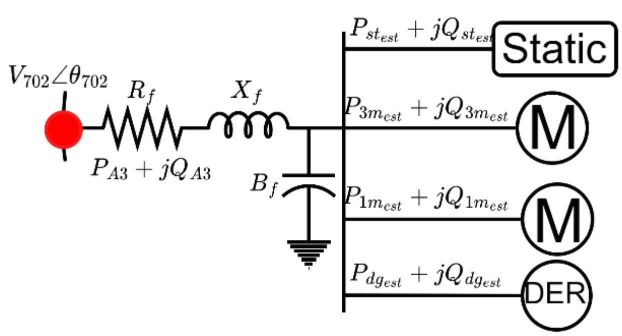

Figure 13 ROM of Area-3 in 37 node distribution system

The real and reactive power at Node 702 in the full distribution system along with the real and reactive power at Noe 702 in distribution system with ROM are shown in Figure . It is evident from the responses that the DS with ROM accurately represents the DS dynamics. After estimating all the ROMs for the subsystems in 37-node distribution system, real and reactive power variations at substation node in both the cases for a voltage dip at the substation are presented in Figure .

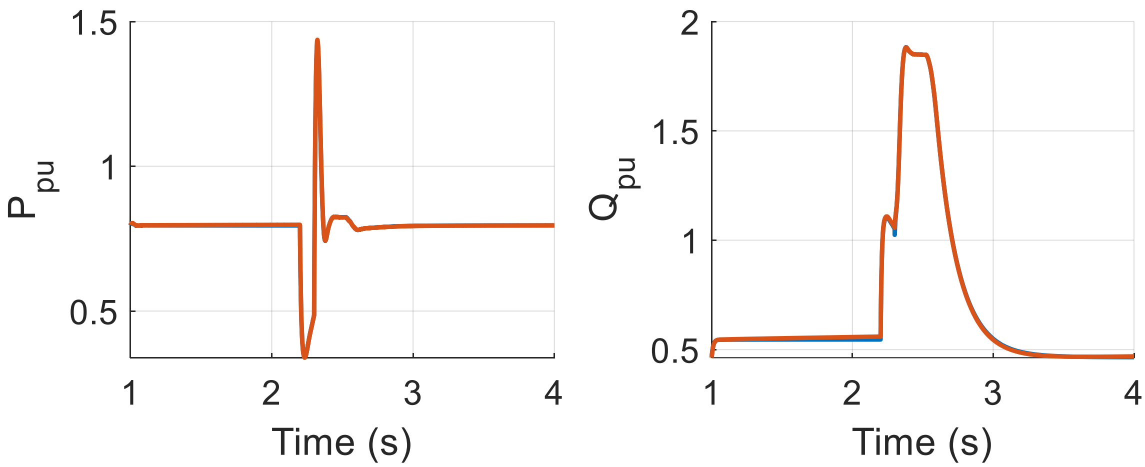

Figure 14 3-Phase real and reactive power at the substation

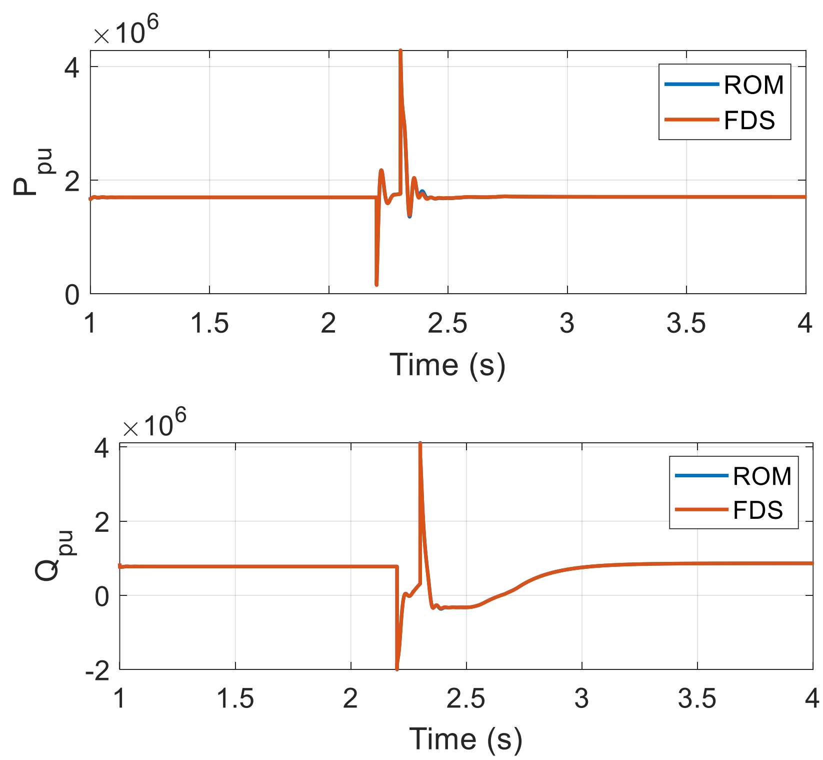

Figure 15 Phase-a real and reactive power at the substation

To test the accuracy of the resulting ROM model, the transmission system with the load represented by ROM is simulated with faults of varying severity levels. The voltages at the point of interconnection are compared, and the error is computed to quantify the accuracy of the ROM. The voltage and reactive power for five fault scenarios are plotted in Figure . It can be seen that there is a close match between the voltages and reactive power with full DS and with the ROM for all the fault levels, making it a much more accurate representation of DS dynamics than a single composite load model. The time-averaged voltage errors for the various fault cases demonstrated that the accuracy is >99% for all the scenarios.

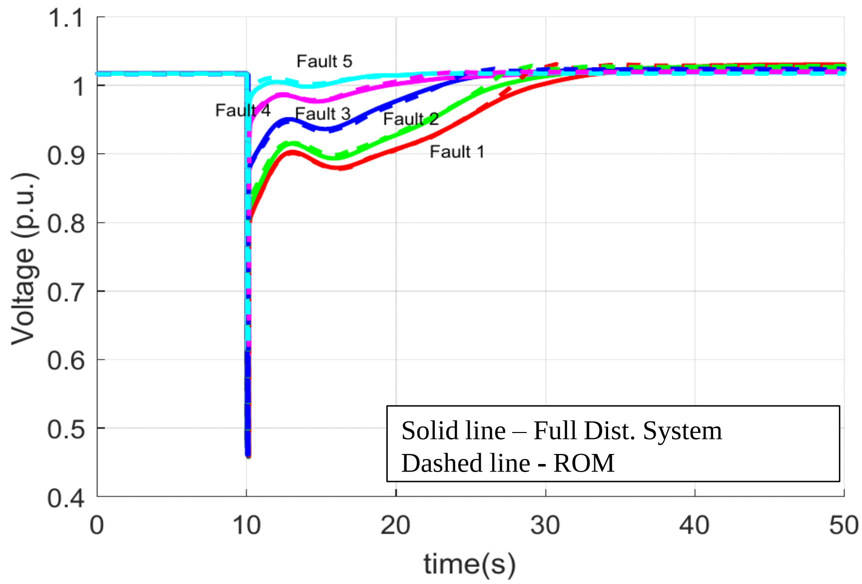

Figure 16 The voltage at the point of interconnection with full DS and the ROM for five fault scenarios

3. Identifying the critical settings of IBRs in distribution system

3.1 Sensitivity analysis of dynamic systems

Dynamic sensitivity analysis evaluates the influences on dependent variables due to variations of parameters, initial conditions, and independent variables. In many practical applications, the input to the system can be time dependent. Sensitivity analysis is also useful in understanding how the parameters and states of a dynamic system influence the output of the system during the disturbances. This sensitivity analysis can be used to tank the parameters in order of influence and obtain initial guesses for parameters for optimal performance of the system. In case the dynamic response of the system is not sensitive to the specific set of parameters then the system is insensitive to those parameters. Sensitivity analysis can be performed using two approaches [24],

- Local sensitivity analysis
- *global sensitivity analysis*

Local sensitivity analysis is derivative based (numerical or analytical) and the sensitivity of the cost function with respect to certain parameters is equal to the partial derivative of the cost function with respect to those parameters. The term *local* refers to the fact that all derivatives are taken at a single point. For simple cost functions, this approach is efficient. However, this approach can be infeasible for complex models, where formulating the cost function (or the partial derivatives) is nontrivial. For example, models with discontinuities do not always have derivatives. Local sensitivity analysis is a *one-at-a-time* techniques which analyzes the effect of one parameter on the model responses at a time, keeping the other parameters fixed. They explore only a small fraction of the design space, especially when there are many parameters. Also, they do not provide insight about how the interactions between parameters influence the desired performance of dynamic system.

G*lobal sensitivity analysis* is based on Monte Carlo techniques which uses a representative (global) set of samples to explore the design space. Global sensitivity analysis is performed using the following steps,

1. Sample the model parameters using their respective normal range. That is, for each parameter, generate multiple values that the parameter can assume. Define the parameter sample space by uniform distributions for each parameter in the specified range. You can also specify parameter correlations.
2. Define system out puts variables to be observed with refer to the parameter variation.
3. Evaluate the variation in output variables at each combination of parameter values using Monte Carlo simulations.
4. Analyze the variation in the output with refer to the parameter sample created.

Relation between the parameters and output measurements is analyzed using the statistical analysis. Statistical analysis can be either linear or ranked analysis. Linear analysis is used when a linear relation between the parameters and output measurements is expected and also the residuals about the best-fit line are expected to be normally distributed. Ranked analysis

(*Spearman* analysis) is used when a nonlinear relation between the parameters and output measurements is expected and the residuals about the best-fit line are not normally distributed.

The correlation between the parameter p(i) and output measurement y(j) is given by [24]

$$R_{ij} = \frac{C_{ij}}{\sqrt{C_{ii}C_{jj}}}$$

Where

$$C_{ij} = cov\big(x(i), y(j)\big) = E\big[(x-\mu_x)(y-\mu_y)\big]$$
$$\mu_x = E[x]$$
$$\mu_y = E[y]$$

x contains N_s samples of N_p model parameters. `y` contains N_s rows, each row corresponds to the cost function evaluation for a sample in `x`. *R* values are in the [-1 1] range. The (i,j) entry of *R* indicates the correlation between *x*(*i*) and *y*(*j*).

- `R(i,j) > 0` — Variables have positive correlation. The variables increase together.
- `R(i,j) = 0` — Variables have no correlation.
- `R(i,j) < 0` — Variables have negative correlation. As one variable increases, the other decreases.

3.2 Positive Sequence Phasor Model of Grid Forming Inverter

A grid-forming inverter behaves as a controllable voltage source behind a coupling reactance [23]. The internal voltage magnitude *E* and angular frequency *ω* are controlled by the droop controller. The inverter main circuit is modeled as a voltage source behind the coupling reactance *XL*, as shown in Figure. The grid-forming controller will adjust the internal voltage magnitude *E* and phase angle δ_E.

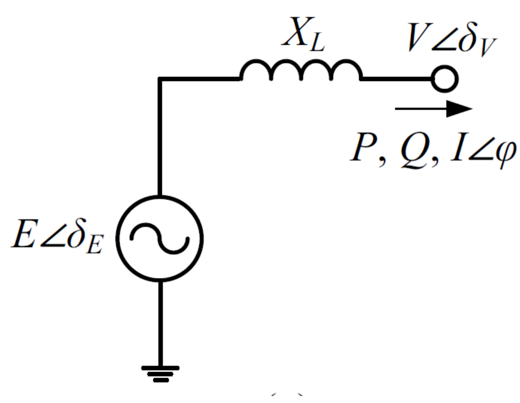

Figure 17 Inverter equivalent circuit with an internal voltage source and the coupling [23]

Figure - Figure show the *P-f* droop control and *Q-V* droop control, which regulate the inverter internal voltage magnitude and phase angle during normal operations. The *P-f* droop control ensures that the phase angles of multiple grid-forming inverters are synchronized during normal operations. When two grid-forming inverters operate in parallel under *P-f* droop control, any disturbance causes an increase in the output power of one inverter. This, causes its *P-f* droop control to reduce the angular frequency ω of the internal voltage so that the phase angle, δ_{droop}, is reduced, preventing the inverter from further increasing its output power. This negative-feedback control mechanism guarantees the synchronization when multiple grid-forming inverters work in parallel. In addition, the controller shown in Figure 18 also prevents the output power of the inverter from exceeding P_{max} or dropping below P_{min}. The *P-f* droop control also achieves load sharing between grid-forming inverters.

The *Q-V* droop control prevents large circulating reactive power between grid-forming inverters. As shown in Figure 19, the *Q-V* droop control guarantees that the magnitude of grid-side voltage has a predefined *Q-V* droop characteristic by regulating E_{droop}, through a proportional-integral controller. In addition, there is also a Q_{max} and Q_{min} controller to prevent the inverter reactive power output from exceeding Q_{max} or dropping below Q_{min}.

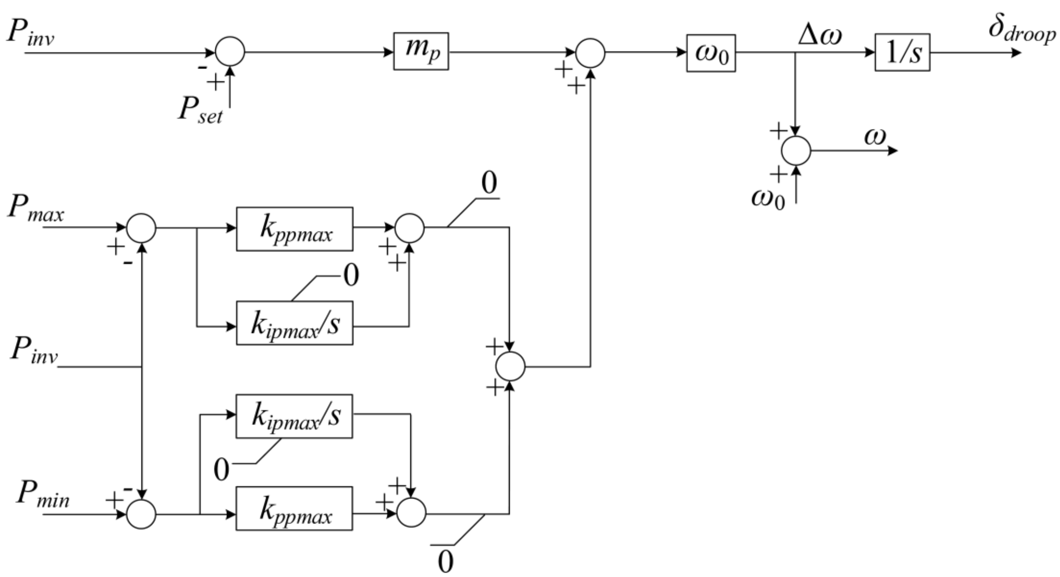

Figure 18 P-f droop control and overload mitigation control of GFM inverter [23]

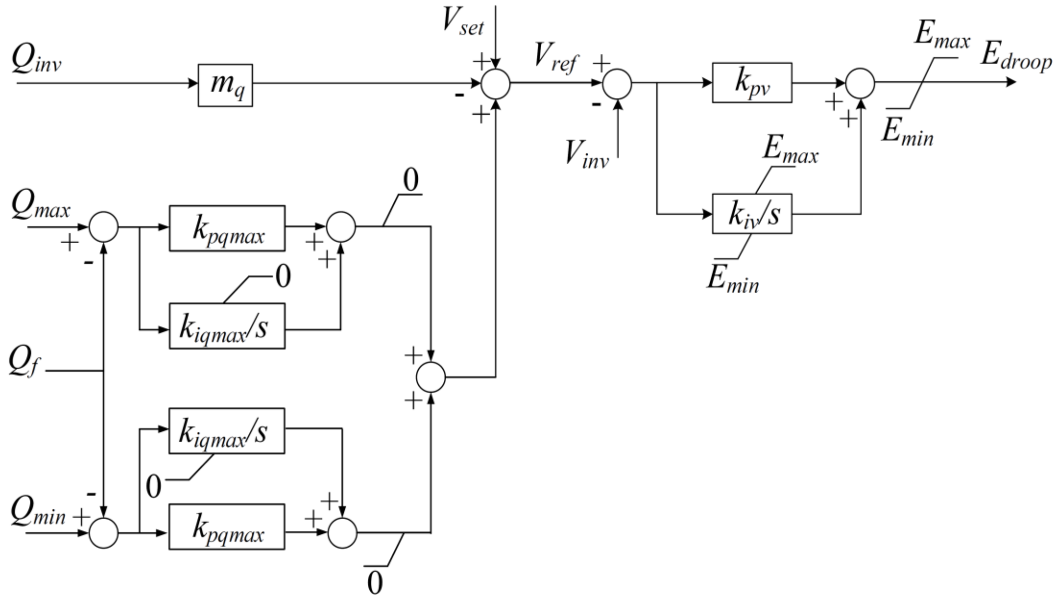

Figure 19 Q-V droop control of GFM inverter [23]

During normal operations, the droop control will control the inverter voltage magnitude and phase angle. However, during short circuit faults, the fault current limiting function will be activated to limit the output current of the inverter. Fig. 4 shows the fault current limiting function. The inverter works in the droop control mode during normal operations and keeps monitoring its output current $I\angle\varphi$. The output current $I\angle\varphi$ is calculated using the equation bellow in each simulation step.

$$I\angle\varphi \ = \ \frac{E_{droop}\angle\delta_{droop} - V\angle\delta_v}{jX_L}$$

When the magnitude of the output current I is smaller than the inverter maximum current limit I_{max}, the inverter internal voltage is governed by the droop control so that $E\angle\delta_E = E_{droop}\angle\delta_{droop}$. However, once I exceed I_{max} because of severe faults, the inverter internal voltage $E\angle\delta_E$ will be calculated based on the inverter terminal voltage $V\angle\delta_V$, the coupling reactance X_L, and the new current phasor $I_{max}\angle\varphi$ as shown by Figure . By doing so the magnitude of the inverter output current I will be limited at I_{max} during faults, but its phase angle φ will remain unchanged compared to the case without the fault current limiting function. Once the fault is cleared, the inverter output current will drop below I_{max} so that the operation mode will autonomously switch back to the droop control mode.

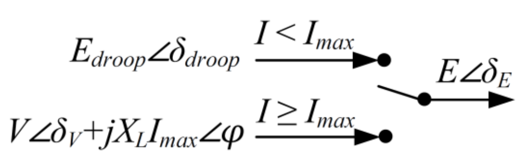

Figure 20 Fault current limiting function in GFM inverter [23]

3.3 Global sensitivity analysis of GFM inverter

Sensitivity analysis is performed for the GFM inverter with it's real and reactive power as output measurements by varying the parameters in the specified rage given in [25]. Initially, local sensitivity analysis is used to find the sensitivity analysis perfomred by analyzing the effect of one parameter on the model responses at a time, keeping the other parameters fixed. Figure - Figure shows the sensitivity of real and reactive power with respect to proportiaonal gain of reactive control (K_{pqmax}) and maximum GFM inverter current (I_{max}) repsectively. When K_{pqmax} is varied from 1 to 5 as per it's nominal range, the variation in the real and reactive power of inverter are insignificant as shown in Figure . This indicates that the GFM inverter responses are insesitive to K_{pqmax}. When I_{max} is varied from 1.5 pu to 3 pu as per it's nominal range, the variation in the real and reactive power of inverter are significantly high as shown in Figure . This indicates that the GFM inverter responses are highly sesitive to I_{max}. Thought the local sensitivity analysis is able to capture the high sensitivity of I_{max}, it failed to capture the sensitivity of K_{pqmax}. This is due to fact that the local sensitivity analysis explores only a small fraction of the design space and do not provide insight about how the interactions between parameters influence the desired performance of dynamic system.

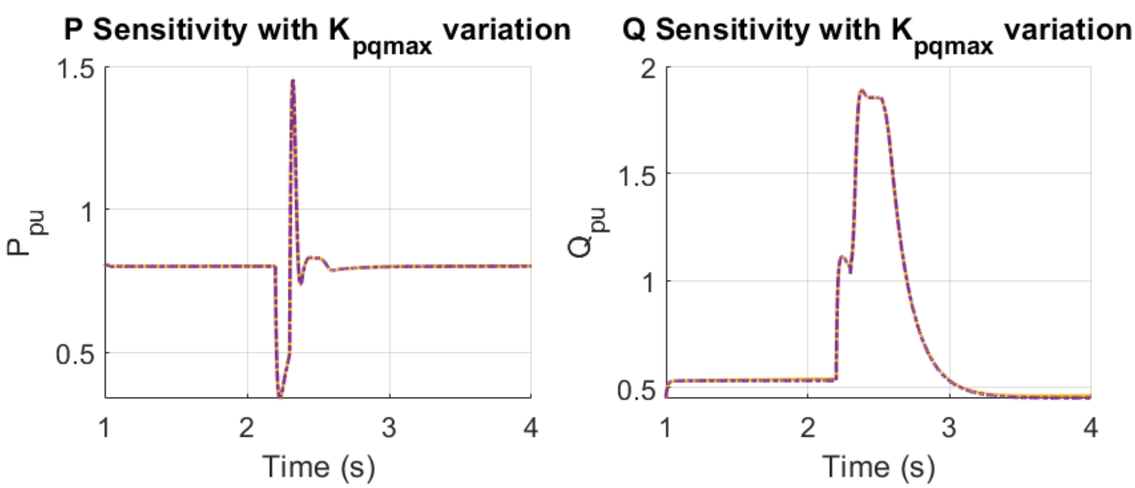

Figure 21 Real and reactive power sensitivity with K_{pqmax}

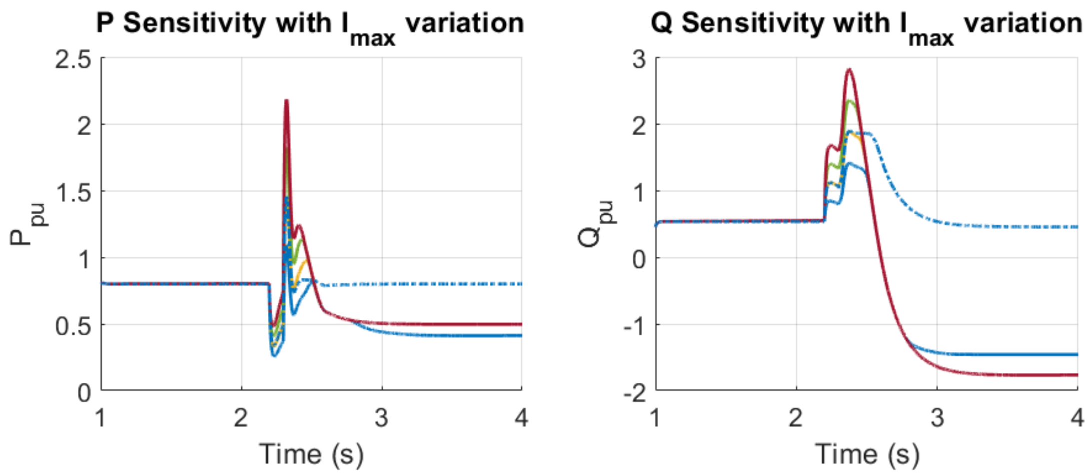

Figure 22 Real and reactive power sensitivity with I_{max}

For the accurate identification of sensitive parameters, G*lobal sensitivity analysis* is performed for the GFM inverter. The parameter sample space is created considering a uniform distribution for each parameter in the specified range. Variation in the output variables is evaluated at each combination of parameter values using Monte Carlo simulations for the parameter sample space created. Correlation between the parameters and output measurements (real and reactive power) is evaluated using the ranked correlation. Figure shows the correlation index for real and reactive power with respect the parameters of GFM inverter.

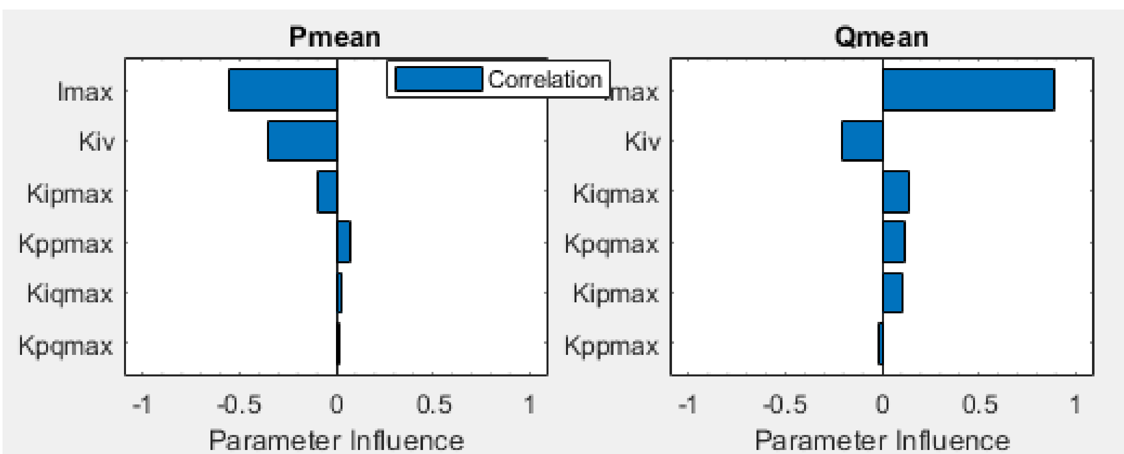

Figure 23 Sensitivity of real and reactive power with GFM inverter parameters

It is evident from the global sensitivity analysis that the maximum current value of the GFM inverter is more critical than the other control parameters and both real and reactive power responses during a disturbance are more sensitive to I_{max}. Global sensitivity analysis also given ranking to the parameters based on their influence on the dynamic response of the real and reactive power. This ranking of the parameters can be utilized for the tuning of the control parameters and for the estimation of the GFM inverter parameters to match their dynamic responses.

4. Conclusions

In this report, a method to identify and reduce distribution system to get a reduced distribution system model (RDSM) is proposed. The proposed RDSM is composed of sub-models that are analogous to the WECC composite load model and aggregates the distribution system into load areas while ensuring the overall dynamics are retained. The modelling approach uses Gridlab-D simulation to generate measurement data using the network topology and load data. This measurement data is employed to estimate the parameters of the RDSM by matching the dynamics of the model to that obtained from the data. The sub-model of the RDSM and CLM used in this study consist of static load, induction motor load, and electronic load along with the distributed energy resources. Proposed RDSM models will facilitates the faster simulation of distribution system models integrated to transmission system for dynamic studies. Single phase models of RDSM can be easily integrated into any transmission system phasor simulation software such as PSS$^{@}$E to further accelerate the co-simulation by eliminating the data exchange delays between the transmission and distribution system simulators. Also, we have analyzed the impact of grid-following and grid-forming inverters on the frequency response of the system after a fault.

Local and global sensitivity analysis is performed on the dynamic models of IBRs to identify the critical parameters. It is evident from the simulation results of local sensitivity analysis that the local sensitivity analyzes the effect of one parameter on the model responses at a time, keeping the other parameters fixed and explore only a small fraction of the design space, especially when there are many parameters. So, the critical parameters of the IBRs are identified though the global sensitivity analysis of grid forming invert based solar photovoltaic (PV) generation. Real and reactive power control loop parameters of GFM inverter along with the maximum current rating are ranked according to their sensitivity on real and reactive power outputs of IBRs during the voltage disturbances.

References

[1] I. T. F. o. L. R. f. D. Performance, "Load Representation for Dynamic Oerformance Analysis," *IEEE Transactions on Power Systems*, pp. 472-482, 1993.

[2] IEEE Task Force on Load Representation for Dynamic Performance, "Standard Load Models for Power Flow and Dynamic Performance Simulation," *IEEE Transactions on Power Systems*, vol. 10, no. 3, pp. 1302-1313, 1995.

[3] I. J. T. Force, "Defination and classification of power system stability," *IEEE Transactions on Power Systems*, vol. 19, no. 2, pp. 1387-1401, 2004.

[4] H.-D. C. e. a. B.-K. Choi, "Development of Composite Load Models of Power Systems using On-line Measurement Data," *IEEE Power and Energy Society General Meeting,* 2006.

[5] A. G. P. P. a. D. B. A. Maitra, "Load model parameter derivation using an automated algorithm and measured data," *IEEE Power and Energy Society General Meeting,* 2008.

[6] M. J. a. D. J. H. H. Renmu, "Composite Load Modeling via Measurement Appoach," *IEEE Transactions on Power Systems*, vol. 21, no. 2, pp. 663-672, 2006.

[7] P. Z. a. V. A. H. Bai, "A Novel Parameter Identification Approach via Hybrid Learning for Aggregate Load Modeling," *IEEE Transactions on Power Systems,* vol. 24, no. 3, pp. 1145-1154, 2009.

[8] D. V.-R. S. D. a. V. T. P. Regulski, "Estimation of Composite Load Model Parameter Estimation Using an Improved Particle Swarm Optimization Method," *IEEE Transactions on Power Delivery,* vol. 30, no. 2, pp. 553-560, 2015.

[9] H. a. I. Dobson, "Cascading Stall of Many Induction Motors in a Simple System," *IEEE Transactions on Power Systems,* vol. 27, no. 4, pp. 2116-2126, 2012.

[10] J. Shaffer, "Air conditioner response to transmission faults," *IEEE Transactions on Power Systems,* vol. 12, no. 23, pp. 614-621, 1997.

[11] A. S. V. A. V. V. N. B. B. a. S. L. M. Paramasivam, "Dynamic Optimization Based Reactive Power Planning to Mitigate Slow Voltage Recovery and Short Term Voltage Instability," *IEEE Transactions on Power Systems,* vol. 28, no. 4, 2013.

[12] WECC, "WECC Dynamic Composite Load Model Specifications," 2015.

[13] \. L. i. L. M. R. D. Quint, "The Composite Load Model, Dynamic Load Modeling and FIDVR Workshop," 2015.

[14] P. M. a. P. P. A. Gaikwad, "Implementation of the WECC Composite Load Model for utilities using the component-based modeling approach," in *IEEE Power and Energy Society Transmission and Distribution Conference and Exposition,*, 2016.

[15] V. V. P. P. a. A. G. P. Mitra, "Load Sensitivity Studies in Power Systems With Non-Smooth Load Behavior," *IEEE Transactions on Power Systems,* vol. 32, no. 1, p. 2017, 2017.

[16] P. M. a. V. Vittal, "Role of Sensitivity Analysis in Load Model Parameter Estimation," in *IEEE Power Energy Society General Meeting*, 2017.

[17] e. a. Chassin D.P., "ARRA Interconnection Planning: Load Modeling Activities," Report-24425 by PNNL, 2015.

[18] e. a. A. Von Meier, "Precision Micro-Synchrophasors for Distribution Systems A Summary of Applications," *IEEE Transactions on Smart Grid,* vol. 8, no. 6, pp. 2926-2936, 2017.

[19] S. A. a. F. J., "High-resolution, time-synchronized grid monitoring devices," Technical Report by NASPI & PNNL.

[20] D. T. Force, "NERC report on distributed energy resources," North American Electric Reliability Corporation, 2017.

[21] S. Report, "Distributed Energy Resources- Technical Considerations for the bulk power system," Docket No AD18-10-000, Federal Energy Regulatory Commission, 2018.

[22] R. Venkatraman, "Combined Transmission-Distribution System (CoTDS) co-simulation modelling and its applications for dynamic studies," PhD Thesis, Iowa State University, 2018.

[23] Z. C. a. D. P. R. Lasseter, "Grid-Forming Inverters: A Critical Asset for the Power Grid," *IEEE Journal of Emerging and Selected Topics in Power Electronics,* 2019.

[24] A. R. M. A. T. C. F. C. J. G. D. S. M. a. T. S. Saltelli, Global Sensitivity Analysis, The Primer, John Wiley and Sons, 2008.

[25] Y. L. F. K. T. R. H. Z. H. Wei Du, "Model Specification of Droop-Controlled, Grid-Forming Inverters (GFMDRP_A)," PNNL-32278, Pacific Northwest National Laboratory, 2021.